NANYANG
TECHNOLOGICAL
UNIVERSITY
SINGAPORE

ADVANCED STRUCTURAL CHARACTERIZATION OF ENERGY STORAGE MATERIALS

DISHA GUPTA

SCHOOL OF MATERIALS SCIENCE AND ENGINEERING

2018

ADVANCED STRUCTURAL CHARACTERIZATION OF ENERGY STORAGE MATERIALS

DISHA GUPTA

SCHOOL OF MATERIALS SCIENCE AND ENGINEERING

A thesis submitted to the Nanyang Technological University
in partial fulfilment of the requirement for the degree of
Doctor of Philosophy

2018

Statement of Originality

I hereby certify that the work embodied in this thesis is the result of original research and has not been submitted for a higher degree to any other University or Institution.

Disha Gupta

Input Date Here	Input Signature Here
06/08/2018	Disha Gupta
Date	Input Name Here

Supervisor Declaration Statement

I have reviewed the content and presentation style of this thesis and declare it is free of plagiarism and of sufficient grammatical clarity to be examined. To the best of my knowledge, the research and writing are those of the candidate except as acknowledged in the Author Attribution Statement. I confirm that the investigations were conducted in accord with the ethics policies and integrity standards of Nanyang Technological University and that the research data are presented honestly and without prejudice.

Dong

Input Date Here
06/08/2018
Date

Input Supervisor Signature Here
Associate Professor Dong Zhili
Input Supervisor Name Here

Authorship Attribution Statement

This thesis contains material from paper accepted at ACS Omega, where I was the first author.

Chapter 7 is submitted as “Electronic and Geometric Structures of Rechargeable Lithium Manganese Sulphate Cathode $Li_2Mn(SO_4)_2$”; Disha Gupta, Aravind Muthiah, Do Minh Phuong, Sankar Gopinathan, Timothy I. Hyde, Mark Copley, Tom Baikie, Yonghua Du, Shibo Xi, Madhavi Srinivasan, ZhiLi Dong; to ACS Omega.

The contributions of the co-authors are as follows:

- Dr Aravind Muthiah and I prepared the manuscript drafts and have equal contributions to the paper. The manuscript was revised by Professor Sankar Gopinathan, Dr Timothy Hyde, Dr Tom Baikie, Assoc. Prof Dong Zhili and Dr Mark Copley.
- I co-designed the study and performed all the laboratory work at the School of Materials Science and Engineering and the Singapore Synchrotron Light Source. I also analyzed the data.
- All sample preparation, diffraction data, electrochemical experiments and X-ray Absorption Spectroscopic studies were conducted by me. The diffraction results were analyzed with the help of Dr Tom Baikie.
- The electrochemical data and X-ray Photoelectron Spectroscopy data were analyzed by Dr Aravind Muthiah.
- Dr Yonghua Du and Dr Shibo Xi assisted in the collection of the X-ray Absorption Spectroscopy data at the Singapore Synchrotron Light Source.
- Do Minh Phuong assisted in the collection of the X-ray Photoelectron Spectroscopy data.

Disha Gupta

06/08/2018

Input Date Here

Input Signature Here

Abstract

Lithium-ion batteries are a promising alternative to the already existing lead batteries, as an efficient, inexpensive energy storage option for the ever increasing demand for energy around the world today. Considering the growing concerns over the environmental impacts of non-renewable energy sources, clean and renewable energy sources is a topic of escalating importance. Lithium being the lightest metal, least dense and providing greatest electrochemical potential, has become an integral part of a battery material component. This thesis aims at studying the structural and chemical properties of some energy storage materials as potential Li-ion cathodes in order to overcome the present drawbacks concerning such materials.

The materials under study in this research involves $LiFePO_4$ (LFP) and Mn-doped $LiFePO_4$ systems – $LiMn_{0.1}Fe_{0.9}PO_4$ (LMFP 0.1), $LiMn_{0.3}Fe_{0.7}PO_4$ (LMFP 0.3), $LiMn_{0.5}Fe_{0.5}PO_4$ (LMFP 0.5). While initial characterization procedures like X-ray Diffraction (XRD), Scanning Electron Microscopy (SEM) and Transmission Electron Microscopy (TEM) have been employed to probe the structure of these materials, the key characterization technique used for analysis of these battery materials have been done using X-ray Absorption Spectroscopy (XAS) studies.

Local electronic and structural changes for LFP, LMFP (0.1-0.5) have been investigated using XAS. For both LFP and LMFPs, the structural comparison has been carried out between two laboratory-synthesized materials using ball milling and flame spray techniques. LFP was also obtained from two commercial sources – Linxi and Targray. Targray LFP showed better electrochemical performance than the Linxi LFP and the XAS studied showed that the structure of Targray LFP matched the literature more closely than the Linxi LFP. The bond length analysis of the Linxi LFP showed much shorter Fe-O bonds than Targray which could hinder the Li-diffusivity and hence effect the performance. The Fe K-edge for both LFPs and LMFPs showed a valence change from 2+ to 3+ while charging and back to 2+ with discharging. Whereas, for low concentrations of Mn, for Mn

K-edge showed no valence change. However, with an Fe:Mn ration of 1:1, partial Mn oxidation was observed. For the first time the P K-edge XAS was also studied to investigate the electronic structure of all the LMFPs electrodes which showed that de-lithiation of all these materials resulted in the hybridization of Fe 3d and P 3p states. Theoretical simulations for near edge XAS data have also been attempted for recreating the model compounds used as reference compounds for the experimental data. These simulations can help in understanding the evolution of the XANES spectra with the inclusion of higher shells, distortion around the absorbing atom, anti-site disorder etc.

Sulphate-based Li-ion battery material, $Li_2Mn(SO_4)_2$ (LMS) was also studied since the sulphate polyanion $(SO_4)^{2-}$ has higher electronegativity compared to $(PO_4)^{3-}$ and achieves higher redox potentials through inductive effects. XAS studies were conducted for the first time for the LMS material for both Mn and S K-edges. However, the electrochemical results showed little redox reactivity and the XAS studies showed very slight change in the structure as well. Therefore, further studies involving X-ray Photoelectron Spectroscopy (XPS) was engaged to study the behavior of this material which showed a possibilty of surface reactions rather than bulk activity.

Lay Summary

Energy and environment are so closely related that sometimes in the quest for a higher standard of living, one ignores the impact it has on the environment. The global energy consumption is increasing multifold and most of the energy comes from burning fossil fuels. This results in the emission of carbon dioxide which creates hazardous effects on our surroundings, especially, global warming. Despite all this, majority of the energy comes from coal, oil and natural gas. However, the good news is that today’s generation is gradually becoming more and more aware of these harmful and perilous effects which are why they are trying to meet the energy demand safely, reliably and affordable. This will definitely require innovation and advanced technology. Besides using renewable energy sources like solar, wind and tide, another great alternative to providing energy whilst maintaining a sustainable and clean environment is the use of batteries. Batteries are electrochemical cells, which generate energy through chemical reactions inside them. This chemical energy can be converted into electrical energy that helps to power all electronic devices to even cars and other heavy vehicles. Among the different batteries available, lithium-ion batteries (LIBs) are highly popular due to its lightweight, large specific energy per weight and most importantly, safety. For this thesis, the main focus is to study the structural changes in Li-ion battery cathode materials. The major factor for influencing the battery energy density as well as accounting for 25% of lithium-ion battery costs depends on the choice of the cathode material. Thus, building better cathode materials is likely to be a crucial driving force towards a clean and green environment.

The key technique used to study these battery materials in this research is called X-ray Absorption Spectroscopy (XAS). This characterization procedure can help in understanding how the material undergoes changes, degradation or distortion by qualitatively and quantitatively providing information about the local structure around a specific atom. This thesis has undertaken the scope of studying one of the most commonly used cathode material $LiFePO_4$ (LFP) using this characterization technique and then extending that study to other potential cathode materials. The other battery materials studied in this thesis are the Mn-doped LFP systems. The focus was to study the changes in the structure of these systems with the insertion of Mn into some of the Fe sites and study the performance of these materials as they charge. The combined structural and electrochemical study of a range of Li-ion battery materials aids in understanding the structural aspects of these materials that lead to long-term stability and for this, there is a requirement to carefully elucidate the chemical changes during the charge-discharge cycle. Therefore, the characterization techniques used to analyze these materials must be advanced and sensitive to the mechanism. The progress in scattering, microscopy and spectroscopy techniques has already provided intriguing insights into the nature of electrochemical processes and kinetics of these energy storage materials.

Acknowledgements

At the very outset of my PhD Thesis, I would like to thank Professor Tim White, Associate Vice President (Infrastructure and Programmes) and Research Director for Engineering and Physical Sciences, President's Office, Nanyang Technological University (NTU), Singapore and Dr Timothy Hyde, Principal Scientist at Johnson Matthey, United Kingdom (JM-UK) for giving me this opportunity to carry out my research in such a prestigious university.

I am deeply grateful to my PhD supervisor from NTU, Assoc. Prof Dong Zhili, for being so positive, supportive and understanding during each step of my project. I am incredibly indebted to my industrial co-supervisor, Professor Sankar Gopinathan, University College London, for teaching me everything that I know about my research today and for being extremely patient with me while I constantly pestered him with innumerable doubts. His conscientious guidance and encouragement have really helped me accomplish this assignment.

I would like to thank Dr Tom Baikie for being an awesome mentor. His constant assistance has helped me proceed in my work much smoother than I would have expected. I am also very thankful to Dr Noelia Cabello for her valuable advice whenever I was stuck with any issues regarding my materials. I would like to extend my deepest thanks to Dr Du Yonghua and Dr Xi Shibo at Singapore Synchrotron Light Source (SSLS) and Dr Pinit Kidkhunthodt and Mr Somboonsup Rodporn at the Synchrotron Light Research Institute (SLRI), Thailand, for giving me hands-on experience with the working of a synchrotron and helping me collect my XAS results over these years. I would also like to thank Prof. Madhavi Srinivasan, Associate Chair (Academic) NTU, for allowing me to use her energy storage laboratory to conduct my synthesis and experiments. My sincere thanks to Dr Srirama Hariharan and Dr Shashwat Shukla for helping me in my initial stages of experimental experience with cells and batteries and giving me the relevant academic exposure towards my research.

I would like to thank all my lab and office mates for creating the perfect research atmosphere and making me feel so comfortable during the entire span of my PhD studies. Special thanks go to my seniors, Dr Rohit Satish and Dr Aravind Muthiah, for their valuable feedback and support whenever I was stuck with any problem during my research work. Also, thanks to my group mate, Yao Bingqing, for helping me collect some last minute data for my thesis. I would also like to acknowledge all the help I received from the academic and technical staff at Nanyang Technological University. I am also so grateful to have met some amazing friends throughout these four years who have helped me grow into a much confident and independent person.

Above all, I am tremendously thankful to my parents for their constant love, support, and sacrifices. Without their faith, guidance, cooperation & encouragement, I would not have made it to where I am today. I would also like to dedicate this thesis to the memory of my grandmother whose role in my life will always remain irreplaceable.

Table of Contents

Chapter 4 Phosphate-based Cathode Material for High Stability 69

Chapter 6 Sulphate-based Cathode Material for Li-ion Batteries 155

Table Captions

Figure Captions

Abbreviations

BM	Ball Milled
BVS	Bond Valence Sum
CN	Coordination Number
DW	Debye-Waller factor (σ^2)
EM	Elemental Mapping
EXAFS	Extended X-ray Absorption Fine Structure
FDMNES	Finite Difference Method Near Edge Structure
FS	Flame Spray
FTIR	Fourier Transform Infrared Spectroscopy
HRTEM	High Resolution Transmission Electron Microscope
LCO	Lithium Cobalt Oxide ($LiCoO_2$)
LIB	Lithium Ion Battery
LMFP (0.1)	Lithium Manganese Iron Phosphate ($LiMn_{0.1}Fe_{0.9}PO_4$)
LMFP (0.3)	Lithium Manganese Iron Phosphate ($LiMn_{0.3}Fe_{0.7}PO_4$)
LMFP (0.5)	Lithium Manganese Iron Phosphate ($LiMn_{0.5}Fe_{0.5}PO_4$)
LMO	Lithium Manganese Oxide ($LiMn_2O_4$)
LMS	Lithium Manganese Sulphate ($Li_2Mn(SO_4)_2$)
LFP	Lithium Iron Phosphate ($LiFePO_4$)
LTO	Lithium Titanium Oxide ($Li_4Ti_5O_{12}$)
NMC	Lithium Nickel Manganese Cobalt Oxide
NMP	N-Methyl-2-pyrrolidone
PVDF	Polyvinylidene fluoride
PXRD	Powder X-ray Diffraction
SEI	Solid- Electrolyte Interphase
SEM	Scanning Electron Microscopy
SIB	Sodium Ion Battery
SLRI	Synchrotron Light Research Institute
SSLS	Singapore Synchrotron Light Source
TEM	Transmission Electron Microscopy

XANES	X-ray Absorption Near Edge Structure
XAS	X-ray Absorption Spectroscopy
XRD	X-ray Diffraction
XPS	X-ray Photoelectron Spectroscopy
Z	Atomic Number

Chapter 1

Introduction and Rationale

This chapter gives a brief overview of the current energy scenario of the world. Even though the majority of the world still depends on non-renewable sources to meet the energy demands, there have been myriad developments in the field of energy storage and batteries that are currently out in the market and slowly take over the ever-growing requirements. This chapter clearly states the objectives, motivation and rationale behind undertaking this project. It also summarizes very briefly an overview of the following chapters, describing the materials used and techniques involved in characterizing those materials. The chapter concludes by trying to understand the impact this research can have on our everyday life. There are innumerable stages that a research idea undergoes to be able to finally affect the practical realm around us but even a step towards that goal is a hope towards a better and cleaner world.

1. Problem Statement

1.1. Energy Issues in the World

With the modernization of the world, there is an enormous demand for energy in every sector [1]. The large-scale use of fossil fuels, which started with the Industrial Revolution, has made these non-renewable sources of energy as the most widely used reservoirs of energy for both commercial and personal purposes. Despite so much advancement in the energy sector, 80% of the world's energy still comes from fossil fuels while renewable energy is less than 14% and the rest is made of nuclear and other energy sources. Energy storage is extremely important for various reasons and applications. However, renewable sources of energy have an inherent flaw of being unpredictable. One of the most challenging aspect is the integration of the renewable energy with electric grid. Thus, energy storage technologies should be directed at accumulating this energy when there is a peak of all this production and augment the grid during high demand.

1.2. How Batteries Can Help

Renewable sources are highly inconsistent and unpredictable. Owing to this issue, it is not enough to just produce clean energy but also develop efficient, viable, and manageable solutions for storing the energy. This is where the role batteries come into play. Batteries have already created a radical change in the society - one would not have a smartphone today if it were not for the advancement in the development of Li-ion batteries (LIBs) and now they are being used to redefine our transportation and energy sectors as well. Thus, today batteries are a crucial building block of a decarbonized economy. Fuel cells [2], capacitors or supercapacitors [3,4] are also alternate solutions for energy storage technologies. However, fuel cells have major drawbacks in terms of safety and operational issues and capacitors and supercapacitors despite their high power densities have low energy densities [5].

In 1991 SONY commercialized the Li-ion battery that revolutionized the whole battery market. Although there are various types of batteries, lead-acid batteries are being used for decades in the automotive industry, especially because they offer an advantage in terms of upfront cost, and have contributed to the largest segment of the market in 2015. On the other hand, Li-ion batteries are mostly used in electronic devices, and the technology is now being adapted for the energy industry. Li-ion batteries have in fact shown a fast growing segment due to their augmented life, recyclability, and environmental friendly properties. They are also appropriate for use in industrial applications where, more than the initial cost of starting material, factors like weight and volume of the material, temperature and maintenance expenses are more crucial focus points.

There is no dearth of research done on lithium iron phosphate $LiFePO_4$ (LFP) since Padhi et al. [6]. However, in spite of being such a great battery cathode, it still faces challenges when it comes to performance – decrease in battery lifetime with high current and voltage rates, increase in internal resistance, capacity fading, anti-site defects leading to an unstable structural framework etc. [7]. The objective of this research is to perform the structural investigation of a commercial LFP material using X-ray Absorption Spectroscopy (XAS) and then extend that to other LFP and Mn-doped LFP systems synthesized using ball milling, and flame spray approaches. In this thesis, a qualitative estimation of the valence of transition metal ions is studied to ensure whether the transition metals are participating in the redox mechanism or behaves like dead weight in the cathode material. Attempt is also made to quantify the structural changes near the absorbing atoms as well. The observed structural variations are then interrelated to the electrochemical performance of cathode materials.

The objectives of the thesis are enumerated in order as follows:

- Developing a characterization methodology using X-ray Absorption Spectroscopy (XAS) to study the combined structural and electrochemical properties of energy storage materials along with other e-beam techniques including X-ray diffraction (XRD), Scanning Electron Microscopy (SEM) and Transmission Electron Microscopy (TEM).
- Using LFP as the model compound to understand the behaviour of phosphate systems and extending it to other systems.

- Developing and designing *in-situ* cell measurement capability to perform *operando* studies.
- Understand degradation processes to improve battery life – monitor structural changes over cycling to predict the failure mechanism.

In order to study the structural degradation, some of the Fe sites in LFP were replaced with Mn - $LiMn_{0.1-0.5}Fe_{0.9-0.5}PO_4$ (LMFPs) and XAS studies were carried out on both the transition metals as well as the polyanion. Mn-based intercalation compounds have been studied previously because manganese is highly abundant, low in price as well as provides high electrochemical performance. Introduction of manganese into cathodes increases the operating voltage window, thus achieving higher capacity. Mn also helps in stabilizing the structure. However, there are still many drawbacks with manganese like dissolution, capacity fading, hysteresis, voltage loss etc. Jahn-Teller (JT) effect, spin change, disproportionate reactions of different valence states of Mn are some of the factors affecting the structure and chemistry. Sulphates and fluorosulphates have traditionally demonstrated electrochemical activity only in Fe based compounds. For the first time through X-ray photoelectron spectroscopy and X-ray absorption spectroscopy studies, the reversible electrochemical mechanism of Mn-based sulphate material, Lithium Manganese Sulphate $Li_2Mn(SO_4)_2$ (LMS), was studied. LMS was found to operate at an average redox potential of 4.85 V confirms the theory that the inductive effect of sulphate groups raises the potential of operation of cathodes.

1.3. Motivation and Challenges

In contrast to $LiCoO_2$ (LCO) and $LiMn_2O_4$ (LMO), LFP provides higher chemical and thermal stability and better safety conditions. Polyanionic structures XO_4^{n-} (where X = P, S, Si, Ge etc.) due to their inductive effect on the M-O-X bond, can tune the redox potentials of transition metals. The phosphate framework, due to their stable structure, can handle higher temperatures compared to oxides and provide safeguard against over-charge and discharge [8]. LFP also has a flexible crystal structure that allows a variety of cation/anion substitutions, which can be very beneficial to enhance its performance. However, these existing batteries still face cost issues and performance challenges, like specific energy, energy density, life cycles, charge efficiency etc. Whatever modifications are made in the battery technology, the core performance still lies in the fundamental behaviour of the electrode materials, dopants, and electrolytes. The complex mechanism of intercalation of Li-ions in and out of the host depends on a multitude of properties. For them to operate successfully, every component inside them must be equally efficient. To achieve long-term stability, there is a requirement to carefully elucidate the chemical and physical aspects. Therefore, the characterization techniques used to analyze these materials must be specific to the structural changes one is looking to probe. The progress in scattering techniques, as well as microscopy and spectroscopy, has already provided intriguing insights into the nature of electrochemical processes and kinetics of these energy storage devices. *In-situ* characterization techniques, even though are a more challenging approach, provide a pivotal role to achieve a better understanding of the operation of batteries. The application of *in-situ* X-ray diffraction and absorption spectroscopy and imaging are considered as some of the most dominant techniques to analyze electrode materials used in electrochemical cells. Advantages like element specificity, short data collection time, very little sample quantity, short-range order probing, and penetrative nature of X-rays are some of the most attractive reasons that make XAS a vital tool for structural analysis for battery materials.

1.4. Research Significance

This thesis aims at characterizing different cathode materials that are used in Li-ion batteries. The primary focus during the four years of research was to undertake a detailed structural investigation of a variety of cathode materials using different characterization techniques XRD, SEM, TEM, and especially XAS. The experimental setup of XAS provides a unique and advantageous opportunity to study the structural and chemical properties of the materials in *operando* mode. This approach helps to understand fundamental reaction kinetics. Both *in-situ* and *ex-situ* XAS studies enable a better understanding to correlate their structural and electrochemical performance of battery materials studied in this thesis.

1.5. Dissertation Overview

The contents of the chapters address the following:

Chapter 1: Introduction and Rationale

This chapter provides a brief summary of the current energy status around the world followed by the objectives and rationale of this thesis. It also gives a dissertation overview of the chapters to follow along with their short synopsis.

Chapter 2: Literature Review

This chapter introduces the working principle and characteristics of lithium batteries. It explains, in detail, the different types of cathode materials – the various synthesis routes and characterization techniques involved in testing their electrochemical and structural performance. The chapter ends with a conclusion stating a summary of gaps in the field of research and something that future research can be focused towards.

Chapter 3: Experimental Methodology

This chapter describes the various characterization techniques used in this work from both the materials as well as the device perspective. Experimental procedures for the synthesis of novel materials, characterization of materials and fabrication of electrodes for the batteries have been detailed. It also lists the softwares used to do all the background corrections, data fittings and analysis.

Chapter 4: Phosphate-based Cathode Material for High Stability

This chapter focuses on the XAS studies of LFP cathode material synthesized via ball milling and flame spray techniques and also compares the results with a commercially procured LFP material. It starts with the introduction of the crystal structure followed by its experimental procedure and initial characterization using XRD, SEM and TEM. After performing electrochemical studies, this material was then subjected to *ex-situ* and *in-situ* XAS studies and their results were compared to see any differences in both modes.

Additionally, the anion P K-edge XAS was also studied for LFP to correlate the bond length changes seen from the cation Fe K-edge XAS.

Chapter 5: High Voltage Mn-doped Cathode Materials

This chapter goes on to explore the effects of Mn-doping into the LFP system. The materials were synthesized using ball milling and flame spray and were subjected to similar characterizations, as used for LFP in Chapter 4. With the different concentration of Mn doping, the changes around the Fe and Mn environment were studied using XAS. Additionally, for the first time the P K-edge XAS was also studied for all the Mn-doped LFP materials to observe any effects on second shell environment due to the $(PO_4)^{3-}$ structure.

Chapter 6: Sulphate-based Cathode Material for Li-ion Batteries

Having studied the phosphate-based Li-ion battery materials in the previous chapters, this Chapter tries to divulge into the sulphate-based materials using the same analysis techniques. The material under study in this Chapter is $Li_2Mn(SO_4)_2$. XAS studies for both, the cation Mn K-edge and the S K-edge of the sulphate polyanion, have been adopted to study the structural and electronic geometry around the absorbing atoms. XAS studies for this system has been carried out for the first time and thus it provide useful insights into considering such high voltage sulphate-based materials as future cathodes for Li-ion batteries.

Chapter 7: Impact, Implications and Future Work

This chapter provides a general conclusion of the findings of this study. It also shows some results that are purely reconnaissance based that did not warrant a complete chapter but did help in leading to apprehend the materials under study in this thesis. The chapter ends with some future work that will be required to achieve the target of building a complete acumen of the results obtained via X-ray Absorption Spectroscopy techniques that can help in commercializing the materials studied in this thesis.

1.6. Findings and Outcomes/Originality

This research leads to several novel outcomes:

- LFP was chosen as a model material to investigate both *ex-situ* and *in-situ* XAS studies. For the *in-situ* studies, three different types of cell window tapes were experimented with – kapton tape, the commercially available 3M brand tapes and polypropylene tape (PP). The kapton tape absorbed majority of the X-rays thus reducing the XAS spectrum intensity extremely low especially for the low edge energies. The 3M tape had too much sulfur contamination, which interfered with the data collection especially in the S and P K-edges. The PP tape worked best for all our samples at different synchrotron facilities without showing any contamination, electrolyte leakage or absorption of excessive X-rays. This tape was thus optimized for use, not only for *in-situ* but also for the *ex-situ* experiments, for sealing the electrodes and it worked perfectly. Secondly, most of the electrodes showed self-discharge within hours, which posed an issue to conduct the *ex-situ* experiments with accuracy. Thus, the experimental procedure had to be modified. It was found that after cycling the cells to the desired voltage and disassembling the cells, if the electrodes were washed in dimethyl carbonate (DMC) multiple times and dried and sealed properly, it stops the Li-diffusivity and these electrodes could be used even months later for XAS studies. This method gave results that were almost comparable to the *in-situ* data thus helped in maximizing the obtained beamtime and reduce errors that usually arise from *in-situ* measurements like leakage of electrolyte, absorption of X-ray intensity etc.

- The results obtained from Mn-doped LFP systems were helpful in establishing relation between its electrochemical studies and its electronic and geometric changes observed from XAS results. Yamada at al. [9] reported in their work on prepared by chemical oxidation that there is severe local lattice deformation around Mn^{3+} (Jahn-Teller effect) at high Mn content therefore focus was given to low Mn concentrations to see if any similar effects were observed. It was found that for very low Mn concentrations (Mn = 0.1, 0.3), Mn did not contribute to the charge compensation but still showed changes in structure, while for an equal Mn/Fe concentration, a partial redox reaction of

Mn^{2+}/Mn^{3+} was also observed. The changes around the Mn absorbing atom for no oxidation changes was thus suspected to be the spin change from high to low spin with charging.

- The behavior of Mn was also studied in a sulphate-based cathode material using XAS techniques. Earlier studies on $LiFe_2(SO_4)_2$ (LFS) showed electrochemical activity with XAS studies showing the valence change of Fe from 2+ to 3+ . Therefore, studies were continued using the Mn analogous compound using XAS and XPS studies to comprehend the bulk and surface reactions. However, LMS did not show as good redox activity as LFS which was further ascertained using XAS, however, XPS results did show changes in the Mn oxidation, thus proving that the slight redox activity that is seen during cyclic voltammetry (CV) and galvanostatic charge discharge (GCD) might be the due to the surface reactivity of LMS.

Overall, the degradation of battery materials with the inclusion of manganese, using a characterization methodology centered on mainly XAS studies were employed and studied during the course of this entire research work.

References

[1]. Le Gallic, T., E. Assoumou, and N. Maizi, Future demand for energy services through a quantitative approach of lifestyles. Energy, **2017** 141:p. 2613-2627.

[2]. Behling, N.H., Fuel Cells: Current Technology Challenges and Future Research Needs. Fuel Cells: Current Technology Challenges and Future Research Needs, **2013**:p. 1-685.

[3]. Sharma, P. and T.S. Bhatti, A review on electrochemical double-layer capacitors. Energy Conversion and Management, **2010** 51 (12):p. 2901-2912.

[4]. Wang, G.P., L. Zhang, and J.J. Zhang, A review of electrode materials for electrochemical supercapacitors. Chemical Society Reviews, **2012** 41 (2):p. 797-828.

[5]. Miller, J.R. and A.F. Burke, Electrochemical Capacitors: Challenges and Opportunities for Real-World Applications. Electrochemical Society Interface, **2008** 17 (1):p. 53-57.

[6]. Padhi, A.K., K.S. Nanjundaswamy, and J.B. Goodenough, Phospho-olivines as positive-electrode materials for rechargeable lithium batteries. Journal of the Electrochemical Society, **1997** 144 (4):p. 1188-1194.

[7]. Tarascon, J.M., Key challenges in future Li-battery research. Philosophical Transactions of the Royal Society a-Mathematical Physical and Engineering Sciences, **2010** 368 (1923):p. 3227-3241.

[8]. Song, Y.N., P.Y. Zavalij, M. Suzuki, and M.S. Whittingham, New iron(III) phosphate phases: Crystal structure and electrochemical and magnetic properties. Inorganic Chemistry, **2002** 41 (22):p. 5778-5786.

[9]. Yamada, A., Y. Kudo, and K.Y. Liu, Phase diagram of $Li_x(Mn_yFe_{1-y})PO_4$ (0 <= x, y <= 1). Journal of the Electrochemical Society, **2001** 148 (10):p. A1153-A1158.

Chapter 2

Literature Review

The goal of this chapter is to develop an understanding of the current status of research on cathodes through a comprehensive review. It begins by providing a basic understanding of the working of lithium ion batteries and its applications in the current era as well as moving forward. This chapter also presents an inclusive research on some of the important battery materials out in the market today and under research. Subsequently, the choice of phosphates and sulphates for this work has been reasoned and finally, the challenges facing such cathodes has been chartered.

2. Introduction

2.1. Background

In 1799, the Italian physicist and chemist, Alessandro Volta, invented the voltaic pile by stacking copper and zinc discs on top of each other separated by pieces of cloth soaked in salt water. This is also considered as the first definitive battery; however, it only offered a short battery life of maximum one hour. Not long after the Voltaic pile was created that William Cruickshank improved the design by laying the plates horizontally in a slotted box which helped prevent the electrolyte from leaking and causing shorts between plates. This was known as the Trough battery. In 1836, John Frederic Daniell pushed the battery further with his Daniell Cell. This cell's defining feature was the use of a porous barrier between two different electrolyte solutions. A copper cathode sits inside a porous earthenware pot filled with copper sulphate. This pot is then submerged inside a container filled with zinc sulphate and then circled by the zinc anode. The porous earthenware allows ions to pass between the electrolytes and hydrogen bubbles are prevented from forming. This greatly increased the lifespan compared to a Voltaic pile. All these batteries are considered *primary* which means once their chemical reactions are depleted, they need to be replaced. While a *secondary* battery can be recharged multiple times and can be used without being replaced. In 1859, French physicist, Gaston Planté, created the first rechargeable battery using a lead anode and a lead dioxide cathode immersed in sulphuric acid. Lead-acid batteries were first used to power lights for train carriages and was an excellent feature, however, its weight and size made it impractical for most uses. However, further modifications were made to the Planté cell in terms of weight and capacity in the following years. In 1866, French scientist Georges Leclanché invented the Carbon-Zinc Battery, composed of a zinc anode with a manganese dioxide cathode wrapped inside a porous material and ammonium chloride solution as the electrolyte. But in 1886, the German scientist, Carl Gassner, further developed this cell by substituting the liquid electrolyte with a paste-like texture, thus, presenting to the world the first dry cell battery. In 1899 the Swedish scientist, Waldermar Jungner, invented the Nickel-Cadmium rechargeable battery using nickel and cadmium electrodes soaked in a potassium hydroxide solution. This also became the first battery to make use of an alkaline electrolyte, thus providing higher energy density than the lead-acid battery. In 1903, American scientist, Thomas Edison, improved the Ni-Cd battery by using iron anode, nickel oxide cathode and potassium chloride as a conductor. This battery found great use in the industrial and railroad around that time since it was strong enough to survive overcharged and uncharged periods. Lew Urry at the Eveready Battery Company developed the alkaline-manganese battery, commonly known as the alkaline battery, in 1949. These alkaline batteries lasted five to eight times longer than zinc-carbon cells, their predecessors. However, as larger applications of batteries were being contemplated, the safety and large quantity of cells had become a more significant consideration.

The first step in tapping the actual potential of Li-ion began in the year 1912 by Gilbert Newton Lewis [1]. It was not until the early 1970's that the first lithium ion non-rechargeable batteries were made commercially available, this was proposed by M. S. Whittingham at Exxon [2]. These batteries were made with TiS_2 as cathode and Li metal as the anode, while the positive cathode worked well, the lithium metal anode was shown to have uneven dendrite growth during cycling leading to passivation and instability phenomena at its interface. One way of overcoming the problem was to replace the lithium anode by a nonmetal compound, which was capable of storing and exchanging a large quantity of lithium ions. In this way, rather than lithium plating and stripping as in the conventional systems, the electrochemical process at the negative electrode would be the uptake of lithium ions during charge and their release during discharge. If another nonmetal Li-accepting compound, was used as the positive electrode, the entire electrochemical process would then involve the cyclic transfer of lithium ions between the two electrodes. This concept was termed as the "rocking chair" as Li-ions rock from one side to the other. This was first introduced by Armand in 1980. A significant advancement in the development of lithium batteries came with the discovery of intercalation materials where lithium was used as an insertion material for rechargeable batteries. In 1981, Dr Akira Yoshino started his research on secondary batteries and in 1985 he invented the $C/LiCoO_2$ battery. This invention has resulted in identifying Yoshino as the true inventor of the lithium ion battery [3]. In 1985 Rachid Yazami et al. [4] showed the electrochemical properties of lithium intercalation in graphite. Around the same time, Dr John Goodenough proposed the materials under the family Li_xMO_2 (M = Co, Mn or Ni) as a cathode material [5] .

2.2. Battery and Working Principle

Batteries are an assemblage of electrochemical cells used for the conversion and storage of energy. They store energy in the form of chemical energy which can be converted to electrical energy by redox reactions at the electrodes. A battery consists of three major components – cathode (positive electrode), an anode (negative electrode) and the electrolyte separating these two electrodes. The electrolyte should have good ionic conductivity. When a voltage is applied between these electrodes, the chemical processes occurring on these electrode materials create a flow of charge flow through the electrolyte, thus providing electrical energy to the system. Batteries can be classified into two types – a primary battery which gives irreversible electrical energy, i.e., once the reactant is exhausted, the battery cannot be reused; a secondary battery which are rechargeable and can repeatedly produce energy. The schematic diagram of the components of a lithium-ion battery and the processes occurring during a charging-discharge process is shown in **Figure 2-1**.

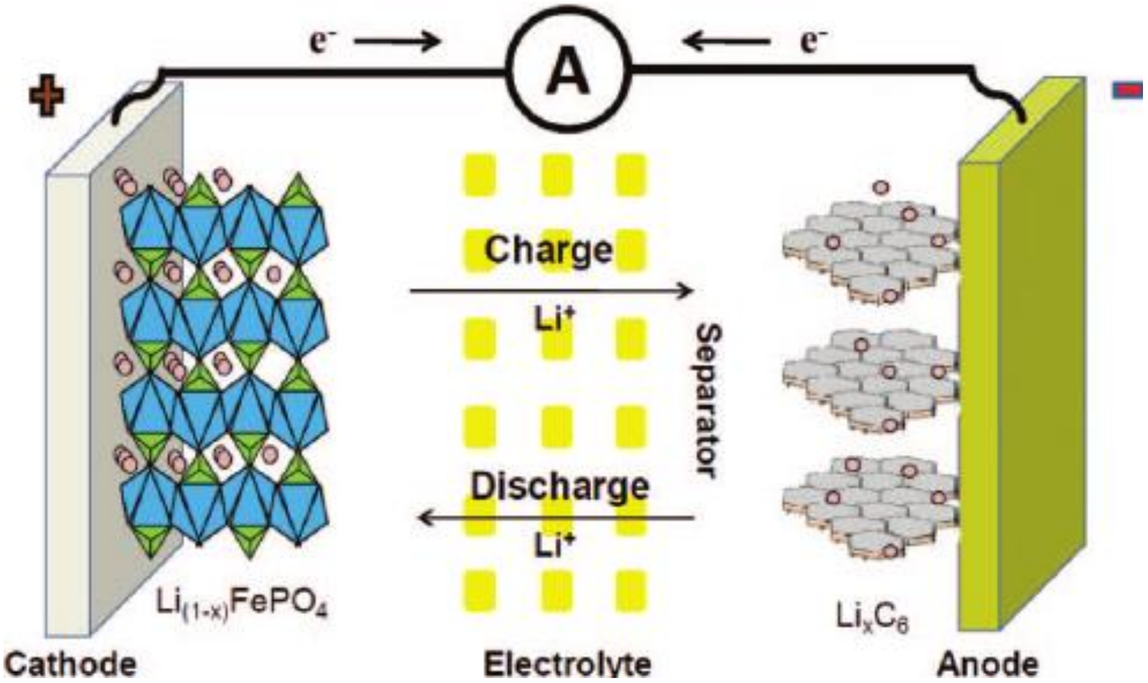

Figure 2-1 A typical Lithium-ion battery showing the migration of Li^+ ions from the cathode to anode and vice versa during charging and discharging respectively [8].

Lithium being the charge carrying species must interact with both cathode and anode. A crucial question associated with the working of Li-ion batteries is the selection of electrolyte solutions. The electrolyte used commonly is a mixture of a lithium salt dissolved in an organic solvent. An electrolyte needs to be ionically conductive rather than being electrically conductive and must support ion transportation between the anode and cathode. Additionally, it should not reduce or oxidize at different voltage range. Intercalation is a phenomenon in which some solid-state structures can accommodate another chemical species without disturbing their principle structure like voids, pores etc. Layered structures usually display the phenomena of intercalation since they have weak ionic bonding between the layers, therefore, they can distort slightly to accommodate certain ionic species. When discharging, lithium ions from anode move to the cathode. Lithium is ionized from metal to positive ions and electrons are injected into the outer circuit. While charging, the lithium is pushed back to the anode from the cathode. When it is saturated with lithium, then charging is complete. A porous flexible material is soaked in the electrolyte and placed in between the cathode and anode, which acts as the separator and is permeable to Li^+ ions. The following reaction equations show the charging reactions on both the anode and cathode considering an LCO cathode and graphite anode:

$$LiCoO_2 \underset{\text{Discharge}}{\overset{\text{Charge}}{\rightleftarrows}} Li_{(1-x)}CoO_2 + x\,Li^+ + x\,e^- \qquad [i]$$

$$C + xLi^+ + xe^- \underset{\text{Discharge}}{\overset{\text{Charge}}{\rightleftarrows}} Li_xC \qquad [ii]$$

2.3. Different Cathode/Anode Materials

For commercial use in Li-ion batteries, the cathode material should possess certain key features for it to be incorporated in a successful battery material. It should have mechanical and chemical stability over time and temperature, high energy density, high power density, low in cost, safe to operate and a good cycle life. Also, the cathode material should have high lithium intercalation, low diffusion barrier, good conductivity, high capacity and a stable structure to prevent any structural anomalousness during charge/discharge process. **Figure 2-2** represents some of the common cathodes with respect to their discharge potential and specific capacities. While graphite has been used as the anode since the commercialization of batteries since the 1990s, the cathode has undergone many different formulations using mixed metal oxides, phosphates, sulphates etc. Keeping all these parameters in mind, a brief literature review has been presented for a variety of positive materials have been developed and researched over the last two decades.

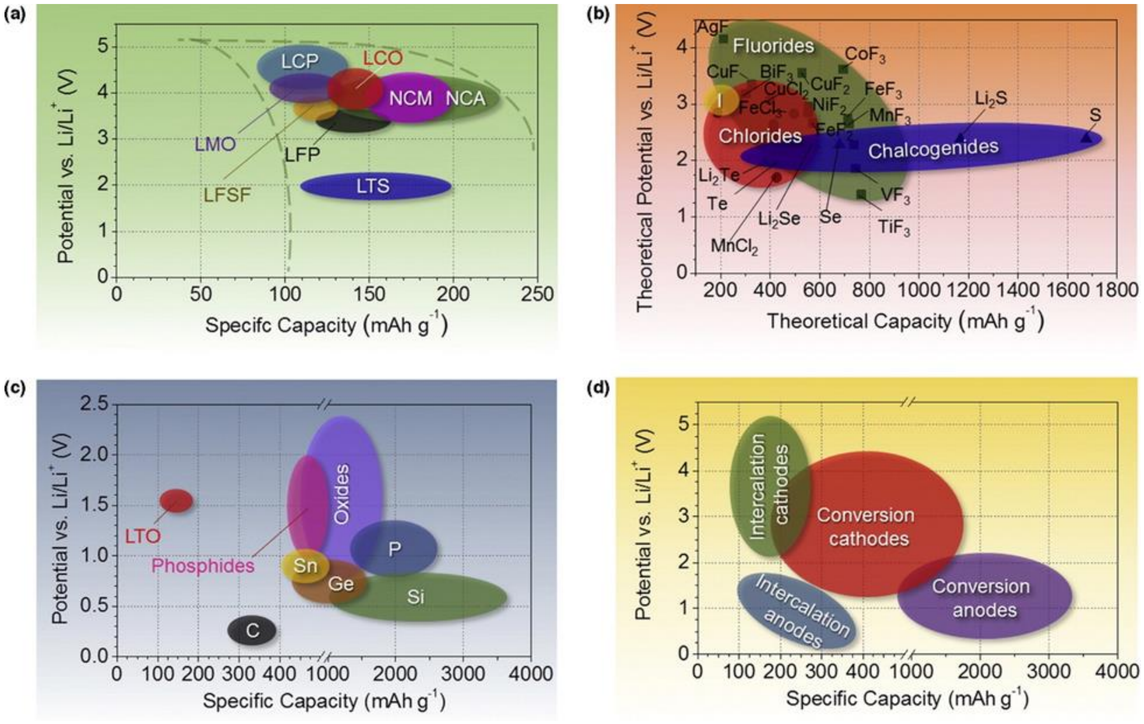

Figure 2-2: Discharge potentials and specific capacity of some of the most common (a) intercalation-type cathodes (experimental), (b) conversion-type cathodes (theoretical), (c) conversion type anodes (experimental), and (d) an overview of the average discharge potentials and specific capacities for all types of electrode [9].

2.3.1. Layered Lithium Transition Metal Oxides – $LiCoO_2$ (LCO)

Layered lithium transition metal oxides which can be generally represented as $LiMO_2$ (M=Co, Ni or Mn) are intercalation compounds that have been a popular study for cathodes materials for lithium-ion batteries. As stated above, LCO was one of the earliest and most dominant layered commercial cathode materials. LCO has the $NaFeO_2$ structure-type with the oxygen in a cubic closed-packed arrangement [6] as shown in **Figure 2-3**. The octahedral sites are occupied by Li and Co ions in alternating layers in a cubic close-packed (ccp) oxygen array, to form a structure with overall hexagonal symmetry (space group R-3m). When the entire lithium is removed from LCO, the oxygen layers rearrange themselves into a closed packed hexagonal structure as in CoO_2.

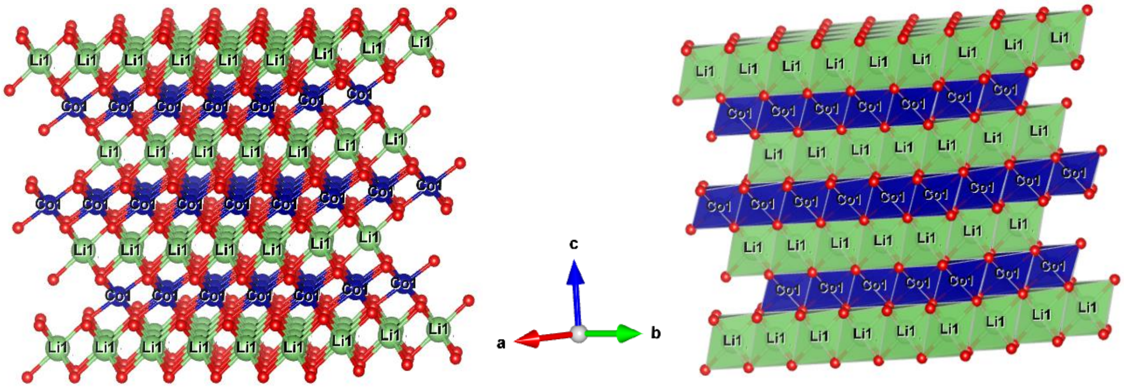

Figure 2-3 Crystal structure of $LiCoO_2$. The green spheres represent lithium; blue spheres represent cobalt while red spheres represent oxygen atoms.

Due to its high cost, environmental impact and chemical hazards associated with cobalt, extensive investigation have been conducted in the past few decades to find improved versions of LCO. LCO was first published by Mizushima et al. [6] and further studied by involving different synthesis techniques like solid-state , ultrasonic spray pyrolysis process, combustion synthesis, co-precipitation method, molten salt synthesis, freeze-drying method, hydrothermal synthesis, mechano-chemical, and microwave synthesis and other methods [10-19]. In spite of its high theoretical capacity of 274 $mAhg^{-1}$, the reported functional discharge capacities of LCO are comparatively low, in the range of 135-150 $mAhg^{-1}$. LCO is normally charged to a delithiated state of $Li_{0.5}CoO_2$ in order to obtain a good cycle stability. The cycling behavior of LCO in the range of 3 – 4.5 V usually shows a rapid capacity fading which is ascribed to irreversible structural changes or severe volume changes of the material. In order to enhance the conductivity, carbon coating and various oxide coatings including $AlPO_4$, Al_2O_3, $FePO_4$, Li_2PO_2N, $Li_4Ti_5O_{12}$, MgO, SrO, TiO_2 have also been studied [20-24]. Various characterization techniques have been applied including X-ray diffraction (XRD), Scanning Electron Microscopy (SEM), Transmission Electron Microscopy (TEM) . Structural changes were observed by *in-situ* X-ray diffraction, *in-situ* XAS, Raman spectroscopy, *in-situ* NMR and XPS analysis to correlate the changes with capacity fading and cycle number [25-32].

The key limitations are its low thermal stability, high cost, quick capacity fading at high current rates or during deep cycling, the high cost of cobalt, lowest thermal stability compared to other metal oxides etc. [33]. Thermal runaway is also the main worry, for example, in the grounding of all Boeing 787 aeroplanes in 2013 [34]. LCO usually shows thermal runaway above 200˚C. It also suffers from deep cycling which induces lattice distortion from hexagonal to monoclinic symmetry, which results in poor cycling performance [35].

2.3.2. Mixed-Metal Oxides (NMC/NCA) Cathode Materials

$LiNi_xCo_yAl_zO_2$ (NCA) [18] and $LiMn_xNi_yCo_zO_2$ (NMC) [45] are improved versions of $LiMO_2$ layered cathode materials that have gained popularity over the last few years as second generation materials. Typically, lithium-ion NCA batteries use a combination of 80% nickel, 15% cobalt and 5% aluminium while NMC batteries use one-third equal parts nickel, manganese, and cobalt. These materials have found a steady market because of their much better stability compared to the existing ones.

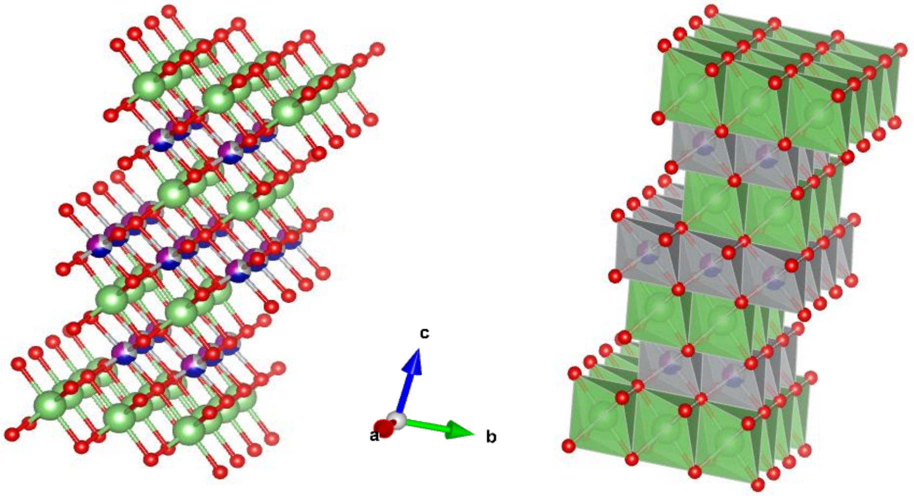

Figure 2-4 Crystal structure of NMC. The green spheres represent lithium; blue/grey/purple spheres represent mixed transition metals while red spheres represent oxygen atoms.

The fractional substitution of Co by Ni and Mn in NMC cathodes opens up the prospect of different cation configurations within the crystal. The nickel, manganese and cobalt ions of $LiNi_{1/3}Mn_{1/3}Co_{1/3}O_2$ are randomly distributed in the transition metal layers without any site preference. Each element in this mixture plays a significant role. The nickel is the electrochemically active species, with its oxidation state retreating back and forth between 2+ and 4+; the manganese remains in 4+ oxidation state and is responsible for the stability of the structure throughout the cycling process, and the cobalt helps in the organization of the lithium and nickel ions. Their superior thermal stability and reversible capacity have developed into a strong candidate for high power rechargeable Li-ion batteries. NMC was first reported by T. Ohzuku et al. in 2001 [36]. This material crystallizes in a layered structure based on a CCP array of oxygen atoms with alternating layers of lithium and layers containing Mn^{4+}, Ni^{2+} and Co^{3+} (**Figure 2-4**). The Ni^{2+} and Co^{3+} cations in $LiNi_{1/3}Mn_{1/3}Co_{1/3}O_2$ act as the electrochemically active species during cycling. While the Mn^{4+} cations are electrochemically inactive, they are generally thought to increase the stability of the material framework. Different synthesis approaches have been undertaken to create NMC including spray pyrolysis, spray-drying, hydrothermal, combustion, wet chemical [36-39, 64]. XRD analysis of NMC gives lattice constants of a = 2.867 Å and c = 14.246 Å [36]. SEM micrographs show that the material particles are made up of clusters of small crystallites. For temperatures around 700 ˚C were more spongy and irregular as compared to highly crystalline rice-like shaped particles at 900 ˚C [38]. TEM analysis also confirms the size and crystallinity as observed from SEM [39]. Other characterization techniques have also given a good depth of knowledge about the structural and electrochemical physiognomies of NMC with different cycling rates, voltages, temperatures and synthesis routes. These include XPS, XAS, Raman and FTIR [40-42]

The cathode material NMC attracted a lot of attention due to its low cost, high capacity and lower toxicity. It has a high specific capacity of around ~160 $mAhg^{-1}$, can operate in the higher voltage range of 2.5–4.4 V and low to mild thermal behaviour during charging [43-44]. In addition, since Mn in NMC always exists in 4+ oxidation state, it avoids the Jahn–Teller effect. However, even though NMC demonstrations excellent properties, it does suffer from some drawbacks such as low tap density and relatively poor cycling stability [155].

On the other hand, $LiNi_{0.8}Co_{0.15}Al_{0.05}O_2$ (NCA) cathode has found relatively widespread commercial use especially in Panasonic batteries for Tesla's electric vehicles. NCA has shown to have a high discharge capacity (~200 mAh/g) and longer cycle lives compared to conventional Co-based oxide cathode. However, it was reported that capacity fade may be severe at elevated temperature (40–70°C) due to solid electrolyte interface (SEI) growth and micro-crack growth at grain boundaries [45-48].

2.3.3. Spinel Lithium Transition Metal Oxides – $LiMn_2O_4$ (LMO)

Manganese dioxide (MnO_2) has been exploited for many years as a battery grade electrode material. The large number of structure types that exists in the lithium-manganese-oxide system is attractive from the point of view that it offers a wide selection of materials [7,49]. On the other hand, the structural versatility of the system can make the processing of a desired single-phase product with a specific composition difficult, particularly when scaling-up the process to the quantities required by the battery industry. The early interest in spinel electrodes for lithium battery applications was spearheaded predominantly by the discovery of the stable framework of $A[B_2]O_4$ and $LiMn_2O_2$ provided a stable host structure for the electrochemical insertion and extraction of lithium. $LiMn_2O_4$ takes the spinel structure with Fd3-m space group as shown in **Figure 2-5.** The edge-shaped MnO_6 octahedral units provide strength and stability to the structure. It provides an uninterrupted and energetically accessible three-dimensional interstitial space of face-sharing tetrahedral Li sites and empty octahedral (16c) sites. Li is found to occupy the tetrahedral 8a sites while Mn is located in octahedral 16d sites in a CCP array of oxygen anions. During the diffusion of Li ions through the structure, they first move from the 8a to 16c and again to following 8a site in a manner that permits 3-dimensional Li-ion diffusion.

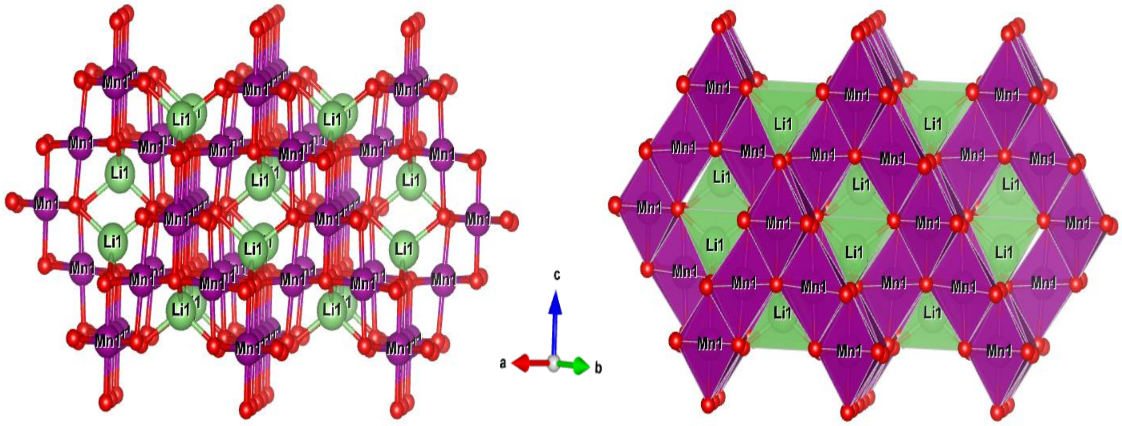

Figure 2-5 Crystal structure of $LiMn_2O_4$. The green spheres represent lithium; purple spheres represent manganese while red spheres represent oxygen atoms.

LMO has a theoretical capacity of 148 mAh/g, which is quite lower than LCO and its derivatives, yet it became a prospective cathode candidate in the study due to its high natural abundance of Mn, non-toxicity, environmentally-benign and low-cost as compared to LCO. Various synthesis processes were investigated to develop LMO, including, solid-state, sol-gel, hydrothermal, combustion and flame-spray [50-54]. Many researchers [55-58] who investigated the electrochemical properties of $LiMn_2O_4$, reported discharge capacity of around 100-120 $mAhg^{-1}$ which is about 65-80% of its theoretical capacity (148 $mAhg^{-1}$). Therefore to enhance the structural and electrochemical stability, partial substitution with metals (M=metals like Zn, Al, Cr, Co etc) [59-61] have been widely investigated. Structural modification, like, coating LMO with LFP, Au, Li_3PO_4, ZnO were also studied to improve the cycling behaviour [62-63,65]. XRD analysis has confirmed LMO to have spinel structure with a space group of Fd-3m [55,75]. The structure and physicochemical properties of spinel $LiMn_2O_4$ were also investigated using other characterization techniques like SEM, TEM, *ex-situ* and *in-situ* XAS, XPS, Raman Spectroscopy and TG-DTA [66-71].

However, the performance of LMO was not satisfactory because of factors like Mn dissolution [72-74] into the electrolyte, development of micro-strains during charge-discharge, which tends to display a capacity fade even in the 4V region, oxygen loss from the delithiated LMO, and even formation of tetragonal LMO on the surface especially at the fast C-rates [76-77]. Mn has a tendency to leach out during cycling and this Mn dissolution occurs due to a disproportionation reaction of Mn^{3+} ions to form Mn^{2+} and Mn^{4+} [28-31]. It is also important to note that all Li–Mn–O cathodes using the $Mn^{4+}/^{3+}$redox couple suffer from Jahn–Teller (JT) effect caused by Mn^{3+} ions at the octahedral sites, which results in a tetragonal distorted phase LMO thus causing a rapid loss of capacity [78-81].

2.3.4. Olivine Lithium Transition Metal Phosphate – $LiFePO_4$ (LFP)

Lithium iron phosphate ($LiFePO_4$ or LFP) has attracted a lot of attention in research as well as industrial applications for being economical, environmental friendly, having high theoretical capacity of 170 mAh/g, flat discharge voltage 3.4 V, low cost, and excellent thermal and chemical stability**.** Ever since the first study of $LiFePO_4$ olivine structure by Padhi et al. in 1997 [82], this cathode material has been the centre of almost all battery research. The crystal structure of $LiFePO_4$ comprises of octahedral LiO_6 and FeO_6 and tetrahedral PO_4 with Pmna space group and an orthorhombic unit cell. The tetrahedral PO_4 groups are linked to them by a common edge with one FeO_6 octahedron and two edges with LiO_6 octahedra. The Li-ions form a 1-dimensional mobility [001] in the framework, which makes the Li-ions to intercalate and deintercalate easily (**Figure 2-6**).

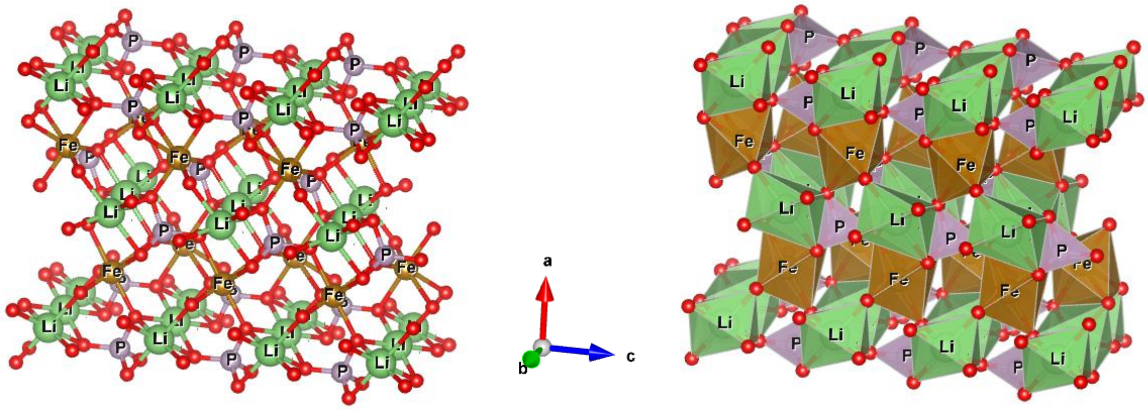

Figure 2-6 Crystal structure of $LiFePO_4$. The green spheres represent lithium; grey spheres represent phosphorus, brown spheres represent iron, while red spheres represent oxygen atoms.

Due to the extensive research was done on LFP, a lot of reviews have been published on the various synthesis and characterization techniques used to analyze this material. Y. Zhang et al. [83] and W.J Zhang et al. [84] have reviewed the different routes taken to synthesize LFP over the years like solid-state, sol-gel method, microwave, hydrothermal, carbo-thermal reduction, spray pyrolysis among other synthetic methods [97-101]. A study of how different synthesis processes affect the electrochemical performance of LFP has also been studied by Franger et al [85]. To improve the conductivity of LFP, various coatings were also applied on LFP SiO_2-coating [86], ZrO_2-coating [87], CeO_2-coating [88-90] etc., however, carbon-coating proved the most effective [91]. Zhao et al. [92] reported an initial capacity of 157 $mAhg^{-1}$ and a capacity loss of ~3.5% after 50 cycles for LFP by solid state synthesis at 650°C. Various team of researchers have reported the positive effect of doping on the rated capacity and cyclic stability of $LiFePO_4$. Among the studied dopants some of them include Nb^{5+}, Zr^{4+}, Ti^{4+}, Mo^{6+}, Mg^{2+}, Cr^{3+}, V^{5+}, Co^{2+}, Cu^{2+}, Cl^-, F^- [93-95]. X-ray diffraction studies and Rietveld refinement on differently prepared LFP have mostly shown similar results with the following parameters: Pnma, a= 10.333, b= 6.011, c= 4.696 [97]. Microscopic techniques like SEM and TEM have also applied to study mainly the surface morphology in terms of particle size, grain size, coating effect, agglomeration etc [83-85] . FTIR and Raman Spectroscopy [102-104] techniques have helped in performing the surface analysis and different modes of vibration, bending and stretching, due to the interaction/deintercalation of ions inside the structure. *In-situ* and *ex-*

situ structural characterization using spectroscopic techniques, mainly, XAS has been extremely helpful in investigating the structure from a bulk perspective. Being element specific, XAS helps to resolve the change in the arrangement of the different atoms in the material in both *ex-situ* and *in-situ* modes [105-109]. Other characterization tools like XPS, DFT, NMR and PDF and Mossbauer study also provide in-depth information about the structure and performance of differently synthesized LFP developed over the years [110-118].

Compared to LCO, LFP avoids issues like cobalt's cost and environmental concerns. It experiences a slower rate of capacity loss and thus has a better calendar life than other Li-ion battery materials [119]. Even after one year of shelf life, LFP has much better energy density than LCO. LFP cells have better thermal and chemical stability, which improves battery safety. LFP is an intrinsically safer cathode material than LCO and LMO. The Fe-O-P interactions are stronger than the Co-O bond so that when used beyond its capacity, the oxygen atoms are much tougher to take out.

However, LFP has a low electrical conductivity due to which its theoretical capacity can be attained only at a low rate capability, or a high temperature. Anti-site defects also lead to low diffusion rate of Li-ions wherein some Fe goes into the Li sites giving rise to detrimental properties [120-123]. Thermal stability and reactivity are critical parameters that should be analyzed well while using LFP, like the charged product, $FePO_4$ will transfer to the spinel phase under high pressure. Despite these problems, lithium-ion batteries still have enough major advantages because of which they are being implemented for large-scale grid storage.

2.3.5. Spinel Lithium Titanium Oxide Anode - $Li_4Ti_5O_{12}$ (LTO)

Considerable efforts are being made to improve the electrode materials appropriate for use in the current cutting-edge battery market. Even though the great emphasis is being given to cathode development, new anode materials also have to be developed that can work at higher potentials compared to the currently used carbon or graphite electrodes. Even though graphite has monopolized the battery anode market yet we still face some issues with it when it comes to EVs and HEVs. The spinel $Li_4Ti_5O_{12}$ (LTO) is a promising candidate because it permits insertion of 3 Li atoms per unit at a potential of 1.5 V [124-125]. It can be crystallographically more accurately labelled as $[Li]_{8a}[Li_{1/3}Ti_{5/3}]_{16d}[O_4]_{32e}$. This formula indicates its atomic occupations. The titanites have a spinel structure where Li occupies tetrahedral (8a) and octahedral (16c, 16d) sites, Ti is located along with Li in a specific ratio, at the 16d sites of a cubic unit cell (Fd3¯m) (**Figure 2-7**).

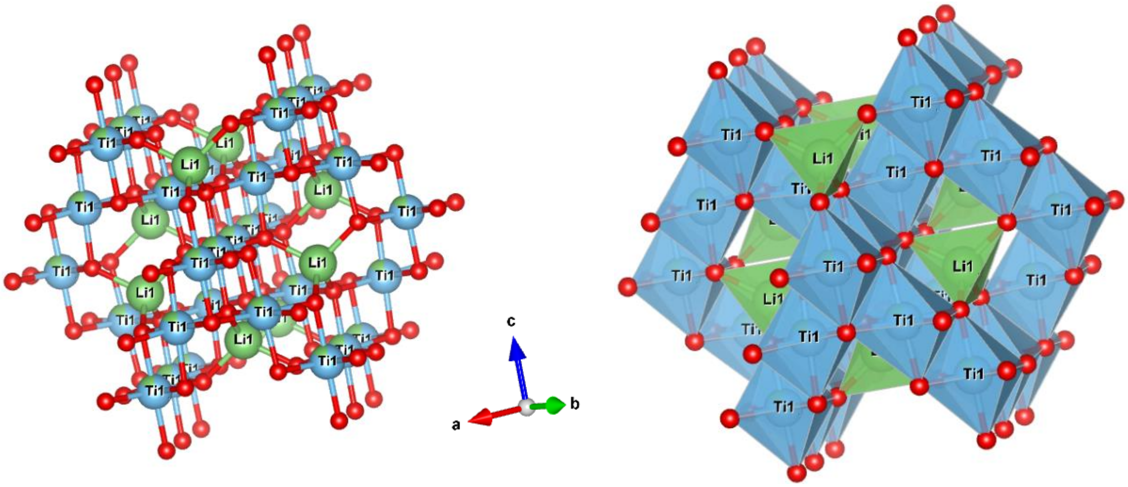

Figure 2-7 Crystal structure of $Li_4Ti_5O_{12}$. The green spheres represent lithium; blue spheres represent titanium while red spheres represent oxygen atoms.

Various synthesis routes have been implied for making LTO including conventional ball milling, sol-gel, solid-state calcination [124,126-131]. Hydrothermal synthesis provides a new approach to the making of nanostructured materials thus offering easy control of various morphologies a novel microwave technique has benefits of lower temperature and shorter reaction time , while combustion process has the advantages of sol-gel as well as solid-state reactions [141-142]. It can be found that the conductivity and electrochemical performance of LTO can be improved by doping some ions like (Co^{3+}, Mg^{2+}, Fe^{3+}, Ni^{3+}, Mn^{3+}, Al^{3+}, Cr^{3+}, etc.) [132-140]. Characterization techniques, like XRD, SEM, TEM, Raman, XAS have also been involved to see the structural and electronic changes in LTO with various synthesis processes and surface modification done [141-143].

Spinel LTO has attracted great attention as a superior electrode and supercapacitor material because of its high lithium mobility and its lack of structural changes during charge-discharge cycling. Even though Ti has a high raw material cost, low voltage and lower capacity (175 mAh/g and 600 mAh/cm^3 theoretical), it has high thermal stability [144], high cycle life, high volumetric capacity. Since phase change during lithiation/delithiation is almost negligible (0.2% change in volume), LTO is considered as a “zero strain” material [145]. LTO can operate in a potential window above 1V due to its high equilibrium potential (~1.55 V vs. Li/Li+). This avoids the formation and growth of the anode SEI, which can slow Li insertion. LTO is also extremely safe because of its high potential inhibits Li dendrite formation.

Unfortunately, LTO anodes suffer surface reactions due to the reaction between the LTO active surface and its organic electrolyte [146]. Carbon coating can help suppress this, however, there is a possibility of carbon catalyzing and accelerating the electrolyte disintegration in the development of an SEI [147]. Despite all this, LTO anodes can last thousands of cycles giving this electrode a distinctive advantage over other anode materials for high-energy applications.

2.4. Phosphate and Sulphate Based Cathode Materials

The major setback with the commercialized layered oxides is the instability of the charged Co^{3+}/$^{4+}$ and Ni^{3+}/$^{4+}$ redox couples associated safety problems. To surmount this drawback in the oxides, Manthiram and Goodenough et al. [148] initiated the polyanion host concept for the lithium intercalation [$Fe_2(XO_4)_3$ (X = S, Mo and W)]. Compared with the simple oxide layers, covalently bonded polyanion hosts lower the redox energies of the redox couples through the inductive effect and increase the cell voltage. Subsequently Padhi et al. [82] showed olivine structured lithium metal phosphates $LiMPO_4$ (M = Mn, Fe, Co and Ni) for the successful lithium intercalation. Phosphate $(PO_4)^{3-}$ polyanion framework offers highly stable 3D network due to strong P-O covalent bonds, which restricts the liberation of oxygen. These characteristic features provide an outstanding safety under abuse situation of the batteries.

Sulphates were tested as intercalation hosts in the late 80s [36, 37]. In 2009, with the synthesis of electrochemically active $FeSO_4(OH)$ [150] sulphates became extensively researched as a potential polyanion for batteries. Subsequently, a novel combination of sulphate with an even more electronegative fluoride group to yield a fluorosulphate of Fe operating at 3.6 V as well as a polymorph of the same fluorosulphates operating at 3.9 V were demonstrated [151-152]. Within the group of sulphates, Co and Fe have shown electrochemical activity [153-154]. Therefore, in this thesis, the activity of Mn in such sulphates has been studies using XAS and XPS studies, a research gap that has been in the group of sulphate-based cathodes.

2.5. Conclusions

Although Li-ion rechargeable batteries have successfully been utilized in portable electronics, and is under active commercial development for power tools and small electric vehicles (EVs), efforts are still underway to develop safe batteries for plug-in hybrid (PHEVs) and larger EVs of greater driving range, faster charging rates, and lower cost. The commercial constraints of safety and cost apply to all applications, but the required energy density versus, cycle life, efficiency, charging times vary greatly between batteries for electronic devices, EVs, and grids. Present-day strategies for the Li-ion battery rely heavily on liquid-carbonate electrolytes and insertion-compound cathodes. We need to address the limitations of these strategies relative to alternatives for batteries that power larger EVs and store electrical energy of the grid. LIBs for high energy or high power demands require high capacity, high capacity retention, high voltage operation, low cost, low weight and volume, etc. and most of these requirements are deeply related to solid electrolyte interphase (SEI) layers. High-voltage operation of LIBs (like NMCs) release minor amount of metals into the electrolyte thus inducing more SEI formation. Even though SEI shields lithium ions from the electrolyte solution, which prevents further electrolyte decomposition, the SEI formation process consumes lithium ions resulting in first-cycle irreversible capacity and lithium ion losses and this might continue if the SEI layer is not well formed. Other major limitations include in gaining high reversible capacities, easy Li-diffusion, eliminating antisite defects and optimizing operating voltage etc. Studies have been reported suggesting 3-5% occupation of Li sites by Fe. These anti-site defects, particularly Fe on Li sites, could have an effect on Li ion conduction. For Mn-based cathodes, high operating voltages can be obtained but at the cost of Mn dissolution into the electrolyte with disproportionation reaction of Mn^{3+} to form Mn^{2+} and Mn^{4+}. Therefore, to get great energy density without compromising the operating voltage and capacity, coupled with low cost and longer shelf life is still a challenge for scientists but efforts are continuously being made to improve this situation.

References

[1]. Bigeleisen, J., Lewis,Gilbert,N. And the Beginnings of Isotope Chemistry. Journal of Chemical Education, **1984** 61 (2):p. 108-116.

[2]. Whittingham, M.S., Electrical Energy-Storage and Intercalation Chemistry. Science, **1976** 192 (4244):p. 1126-1127.

[3] Yoshino A. The Birth of the Lithium-Ion Battery. Angewandte Chemie International Edition. **2012** Jun 11;51(24):5798-800.

[4]. Yazami, R. and P. Touzain, Lithium Graphite Oxide Cells .3. Effect of Origin and Oxidation of Graphite on Batteries Performances. Synthetic Metals, **1985** 12 (1-2):p. 499-503.

[5]. Goodenough, J.B., M.M. Thackeray, W.I.F. David, and P.G. Bruce, Lithium Insertion Extraction Reactions with Manganese Oxides. Revue De Chimie Minerale, **1984** 21 (4):p. 435-455.

[6]. Mizushima, K., P.C. Jones, P.J. Wiseman, and J.B. Goodenough, Li_xCoO_2 (O Less-Than X Less-Than-or-Equal-to 1) - a New Cathode Material for Batteries of High-Energy Density. Solid State Ionics, **1981** 3-4 (Aug):p. 171-174.

[7]. Thackeray, M.M., W.I.F. David, P.G. Bruce, and J.B. Goodenough, Lithium Insertion into Manganese Spinels. Materials Research Bulletin, **1983** 18 (4):p. 461-472.

[8]. Zhang, X.W., L.W. Ji, O. Toprakci, Y.Z. Liang, and M. Alcoutlabi, Electrospun Nanofiber-Based Anodes, Cathodes, and Separators for Advanced Lithium-Ion Batteries. Polymer Reviews, **2011** 51 (3):p. 239-264.

[9]. Nitta, N., F.X. Wu, J.T. Lee, and G. Yushin, Li-ion battery materials: present and future. Materials Today, **2015** 18 (5):p. 252-264.

[10]. Periasamy, P., B.R. Babu, R. Thirunakaran, N. Kalaiselvi, T.P. Kumar, N.G. Renganathan, M. Raghavan, and N. Muniyandi, Solid-state synthesis and characterization of $LiCoO_2$ and $LiNi_yCo_{1-y}O_2$ solid solutions. Bulletin of Materials Science, **2000** 23 (5):p. 345-348.

[11]. Choi, K.Y., K.D.K. Kim, and J.W. Yang, Optimization of the synthesis conditions of $LiCoO_2$ for lithium secondary battery by ultrasonic spray pyrolysis process. Journal of Materials Processing Technology, **2006** 171 (1):p. 118-124.

[12]. Gan, Y.L., L. Zhang, Y.X. Wen, F. Wang, and H.F. Su, Carbon combustion synthesis of lithium cobalt oxide as cathode material for lithium ion battery. Particuology, **2008** 6 (2):p. 81-84.

[13]. Kalyani, P., N. Kalaiselvi, and N. Muniyandi, A new solution combustion route to synthesize $LiCoO_2$ and $LiMn_2O_4$. Journal of Power Sources, **2002** 111 (2):p. 232-238.

[14]. Wang, X., H. Liang, J.C. Huang, and X.M. Pang, Investigation of the high temperature crystal phase change of $LiCoO_2$ prepared by chemical co-precipitation process. Rare Metal Materials and Engineering, **2007** 36:p. 654-657.

[15]. Tan, K.S., M.V. Reddy, G.V.S. Rao, and B. Chowdari, High-performance $LiCoO_2$ by molten salt ($LiNO_3$: LiCl) synthesis for Li-ion batteries. Journal of Power Sources, **2005** 147 (1-2):p. 241-248.

[16]. Buyukburc, A. and M.K. Aydinol, Effect of Cr and Mo doping on the electrochemical properties of freeze-dried $LiCoO_2$. International Journal of Materials Research, **2014** 105 (10):p. 983-991.

[17]. Nakamura, T. and A. Kajiyama, Synthesis of $LiCoO_2$ particles with uniform size distribution using hydrothermally precipitated Co_3O_4 fine particles. Solid State Ionics, **1999** 123 (1-4):p. 95-101.

[18]. Kosova, N. and E. Devyatkina, On mechanochemical preparation of materials with enhanced characteristics for lithium batteries. Solid State Ionics, **2004** 172 (1-4):p. 181-184.

[19]. Yan, H.W., X.J. Huang, Z.H. Lu, H. Huang, R.J. Xue, and L.Q. Chen, Microwave synthesis of $LiCoO_2$ cathode materials. Journal of Power Sources, **1997** 68 (2):p. 530-532.

[20]. Li, G., Z.X. Yang, and W.S. Yang, Effect of FePO4 coating on electrochemical and safety performance of $LiCoO_2$ as cathode material for Li-ion batteries. Journal of Power Sources, **2008** 183 (2):p. 741-748.

[21]. Wang, H., Z.Q. Deng, and M.C. Chen, Effects of SrO/Li2O/La2O3/Ta2O5/TiO2-coating on electrochemical performance of $LiCoO_2$. Journal of Rare Earths, **2009** 27 (2):p. 234-239.

[22]. Yi, T.F., J. Shu, C.B. Yue, X.D. Zhu, A.N. Zhou, Y.R. Zhu, and R.S. Zhu, Enhanced cycling stability of microsized $LiCoO_2$ cathode by $Li_4Ti_5O_{12}$ coating for lithium ion battery. Materials Research Bulletin, **2010** 45 (4):p. 456-459.

[23]. Cao, Q., H.P. Zhang, G.J. Wang, Q. Xia, Y.P. Wu, and H.Q. Wu, A novel carbon-coated $LiCoO_2$ as cathode material for lithium ion battery. Electrochemistry Communications, **2007** 9 (5):p. 1228-1232.

[24]. Lu, C.Z., J.M. Chen, Y.D. Cho, W.H. Hsu, P. Muralidharan, and G.T.K. Fey, Electrochemical performance of $LiCoO_2$ cathodes by surface modification using lanthanum aluminum garnet. Journal of Power Sources, **2008** 184 (2):p. 392-401.

[25]. Shlyakhtin, O.A., S.H. Choi, Y.S. Yoon, and Y.J. Oh, Characterization of nanocrystalline HT-$LiCoO_2$ cathode materials for secondary lithium batteries. Electrochimica Acta, **2004** 50 (2-3):p. 511-516.

[26]. Wang, M.J. and A. Navrotsky, Enthalpy of formation of $LiNiO_2$, $LiCoO_2$ and their solid solutions $LiNi_{1-x}Co_xO_2$. Solid State Ionics, **2004** 166 (1-2):p. 167-173.

[27]. Patridge, C.J., C.T. Love, K.E. Swider-Lyons, M.E. Twigg, and D.E. Ramaker, In-situ X-ray absorption spectroscopy analysis of capacity fade in nanoscale- $LiCoO_2$. Journal of Solid State Chemistry, **2013** 203:p. 134-144.

[28]. Takamatsu, D., Y. Koyama, Y. Orikasa, S. Mori, T. Nakatsutsumi, T. Hirano, H. Tanida, H. Arai, Y. Uchimoto, and Z. Ogumi, First In Situ Observation of the $LiCoO_2$

Electrode/Electrolyte Interface by Total-Reflection X-ray Absorption Spectroscopy. Angewandte Chemie-International Edition, **2012** 51 (46):p. 11597-11601.

[29]. Inaba, M., Y. Iriyama, Z. Ogumi, Y. Todzuka, and A. Tasaka, Raman study of layered rock-salt $LiCoO_2$ and its electrochemical lithium deintercalation. Journal of Raman Spectroscopy, **1997** 28 (8):p. 613-617.

[30]. Daheron, L., R. Dedryvere, H. Martinez, M. Menetrier, C. Denage, C. Delmas, and D. Gonbeau, Electron transfer mechanisms upon lithium deintercalation from $LiCoO_2$ to CoO_2 investigated by XPS. Chemistry of Materials, **2008** 20 (2):p. 583-590.

[31]. Nakamura, K., M. Yamamoto, K. Okamura, Y. Michihiro, I. Nakabayashi, and T. Kanashiro, NMR investigation on the motion of Li+ defects in $LiCoO_2$ and $LiNiO_2$. Solid State Ionics, **1999** 121 (1-4):p. 301-306.

[32]. Shimoda, K., M. Murakami, D. Takamatsu, H. Arai, Y. Uchimoto, and Z. Ogumi, In situ NMR observation of the lithium extraction/insertion from $LiCoO_2$ cathode. Electrochimica Acta, **2013** 108:p. 343-349.

[33]. Dahn, J.R., E.W. Fuller, M. Obrovac, and U. Vonsacken, Thermal-Stability of Li_xCoO_2, Li_xNiO_2 and λ-MnO_2 and Consequences for the Safety of Li-Ion Cells. Solid State Ionics, **1994** 69 (3-4):p. 265-270.

[34]. Williard, N., W. He, C. Hendricks, and M. Pecht, Lessons Learned from the 787 Dreamliner Issue on Lithium-Ion Battery Reliability. Energies, **2013** 6 (9):p. 4682-4695.

[35]. Reimers, J.N. and J.R. Dahn, Electrochemical and Insitu X-Ray-Diffraction Studies of Lithium Intercalation in Li_xCoO_2. Journal of the Electrochemical Society, **1992** 139 (8):p. 2091-2097.

[36]. Ohzuku T, Makimura Y. Layered lithium insertion material of $LiNi_{1/3}Co_{1/3}Mn_{1/3}O_2$ for lithium-ion batteries. Chemistry Letters. **2001** Jul; 30(7):642-3.

[37] Zhang, X.Y., A. Mauger, Q. Lu, H. Groult, L. Perrigaud, F. Gendron, and C.M. Julien, Synthesis and characterization of $LiNi_{1/3}Co_{1/3}Mn_{1/3}O_2$ by wet-chemical method. Electrochimica Acta, **2010** 55 (22):p. 6440-6449.

[38]. Kiziltas-Yavuz, N., M. Herklotz, A.M. Hashem, H.M. Abuzeid, B. Schwarz, H. Ehrenberg, A. Mauger, and C.M. Julien, Synthesis, structural, magnetic and electrochemical properties of $LiNi_{1/3}Co_{1/3}Mn_{1/3}O_2$ prepared by a sol-gel method using table sugar as chelating agent. Electrochimica Acta, **2013** 113:p. 313-321.

[39]. Wu, F., M. Wang, Y.F. Su, L.Y. Bao, and S. Chen, A novel method for synthesis of layered $LiNi_{1/3}Co_{1/3}Mn_{1/3}O_2$ as cathode material for lithium-ion battery. Journal of Power Sources, **2010** 195 (8):p. 2362-2367.

[40]. Kobayashi, H., Y. Arachi, S. Emura, H. Kageyama, K. Tatsumi, and T. Kamiyama, Investigation on lithium de-intercalation mechanism for $LiNi_{1/3}Co_{1/3}Mn_{1/3}O_2$. Journal of Power Sources, **2005** 146 (1-2):p. 640-644.

[41]. Kobayashi, H., Y. Arachi, S. Emura, K. Handa, and K. Tatsumi, Observation of valence state change in layered $LiNi_{1/3}Co_{1/3}Mn_{1/3}O_2$. X-Ray Absorption Fine Structure-Xafs13, **2007** 882:p. 478-+.

[42]. Nayak, P.K., J. Grinblat, M. Levi, Y. Wu, B. Powell, and D. Aurbach, TEM and Raman spectroscopy evidence of layered to spinel phase transformation in layered $LiNi_{1/3}Co_{1/3}Mn_{1/3}O_2$ upon cycling to higher voltages. Journal of Electroanalytical Chemistry, **2014** 733:p. 6-19.

[43]. Li, D.C., Y. Kato, K. Kobayakawa, H. Noguchi, and Y. Sato, Preparation and electrochemical characteristics of $LiNi_{1/3}Co_{1/3}Mn_{1/3}O_2$ coated with metal oxides coating. Journal of Power Sources, **2006** 160 (2):p. 1342-1348.

[44]. Tan, L. and H.W. Liu, Influence of ZnO coating on the structure, morphology and electrochemical performances for $LiNi_{1/3}Co_{1/3}Mn_{1/3}O_2$ material. Russian Journal of Electrochemistry, **2011** 47 (2):p. 156-160.

[45]. Fan, Z.Y., E.M. Jin, and S.M. Jeong, Enhanced Electrochemical Properties of NCA Cathode Materials for Lithium Ion Battery by Doping Effect. Korean Chemical Engineering Research, **2017** 55 (6):p. 861-867.

[46]. Jin, E.M., G.E. Lee, B.K. Na, and S.M. Jeong, Electrochemical Properties of Commercial NCA Cathode Materials for High Capacity of Lithium Ion Battery. Korean Chemical Engineering Research, **2017** 55 (2):p. 163-169.

[47]. Wan, D.Y., Z.Y. Fan, Y.X. Dong, E. Baasanjav, H.B. Jun, B. Jin, E.M. Jin, and S.M. Jeong, Effect of Metal (Mn, Ti) Doping on NCA Cathode Materials for Lithium Ion Batteries. Journal of Nanomaterials, **2018**:p.

[48]. Yoo, G.W., B.C. Jang, and J.T. Son, Novel design of core shell structure by NCA modification on NCM cathode material to enhance capacity and cycle life for lithium secondary battery. Ceramics International, **2015** 41 (1):p. 1913-1916.

[49]. Thackeray, M.M., M.H. Rossouw, A. Dekock, A.P. Delaharpe, R.J. Gummow, K. Pearce, and D.C. Liles, The Versatility of MnO_2 for Lithium Battery Applications. Journal of Power Sources, **1993** 43 (1-3):p. 289-300.

[50]. David, W.I.F., M.M. Thackeray, L.A. Depicciotto, and J.B. Goodenough, Structure Refinement of the Spinel-Related Phases $Li_2Mn_2O_4$ and $Li_{0.2}Mn_2O_4$. Journal of Solid State Chemistry, **1987** 67 (2):p. 316-323.

[51]. Kim, D.K., P. Muralidharan, H.W. Lee, R. Ruffo, Y. Yang, C.K. Chan, H. Peng, R.A. Huggins, and Y. Cui, Spinel $LiMn_2O_4$ Nanorods as Lithium Ion Battery Cathodes. Nano Letters, **2008** 8 (11):p. 3948-3952.

[52]. Li, T., W.H. Qiu, H.L. Zhao, and J.J. Liu, Effect of lithium content on the electrochemical properties of solid-state-synthesized spinel $LiMn_2O_4$. Rare Metals, **2007** 26 (3):p. 280-285.

[53]. Zhang, P.F., H.Q. Fan, Y.F. Fu, Z. Li, and Y.L. Deng, Synthesis and electrochemical properties of sol-gel derived $LiMn_2O_4$ cathode for lithium-ion batteries. Rare Metals, **2006** 25:p. 100-104.

[54]. Zhang, X.F., H.H. Zheng, V. Battaglia, and R.L. Axelbaum, Electrochemical performance of spinel $LiMn_2O_4$ cathode materials made by flame-assisted spray technology. Journal of Power Sources, **2011** 196 (7):p. 3640-3645.

[55]. Yi, T.F., C.L. Hao, C.B. Yue, R.S. Zhu, and J. Shu, A literature review and test: Structure and physicochemical properties of spinel $LiMn_2O_4$ synthesized by different temperatures for lithium ion battery. Synthetic Metals, **2009** 159 (13):p. 1255-1260.

[56]. Guyomard, D. and J.M. Tarascon, The Carbon $Li_{1+X}Mn_2O_4$ System. Solid State Ionics, **1994** 69 (3-4):p. 222-237.

[57]. Santiago, E.I., S.T. Amancio, P.R. Bueno, and L.O.S. Bulhoes, Electrochemical performance of cathodes based on $LiMn_2O_4$ spinel obtained by combustion synthesis. Journal of Power Sources, **2001** 97-8:p. 447-449.

[58]. Eriksson, T. $LiMn_2O_4$ as a Li-Ion battery cathode. From bulk to electrolyte interface. **2001**.

[59]. Arumugam, D. and G.P. Kalaignan, Synthesis and electrochemical characterizations of nano size Ce doped $LiMn_2O_4$ cathode materials for rechargeable lithium batteries. Journal of Electroanalytical Chemistry, **2010** 648 (1):p. 54-59.

[60]. Liu, R.S. and C.H. Shen, Structural and electrochemical study of cobalt doped $LiMn_2O_4$ spinels. Solid State Ionics, **2003** 157 (1-4):p. 95-100.

[61]. Zhang, D., B.N. Popov, and R.E. White, Electrochemical investigation of $CrO_{2.65}$ doped $LiMn_2O_4$ as a cathode material for lithium-ion batteries. Journal of Power Sources, **1998** 76 (1):p. 81-90.

[62]. Liu, D., J. Trottier, P. Charest, J. Frechette, A. Guerfi, A. Mauger, C.M. Julien, and K. Zaghib, Effect of nano $LiFePO_4$ coating on $LiMn_{1.5}Ni_{0.5}O_4$ 5V cathode for lithium ion batteries. Journal of Power Sources, **2012** 204:p. 127-132.

[63]. Tu, J., X.B. Zhao, G.S. Cao, J.P. Tu, and T.J. Zhu, Improved performance of $LiMn_2O_4$ cathode materials for lithium ion batteries by gold coating. Materials Letters, **2006** 60 (27):p. 3251-3254.

[64]. Hashem, A.M., R.S. El-Taweel, H.M. Abuzeid, A.E. Abdel-Ghany, A.E. Eid, H. Groult, A. Mauger, and C.M. Julien, Structural and electrochemical properties of $LiNi_{1/3}Co_{1/3}Mn_{1/3}O_2$ material prepared by a two-step synthesis via oxalate precursor. Ionics, **2012** 18 (1-2):p. 1-9.

[65]. Sun, Y.K., C.S. Yoon, and I.H. Oh, Surface structural change of ZnO-coated $LiNi_{0.5}Mn_{1.5}O_4$ spinel as 5 V cathode materials at elevated temperatures. Electrochimica Acta, **2003** 48 (5):p. 503-506.

[66]. Chan, H.W., J.G. Duh, and J.F. Lee, Valence change by in situ XAS in surface modified $LiMn_2O_4$ for Li-ion battery. Electrochemistry Communications, **2006** 8 (11):p. 1731-1736.

[67]. Dupont, L., M. Hervieu, G. Rousse, C. Masquelier, M.R. Palacin, Y. Chabre, and J.M. Tarascon, TEM studies: The key for understanding the origin of the 3.3 V and 4.5 V steps observed in $LiMn_2O_4$-based spinels. Journal of Solid State Chemistry, **2000** 155 (2):p. 394-408.

[68]. Jiang, C.H., S.X. Dou, H.K. Liu, M. Ichihara, and H.S. Zhou, Synthesis of spinel $LiMn_2O_4$ nanoparticles through one-step hydrothermal reaction. Journal of Power Sources, **2007** 172 (1):p. 410-415.

[69]. Pistoia, G. and R. Rosati, Synthesis of an efficient $LiMn_2O_4$ for lithium-ion cells. Journal of Power Sources, **1996** 58 (2):p. 135-138.

[70]. Ramana, C.V., M. Massot, and C.M. Julien, XPS and Raman spectroscopic characterization of $LiMn_2O_4$ spinels. Surface and Interface Analysis, **2005** 37 (4):p. 412-416.

[71]. Urian, R., & Mukerjee, S, Temperature Dependent Performance of $LiMn_2O_4$: In situ XRD and XAS Studies N. U, Editor.

[72]. Kim, D., S. Park, O.B. Chae, J.H. Ryu, Y.U. Kim, R.Z. Yin, and S.M. Oh, Re-Deposition of Manganese Species on Spinel $LiMn_2O_4$ Electrode after Mn Dissolution. Journal of the Electrochemical Society, **2012** 159 (3):p. A193-A197.

[73]. Kim, Y., J. Lim, and S. Kang, Investigation on the dissolution of Mn ions from $LiMn_2O_4$ cathode in the application of lithium ion batteries: First principle molecular orbital method. International Journal of Quantum Chemistry, **2013** 113 (78-82):p. 148-154.

[74]. Terada, Y., Y. Nishiwaki, I. Nakai, and F. Nishikawa, Study of Mn dissolution from $LiMn_2O_4$ spinel electrodes using in situ total reflection X-ray fluorescence analysis and fluorescence XAFS technique. Journal of Power Sources, **2001** 97-8:p. 420-422.

[75]. Xia, H., Z.T. Luo, and J.P. Xie, Nanostructured $LiMn_2O_4$ and their composites as high-performance cathodes for lithium-ion batteries. Progress in Natural Science-Materials International, **2012** 22 (6):p. 572-584.

[76]. Thackeray, M.M., L.A. Depicciotto, A. Dekock, P.J. Johnson, V.A. Nicholas, and K.T. Adendorff, Spinel Electrodes for Lithium Batteries - a Review. Journal of Power Sources, **1987** 21 (1):p. 1-8.

[77]. Thackeray, M.M., Spinel electrodes for lithium batteries. Journal of the American Ceramic Society, **1999** 82 (12):p. 3347-3354.

[78]. Liu, W.W., D. Wang, Z.F. Wang, J.G. Deng, W.M. Lau, and Y.N. Zhang, Influence of magnetic ordering and Jahn-Teller distortion on the lithiation process of $LiMn_2O_4$. Physical Chemistry Chemical Physics, **2017** 19 (9):p. 6481-6486.

[79]. Nie, Z.X., C.Y. Ouyang, J.Z. Chen, Z.Y. Zhong, Y.L. Du, D.S. Liu, S.Q. Shi, and M.S. Lei, First principles study of Jahn-Teller effects in $LiMn_2O_4$. Solid State Communications, **2010** 150 (1-2):p. 40-44.

[80]. Ouyang, C.Y., S.Q. Shi, and M.S. Lei, Jahn-Teller distortion and electronic structure of $LiMn_2O_4$. Journal of Alloys and Compounds, **2009** 474 (1-2):p. 370-374.

[81]. Radin, M.D. and A. Van der Ven, Simulating Charge, Spin, and Orbital Ordering: Application to Jahn-Teller Distortions in Layered Transition-Metal Oxides. Chemistry of Materials, **2018** 30 (3):p. 607-618.

[82]. Padhi, A.K., K.S. Nanjundaswamy, and J.B. Goodenough, Phospho-olivines as positive-electrode materials for rechargeable lithium batteries. Journal of the Electrochemical Society, **1997** 144 (4):p. 1188-1194.

[83]. Zhang, Y., Q.Y. Huo, P.P. Du, L.Z. Wang, A.Q. Zhang, Y.H. Song, Y. Lv, and G.Y. Li, Advances in new cathode material $LiFePO_4$ for lithium-ion batteries. Synthetic Metals, **2012** 162 (13-14):p. 1315-1326.

[84]. Zhang, W.J., Structure and performance of $LiFePO_4$ cathode materials: A review. Journal of Power Sources, **2011** 196 (6):p. 2962-2970.

[85]. Franger, S., F. Le Cras, C. Bourbon, and H. Rouault, Comparison between different $LiFePO_4$ synthesis routes and their influence on its physico-chemical properties. Journal of Power Sources, **2003** 119:p. 252-257.

[86]. Li, Y.D., S.X. Zhao, C.W. Nan, and B.H. Li, Electrochemical performance of SiO2-coated $LiFePO_4$ cathode materials for lithium ion battery. Journal of Alloys and Compounds, **2011** 509 (3):p. 957-960.

[87]. Liu, H., G.X. Wang, D. Wexler, J.Z. Wang, and H.K. Liu, Electrochemical performance of $LiFePO_4$ cathode material coated with ZrO2 nanolayer. Electrochemistry Communications, **2008** 10 (1):p. 165-169.

[88]. Yao, J.W., F. Wu, X.P. Qiu, N. Li, and Y.F. Su, Effect of CeO2-coating on the electrochemical performances of $LiFePO_4$/C cathode material. Electrochimica Acta, **2011** 56 (16):p. 5587-5592.

[89]. Doeff, M.M., Y.Q. Hu, F. McLarnon, and R. Kostecki, Effect of surface carbon structure on the electrochemical performance of $LiFePO_4$. Electrochemical and Solid State Letters, **2003** 6 (10):p. A207-A209.

[90]. Julien, C.M., K. Zaghib, A. Mauger, M. Massot, A. Ait-Salah, M. Selmane, and F. Gendron, Characterization of the carbon coating onto $LiFePO_4$ particles used in lithium batteries. Journal of Applied Physics, **2006** 100 (6):p.

[91]. Shin, H.C., W.I. Cho, and H. Jang, Electrochemical properties of the carbon-coated $LiFePO_4$ as a cathode material for lithium-ion secondary batteries. Journal of Power Sources, **2006** 159 (2):p. 1383-1388.

[92]. Zhao, T., W.S. Chu, H.F. Zhao, X.Q. Liang, W. Xu, M.J. Yu, D.G. Xia, and Z.Y. Wu, XAS study of $LiFePO_4$ synthesized by solid state reactions and hydrothermal method. Nuclear Instruments & Methods in Physics Research Section a-Accelerators Spectrometers Detectors and Associated Equipment, **2010** 619 (1-3):p. 122-127.

[93]. Chen, Y., Z.L. Wang, C.Y. Yu, D.G. Xia, and Z.Y. Wu, Electrochemical properties of Mo-doped $LiFePO_4$ cathode material. Acta Physico-Chimica Sinica, **2008** 24 (8):p. 1498-1502.

[94]. Cho, Y.D., G.T.K. Fey, and H.M. Kao, Physical and electrochemical properties of La-doped $LiFePO_4$/C composites as cathode materials for lithium-ion batteries. Journal of Solid State Electrochemistry, **2008** 12 (7-8):p. 815-823.

[95]. Yang, M.R. and W.H. Ke, The doping effect on the electrochemical properties of $LiFe_{(0.95)}M_{(0.05)}PO_{(4)}$ (M=$Mg^{(2+)}$, $Ni^{(2+)}$, $Al^{(3+)}$, or $V^{(3+)}$) as cathode materials for lithium-ion cells. Journal of the Electrochemical Society, **2008** 155 (10):p. A729-A732.

[96]. Andersson, A.S., J.O. Thomas, B. Kalska, and L. Haggstrom, Thermal stability of $LiFePO_4$-based cathodes. Electrochemical and Solid State Letters, **2000** 3 (2):p. 66-68.

[97]. Nakamura, T., Y. Miwa, M. Tabuchi, and Y. Yamada, Structural and surface modifications of $LiFePO_4$ olivine particles and their electrochemical properties. Journal of the Electrochemical Society, **2006** 153 (6):p. A1108-A1114.

[98]. Yamada, A., S.C. Chung, and K. Hinokuma, Optimized $LiFePO_4$ for lithium battery cathodes. Journal of the Electrochemical Society, 2001 148 (3):p. A224-A229.

[99]. Gul, H.B., D.K. Jun, G.C. Park, B. Jin, and E.M. Jin, Nanosized $LiFePO_4$ Cathode materials for lithium ion batteries. Journal of Nanoscience and Nanotechnology, **2007** 7 (11):p. 3980-3984.

[100]. Palomares, V., A. Goni, L.G. de Muro, I. de Meatza, M. Bengoechea, O. Miguel, and T. Rojo, New freeze-drying method for $LiFePO_4$ synthesis. Journal of Power Sources, **2007** 171 (2):p. 879-885.

[101]. Zhang, S.P., J.F. Ni, H.H. Zhou, and Z.J. Zhang, Controllable synthesis of regular $LiFePO_4$ particles via solvothermal reaction. Acta Physico-Chimica Sinica, **2007** 23 (6):p. 830-834.

[102]. Burba, C.M. and R. Frech, In situ transmission FTIR spectroelectrochemistry: A new technique for studying lithium batteries. Electrochimica Acta, **2006** 52 (3):p. 780-785.

[103]. Julien, C.M., A.A. Salah, F. Gendron, J.F. Morhange, A. Mauger, and C.V. Ramana, Microstructure of $LiXPO_4$ (X = Ni, Co, Mn) prepared by solid state chemical reaction. Scripta Materialia, **2006** 55 (12):p. 1179-1182.

[104]. Salah, A.A., P. Jozwiak, K. Zaghib, J. Garbarczyk, F. Gendron, A. Mauger, and C.M. Julien, FTIR features of lithium-iron phosphates as electrode materials for rechargeable lithium batteries. Spectrochimica Acta Part a-Molecular and Biomolecular Spectroscopy, **2006** 65 (5):p. 1007-1013.

[105]. Deb, A., U. Bergmann, E.J. Cairns, and S.P. Cramer, X-ray absorption spectroscopy study of the $LiFePO_4$ cathode during cycling using a novel electrochemical in situ reaction cell. Journal of Synchrotron Radiation, **2004** 11:p. 497-504.

[106]. Deb, A., U. Bergmann, S.P. Cramer, and E.J. Cairns, Structural investigations of $LiFePO_4$ electrodes and in situ studies by Fe X-ray absorption spectroscopy. Electrochimica Acta, **2005** 50 (25-26):p. 5200-5207.

[107]. Haas, O., A. Deb, E.J. Cairns, and A. Wokaun, Synchrotron X-ray absorption study of $LiFePO_4$ electrodes. Journal of the Electrochemical Society, **2005** 152 (1):p. A191-A196.

[108]. Prince, A.A.M., S. Mylswamy, T.S. Chan, R.S. Liu, B. Hannoyer, M. Jean, C.H. Shen, S.M. Huang, J.F. Lee, and G.X. Wang, Investigation of Fe valence in $LiFePO_4$ by Mossbauer and XANES spectroscopic techniques. Solid State Communications, **2004** 132 (7):p. 455-458.

[109]. Wang, X.J., C. Jaye, K.W. Nam, B. Zhang, H.Y. Chen, J.M. Bai, H. Li, X.J. Huang, D.A. Fischer, and X.Q. Yang, Investigation of the structural changes in $Li_{1-x}FePO_4$ upon charging by synchrotron radiation techniques. Journal of Materials Chemistry, **2011** 21 (30):p. 11406-11411.

[110]. Castro, L., R. Dedryvere, M. El Khalifi, P.E. Lippens, J. Breger, C. Tessier, and D. Gonbeau, The Spin-Polarized Electronic Structure of $LiFePO_4$ and $FePO_{(4)}$ Evidenced by in-Lab XPS. Journal of Physical Chemistry C, **2010** 114 (41):p. 17995-18000.

[111]. Castro, L., R. Dedryvere, J.B. Ledeuil, J. Breger, C. Tessier, and D. Gonbeau, Aging Mechanisms of $LiFePO_4$ // Graphite Cells Studied by XPS: Redox Reaction and Electrode/Electrolyte Interfaces. Journal of the Electrochemical Society, **2012** 159 (4):p. A357-A363.

[112]. Orliukas, A.F., K.Z. Fung, V. Venckute, V. Kazlauskiene, J. Miskinis, A. Dindune, Z. Kanepe, J. Ronis, A. Maneikis, T. Salkus, and A. Kezionis, SEM/EDX, XPS, AND IMPEDANCE SPECTROSCOPY OF $LiFePO_4$ AND $LiFePO_4$/C CERAMICS. Lithuanian Journal of Physics, **2014** 54 (2):p. 106-113.

[113]. Castets, A., D. Carlier, Y. Zhang, F. Boucher, N. Marx, L. Croguennec, and M. Menetrier, Multinuclear NMR and DFT Calculations on the $LiFePO_4$ center dot OH and $FePO_4$ center dot H2O Homeotypic Phases. Journal of Physical Chemistry C, **2011** 115 (32):p. 16234-16241.

[114]. Cuisinier, M., N. Dupre, J.F. Martin, R. Kanno, and D. Guyomard, Evolution of the $LiFePO_4$ positive electrode interface along cycling monitored by MAS NMR. Journal of Power Sources, **2013** 224:p. 50-58.

[115]. Cuisinier, M., N. Dupre, P. Moreau, and D. Guyomard, NMR monitoring of electrode/electrolyte interphase in the case of air-exposed and carbon coated $LiFePO_4$. Journal of Power Sources, **2013** 243:p. 682-690.

[116]. Shimoda, K., H. Sugaya, M. Murakami, H. Arai, Y. Uchimoto, and Z. Ogumi, Characterization of Bulk and Surface Chemical States on Electrochemically Cycled $LiFePO_4$: A Solid State NMR Study. Journal of the Electrochemical Society, **2014** 161 (6):p. A1012-A1018.

[117]. Bini, M., S. Ferrari, D. Capsoni, P. Mustarelli, G. Spina, F. Del Giallo, M. Lantieri, C. Leonelli, A. Rizzuti, and V. Massarotti, Pair distribution function analysis and Mossbauer study of defects in microwave-hydrothermal $LiFePO_4$. Rsc Advances, **2012** 2 (1):p. 250-258.

[118]. Reklaitis, J., R. Davidonis, A. Dindune, D. Valdniece, V. Jasulaitiene, and D. Baltrunas, Characterization of $LiFePO_4$/C composite and its thermal stability by Mossbauer and XPS spectroscopy. Physica Status Solidi B-Basic Solid State Physics, **2016** 253 (11):p. 2283-2288.

[119]. Wen, J.W., Y. Yu, and C.H. Chen, A Review on Lithium-Ion Batteries Safety Issues: Existing Problems and Possible Solutions. Materials Express, **2012** 2 (3):p. 197-212.

[120]. Chen, J.J. and J. Graetz, Study of Antisite Defects in Hydrothermally Prepared $LiFePO_4$ by in Situ X-ray Diffraction. Acs Applied Materials & Interfaces, **2011** 3 (5):p. 1380-1384.

[121]. Chung, S.Y., S.Y. Choi, S. Lee, and Y. Ikuhara, Distinct Configurations of Antisite Defects in Ordered Metal Phosphates: Comparison between $LiMnPO_4$ and $LiFePO_4$. Physical Review Letters, **2012** 108 (19):p.

[122]. Chung, S.Y., S.Y. Choi, T. Yamamoto, and Y. Ikuhara, Atomic-scale visualization of antisite defects in $LiFePO_4$. Physical Review Letters, **2008** 100 (12):p.

[123]. Zhang, H., Y.H. Tang, W.W. Zhou, P.J. Li, and S.Q. Shi, Antisite defect of $LiFePO_4$: A first-principles study. Acta Physica Sinica, **2010** 59 (7):p. 5135-5140.

[124]. Aldon, L., P. Kubiak, M. Womes, J.C. Jumas, J. Olivier-Fourcade, J.L. Tirado, J.I. Corredor, and C.P. Vicente, Chemical and electrochemical Li-insertion into the $Li_4Ti_5O_{12}$ spinel. Chemistry of Materials, **2004** 16 (26):p. 5721-5725.

[125]. Pyun, S.I., S.W. Kim, and H.C. Shin, Lithium transport through $Li_{1+delta}[Ti_{2-y}Li_y]O_4$ (y=0; 1/3) electrodes by analysing current transients upon large potential steps. Journal of Power Sources, **1999** 81:p. 248-254.

[126]. Zaghib, K., M. Simoneau, M. Armand, and M. Gauthier, Electrochemical study of $Li_4Ti_5O_{12}$ as negative electrode for Li-ion polymer rechargeable batteries. Journal of Power Sources, **1999** 81:p. 300-305.

[127]. Guerfi, A., S. Sevigny, M. Lagace, P. Hovington, K. Kinoshita, and K. Zaghib, Nano-particle $Li_4Ti_5O_{12}$ spinel as electrode for electrochemical generators. Journal of Power Sources, **2003** 119:p. 88-94.

[128]. Hsiao, K.C., S.C. Liao, and J.M. Chen, Microstructure effect on the electrochemical property of $Li_4Ti_5O_{12}$ as an anode material for lithium-ion batteries. Electrochimica Acta, **2008** 53 (24):p. 7242-7247.

[129]. Fattakhova, D., V. Petrykin, J. Brus, T. Kostlanova, J. Dedecek, and P. Krtil, Solvothermal synthesis and electrochemical behavior of nanocrystalline cubic Li-Ti-O oxides with cationic disorder. Solid State Ionics, **2005** 176 (23-24):p. 1877-1885.

[130]. Tang, Y.F., L. Yang, Z. Qiu, and J.S. Huang, Preparation and electrochemical lithium storage of flower-like spinel $Li_4Ti_5O_{12}$ consisting of nanosheets. Electrochemistry Communications, **2008** 10 (10):p. 1513-1516.

[131]. Yuan, T., K. Wang, R. Cai, R. Ran, and Z.P. Shao, Cellulose-assisted combustion synthesis of $Li_4Ti_5O_{12}$ adopting anatase TiO(2) solid as raw material with high electrochemical performance. Journal of Alloys and Compounds, **2009** 477 (1-2):p. 665-672.

[132]. Bai, Y.J., C. Gong, Y.X. Qi, N. Lun, and J. Feng, Excellent long-term cycling stability of La-doped $Li_4Ti_5O_{12}$ anode material at high current rates. Journal of Materials Chemistry, **2012** 22 (36):p. 19054-19060.

[133]. Ji, S.Z., J.Y. Zhang, W.W. Wang, Y. Huang, Z.R. Feng, Z.T. Zhang, and Z.L. Tang, Preparation and effects of Mg-doping on the electrochemical properties of spinel $Li_4Ti_5O_{12}$ as anode material for lithium ion battery. Materials Chemistry and Physics, **2010** 123 (2-3):p. 510-515.

[134]. Lu, P., X.B. Huang, Y.R. Ren, J.N. Ding, H.Y. Wang, S.B. Zhou, Y.D. Chen, and X. Ding, Na+ and Zr4+ co-doped $Li_4Ti_5O_{12}$ as anode materials with superior electrochemical performance for lithium ion batteries. Rsc Advances, **2016** 6 (93):p. 90455-90461.

[135]. Ncube, N.M., W.T. Mhlongo, R.I. McCrindle, and H.T. Zheng, The electrochemical effect of Al-doping on $Li_4Ti_5O_{12}$ as anode material for lithium-ion batteries. Materials Today-Proceedings, **2018** 5 (4):p. 10592-10601.

[136]. Repp, S., E. Harputlu, S. Gurgen, M. Castellano, N. Kremer, N. Pompe, J. Worner, A. Hoffmann, R. Thomann, F.M. Emen, S. Weber, K. Ocakoglu, and E. Erdem, Synergetic effects of Fe3+ doped spinel $Li_4Ti_5O_{12}$ nanoparticles on reduced graphene oxide for high surface electrode hybrid supercapacitors. Nanoscale, **2018** 10 (4):p. 1877-1884.

[137]. Yi, T.F., Y. Xie, L.J. Jiang, J. Shu, C.B. Yue, A.N. Zhou, and M.F. Ye, Advanced electrochemical properties of Mo-doped $Li_4Ti_5O_{12}$ anode material for power lithium ion battery. Rsc Advances, **2012** 2 (8):p. 3541-3547.

[138]. Zhang, B.A., H.D. Du, B.H. Li, and F.Y. Kang, Structure and Electrochemical Properties of Zn-Doped $Li_4Ti_5O_{12}$ as Anode Materials in Li-Ion Battery. Electrochemical and Solid State Letters, **2010** 13 (4):p. A36-A38.

[139]. Zhang, Q.Y. and X. Li, Recent Developments in the Doped-$Li_4Ti_5O_{12}$ Anode Materials of Lithium-Ion Batteries for Improving the Rate Capability. International Journal of Electrochemical Science, **2013** 8 (5):p. 6449-6456.

[140]. Zhao, Z., Y.L. Xu, M.D. Ji, and H. Zhang, Synthesis and electrochemical performance of F-doped $Li_4Ti_5O_{12}$ for lithium-ion batteries. Electrochimica Acta, **2013** 109:p. 645-650.

[141]. Chou, S.L., J.Z. Wang, H.K. Liu, and S.X. Dou, Rapid Synthesis of $Li_4Ti_5O_{12}$ Microspheres as Anode Materials and Its Binder Effect for Lithium-Ion Battery. Journal of Physical Chemistry C, **2011** 115 (32):p. 16220-16227.

[142]. Li, J.R., Z.L. Tang, and Z.T. Zhang, Controllable formation and electrochemical properties of one-dimensional nanostructured spinel $Li_4Ti_5O_{12}$. Electrochemistry Communications, **2005** 7 (9):p. 894-899.

[143]. Lippens, P.E., M. Womes, P. Kubiak, J.C. Jumas, and J. Olivier-Fourcade, Electronic structure of the spinel $Li_4Ti_5O_{12}$ studied by ab initio calculations and X-ray absorption spectroscopy. Solid State Sciences, **2004** 6 (2):p. 161-166.

[144]. Doughty, D. and E.P. Roth, A General Discussion of Li Ion Battery Safety. Electrochemical Society Interface, **2012** 21 (2):p. 37-44.

[145]. Ohzuku, T., A. Ueda, and N. Yamamoto, Zero-Strain Insertion Material of $Li[Li_{1/3}Ti_{5/3}]O_4$ for Rechargeable Lithium Cells. Journal of the Electrochemical Society, **1995** 142 (5):p. 1431-1435.

[146]. He, Y.B., B.H. Li, M. Liu, C. Zhang, W. Lv, C. Yang, J. Li, H.D. Du, B.A. Zhang, Q.H. Yang, J.K. Kim, and F.Y. Kang, Gassing in $Li_4Ti_5O_{12}$-based batteries and its remedy. Scientific Reports, **2012** 2:p.

[147]. He, Y.B., M. Liu, Z.D. Huang, B. Zhang, Y. Yu, B.H. Li, F.Y. Kang, and J.K. Kim, Effect of solid electrolyte interface (SEI) film on cyclic performance of $Li_4Ti_5O_{12}$ anodes for Li ion batteries. Journal of Power Sources, **2013** 239:p. 269-276.

[148]. Manthiram, A. and J.B. Goodenough, Lithium Insertion into $Fe_2(MO_4)_3$ Frameworks - Comparison of M = W with M = Mo. Journal of Solid State Chemistry, **1987** 71 (2):p. 349-360.

[149]. Rousse, G. and J.M. Tarascon, Sulfate-Based Polyanionic Compounds for Li-Ion Batteries: Synthesis, Crystal Chemistry, and Electrochemistry Aspects. Chemistry of Materials, **2014** 26 (1):p. 394-406.

[150]. Reddy, M.A., V. Pralong, V. Caignaert, U.V. Varadaraju, and B. Raveau, Monoclinic iron hydroxy sulphate: A new route to electrode materials. Electrochemistry Communications, **2009** 11 (9):p. 1807-1810.

[151]. Barpanda, P., M. Ati, B.C. Melot, G. Rousse, J.N. Chotard, M.L. Doublet, M.T. Sougrati, S.A. Corr, J.C. Jumas, and J.M. Tarascon, A 3.90 V iron-based fluorosulphate material for lithium-ion batteries crystallizing in the triplite structure. Nature Materials, **2011** 10 (10):p. 772-779.

[152] Yahia MB, Lemoigno F, Rousse G, Boucher F, Tarascon JM, Doublet ML. Origin of the 3.6 V to 3.9 V voltage increase in the $LiFeSO_4F$ cathodes for Li-ion batteries. Energy & Environmental Science. **2012**;5(11):9584-94.

[153]. Muthiah, A., T. Baikie, S. Shukla, S. Ball, M. Copley, T.I. Hyde, Y.H. Du, G. Sankar, V. Aravindan, and M. Srinivasan, Ex situ XAS investigation of effect of binders on electrochemical performance of $Li_2Fe(SO_4)(_2)$ cathode. Journal of Materials Chemistry A, **2017** 5 (37):p. 19963-19971.

[154]. Muthiah, A., T. Baikie, M. Ulaganathan, M. Copley, G. Yang, V. Aravindan, and M. Srinivasan, Structural, Thermal, and Electrochemical Studies of Novel $Li_2Co_xMn_{1-x}(SO_4)(_2)$ Bimetallic Sulfates. Journal of Physical Chemistry C, **2017** 121 (45):p. 24971-24978.

[155]. Schipper F, Erickson EM, Erk C, Shin JY, Chesneau FF, Aurbach D. Recent advances and remaining challenges for lithium ion battery cathodes I. Nickel-Rich, $LiNi_xCo_yMn_zO_2$. Journal of The Electrochemical Society. **2017** Jan 1;164(1):A6220-8.

Chapter 3

Experimental Methodology

This chapter starts with an introduction of the different synthesis routes applied to make most of the battery materials studied in this thesis, while others were commercially purchased. This is followed by a brief description of the structural and morphological characterizations performed on the material and sheds light on the rationale for the selection of these techniques. The techniques include X-ray diffraction, scanning electron microscopy, transmission electron microscopy, X-ray absorption spectroscopy and X-ray Photoelectron Spectroscopy.

3. Introduction

3.1. Synthesis

Researchers at Johnson Matthey have used various synthesis processes including both solid-state chemistry and solution chemistry to produce LFP and other cathode materials. Among the solid-state chemistry and solution chemistry processes, they tried to optimize the ball-milling and flame spray synthesis techniques. High-energy ball milling results in pulverization, intimate powder mixing, and then solid-state reaction to a new phase which has shown to improve the electronic conductivity due to very small size of the particles and their large specific surface area. This process is also effective in terms of homogeneity and particle size. On the other hand, flame spray pyrolysis is considered an effective technique for producing fine particles with homogeneous chemical composition in a short time. The particle size distribution produced by ultrasonic spray pyrolysis is narrow and controllable, the purity of the products is high, and the composition of the powders is easy to control. The reason for Johnson Matthey to choose these two synthesis processes was related to the performance. The ball milled LFP gave poorer performance compared to the flame spray method. Therefore, they required advanced characterization techniques to understand why flame spray produced a more active material. Similarly, the Mn-doped LFP materials were also synthesized using these two approaches and characterized to analyze their performance.

3.1.1. Ball Milling

Ball milling is usually done in a planetary ball mill at different speeds and to different times to produce distinct particle size. For synthesizing LFP via a mechanical/chemical reaction using ball milling procedure, the first step is to start with the stoichiometric ratios of starting materials – metal iron powder, iron (III) phosphate and trilithium phosphate. Sucrose is added as a conductive additive precursor. The mixture of the powders is then ball milled for 24 hours. The resulting powder is heat treated under argon at around 600˚C for 30 mins to carbonize the sucrose to obtain the final LFP/C samples. The same procedure can also be repeated to get LFP powder without carbon. Some of the research work using ball milling synthesis of LFP includes that of Kwon et al. [2], Kosova et al.[3] , Kim et al.[4] etc. The working principle of a ball mill is shown in **Figure 3-1.**

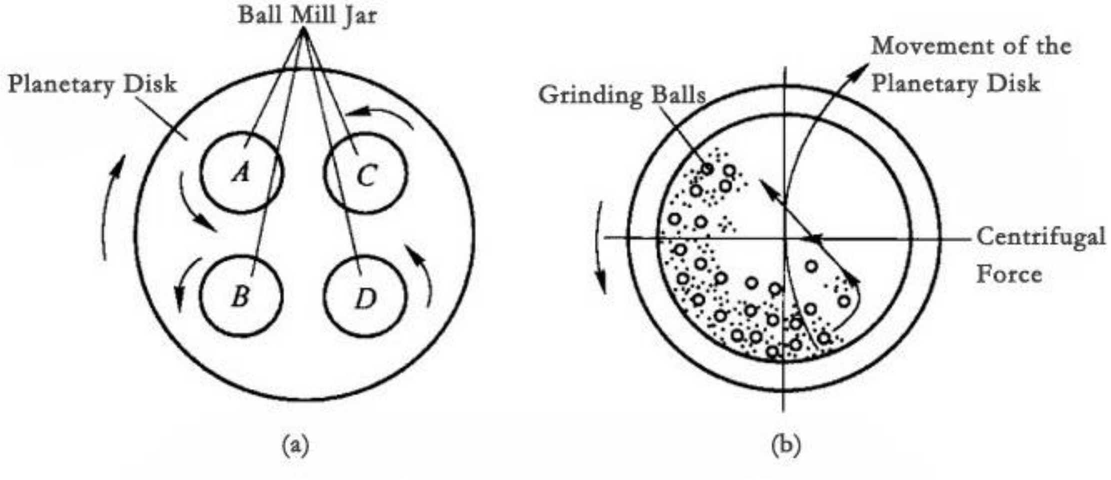

Figure 3-1 Working principle of a lab planetary ball mill; (a) overall layout of the planetary disk; (b) horizontal section of the grinding jar (*Tools for Micro and Nano Research website)*.

3.1.2. Flame Spray

Flame spray technique has been explained in the literature by Madler et al. [5]. The starting materials, $LiOH.2H_2O$, $FeSO_4.7H_2O$ and $(NH_4)_2HPO_4$, are dissolved in 0.1M aqueous HNO_3 solution stoichiometrically. An ultrasonic nebulizer is used to atomize the solution into droplets which are carried by air pressure into the pipe burner through the cyclone. The spray was ignited by commercial LPG and air from the compressor is used as an oxidizer. An electrostatic precipitator is used to collect the produced powder thus synthesized using the flame spray pyrolysis method. Yang et al. [6], Konarova et al.[7] , Bewley et al. [8], and others have shown the effect of flame spray pyrolysis on the performance of LFP cathode material in their work. **Figure 3-2** shows the schematic of a flame spray pyrolysis set up.

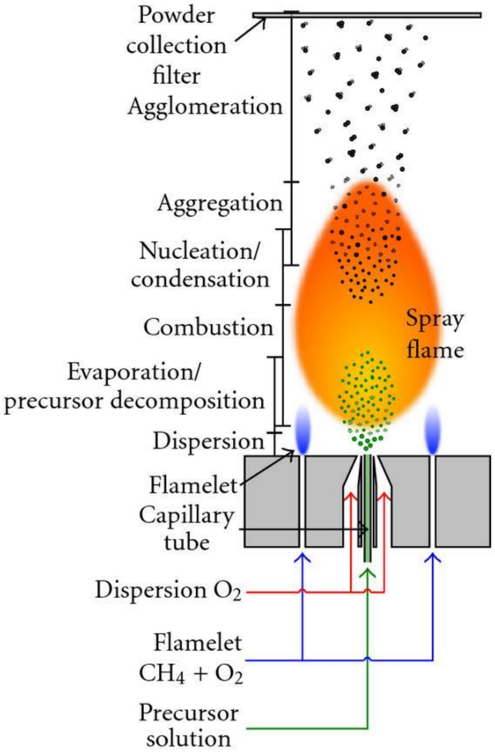

Figure 3-2 Working principle of a flame spray labelled with the different parts it comprises [9].

3.2. Material Characterization

3.2.1. X-ray Diffraction (XRD)

Theory

X-ray powder diffraction (XRD) analysis is one of the most extensively used characterization technique for analyzing materials. For Powder XRD (PXRD), the sample is usually prepared in a powder form or crushed using a pestle and mortar to a fine powder of crystalline material, which is then studied. The powdered sample consists of the crystalline domains randomly oriented which helps in better understanding of the material as a whole. When the 2D diffraction pattern of the sample is recorded, the different d-spacings show concentric rings corresponding to the scattering peaks within the crystal lattice. The positions and intensities of these peaks are used to identify the principal phase of the material. For example, even though graphite and diamond are made of the same element carbon, their diffraction peaks would be different since their structure is different from one another. This phase identification is significant because the material's property are highly dependent on its structure.

Max Von Laue was the first to discover that X-rays could be used to study crystalline materials. The individual layers in a crystalline material act as miniature diffraction gratings for X-rays. These days X-ray diffraction has become an increasingly common technique to study crystalline materials. It is based on the constructive interference of monochromatic X-rays with a crystalline sample. The X-rays are generated by a cathode ray tube, filtered to produce monochromatic radiation, collimated to concentrate and directed towards the sample surface. The interaction of the incident X-rays with the sample is considered constructive interference when the conditions satisfy the Bragg's law

$$\boxed{\lambda = nd\sin\theta}$$

where λ is the wavelength of the incident X-ray beam, *d* is the distance between adjacent planes of atoms (the *d*-spacings), and θ is the angle of incidence of the X-ray beam.

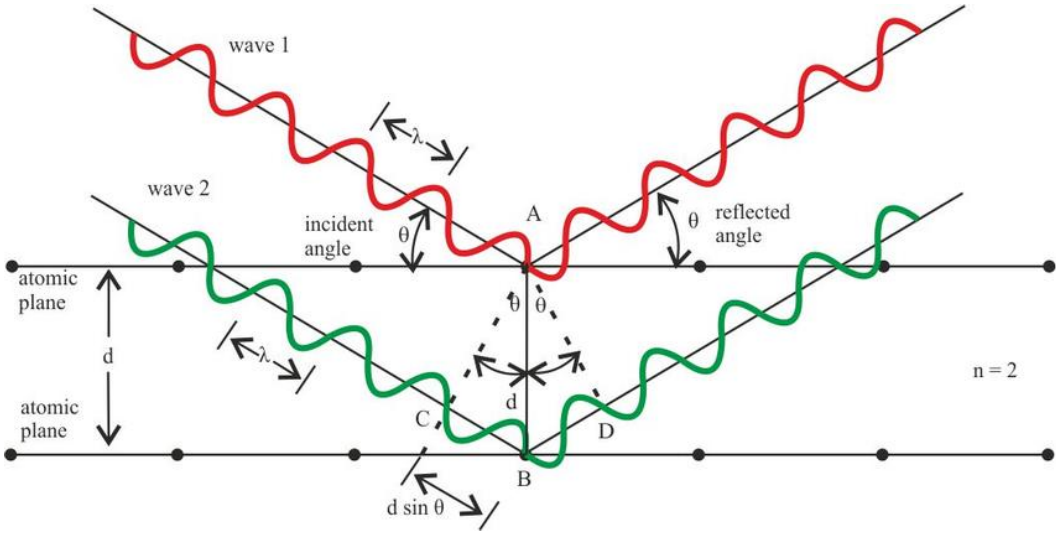

Figure 3-3 Schematic diagram of Bragg's law which can be derived from the triangle ABC [10].

The diffracted X-rays are then detected, counted and processed. By scanning the sample through a range of 2θ angles, all possible diffraction directions of the lattice should be attained due to the random orientation of the powdered materials. Conversion of the peak positions to a d-spacing format allows the comparison of the diffraction pattern with a database of crystal structures.

Instrumentation

X-ray diffractometers consist of three basic elements:

- X-ray tube/Source
- Primary Optics
- Sample Holder
- Secondary Optics
- Detector

X-rays are generated in a cathode ray tube by heating a filament to produce electrons. These electrons are then accelerated towards a target by applying a high voltage. When the electrons have enough energy to dislodge electrons from the inner shells of the target characteristic X-ray pattern are produced. The spectra consists of several parts but the most important being K_α and K_β. The wavelength of the X-rays generated is characteristic of the target material and is almost monochromatic in nature. Filtering, by foils or crystal monochromators is required to generate perfect monochromatic X-rays. Copper is the most common target CuK_α= 1.5418 Å. Most commonly the sample holder is stationary stage which can be rotated or not depending upon the measurement requirement. The stage is so placed that maximum X-rays can be received by the detector. Depending on the nature of the sample the holder varies. For most common powder measurements, the holder is a simple container transparent to X-rays, in the case of the thin films or single crystal measurements the geometry of the holder changes to suit the measurement. In general during sample preparation care needs to be taken to ensure that the sample surface is smooth and flat such that the normal from the surface of the sample subtends an equal angle at the source and detector. In addition, another fact to be taken care of is that excessive compaction of a powder sample might lead to the development of preferred orientation in the crystals which will lead to the production of erroneous diffraction data. As the incoming radiation impinges on the sample and the Braggs law is satisfied (constructive interference occurs). A detector records the X-ray signal and converts the signal to a count rate, which is then analyzed by the user. Broadly classified there are mainly two types of detectors a scintillation detector and a gas filled detector. A scintillation detector has a large number of losses, which makes the energy resolution of this kind of detector poor making it unsuitable to differentiate between K_α and K_β and radiation. However, it has high quantum yield making it ideal for point intensity measurements. A gas filled detector uses an inert gas like Ar or Xe, incoming X-ray photons ionize the inert gas into Ar^+ and an e^-. The energy required to ionize the inert gas is much lower than the energy of the X-ray photons, hence a few photons can ionize a large amount of the gas generating a large number of electrons. These electrons are then accelerated onto a wire, which is kept at a potential of about 1 kV. The burst of electrons on the wire is converted to a voltage pulse, which is then shaped and counted by the electronics. Gas filled detectors have a good energy resolution but display a loss in linearity at high count rates.

Applications

Powder samples were analyzed and the resulting XRD spectra were subjected to Rietveld refinement for calculation of crystallographic parameters and estimation of compositions. The type of XRD used during this study was Bruker D8 Advance XRD and was mainly used for newly synthesized materials to check their purity and crystallinity and the change in the lattice parameters, especially in the Mn-doped LFP materials with the increasing concentration of Mn.

3.2.2. Scanning Electron Microscope

Theory

The earliest known work describing the concept of a Scanning Electron Microscope (SEM) was by M. Knoll (1935) [11]. The primary reason for the usefulness of an SEM is the high resolution that can be obtained when bulk objects are examined. Advanced research instruments claim to go down to a resolution of 10 nm. Another important feature of the SEM is the three dimensional appearance of the specimen, which is a direct result of a large depth of field and shadow-relief effect of secondary and backscattered electrons.

Instrumentation

While the variations from model to model, all SEMs share the same basic parts.

- Electron gun
- Lenses
- Sample chamber
- Detectors
- Vacuum Chamber

In most SEM's electrons are created at a tungsten filament. High currents are passed through the filament which heats up and ejects free electrons. This process is called thermionic emission. These free electrons are accelerated by an applied voltage away from the filament and towards the sample. The electrons then pass through a magnetic lens (condenser lens) which focus them to a spot, and then a through scanning coil/ objective lens which bends the beam to the spot on the sample where one wants the image. By varying the current through the scanning coils, the position of the beam can be rastered. SEM images are not created all at once. The beam is rastered in a grid that is user-specified and for each pixel in the grid, data is collected. The lens and scan coils are simply current loops and currently creates magnetic fields. These magnetic fields exert forces on moving charged particles. These forces alter the path of the electrons, focusing them in a spot. The primary electron beam (~ 5keV or above) interacts with the sample. Some of these electrons simple reflect off the sample. These back-scattered electrons are high energy electrons (~keV). Some secondary electrons are created from the interaction of the primary beam with the material which is of much lower energy (~ less than 100s of eV). X-rays are also created when core electrons in the sample are knocked loose and valence electrons fall into the vacancies. The electron beam is raster scanned across the ample. The image size and pixel are user-defined. For each pixel, the signal comes from the detectors. The brightness of each pixel is dependent on the strength of the signal from the detector. For the secondary electron signal, the brightness corresponds to the number of secondary electrons generated. It is used to detect and amplify the signal of the secondary electrons.

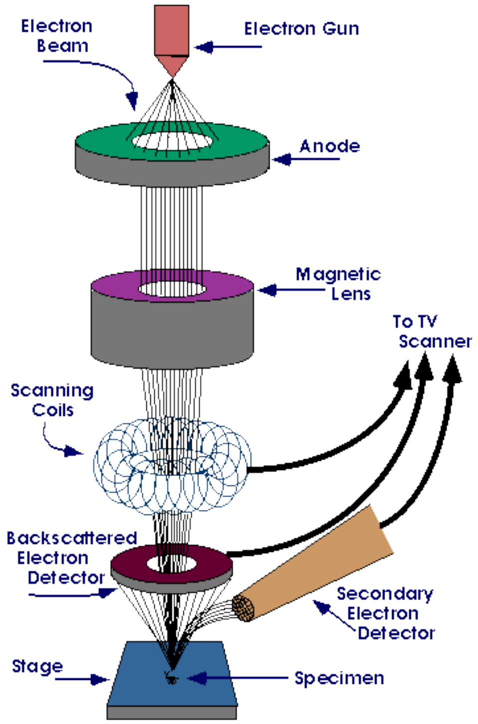

Figure 3-4 Labelled schematic diagram of the different parts of an SEM [12].

Applications:

There are numerous different types of SEMs available, according to specific needs [13-16]. SEM has various applications, for example, it can help in determining the surface feature, elemental composition and homogeneity of the same sample in a single experiment. The SEM used in this work was the JEOL FESEM 6340 F and the purpose of using FESEM was to study the morphology of the materials synthesized and the size of the particles formed with different synthesis techniques.

3.2.3. Transmission Electron Microscope (TEM)

Theory

The invention of the electron microscope was in 1931 by Ernst Ruska along with Max Knoll. The first commercial TEM was developed by Siemens in 1939. This paved the way for other researchers to follow suit and develop better TEMs [17-20]. It is a technique wherein a thin beam of electrons is fired through a thin sample, interacting with the sample as it goes through. The ejected electrons are analyzed either using a fluorescent detector or by sensors such as CCD camera. The resolution of a TEM device is much higher than the best light microscope this is mainly because the source of illumination in the case of a TEM is a stream of electrons instead of photons in the visible spectrum. The low wavelength of electrons leads to a very high resolution (0.2 nm) allowing a TEM to resolve even rows of individual atoms.

Instrumentation

In order to understand how a TEM uses electrons to create magnified images, it is necessary to understand how the instrument operates. A TEM can be broken down into three major sections:

- Electron Gun
- Condenser System
- The Image- Producing System

A TEM uses a beam of electrons instead of light exploiting the wave-particle duality of electrons. A very thin sample is placed along the beam of electron. The lenses help in focusing the accelerated beam produced by the electron gun. The beam passes through the sample and imprints its image. A TEM can magnify images of the very thin sample down to its atomic resolutions. One type of transmission microscope is the Scanning Transmission Microscope (STEM) where the electron beam is focused on a specific point of the sample rather than the whole surface. The transmitted beam from this point or surface is then detected. In addition, one can measure some of the transmitted beam characteristics at different locations of the sample. For example, one can measure the electron energy loss (EELS) and to do so a magnetic prism is used to deflect the beam more or less depending on its energy. The more the beam loses energy, the more it is deflected. The measure of the deflection allows characterizing different parts of the sample. This technique allows not only visualizing but also identifying the chemical nature of atoms in ultra-thin samples.

Applications

During the course of this thesis the dominant role of TEM was to utilize its elemental mapping feature to map different regions of the electrode before and after charging to evaluate the ratio of Mn and Fe in the Mn-doped LFP samples to observe any changes during the electrochemical process. All the measurements were conducted on a JEOL JSM 2100 F.

3.2.4. X-ray Absorption Spectroscopy (XAS)

Theory

In 1943 Oliphant [21] proposed the idea of a pulsed magnet ring and was followed by Veksler [22] in 1944 and McMillan [23] in 1945. This led to the manifestation of an 8 MeV accelerated synchrotron by Goward and Barnes [24]. Two months later, General Electric Laboratory's operated a 70 MeV synchrotron with the help of Gurewitsch, Langmuir and Pollock [25]. X-rays were discovered by Rontgen in 1895 and by 1947 Elder et al had already observed synchrotron radiation and a synchrotron for the production of 70-MeV X-rays has been built and tested [26]. This was a huge success since many followed suit with even more powerful synchrotrons emerging over time [27-32]. There are now more than 60 synchrotrons and FELs around the world dedicated to applications in physics, engineering, pharmacology, and new materials.

The discovery of X-rays by Rontgen over more than 100 years ago [33] has proven to be one of the most revolutionary aspects in the field of materials characterization. The scattering, absorption and emission properties of X-rays enable a non-destructive and detailed material analysis at an atomic scale, to probe the relationship between the structure of materials to their physical and electrochemical characteristics. X-ray emission spectroscopy facilitates the determination of the chemical composition of the compound by looking at the various X-ray fluorescent lines. With the advancement in the X-ray source technology, we can now verify even the fine structures in the X-ray absorption spectra, also known as an X-ray absorption fine structure or XAFS. XAFS consists of two distinct parts – X-ray absorption near edge structure (XANES) and extended X-ray absorption fine structure (EXAFS). Thus, XANES and EXAFS combined is a very powerful tool to analyze the entire crystal structure of a given compound. There have been reviews on the application of the theory of EXAFS [34] with regard to catalysis [35] liquids [36] and electrochemical interfaces [37]. XAS measures the X-ray absorption coefficient in the given energy range of the selected element, i.e. before and after the absorption edge. Since every element has its unique absorption edge, therefore, XAFS measurement is element specific. XANES comprises of the absorption edge and just beyond it (~ 100eV after the edge) while EXAFS can be analyzed until 1000eV beyond the absorption edge giving quantitative information of the structure like first shell distances and coordination number.

The absorption coefficient μ(E) gives an idea on how X-rays are absorbed by the matter as a function of the energy E. If I_0 is the incident intensity of the X-ray falling on a sample, E is the photon energy and t is the sample thickness, then according to Beer's Law, the transmitted intensity is given by:

$$\boxed{\mathbf{I_t\ (t) = I_0} e^{-\mu(E)t}}$$

Where μ(E) is the energy-dependent X-ray absorption coefficient, given as,

$$\boxed{\mu(E) \sim \frac{d\,Z^4}{m\,E^3}}$$

At a certain value of energy, we observe a dramatic increase in μ(E). This sharp increase in energy is called the absorption edge and this phenomenon can be explained by the photoelectric effect. When the electron absorbs X-ray photons, the excess energy that is left after the binding energy of the electron is overcome, is transferred to the electron as its kinetic energy. This ejected electron is known as the photoelectron, which is responsible for EXAFS mechanism. This electron vacancy leaves the atom in a very unstable position which can be followed by either two processes – either a higher energy electron replaces the core vacancy thus giving rise to a characteristic X-ray emission; or a higher electron occupies the vacancy and releases energy, which in turn ejects another electron into the continuum, also known as Auger effect.

Instrumentation

A synchrotron has the following main parts:

(1) Electron gun
(2) LINAC
(3) Booster ring
(4) Storage ring
(5) Beamline
(6) End station

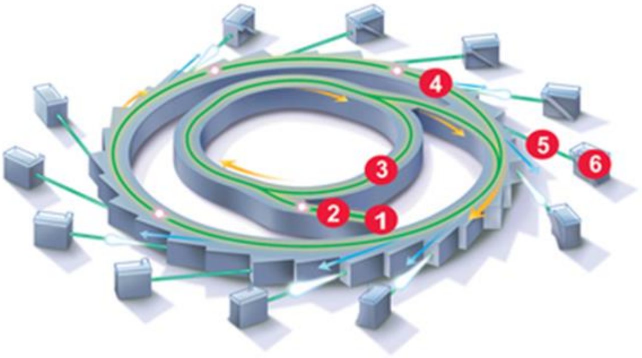

Figure 3-5 Parts of a synchrotron labelled (courtesy website: odec.ca)

Electrons are produced at the electron gun by thermionic emission from a heated tungsten matrix cathode. The electrons are then accelerated inside the linear accelerator (LINAC) by electric fields. The electrons then enter the booster ring where they are further accelerated with the help of magnetic fields produced by the bending magnets almost to the speed of light. After this the electrons are inserted into a storage ring, where they flow in a circular trajectory with constant speed. These electrons are then deflected several degrees its straight path and this sudden change of direction causes the emission of synchrotron light. A succession of optical systems such as apertures, silicon mirrors, and crystals are employed to screen the synchrotron light and focus the beam. The beam is then incident on the material of interest and interacts with its atoms and molecules. With the help of detectors, information on the interaction between the X-ray beam and the material is recorded. This information is extracted, prepared and stored for analysis at the end station.

Scope and Applications of XAS

The XANES part of the XAS provides us with key information about any particular element under investigation. The edge energy helps to determine the oxidation state of the element. If the element has higher oxidation number then it means that it has higher charge, therefore, it would take higher energy to eject the electron from its core. The pre-edge is another important aspect of the XANES region. The pre-edge region is the part observed before the rising of the K-edge spectrum. This pre-edge region can have low intensity peaks that correspond to 1s-3d transitions in transition metal containing compounds. There is a difference in the intensity of pre-edge features for different crystal structures, and therefore, it is easier to differentiate between tetrahedral and octahedral coordination. Usually, the intensity increases in the order: octahedral < square pyramidal < tetrahedral. This feature is very weak or absent when the transition element is present in sites with a center of symmetry. The EXAFS mechanism can be understood by analyzing the interference resulting from the interaction of the photoelectron with the possible neighbouring atoms. A typical X-ray absorption spectra look like that shown in **Figure 3-6.** If it is an isolated atom, the EXAFS spectrum will be smooth and without any distinct features. But for an atom in a crystal structure that is surrounded by multiples atoms, the EXAFS spectrum depicts oscillations which may be due to the constructive or destructive interference of the photoelectron with the neighbouring atoms. However, with EXAFS we cannot probe long distances so we only get local structural information, which means the photoelectron energy reduces with time and space.

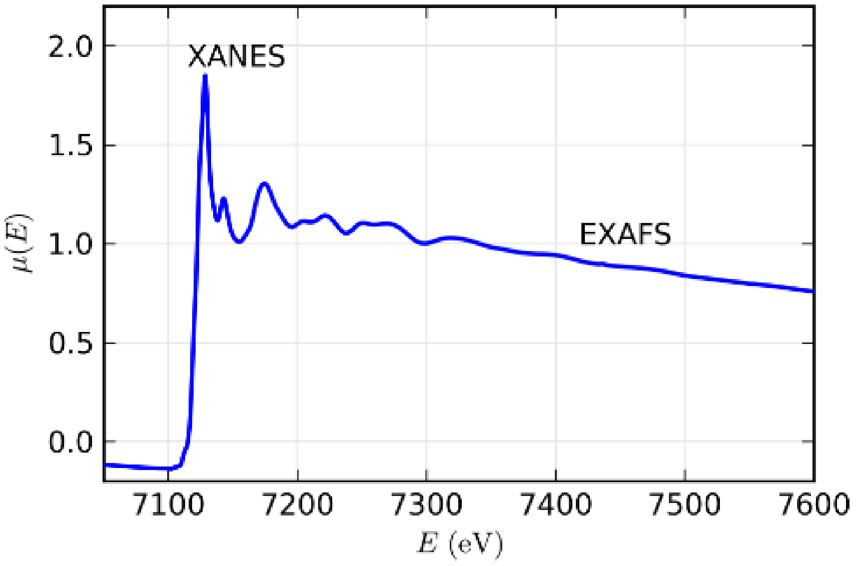

Figure 3-6 Typical XAS images for Fe K-edge (Newville, 2018)

3.2.5. X-ray Photoelectron Spectroscopy

Theory

XPS is a quantitative spectroscopic technique that is sensitive to surface phenomena. XPS spectra are obtained by shining the sample with a beam of X-rays and measuring the kinetic energy and count of electrons that are subsequently emitted. It can be used to measure elemental composition and oxidation state of the elements that exist within a material. The governing equation for XPS studies is based on Ein*stein's theory of photoelectric* emission*:*

$$\boxed{h\upsilon = KE + BE + W}$$

Where, hυ is the energy of the source radiation, KE is the energy of the photon that is ejected from the sample surface after the source radiation interacts with it, BE is the minimum amount of energy required to eject an electron from a specific orbital and W is the spectrometer work function.

Binding energy (BE) is characteristic of each core atomic orbital of an element making XPS an extremely useful fingerprinting tool. A general XPS spectrum has been shown in **Figure 3.7**. The spectra pertains to a scan of an activated carbon sample obtained from human hair [38]. Each peak in the spectra corresponds to photoelectrons emitted from a particular core level with a characteristic BE.

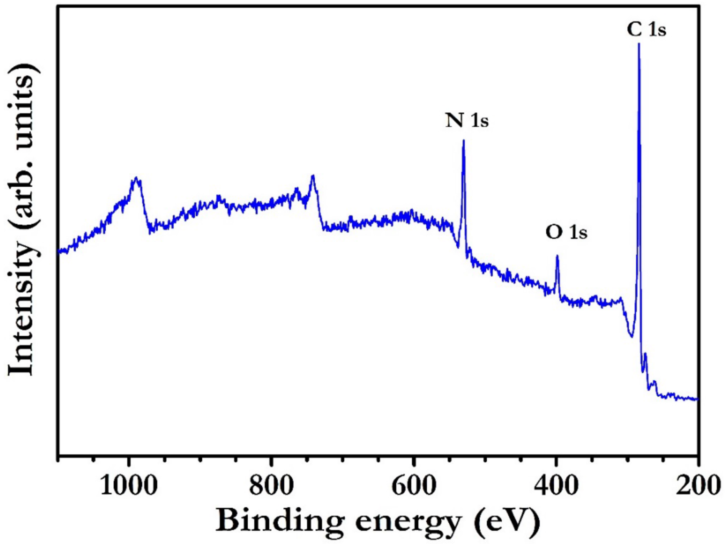

Figure 3-7: X-ray Photoelectron survey spectra of an Activated carbon sample obtained from human hair (obtained with permission from a postdoc in our lab).

Applications

XPS has been used in this work as an analytical tool to determine any change in the oxidation state of a specific element. The data specific to elements was obtained by carrying out high resolution scans in a narrow energy band around the reported binding energy of the element. An increase in binding energy implies that the net nuclear charge of the remaining electrons increases which is indicative of an increased oxidation state. This increased oxidation state leads to a chemical shift wherein the spectra shift to a higher energy. Sample preparation was of paramount importance as the battery materials are sensitive to the ultrahigh vacuum conditions in the XPS system. The samples were dried and degassed in an inert environment before analysis.

3.2.6. Finite Difference Method Near Edge Spectroscopy (FDMNES)

Along with experimental XANES of model compounds, this chapter also incorporates a theoretical tool for modelling their XANES spectra computationally. The software package which aids in carrying out these simulations is called Finite Difference Method Near Edge Spectroscopy, or FDMNES [39]. FDMNES is a calculation program for XAS where it calculates the absorption cross-section, structure factors and the intensities of anomalous (resonant) diffraction. FDMNES provides both cartesian and spherical tensors, that are used for the peak-description of XAS [40]. Parameters for simulation are defined in an input file. FDMNES reads this file and starts the calculation of the XANES. After the calculation, the convolution of the data is following. The calculated data can be compared with the experimental spectra [41-44].

FDMNES takes atoms in local clusters around the absorbing atom into account. For calculation of the absorption signal, the calculation of density of states (DOS) and the initial states ψ_i are necessary. Therefore the atomic configuration must be given to calculate the DOS for the electrons in the cluster and the initial states of the absorber. Optionally the "self-consistent-field" (SCF) theory can be used that minimizes the energy of the cluster to obtain the electron configurations. In order to calculate the absorption signal, an excited state for the absorbing atom is assumed by placing the core electron on the first available unoccupied level. The atomic densities are superimposed to get the charge density of the cluster and the Poisson equation is then solved to get the Columbic potential [45, 46]. Once the potential has been constructed, the Schrodinger-like equation (SE) is solved to get the final states $\psi_f(r)$. The general structure of an indata file looks somewhat like as shown below. The atomic positions and cell parameters used in these indata files can be obtained from the Rietveld refinement of the XRD data of these materials.

```
! Fdmnes indata file

! Calculation for the iron K-edge in FeO


Filout

FeO_Fe-edge                         // the name of the output file without
extension.


Range

-2. 0.2 5. 0.5 10. 1. 40.


Radius                              // cluster radius

3.0


Molecule

1 1 1  90. 90. 90.                  //Unit cell parameters


26      0       0       0           // Atomic number, position

8       2.1554  0       0

8       -2.1554 0       0

8       0       2.1554  0

8       0       -2.1554 0

8       0       0       2.1554

8       0       0       -2.1554


Green                               //calculated in multiple scattering mode and
                                    uses a muffin –tin approximation and much
                                    faster than finite difference method

Quadrupole
```

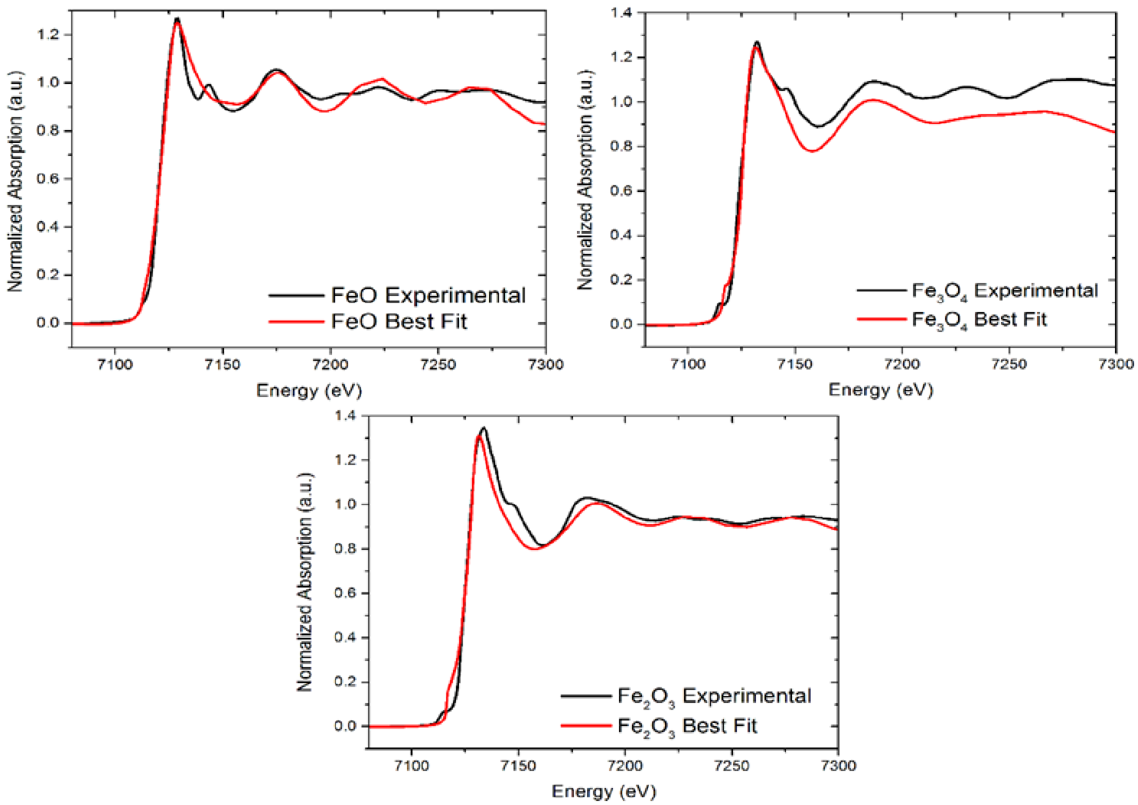

Figure 3-8: FDMNES simulations for FeO (a), Fe_3O_4 (b) and Fe_2O_3 (c) (red) compared with their actual experimental XANES data (black).

Figure 3-8 shows the best fit obtained for FeO, Fe_3O_4 and Fe_2O_3. The simulation was conducted with a cluster size of 3.5 Å and including Green function and SCF. The convolution parameters were adjusted and optimized to get the closest fit possible. The main rising edge was almost perfectly overlapping. A pre-edge was also observed for the theoretical model though there was a shift observed between the experimental and theoretical pre-edge. The Fermi energy had to be shifted for each of these calculations since the oxidation of Fe changes for each material. For Fe_2O_3, however, it was a bit more difficult to get a good fit with the same convolution parameters. Attempts are still being made to improve the fittings by obtaining better-optimized values. The reason for the discrepancy between the experimental and fits are still unknown, but the results do over offer significantly better agreement with experiment with continued optimization.

Regarding theoretical modelling, there is still plenty of work to be done and the many facades of this project lead to no shortage of options that can be looked at in the future. The main reason for undertaking this approach was to understand how the XANES spectra develop with cluster modelling and how the parameters affect the shape and development of the curve. Precise and accurate calculations of all spectral features are still difficult, time-consuming, and not always reliable. This situation is improving, but at this point, quantitative analyses of XANES using ab initio calculations are very rare. Still, such calculations can help explain which bonding orbitals or structural characteristics give rise to certain spectral features. Moreover, modelling gives us the opportunity to play around with the lattice parameters, site sensitivity, temperature and other factors that can affect the actual XANES spectra and thus give a better understanding of the experimental patterns.

References

[1]. Le Gallic, T., E. Assoumou, and N. Maizi, Future demand for energy services through a quantitative approach of lifestyles. Energy, **2017** 141:p. 2613-2627.

[2]. Kwon, S.J., C.W. Kim, W.T. Jeong, and K.S. Lee, Synthesis and electrochemical properties of olivine $LiFePO_4$ as a cathode material prepared by mechanical alloying. Journal of Power Sources, **2004** 137 (1):p. 93-99.

[3]. Kosova, N. and E. Devyatkina, On mechanochemical preparation of materials with enhanced characteristics for lithium batteries. Solid State Ionics, **2004** 172 (1-4):p. 181-184.

[4]. Kim, C.W., M.H. Lee, W.T. Jeong, and K.S. Lee, Synthesis of olivine $LiFePO_4$ cathode materials by mechanical alloying using iron(III) raw material. Journal of Power Sources, **2005** 146 (1-2):p. 534-538.

[5]. Madler, L., H.K. Kammler, R. Mueller, and S.E. Pratsinis, Controlled synthesis of nanostructured particles by flame spray pyrolysis. Journal of Aerosol Science, **2002** 33 (2):p. 369-389.

[6]. Yang, M.R., T.H. Teng, and S.H. Wu, $LiFePO_4$/carbon cathode materials prepared by ultrasonic spray pyrolysis. Journal of Power Sources, **2006** 159 (1):p. 307-311.

[7]. Konarova, M. and I. Taniguchi, Preparation of $LiFePO_4/C$ composite powders by ultrasonic spray pyrolysis followed by heat treatment and their electrochemical properties. Materials Research Bulletin, **2008** 43 (12):p. 3305-3317.

[8]. Bewlay, S.L., K. Konstantinov, G.X. Wang, S.X. Dou, and H.K. Liu, Conductivity improvements to spray-produced $LiFePO_4$ by addition of a carbon source. Materials Letters, **2004** 58 (11):p. 1788-1791.

[9]. T. Karhunen, A.L., J. Leskinen, R. Buchel, O. Waser, U. Tapper, J. Jokiniemi, Transition Metal-Doped Lithium Titanium Oxide Nanoparticles Made Using Flame Spray Pyrolysis. ISRN Nanotechnology, **2011** (2011):p. 1-6.

[10]. Waeselmann, N., Structural transformations in complex perovskite-type relaxor and relaxor-based ferroelectrics at high pressures and temperatures. **2012**, Fachbereich Geowissenschaften der Universität Hamburg: Hamburg.

[11]. Nixon, W., History and early developments of the scanning electron microscope within Cambridge University. Electron Microscopy 1998, Vol 1, **1998**:p. 27-28.

[12]. Walock, M., Nanocomposite coatings based on quaternary metal-nitrogen and nanocarbon systems, in **Physics**. **2012**, University of Alabama at Birmingham

[13]. Devaney, J.R., Application of Scanning Electron Microscopy. Applied Spectroscopy, **1969** 23 (6):p. 676-&.

[14]. Johansson, S., J. Moverare, and R. Peng, Recent Applications of Scanning Electron Microscopy. Praktische Metallographie-Practical Metallography, **2013** 50 (12):p. 810-820.

[15]. Mercer, H.N., Selected Applications of Scanning Electron Microscopy. Texas Reports on Biology and Medicine, **1971** 29 (3):p. 423-&.

[16]. Olavarria, J.C., Applications and Limits of the Scanning Electron-Microscopy. Archivos De Biologia Y Medicina Experimentales, **1979** 12 (4):p. 492-492.

[17]. Amelinckx, S., Gevers, R., and Van Landuyt, Diffraction and Imaging Techniques in Material Science, ed. E. North-Holland. **1978**, North-Holland Pub. Co.. Sole distributors for the USA and Canada.

[18]. David B. Williams, C.B.C., The Transmission Electron Microscope. **1996**: Springer, Boston, MA.

[19]. Hall, C.E., Introduction to electron microscopy. **1953**: McGra-hill Publishing Company Ltd; London.

[20]. Heidenreich, R.D., Fundamentals of transmission electron microscopy. **1964**.

[21]. Oliphant, M.L., J.S. Gooden, and G.S. Hide, The Acceleration of Charged Particles to Very High Energies. Proceedings of the Physical Society of London, **1947** 59 (334):p. 666-677.

[22]. Veksler, V.I., A new method for acceleration of relativistic particles. Comptes Rendus De L Academie Des Sciences De L Urss, **1944** 43:p. 329-331.

[23]. Mcmillan, E.M., The Synchrotron - a Proposed High Energy Particle Accelerator. Physical Review, **1945** 68 (5-6):p. 143-144.

[24]. Goward, F.K. and D.E. Barnes, Experimental 8 Mev Synchrotron for Electron Acceleration. Nature, **1946** 158 (4012):p. 412-412.

[25]. Elder, F.R., A.M. Gurewitsch, R.V. Langmuir, and H.C. Pollock, A 70-Mev Synchrotron. Journal of Applied Physics, **1947** 18 (9):p. 810-818.

[26]. Pollock, H.C., R.V. Langmuir, F.R. Elder, J.P. Blewett, and A.M. Gurewitsch, Design of a 70-Mev Synchrotron. Physical Review, **1946** 70 (9-10):p. 798-798.

[27]. Bathow, G., E. Freytag, and R. Haensel, Measurement of Synchrotron Radiation in X-Ray Region. Journal of Applied Physics, **1966** 37 (9):p. 3449-&.

[28]. Ershov, A.G., F.A. Korolev, O.F. Kulikov, and B.I. Shkurskii, Experimental Investigations of the Compression of a Lump of Electrons in a 280 Mev Synchrotron. Doklady Akademii Nauk Sssr, **1960** 133 (3):p. 554-557.

[29]. Hartman, P.L. and D.H. Tomboulian, Ultraviolet Radiation from the Cornell Synchrotron. Physical Review, **1952** 87 (1):p. 233-233.

[30]. Madden, R.P. and K. Codling, New Autoionizing Atomic Energy Levels in He, Ne, and Ar. Physical Review Letters, **1963** 10 (12):p. 516-&.

[31]. Tomboulian, D.H. and D.E. Bedo, Absorption and Emission Spectra of Silicon and Germanium in the Soft X-Ray Region. Physical Review, **1956** 104 (3):p. 590-597.

[32]. Tomboulian, D.H. and P.L. Hartman, Spectral and Angular Distribution of Ultraviolet Radiation from the 300-Mev Cornell Synchrotron. Physical Review, **1956** 102 (6):p. 1423-1447.

[33]. Harris, R.D., Fundamentals of Radiology, 3rd Edition - Squire,Lf. Jama-Journal of the American Medical Association, **1983** 249 (20):p. 2827-2827.

[34]. Rehr, J.J. and R.C. Albers, Theoretical approaches to x-ray absorption fine structure. Reviews of Modern Physics, **2000** 72 (3):p. 621-654.

[35]. Carrier, X., E. Marceau, H. Carabineiro, V. Rodriguez-Gonzalez, and M. Che, EXAFS spectroscopy as a tool to probe metal-support interaction and surface molecular structures in oxide-supported catalysts: application to Al_2O_3-supported Ni(II) complexes and ZrO_2-supported tungstates. Physical Chemistry Chemical Physics, **2009** 11 (35):p. 7527-7539.

[36]. Filipponi, A., EXAFS for liquids. Journal of Physics-Condensed Matter, **2001** 13 (7):p. R23-R60.

[37]. Dewald, H.D., Use of Exafs to Probe Electrode Solution Interfaces. Electroanalysis, **1991** 3 (3):p. 145-155.

[38]. Satish, R., V. Aravindan, W.C. Ling, N.K. Woei, and S. Madhavi, Macroporous carbon from human hair: A journey towards the fabrication of high energy Li-ion capacitors. Electrochimica Acta, **2015** 182:p. 474-481.

[39]. Joly, Y., Finite-difference method for the calculation of low-energy positron diffraction. Physical Review B, **1996** 53 (19):p. 13029-13037.

[40]. Bunau, O. and Y. Joly, Self-consistent aspects of x-ray absorption calculations. Journal of Physics-Condensed Matter, **2009** 21 (34):p.

[41]. Bourke, J.D., C.T. Chantler, and Y. Joly, FDMX: extended X-ray absorption fine structure calculations using the finite difference method. Journal of Synchrotron Radiation, **2016** 23:p. 551-559.

[42]. Joly, Y., FDMNES User's Guide: Manuel FDMNES. Institut N´eel:p.

[43]. Joly, Y., O. Bunau, J.E. Lorenzo, R.M. Galera, S. Grenier, and B. Thompson, Self-consistency, spin-orbit and other advances in the FDMNES code to simulate XANES and RXD experiments. 14th International Conference on X-Ray Absorption Fine Structure (Xafs14), Proceedings, **2009** 190:p.

[44]. Smolentsev, G., A.V. Soldatov, Y. Joly, S. Pascarelli, and G. Aquilanti, Beyond muffin-tin model for theoretical analysis of as K-edge XANES of InAs. Radiation Physics and Chemistry, **2006** 75 (11):p. 1571-1573.

[45]. Hedin, L. and Lundqvis.Bi, Explicit Local Exchange-Correlation Potentials. Journal of Physics Part C Solid State Physics, **1971** 4 (14):p. 2064-&.

[46]. Perdew, J.P. and Y. Wang, Accurate and Simple Analytic Representation of the Electron-Gas Correlation-Energy. Physical Review B, **1992** 45 (23):p. 13244-13249.

Chapter 4

Phosphate-based Cathode Material for High Stability

This Chapter focuses on the one of the most important battery cathode material, $LiFePO_4$ (LFP). It starts with a brief introduction and previous research done on LFP and how studies are still continuing on this material despite there being so many other materials out there in the market. This is followed by some initial characterization including XRD, SEM and TEM of the pristine material before doing the electrochemical studies. The second section of the chapter focuses on primarily the electronic and structural investigation using X-ray Absorption spectroscopy on the transition metal edge, Fe, along with phosphorus P K-edge as well. This chapter also shows in-situ results for LFP Fe K-edge and reports the drawbacks of the in-situ approach and how further experiments were continued using an alternative technique which gives an equally good analysis as compared to in-situ studies.

4. Introduction

4.1. Background

As discussed in Chapter 2, LFP, first reported by Padhi et al [1], has been a great success both in performance and commercialization due to its high safety and unique crystal structure. While it has some crucial advantages over other cathode materials, like flat voltage profile, low material cost, abundant material supply and better environmental compatibility, it also faces some challenges like relatively low theoretical capacity, low density, poor electronic conductivity and low ionic diffusivity. It is because of these reasons that LFP is still one of the most researched battery materials. A comparison of the rate capabilities of LFP has been reviewed by Zhang [2] where he has compared the performance of various LFP materials considering many parameters such as conductive carbon loading, powder mixing procedure, carbon coating, a carbon precursor, doping, particle size, and heat-treatment. LFP has shown to have a wide range of capacities (60mAh/g at high C rates to 170 mAh/g at low C rates) based on the above parameters. While some LFP showed a good capacity at high current rates, others showed a sharp drop with high current. Particle size reduction has always been an important focus to increase the capacity; recent studies have shown that the specific capacity has no clear dependence on the low range particle size. Other studies show that the electronic conductivity between the LiFePO4 powders and the current collector plays a determining role in the high rate performance of the battery cell. Studies have also shown that the synthesis techniques also affect the performance to an extensive rate [3-13].

4.2. Experimental Procedure

The LFP powders studied in this chapter include commercial LFP materials from Targray (LFP-T) and Linxi (LFP-L), as well as LFP powder synthesized by Johnson Matthey by ball milling LFP (BM) and flame spray LFP (FS) techniques.

4.2.1. Electrode Preparation

To prepare the electrode, the first step is to mix the binder polyvinylidene fluoride (PVDF) with a few ml of N-Methyl-2-pyrrolidone (NMP) and stir for about 5 mins. Carbon super P is added to the PVDF solution and stirred again for 5 more minutes. Synthesized LFP powder is then added to this mixture with a few more drops of NMP so that the slurry is not too thick and stirred overnight to get a smooth homogenous suspension. The approximate percentage weight ratio of the active material, carbon black and PVDF is around 85:10:5. The slurry should have a good consistency – excess NMP leads to cracked coating while insufficient NMP can result in a porous coating. The mixture is rolled on an aluminium sheet and vacuum heated at 120˚C for around 4-6 hours. The dried electrodes are then cut into circular discs of 14mm diameter and stored in the vacuum chamber. Before assembling the cells inside the glove box, each electrode is weighed as the active material weight enables the calculation of the current range during cell testing.

4.2.2. Cell Assembly

Cell assembly is done inside the glove box. Ideally, the working conditions for a glove box should have oxygen and moisture levels less than 0.1 ppm, however, practically it should not rise beyond 2.5-3 ppm at max. After all the necessary cell components are put inside the vacuum chamber, it is flushed with argon at least 5 times to remove all possible moisture and oxygen, before taking the cell parts inside the glove box. The can of the cell is first placed on the working board and the electrode carefully placed inside it on the centre. One piece of the separator (Whatman Cat No. 1825-047 UK) is then placed over the electrode so that the electrode is fully covered. A few drops of electrolyte, 1M $LiPF_6$ dissolved in a 1:1 volume ratio of ethylene carbonate (EC): dimethyl carbonate (DMC), is poured over the separator in droplets to moisten it completely. On top of the separator, a small circular piece of polished lithium foil is placed and over it a spacer and a spring are positioned for mechanical support. The cap, with a vacuum O-ring, is then carefully placed over all the cell components and crimped in a crimping machine. The crimped cell is always handled with plastic tweezers to avoid short circuit and the excess electrolyte that creeps out during crimping is wiped off with a tissue. A badly crimped coin cell can split open after a few hours in ambient due to the swelling of lithium foil after reaction with moisture so proper crimping is extremely important before the cell is brought outside the glove box. For *in-situ* cells, there is no difference in the assembly of the cell parts except for the cap, spacer and can have holes (5mm diameter) drilled in the centre (**Figure 4-1**). The holes on the cap and can are sealed with polypropylene tape (PP) for X-rays to pass through it while the cells are charging and discharging. Any excess electrolyte after crimping can take away the adhesion of the tape and expose the lithium inside the cell to moisture which is extremely dangerous so the sealing of the holes with the tape should be carefully handled.

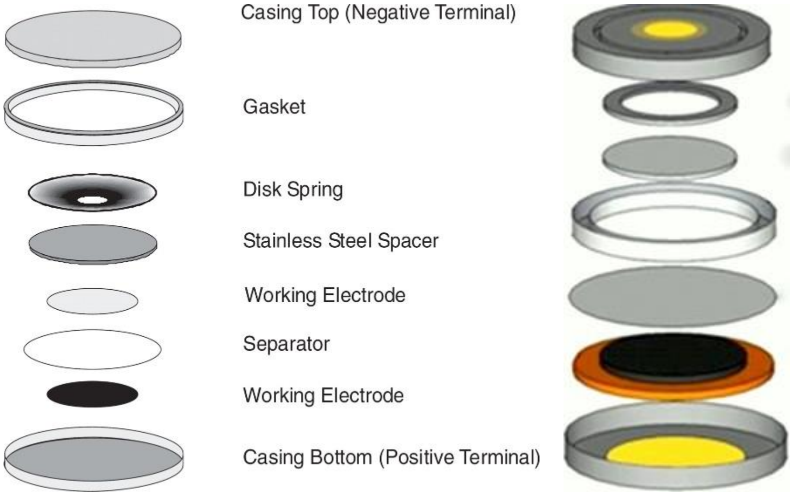

Figure 4-1 Cell assembly for an *ex-situ* and *in-situ* coin cell [14].

4.2.3. Electrochemistry

Electrochemical studies were performed in a CR-2016 coin cell configuration and the *ex-situ* cyclic voltammetry (CV) experiments were performed at room temperature between 2.6 V and 4.2 V at different current densities using a Neware battery test system (Neware, BTS-5V10 mA, China) and Arbin BT 2000 in ambient temperature. For *in-situ* experiments, CV testing was done on BioLogic SP300 potentiostat.

4.3. Characterization

Sample purity was established and structural refinements carried out from powder X-ray diffraction (PXRD) patterns collected with a Bruker D8 diffractometer (Bragg-Brentano geometry) equipped with a Cu Kα X-ray tube operated at 40kV and 40mA. The manually ground powders were mixed with a Si standard (20wt% a = 5.43199 Å) and mounted in a top-loaded sample holder with data accumulated from 10-120° 2θ using a step size of 0.02° and a dwell time of 2s per step. Rietveld refinement of the XRD data was carried out with TOPAS V4.1 (Bruker, 2008), using the fundamental parameters approach (Cheary & Coelho, 1992). The specimen-dependent parameters refined were the zero error, a user-specified number of coefficients for the Chebyshev polynomial fitting of the background, and the 'Crystallite Size' to model microstructure-controlled line broadening.

Secondary electron images of LFP that had been deposited on a carbon tape and coated with Pt at 20mA for 45 secs, were collected on a JEOL field emission scanning electron microscope (JSM 6340F) operated at 2.0 – 5.0 kV.

For TEM measurements, the powder electrode material was finely crushed and mixed with few drops of ethanol. This was then dropped over the tiny circular carbon mesh which is used as the sample holder for TEM analysis. The electrode material was then analyzed using TEM JEOL 2100F with an accelerating voltage of 200KV.

For the *ex-situ* and *in-situ* analysis of the Fe K-edge, LFP data was collected at the Singapore Synchrotron Light Source, XAFCA (SSLS) at National University of Singapore (NUS). The QEXAFS Transmission mode was used for the *ex-situ* cells with Fe K-edge at 7113eV. For the P K-edge, all the XAS data were collected at SUT-NANOTEC-SLRI beamline (BL5.2), Thailand in fluorescence mode.

4.4. Results and Discussion

4.4.1. Electrochemistry

Figure 4-2 (a), (b), (c) shows the electrochemical performance of LFP-T, LFP (BM) and LFP (FS) respectively. The cell was cycled for 10 cycles at 0.1C-rate. Columbic efficiency tends to increase over charge-discharge cycles because the buildup of SEI layer slows down further parasitic reactions and stabilizes the electrode. Initially, when the electrode was new, the SEI layer is thin and parasitic reactions are quick which leads to lower columbic efficiency. For the commercial LFP-T, the discharge capacity stabilized around 120 mAh/g after the first few cycles. The ball milled samples showed similar capacity of around 125 mAh/g at 0.1C while the flame spray LFP showed the best results giving a capacity of almost 160 mAh/g at 0.1C.

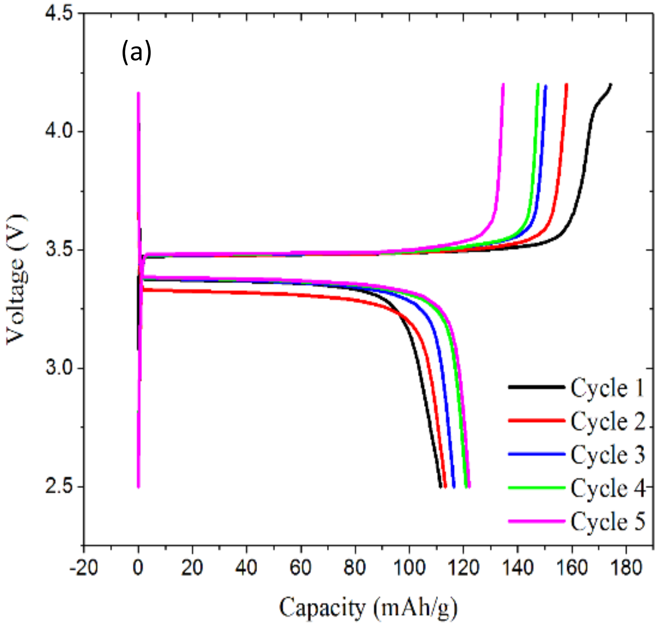

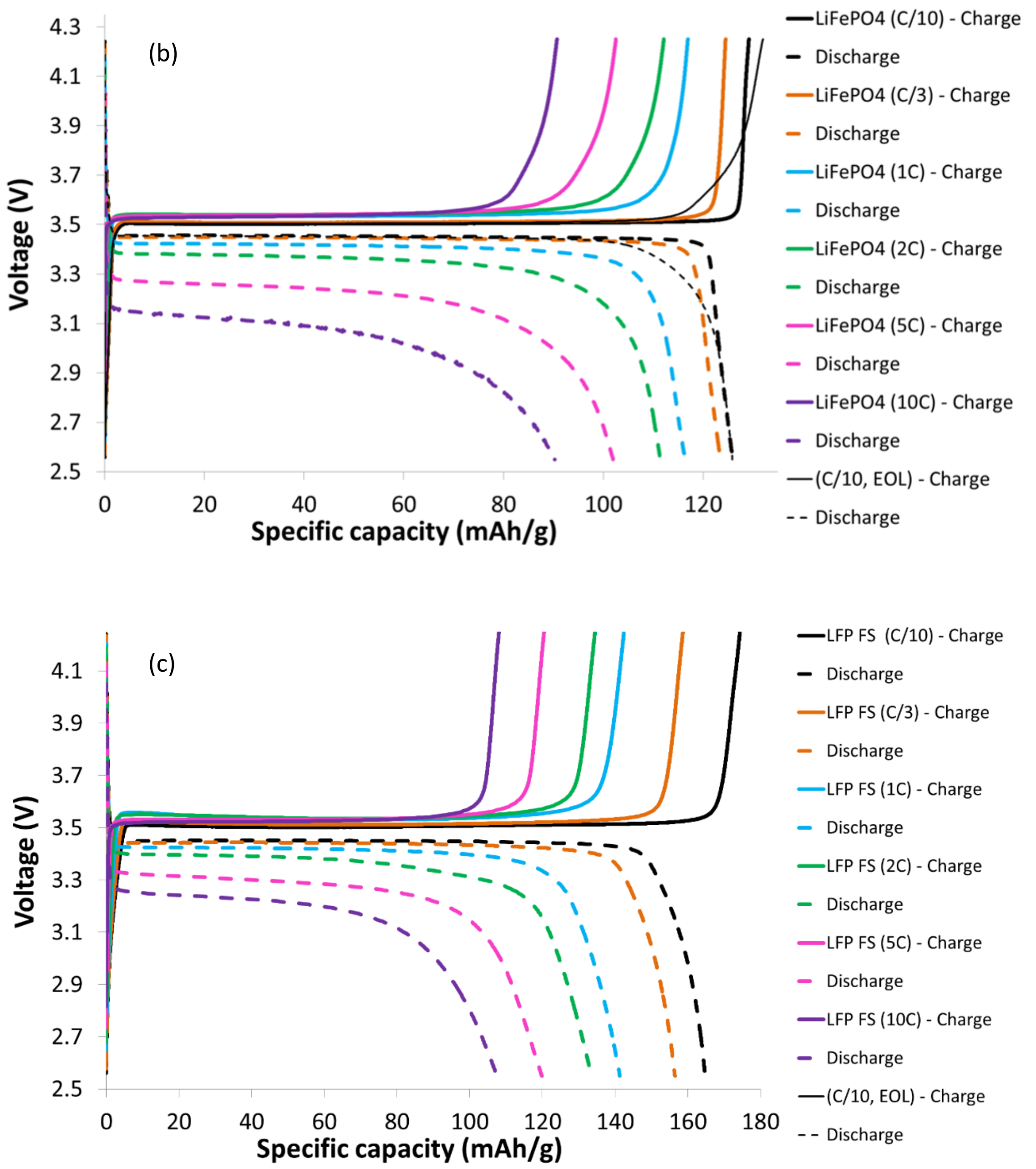

Figure 4-2 Galvanostatic charge discharge curves for (a) LFP- T (commercial), (b) LFP (BM) ball milled and (c) LFP (FS) flame spray samples. The ball milled and flame spray electrochemical studies were done at Johnson Matthey, UK.

4.4.2. XRD and Crystal Structure

XRD confirmed the LFP single phase and displayed a high degree of crystallinity as indicated by the sharp diffraction reflections. Rietveld analysis of the data using the reported crystal structures gave an excellent fit to the data as shown in **Figure 4-3** and the refined lattice parameters and atomic positions are shown in **Tables 4-1, 4-2**. Polyhedral representations of the refined structures are shown in **Figures 4-4**.The results obtained were similar to reported in previous XRD studies of LFP materials in the literature [15]. LFP belongs to the class of orthophosphates and the spacegroup Pnma (62). The structure of LFP is a close-packed hexagonal with Fe $^{2+}$ ions occupying corner shared octahedral and phosphorous ions located at the tetrahedral sites. Each FeO_6 octahedron is connected to four other FeO_6 octahedra by four vertices and four PO_4 tetrahedra, with one PO_4 sharing an edge with FeO_6. Similarly, each PO_4 tetrahedra is connected to five FeO_6 with one FeO_6 sharing an edge. In the [001] direction, clear 1D tunnels of Li-ions can be seen along with they can easily intercalate and deintercalate into the structure during discharge and charge respectively.

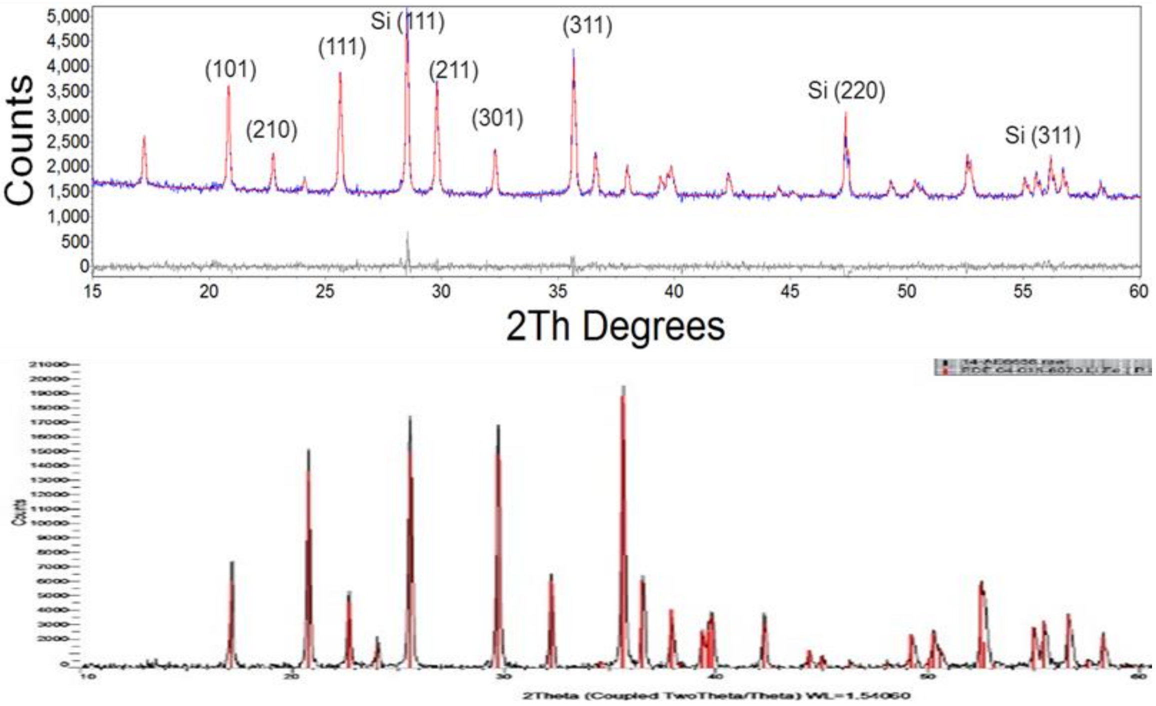

Figure 4-3 XRD pattern for powder (a) LFP-T commercial along with a Si internal reference (clearly marked) and (b) LFP (BM) ball milled.

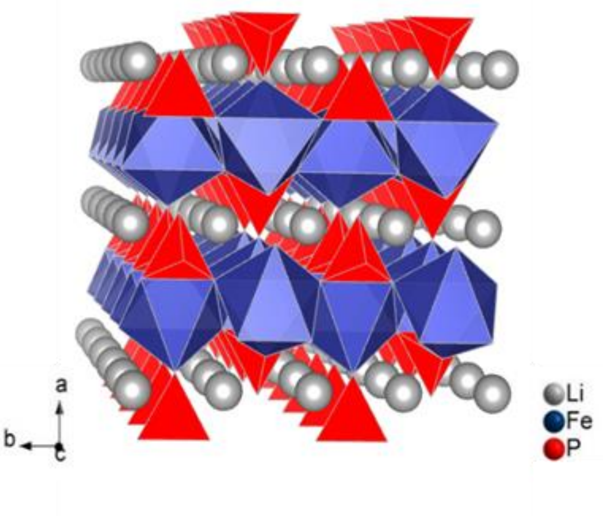

Figure 4-4 Crystal stricture of LFP obtained from XRD

Table 4-1: Rietveld Analysis of powder LFP

Quantitative Analysis - Rietveld	
Phase 1	Silicon 19.37%
Phase 2	$LiFePO_4$ 80.63%
Phase Name	Lithium Iron Phosphate
R- Bragg	0.698
Spacegroup	Pnma
Rexp (%)	2.57
Rwp (%)	2.85
Rp (%)	2.24
GOF	1.11
Cell Mass	631.036
Cell Volume (Å^3)	290.856(23)
a (Å)	10.32434(47)
b (Å)	6.00480(25)
c (Å)	4.69156(24)

Table 4-2 Rietveld analysis of powder LFP (continued)

Site	Np	x	y	z	Atom	Occ	Beq
Li1	4	0	0	0	Li+1	1	1
Fe1	4	0.28245(34)	0.25	0.9728(11)	Fe+2	1	1
P1	4	0.09637(77)	0.25	0.4175(17)	P	1	1
O1	4	0.0962(15)	0.25	0.7431(28)	O-2	1	1
O2	4	0.4536(20)	0.25	0.2193(21)	O-2	1	1
O3	8	0.16658(12)	0.0405(18)	0.2796(17)	O-2	1	1

4.4.3. Scanning Electron Microscopy

From the Field Emission SEM (FESEM) images in **Figure 4-5,** the particle sizes and the distribution can be observed for LFP-T (commercial), LFP (BM) ball milled and LFP (FS) flame spray samples. The particle size of LFP-T varies from 200 nm -1 μm; LFP (BM) sample shows particle size variation of around 120-200 nm and flame spray LFP sample shows particle sizes to be around 5-10 μm. While the size distribution is more uniform for the commercial and ball milled samples, the flame spray samples show a non-uniform and agglomerated distribution of particles.

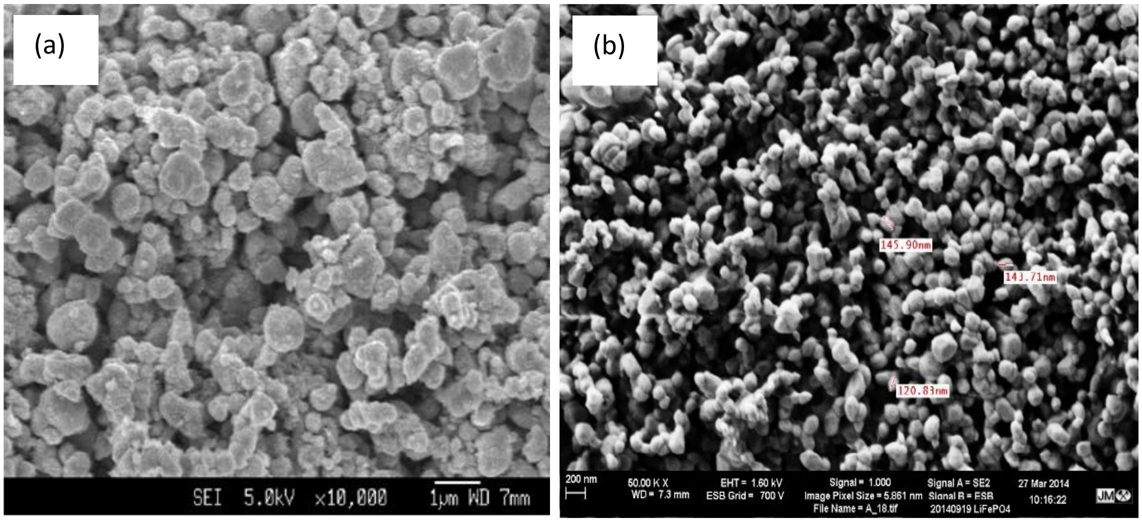

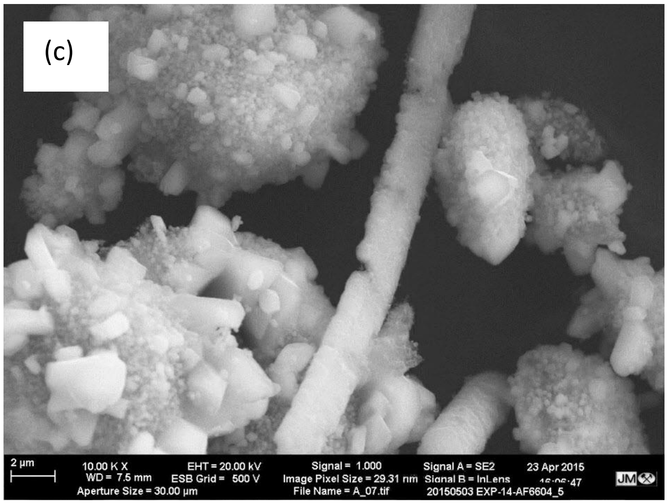

Figure 4-5 SEM images for (a) LFP –T commercial; (b) LFP (BM) ball milled and (c) LFP (FS) flame spray samples.

4.4.4. Transmission Electron Microscopy

The TEM analysis of the LFP sample was done at different magnifications as shown in **Figure 4-6**.

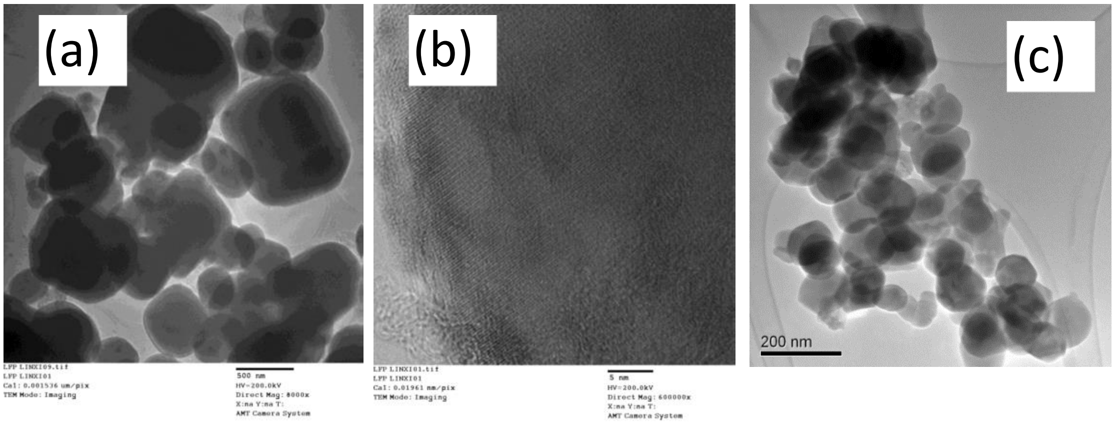

Figure 4-6 The TEM micrograph for powdered LFP-T commercial sample are shown in (a) and (b) and LFP (BM) ball milled is shown in (c). The particle size as seen from the TEM image (a) ranges from around 200nm to about 1 micrometre. The HRTEM image (b) shows a pure and crystalline phase of LFP.

The results are in accordance with what is observed in the FESEM images. The particle size, as seen from a magnification of 8000x, range from around 200nm to 1 micrometre. The High-Resolution TEM (HRTEM) taken at 600000x shows a uniform lattice structure without any deformations or grain boundaries which means the sample is pure and crystalline which is also matches the XRD results.

4.4.5. X-ray Absorption Spectroscopy

Since the main focus was to observe the structural changes of LFP *in-operando* mode, XAS data were collected while the cell was being cycled in the portable potentiostat. The cell was subjected to one electrochemical cycle at a 0.1C rate and the XAS data collection was around 15 mins for each data set. The points along the charging cycle where the data was approximately collected are marked in **Figure 4-7.**

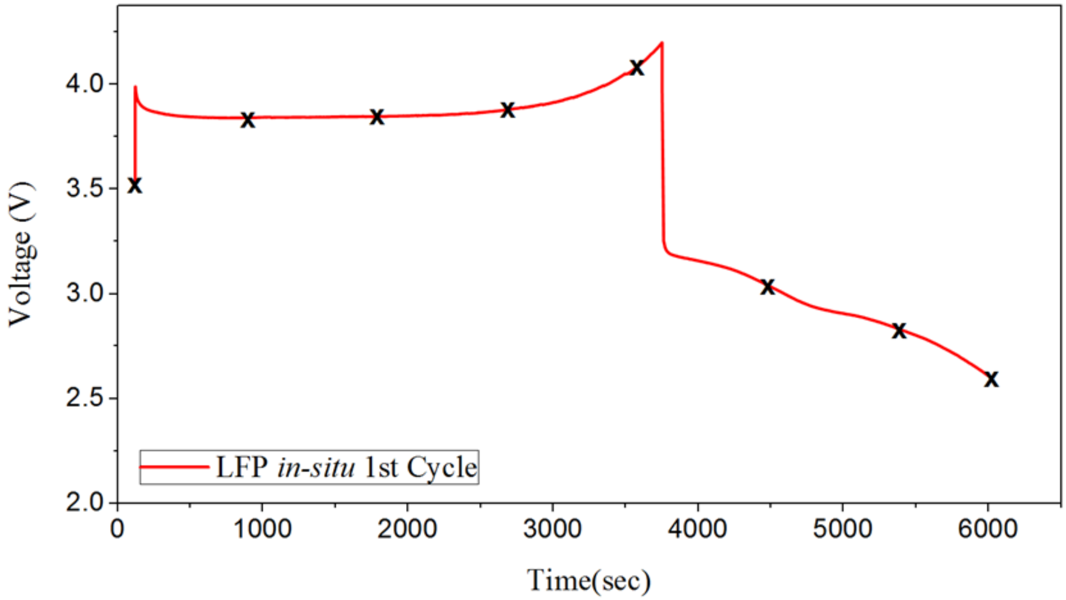

Figure 4-7: The points on the charge-discharge cycles where the XAS data were collected for LFP during the *in-situ* experiment.

4.4.5.1. *In-situ* XAS of Linxi LFP (LFP-L)– XANES and EXAFS

Figure 5-8 shows the *in-situ* Fe K-edge XANES for full one cycle of LFP-L. The solid lines represent the XANES spectra during the charging phase while the dotted lines are during the discharge period. The full cycle XANES spectra have been compared to two Fe standards – Fe(II) EDS Hydrate (Fe^{2+}) and $FePO_4.2H_2O$ (Fe^{3+}). Fe in LFP-L is present in oxidation state 2+. As the electrode is charged, Li from the cathode travels from the positive to the negative electrode (anode), in this case, the Li foil. Once the electrode is fully charged and all the Li ions have deintercalated from the cathode, Fe present in the cathode, $FePO_4$, is present in oxidation state 3+. In the XANES spectra, the main peak position of the pristine state (solid red line) coincides with the FeO standard, thus, confirming that Fe is present in the 2+ state in the pristine LFP-L. As the electrode is charged, a shift in the main peak of LFP-L towards higher energy (from solid red to solid pink) is observed. When the electrode is fully charged, the main peak of the charged state matches the peak position of that of $FePO_4 .2H_2O$. This shows that the oxidation state of Fe in the fully charged state is present at 3+. Thus, the XANES spectra during the charging process show a beautiful trend of the main absorption peak of the Fe K-edge increasing in energy from around 7121 eV to around 7124 eV, thus, showing a transition of Fe from 2+ to 3+ oxidation state during charging. Similarly, during discharge, as the Li intercalates back into cathode from the anode, the energy of absorption peak decreasing back to its original state till the cell completely discharges (from dotted pink to dotted red). Also, a tiny peak is observed just before the main edge rises, around 7112 eV. This peak is called the pre-edge and gives us information about the local geometry around the absorbing atom. The pre-edge peak in case of LFP-L shows that the coordination around the Fe atom is octahedral, i.e., Fe is surrounded by six oxygen atoms. The local geometry of six coordinating oxygen atoms around the Fe atom remains unchanged during cycling which is why no change is seen in the pre-edge peak intensity.

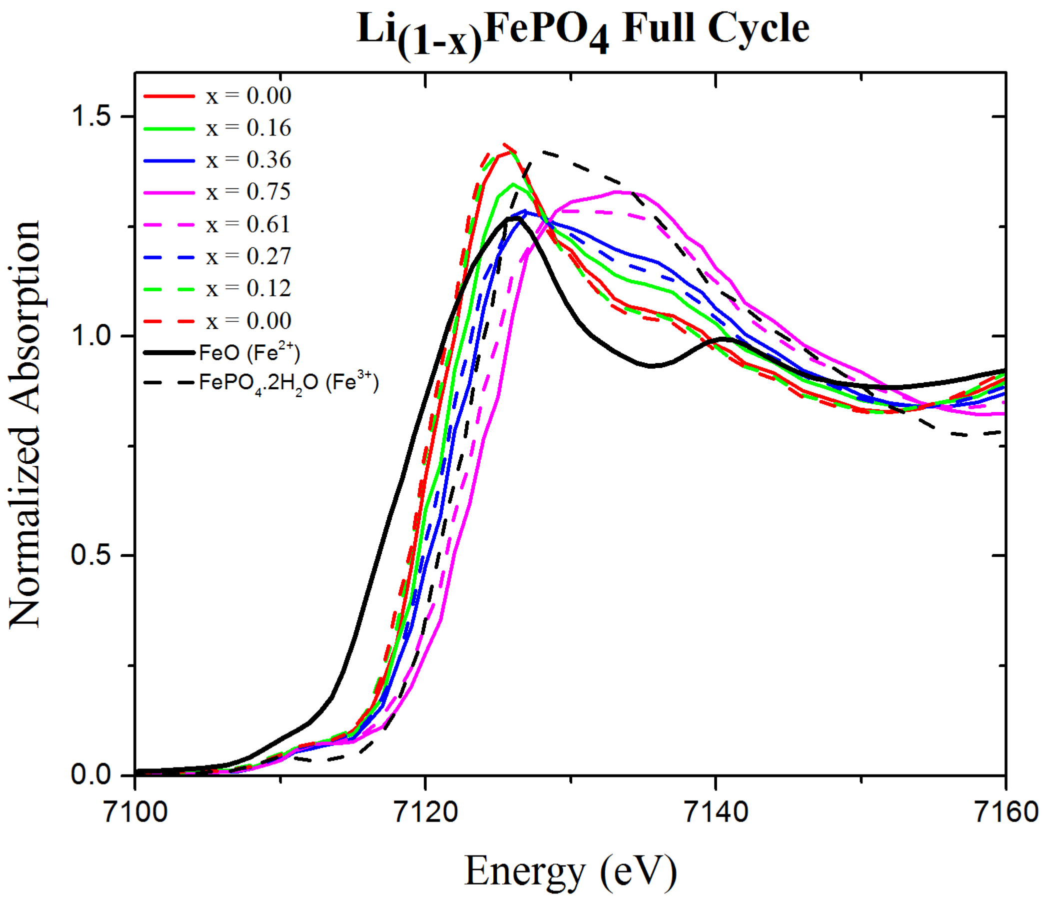

Figure 4-8: The Fe K-edge XANES spectra for the entire cycle of LFP-L *in-situ* XAS experiment. The shift towards higher energy can be observed as the cell is charged and again as the cell undergoes discharge, the energy shifts back to its original state.

Another important feature of the XANES spectra is the white line intensity. In its pristine state (solid red line), the white line intensity of the LFP-L electrode is around 1.42. However, as the electrode is completely charged, the white line intensity decreases to around 1.3 (**Figure 4-9**). This indicates a disorder around the absorbing atom, Fe, with charge. But as the electrode is discharged back to its original state, the white line intensity increases back to 1.42. Therefore, with the first cycling of LFP-L, a reversible disorder is seen around Fe. White line intensity depends mostly on the coordination environment of the absorbing atom. Compared to a tetrahedral geometry, an octahedral has more atoms in a symmetrical arrangement; therefore, the white line intensity of an atom with octahedral coordination usually will have a higher white intensity. The amount of Li shown in the figure at different points on the cycling process has been estimated from the Linear Combination Fitting (LCF) of each data set with the Fe^{2+} and Fe^{3+} standards.

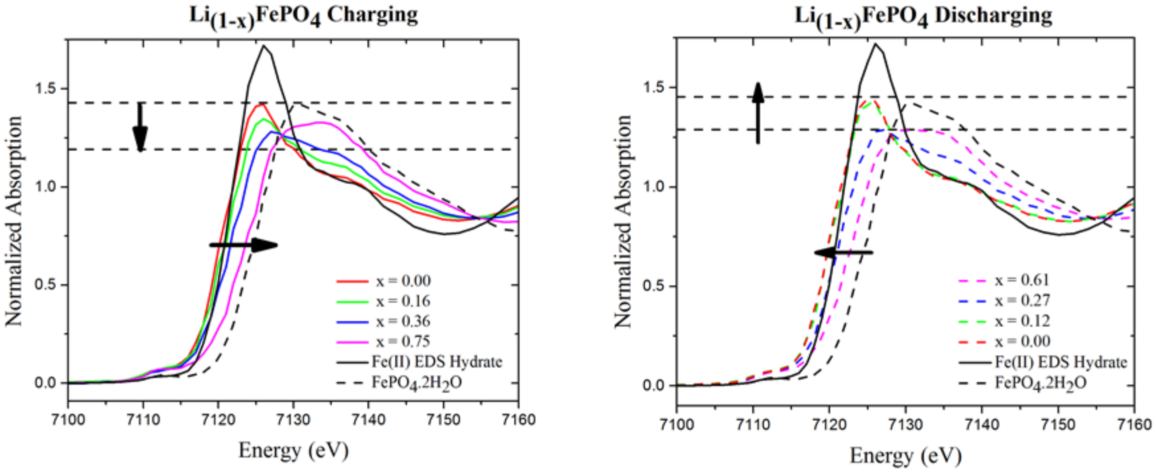

Figure 4-9: The charge (left) and the discharge (right) Fe – edge XANES spectra for the LFP-L *in-situ* XAs experiment along with the Fe^{2+} and Fe^{3+} model compounds for comparison.

Table 4-3 shows that the average bond length for the first shell, i.e., Fe coordinated to six oxygen atoms, gradually decrease with charging from 2.06 to 1.99 Å and again increases back to 2.06 Å with discharge with a high degree of error as the electrode is discharged. This might be because as the electrode is discharged, the even though the average bond seems to increase towards its original state, however, there is a distortion in the structure and all the bonds do not come back to its original positions. For all the first shell fittings, the coordination number (CN) of oxygen was fixed to 6 and there is a high probability that the coordination sphere and the number of oxygen atoms change with cycling. The Debye-Waller factor (σ^2) values determine the vibrations in the structure. In our case, since the temperature is constant, the value of σ^2 is solely from the static vibrations occurring due to the changes in bond lengths. σ^2 values for all the cycling points lie between 0.001-0.003 which suggests that there are not many vibrational fluctuations in the structure. R-factor is one of the significant parameters as it refers to the goodness of fit. R-factor values lower than 0.04~0.05 is considered to be a good fit while R-factor > might suggest that there is something wrong with the fit. EXAFS fittings for all the LFP-L *in-situ* electrodes are shown in **Figure 4-10.**

Table 4-3 EXAFS analysis of LFP-L *in-situ* Fe K-edge XAS experiment for the first and second shell (*CN: Coordination number; σ^2: EXAFS Debye-Waller factor or disorder factor; R: Bond distance obtained after Fourier Transform fitting; R-factor: goodness of fit)

$Li_{(1-x)}FePO4$	Charging State	Bond	CN*	σ^2	R	R-factor
x = 0.00	Charging	Fe-O	6	0.001 (0.005)	2.06 (0.01)	0.02
		Fe-P	4	0.007 (0.004)	3.24 (0.04)	
x = 0.16	Charging	Fe-O	6	0.003 (0.001)	2.04 (0.01)	0.04
		Fe-P	4	0.008 (0.005)	3.21 (0.05)	
x = 0.36	Charging	Fe-O	6	0.003 (0.001)	2.02 (0.01)	0.03
		Fe-P	4	0.009 (0.005)	3.21 (0.05)	
x = 0.75	Charging	Fe-O	6	0.002 (0.006)	1.99 (0.02)	0.06
		Fe-P	4	0.009 (0.006)	3.19 (0.05)	
x = 0.61	Discharging	Fe-O	6	0.002 (0.002)	2.01 (0.02)	0.03
		Fe-P	4	0.008 (0.004)	3.20 (0.04)	
x = 0.27	Discharging	Fe-O	6	0.003 (0.007)	2.03 (0.05)	0.04
		Fe-P	4	0.006 (0.004)	3.22 (0.04)	
x = 0.12	Discharging	Fe-O	6	0.003 (0.003)	2.05 (0.03)	0.02
		Fe-P	4	0.005 (0.002)	3.23 (0.05)	
x = 0.00	Discharging	Fe-O	6	0.003 (0.003)	2.06 (0.02)	0.01
		Fe-P	4	0.004 (0.002)	3.23 (0.05)	

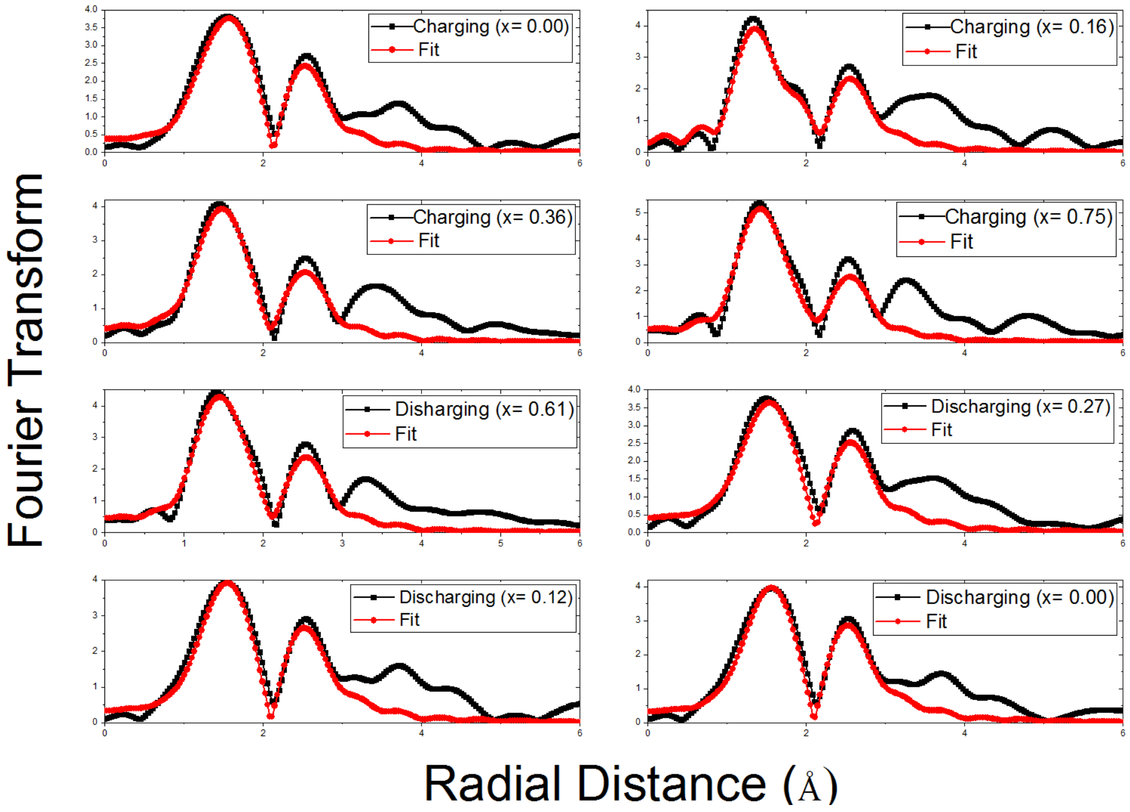

Figure 4-10: EXAFS fittings for all the LFP-L *in-situ* electrodes for first and second shell.

4.4.5.2. Issues with the *in-situ* approach

While conducting the above *in-situ* XAS experiments, some issues were encountered which hindered with the swiftness of our experimentation. Firstly, to conduct the XAS experiments, the samples had to be taken to the Singapore Synchrotron Light Source (SSLS) at National University of Singapore (NUS). This required us to carry the portable potentiostat every time across the city. The potentiostat was quite heavy and to carry such an expensive equipment around multiple times could have caused damage to the instrument. However, this was not the major issue for conducting proper *in-situ* experiments. The type of tapes that were used to experiment with in order to seal the holes of the coin cells was our major concern. The initial tape that was used to seal the *in-situ* cell was the kapton tape. The key problem with the kapton tape was the sealing of the cells. Most of our cells started leaking the electrolyte through the sides of the tape even though they were professionally sealed from a vendor. This is a great concern because the leakage of electrolyte also meant that the Li foil inside the cell was getting exposed to air and this could lead to serious implications. Another factor that made us rethink about the use of kapton was the amount of energy it absorbed during the experiment. Especially for low edge energy elements, the kapton tape absorbed most of the X-ray energies thus reducing the XAS spectra intensity by almost 10%. The second tape that was used to test our *in-situ* cells, was the 3M tape. This tape gave a solid sealing but it had too much sulphur contamination which resulted in interference in the XAS spectra, especially for edge energies close to the sulphur edge. The final tape that finally worked with the sealing as well as had no contamination of elements with edge energy in the vicinity of the edges of interest, was the polypropylene (PP) tape. But now that the tape issues was solved, there was another trouble of doing the *in-situ* measurements for low edge energies, mainly the P K-edge and S K-edge. These low edge energy XAS could not be performed at SSLS which is why proposals had to be submitted to some nearby synchrotrons where the samples could travel as fast as possible for the experiments. All the P and S K-edge XAS data collection were done at SLRI, Thailand. However, the synchrotron at Thailand did not have a laboratory with a glove box to assemble the cells and the assembled cells could not carry with lithium inside, through customs.

Another major reason to adopt an *ex-situ* approach was that *in-situ* P K-edge was not feasible to perform at such low energy and also low P concentration. Therefore, to keep a reliability of the results obtained for both Fe and P K-edges, it had to be made sure that the same samples can be used at the same conditions to collect the data. Because of these reasons, an alternative route to performing experiments which would give, if not exact, at least similar results to those of the actual *in-situ* ones, had to be adopted. This approach included making the cells in the usual *ex-situ* way, performing the necessary electrochemistry, disassembling the cells inside the glove box and treating the electrodes in beaker full of Dimethyl Carbonate (DMC). DMC is an organic, flammable liquid and is quite commonly used in laboratory based experiments. For future experiments, DMC was used to immerse the electrodes for around 10 mins to wash off all the salts from the electrolyte that could have deposited over the electrode during cycling. Once all the salts are washed off, the electrodes were rinsed again in fresh DMC, dried and sealed in Argon and stored inside the glove box till the XAS experiments are scheduled to happen. All the results in the following sections and chapters has been done with this DMC method, unless otherwise specified.

4.4.5.3. *Ex-situ* XAS Analysis of Targray LFP (LFP-T)

There is no change in the way the cells are assembled and cycled and the electrochemical performance of the cells remain almost similar to the one mentioned in the starting of the discussion. Since the DMC method is mainly done to reproduce data similar to *in-situ*, different cut-off voltages were assigned. The cells were cycled until the cut-off potentials and immediately stopped, taken inside the glove box, washed in the DMC and sealed properly. This entire process has to be done as fast as possible so that the cell does not have enough time to self-discharge, which is one of the main drawbacks of LFP as a material.. **Table 4-4** shows the potential points at which the LFP-T electrodes were stopped for further XAS experiments.

Table 4-4: The cut-off potentials for each electrode that was used to collect *ex-situ* Fe and P K-edge XAS data, is listed below.

Electrode	State of Charge	Potential (w.r.t. Li) (V)
Point A	Pristine electrode, open circuit voltage	3.1
Point B	Charging	3.7
Point C	Fully Charged	4.2
Point D	Discharging	3.1
Point E	Fully Discharged	2.5

4.4.5.3.1. LFP-T Fe K-edge XANES and EXAFS

The Fe K-edge for all the electrodes were done at SSLS, NUS at transmission mode. **Figure 4-11 (a)** shows the XANES for the all the LFP-T electrodes at the different cut off potentials. The solid lines (red, green and blue) represent the charging process with red being pristine and blue being at fully charged state and the dotted lines (red, green and blue) denote the discharge process with red showing the fully discharged state. The black solid and dotted lines represent the Fe standards, FeO and $FePO_4.2H_2O$ respectively used for comparison. **Fig 4-11 (b)** shows that the pristine sample (solid red) at the same edge position as that of FeO standard, thus confirming that Fe in pristine LFP-T is at Fe^{2+} oxidation state. As the electrode is charged, the main absorption peak position shifts towards higher energy and the fully charged electrode (solid blue) now coincides with the edge energy of $FePO_4.2H_2O$, which shows that Fe in a fully charged LFP-T electrode is at Fe^{3+} state. Also, as LFP-T is charged, the white line intensity decreases by 0.5 which means that there is a disorder around the absorbing atom with charge. This disorder can also be seen from the zoomed inset in (b) showing the pre-edge intensity of LFP-T with charge. The pre-edge peak in pristine LFP-T indicates the presence of an octahedral geometry around Fe. However, with charge, this pre-edge peak shifts towards higher energy and also in intensity. The shift towards higher energy specifies the oxidation change of Fe from 2+ to 3+ while the increase in the intensity of the peak can be attributed towards a more distorted octahedral environment around Fe.

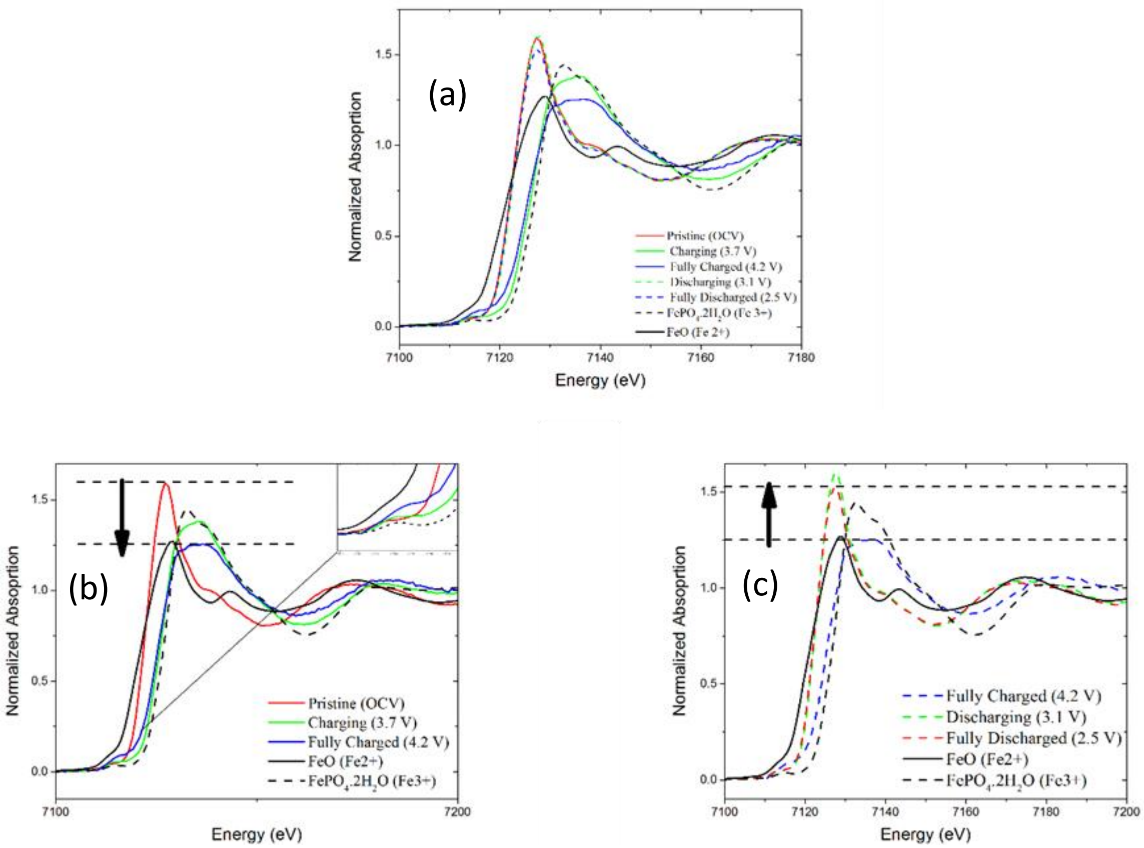

Figure 4-11: Fe K-edge *ex-situ* XANES spectra for LFP-T (a) full cycle; (b) charging period; (c) discharging period.

Figure 4-11 (c) shows the discharge process of LFP-T as it comes back to its original state. Again, as the electrodes discharge from 4.2 V to 2.5 V, the absorption peak shifts back in energy to its original pristine state conditions with its edge energy coinciding with FeO (Fe^{2+}) and its white line increased back to almost its original intensity. Even the pre-edge position and intensity almost shift back to its initial state. The word “almost” is used here because on closer inspection, it can be seen that the white line intensity does not exactly coincide with the pristine state and it is a little bit lower in intensity than it should be. The electrode which was stopped at the discharging state (at 3.1 V) gives a more accurate representation of the original pristine state (whose open circuit voltage was also around 3.1 V) with its white line intensity matching exactly with the pristine state and also its edge position at Fe^{2+} state. But as the electrode is further discharged till 2.5 V, even though the absorption edge energy stays at Fe^{2+} state, but the white line intensity slightly decreases showing that the fully discharged state is not as ordered as it original starting state. These changes are not an artefact of the background corrections since this is also reflected in the EXAFS fittings. To get more quantitative results of the effects seen in the XANES analysis, the first, second and third shell EXAFS fittings were done for all the electrodes. **Table 4-5** shows the bond lengths obtained from the EXAFS analysis, along with certain other parameters, which will be explained later. The fittings were done taking the LFP crystallographic file, which was obtained from the Rietveld analysis, as the reference. The first shell, i.e., Fe coordinated with six oxygen atoms, was found to be at an average distance of 2.18 Å. As the electrode was charged, the bond length decreased to 1.94 Å for the fully charged LFP and on discharging the bond length increased back to around 2.15 Å. These bond lengths can be compared to the standard Fe^{2+} and Fe^{3+} distances as shown in the table. The Fe-O bond length for a Fe^{2+} is around 2.13 Å while for Fe^{3+} standard, the bond length is around 1.99Å. The trend in the change in bond length with cycling is consistent with the XANES results. In addition, during XANES analysis, there was a slight abnormality in the fully discharged sample where the white line intensity did not increase back to its original position. When the same sample is analyzed in EXAFS, a similar result can be seen here as well. Even though the bond length of the fully discharged sample increases back, but it still does not return to its original bond length of 2.18 Å (the pristine sample). Also, the σ^2 value for this sample is much higher than the previous discharging sample (at 3.1 V). This shows that even though the sample is at the fully discharged state, there are some vibrations going on inside the structure that is creating some sort of minor disorder in the structure. This disorder can either be due to the electrode being held at the discharged state of 2.5 V for too long before it was taken out of the cell or it can be due to some intrinsic property of the material itself. As the electrodes are charged and the bond length decreases, the white line intensity decreases and σ^2 factor increases indicating the increasing level of disorder with charging. Vice versa, during discharge, the white line intensity increases back and the σ^2 value also decreases indicative of a more ordered system with discharge. EXAFS fittings for all the LFP-T *ex-situ* electrodes are shown in **Figure 4-12.**

Table 4-5 EXAFS fittings for all the Fe K-edge LFP-T *ex-situ* electrodes at different cut-off potentials.

SoC	**Bond**	**CN**	**σ^2**	**R (Å)**	**R-factor**	**E_0**
FeO (Fe^{2+})				2.13		7121.17
Fe_2O_3 (Fe^{3+})				1.99		7125.59
Pristine	Fe-O	6	0.005	2.18	0.06	7122.72
	Fe-P1	1	0.001	2.86		
	Fe-P2	4	0.010	3.28		
	Fe-Fe	4	0.013	3.86		
Partial Charge (3.7 V)	Fe-O	6	0.012	2.04	0.01	7125.92
	Fe-P1	1	0.002	2.78		
	Fe-P2	4	0.011	3.19		
	Fe-Fe	4	0.007	3.76		
Fully Charged (4.2 V)	Fe-O	6	0.020	1.94	0.01	7125.93
	Fe-P1	1	0.001	2.91		
	Fe-P2	4	0.005	3.16		
	Fe-Fe	4	0.009	3.73		
Partial Discharge (3.1 V)	Fe-O	6	0.006	2.06	0.03	7122.93
	Fe-P1	1	0.007	2.88		
	Fe-P2	4	0.005	3.21		
	Fe-Fe	4	0.022	3.78		
Fully Discharged (2.5 V)	Fe-O	6	0.013	2.15	0.04	7122.63
	Fe-P1	1	0.001	2.90		
	Fe-P2	4	0.005	3.24		
	Fe-Fe	4	0.017	3.81		

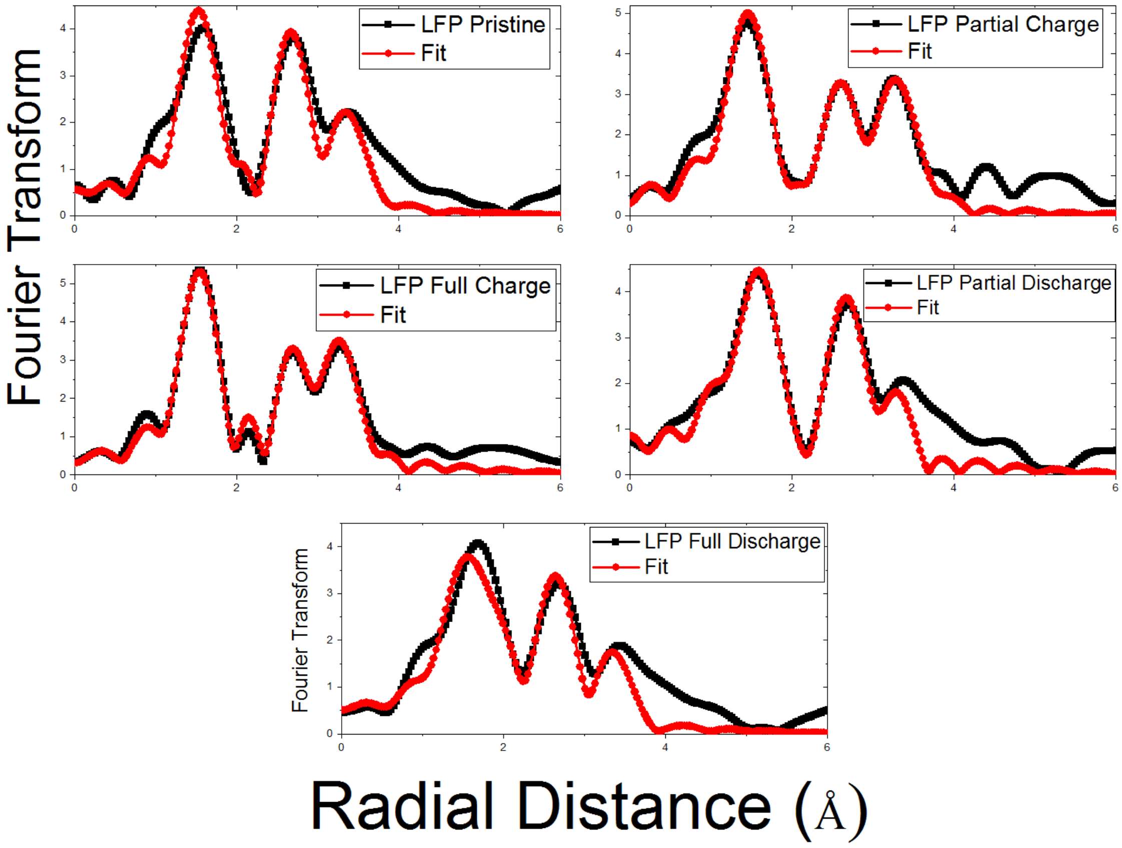

Figure 4-12: EXAFS fittings for all the LFP-T *ex-situ* electrodes for first, second and third shell.

4.4.5.3.2. LFP –T P K-edge XANES and EXAFS

Data for P K-edge was collected at the XAS beamline in SLRI, Thailand. **Figure 4-13 (a)** shows the main absorption peak of P K-edge at different charging-discharging points and **(b)** shows the equivalent first derivative peaks. The main peak around ~2155 eV corresponds to the transition of the 1s core electron of the P atom to higher vacant electronic states due to the overlap of P sp3 and O 2p orbitals [16]. As the electrodes are charged, the main absorption peak gradually moves towards higher energy, but does not move too much which could indicate a change in oxidation state. From **Figure 4-13 (b)** the shift in energy can be accounted to around 0.5 eV from pristine to fully charged state. When LFP-T is charged, Li is extracted from LFP-T and this is compensated by Fe changing from 2+ state to 3+ state. This results in more covalent Fe-O bond, which in turn produces and inductive effect on the P-O bond. Thus, the shift in the main absorption peak might be a manifestation of the change in the degree of covalency of the P-O bond with cycling.

The most interesting feature in the P K-edge XANES for LFP-T during cycling is the pre-edge feature around 2151 eV. In the pristine and fully discharged states, no pre-edge feature is observed for the LFP-T electrodes. However, in the partial charged and discharged states, an extremely distinct pre-edge feature can be seen. This pre-edge feature increases as the electrode are charged with its maximum intensity being at the fully charged state. As the electrode is discharged, the pre-edge peak intensity starts decreasing till it vanishes for the fully discharged state. This is due to the effect of second coordination environment of P, which is nothing but the effect of Fe on P. This is surprising, since Fe and P and not directly connected but rather share an oxygen atom. Thus, the pre-edge feature observed in the XANES is due to the interaction between metal 3d and P 3p states through this shared oxygen atom [16-18].

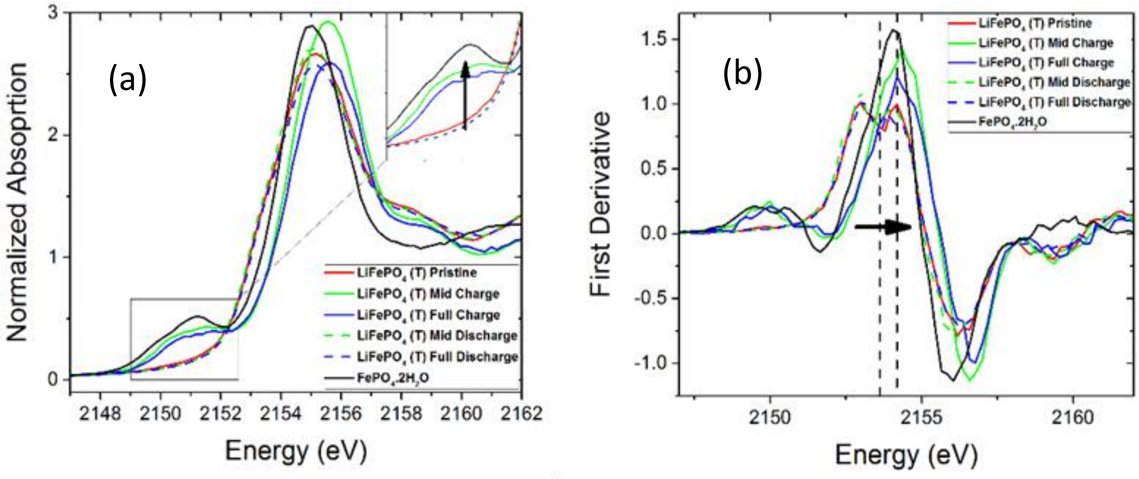

Figure 4-13: Normalized XANES spectra for LFP-T P K-edge showing the main absorption peak position in (a) and the first derivative plot in (b). The zoomed inset in (a) shows the pre-edge intensity of all the electrodes with charge-discharge.

Table 4-6: EXAFS fittings for all the P K-edge LFP-T *ex-situ* electrodes at different cut-off potentials

SoC	**Bond**	**CN**	**σ^2**	**R**	**R-factor**
$FePO_4.2H_2O$ (P^{5+})	**P-O**	**4**	**0.002 (0.001)**	**1.53 (0.02)**	**0.02**
Pristine (OCV)	P-O	4	0.001 (0.001)	1.51 (0.03)	0.07
	P-Fe	4	0.006 (0.004)	3.22 (0.07)	
Partial Charge (3.7 V)	P-O	4	0.001 (0.001)	1.49 (0.03)	0.05
	P-Fe	4	0.005 (0.002)	3.15 (0.07)	
Fully Charged (4.2 V)	P-O	4	0.001 (0.001)	1.49 (0.03)	0.09
	P-Fe	4	0.006 (0.003)	3.15 (0.07)	
Partial Discharge (3.1 V)	P-O	4	0.001 (0.001)	1.50 (0.03)	0.06
	P-Fe	4	0.006 (0.003)	3.21 (0.07)	
Fully Discharged (2.5 V)	P-O	4	0.001 (0.001)	1.51 (0.03)	0.07
	P-Fe	4	0.007 (0.003)	3.22 (0.07)	

EXAFS fittings (**Table 4-6**) were carried out to quantify the exact change in bond lengths caused due to the inductive effect of the Fe $^{2+}$ to Fe $^{3+}$ had on the first coordination shell of P. The EXAFS fittings were done for the first and second shell since it was the second coordination environment which was affecting the change in the P K-edge energy. Technically, while charging when Li is extracted from the structure, LFP-T changes into $FePO_4$. Since only Fe in the system is changing oxidation state, therefore, the local geometry around Fe should be the only thing changing. The PO_4 tetrahedra should remain constant since there is no change in the oxidation state of P. From the EXAFS fittings of the firsts and second shell of P K-edge, it can be seen that the P-O first shell bond length changes only from 1.51 Å to 1.49 Å, i.e., only 0.02 Å from the pristine state. Such a small change can only be due to the inductive effect and does not contribute to any real change in the system due to oxidation change. Also, on discharging, the P-O bond again increases back to 1.52 Å. Comparing this bond length with that of a standard, $FePO_4.2H_2O$, whose bond length is calculated to be around 1.53 Å, it can be safely concluded that the coordination geometry does not change much with cycling. For the second shell, which is the P-Fe bond, as the electrode is charged, there is a decrease in the bond length from 3.21

Å at the pristine state to 3.15 Å at fully charged state. This change is a bit more pronounced as compared to the first shell. However, Fe and P do not share a direct bond but rather are connected by a shared oxygen atom. Therefore, the change in the P-Fe bond distance can be due to the fact that during charge, since the coordination geometry around Fe is fluctuating, the Fe-O bond length variation affects the Fe-O-P bond angle which results in the expansion of the P-Fe bond distance as seen from the P-edge EXAFS. The variation in the bond angle between Fe-O-P was calculated from the EXAFS fitting results and is plotted in **Figure 4-14.** According to XRD data the bond angle between Fe-O-P in LFP is 129˚ and in $FePO_4$ is 142˚. According to my XAS fittings of the commercial LFP the bond angles between Fe-O-P in pristine sample and fully charged sample are roughly around 135˚ and 155˚. If the bond angle changes too much, it may affect the P 3p and Fe 3d orbital hybridization which would be reproduced in the absorption edge change in the P K-edge.

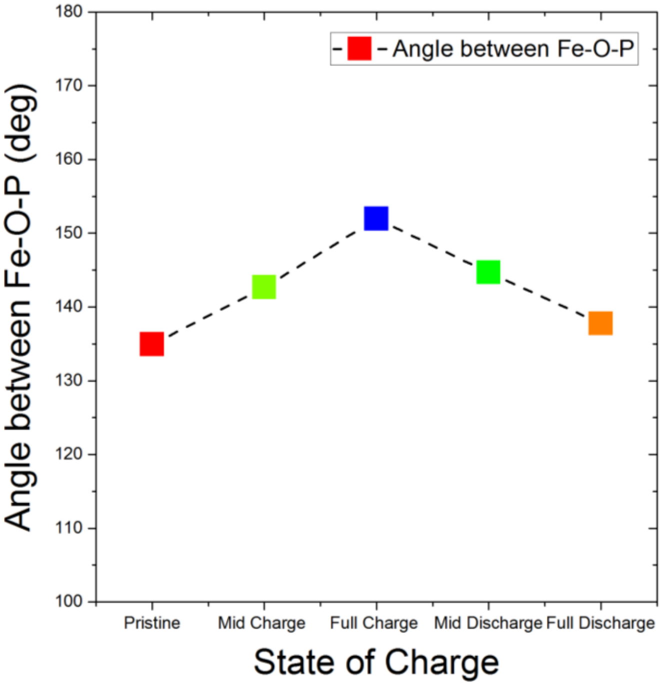

Figure 4-14: Variation in the bond angle between Fe-O-P as the LFP-T cell is charged.

4.4.5.4. XAS Analysis of LFP Ball milled and LFP Flame Spray

Once the DMC method was tested on the model LFP commercial samples, the same method was applied to treat future LFP and Mn-doped LFP samples for XAS studies as well. Since the electrochemical data showed better performance for the LFP flame spray (LFP-FS) samples compared to the ball milled (LFP-BM), this section tries to analyze the structure after 50 cycles of charge discharge of both the ball milled and flame spray LFP. **Figure 4-15** shows the Fe K-edge XANES for the LFP-BM and LFP-FS.

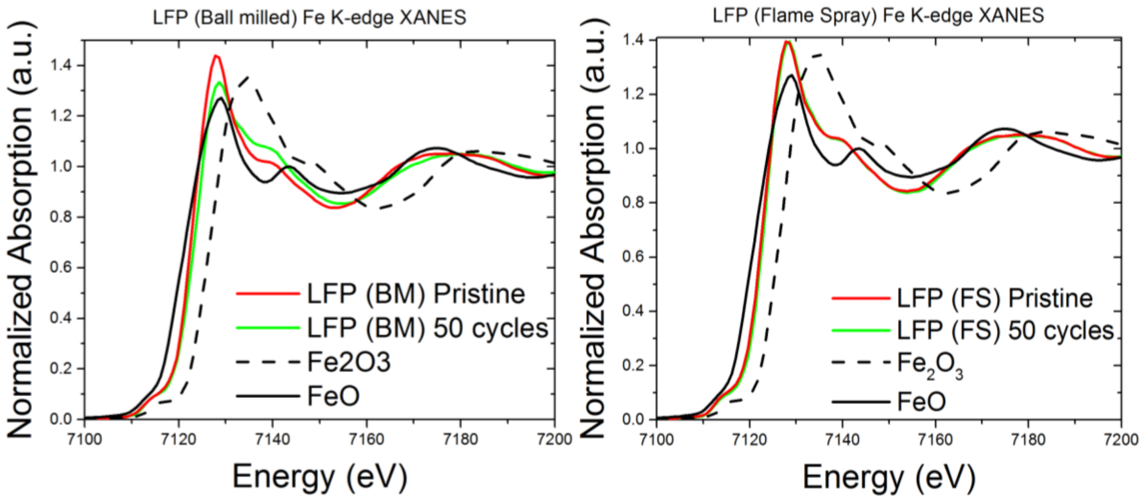

Figure 4-15: Fe K-edge XANES main absorption peak spectra for LFP (Ball Milled) and LFP (Flame Spray) for the pristine state and after 50 cycles, along with the Fe^{2+} and Fe^{3+} standards.

The LFP-FS shows a perfect overlap of the XANES spectra before and after 50 cycles indicating that the structure around the Fe atom shows a complete reversibility and remains unchanged even after 50 cycles. However, for the LFP-BM, the main absorption edge of XANES after 50 cycles shows a lower edge intensity as well as the spectra after the absorption edge shows variation compared to its pristine state, thus, suggestive of a disorder around the Fe neighbor. EXAFS analysis of both the LFP-BM and LFP-FS are shown in **Tables 4-7 and 4-8.**

Table 4-7: Fe K- edge EXAFS fittings for LFP-BM pristine and after cycling for 50 cycles.

SoC	Bond	CN	σ^2	R	R-factor	E_0
FeO (Fe^{2+})				2.13		7121.17
Fe_2O_3 (Fe^{3+})				1.99		7125.59
Pristine	Fe-O	6	0.004	2.08	0.03	7123.02
	Fe-P1	1	0.001	2.87		
	Fe-P2	4	0.008	3.22		
	Fe-Fe	4	0.016	3.81		
After 50 cycles	Fe-O	6	0.009	2.10	0.02	7124.49
	Fe-P1	1	0.001	2.86		
	Fe-P2	4	0.011	3.23		
	Fe-Fe	4	0.014	3.79		

Table 4-8: Fe K- edge EXAFS fittings for LFP (FS) pristine and after cycling for 50 cycles.

SoC	Bond	CN	σ^2	R	R-factor	E_0
FeO (Fe^{2+})				2.13		7121.17
Fe_2O_3 (Fe^{3+})				1.99		7125.59
Pristine	Fe-O	6	0.005	2.10	0.03	7123.45
	Fe-P1	1	0.002	2.87		
	Fe-P2	4	0.009	3.24		
	Fe-Fe	4	0.014	3.82		
After 50 cycles	Fe-O	6	0.006	2.10	0.03	7123.90
	Fe-P1	1	0.002	2.87		
	Fe-P2	4	0.008	3.24		
	Fe-Fe	4	0.015	3.82		

The EXAFS analysis shows that the structure of LFP-FS remains completely unchanged with the first shell Fe-O bond remaining unchanged at 2.10 Å at the pristine state and after 50 cycles. The higher shells also show complete reversibility in their bond distances as seen from **Table 4-8**. The $\boldsymbol{\sigma^2}$ factor for first shell after and before cycling remains quite consistent showing low vibrational fluctuations inside the structure. Whereas, for the LFP-BM, the first shell Fe-O bond in its pristine state shows relatively shorter average bond length of 2.08 Å and after charging and discharging for 50 cycles. The bond length of the Fe-O does not come back to its original average length but in fact shows longer distance of around 2.10 Å which means that the octahedral coordination around Fe atom distorts after cycling over 50 times. The $\boldsymbol{\sigma^2}$ factor for the LFP-BM are also higher which corresponds to vibrational fluctuations inside the structure due to the distortion.

4.5. Conclusion

LFP is an extremely versatile cathode material and used almost in every energy appliance used today. Therefore, there is no dearth of research done on this material in the past. However, this chapter focuses on an in-depth electronic and structural analysis using one of most powerful characterization techniques, X-ray Absorption Spectroscopy (XAS). Both, near-edge (XANES) and extended edge (EXAFS) were adopted to study both the Fe and P K-edges with cycling. Initially, *in-situ* XAS studies were performed for a commercial LFP sample from Linxi. The Fe K-edge XANES showed that as LFP-L is cycled, Fe valence state changes from 2+ to 3+ on charge and back to 2+ with discharge. The white line intensity changes also showed that charging induces disorder around the absorbing atom Fe. EXAFS analysis for one entire cycle showed how the Fe-O first shell bond length decreases from 2.06 Å to 1.99 Å with charging and increases back to 2.06 Å with discharge. While there was good reversibility observed in the bond length with cycling, the errors observed for these bond lengths were quite high which shows a possibility of distortion around the coordination environment of Fe. Also, the bond lengths observed for LFP-L was much shorter than the bond lengths reported literature [19-22].

However, due to issues with the *in-situ* approach, an alternative *ex-situ* method was adopted and both the Fe and P K-edge were studied for commercial Targray as well as ball milled and flame spray LFP materials. LFP (BM) also showed relatively shorter bond lengths as compared to the Targray commercial sample. In addition, XAS results showed that compared to LFP (BM), LFP (FS) gave a better reversibility in the structure after 50 cycles.

Nevertheless, this alternative method, which involved washing the electrodes with DMC before sealing and testing them, was extremely successful as the *ex-situ* Fe-edge XAS showed a similar trend in the results as the *in-situ* outcomes, with its valence state changing from Fe^{2+} to Fe^{3+} and back with charge-discharge. This alternative method also helped in utilizing these electrodes for examining the P K-edge XAS which was one of the major drawbacks of the *in-situ* process. While P K-edge XANES showed no change in absorption peak corresponding to the oxidation state of P, the hybridization of the 3p and 3d orbitals of P and Fe could be seen from the pre-edge changes.

Thus, an effective way of doing "*in-situ like*" experiments using an *ex-situ* approach was shown in this chapter and this can be extremely useful especially for materials where doing *in-situ* experiments can be a challenge. In addition, a holistic structural and electronic characterization was performed on commercial LFP materials, thus, showing that even LFP, one of the most common and abundantly used cathode, can lead to different structural results if obtained from different sources, hence, different synthesis routes. Using similar methodology, the materials in the following chapters have been analyzed as well.

References

[1]. Padhi, A.K., K.S. Nanjundaswamy, and J.B. Goodenough, Phospho-olivines as positive-electrode materials for rechargeable lithium batteries. Journal of the Electrochemical Society, **1997** 144 (4):p. 1188-1194.

[2]. Zhang, W.J., Comparison of the Rate Capacities of $LiFePO_4$ Cathode Materials. Journal of the Electrochemical Society, **2010** 157 (10):p. A1040-A1046.

[3]. Beninati, S., L. Damen, and M. Mastragostino, MW-assisted synthesis of $LiFePO_4$ for high power applications. Journal of Power Sources, **2008** 180 (2):p. 875-879.

[4]. Dominko, R., M. Bele, M. Gaberscek, M. Remskar, D. Hanzel, J.M. Goupil, S. Pejovnik, and J. Jamnik, Porous olivine composites synthesized by sol-gel technique. Journal of Power Sources, **2006** 153 (2):p. 274-280.

[5]. Dominko, R., M. Bele, J.M. Goupil, M. Gaberscek, D. Hanzel, I. Arcon, and J. Jamnik, Wired porous cathode materials: A novel concept for synthesis of $LiFePO_4$. Chemistry of Materials, **2007** 19 (12):p. 2960-2969.

[6]. Dominko, R., J.M. Goupil, M. Bele, M. Gaberscek, M. Remskar, D. Hanzel, and J. Jamnik, Impact of $LiFePO_4$/C composites porosity on their electrochemical performance. Journal of the Electrochemical Society, **2005** 152 (5):p. A858-A863.

[7]. Kim, D.H. and J. Kim, Synthesis of $LiFePO_4$ nanoparticles in polyol medium and their electrochemical properties. Electrochemical and Solid State Letters, **2006** 9 (9):p. A439-A442.

[8]. Meligrana, G., C. Gerbaldi, A. Tuel, S. Bodoardo, and N. Penazzi, Hydrothermal synthesis of high surface $LiFePO_4$ powders as cathode for Li-ion cells. Journal of Power Sources, **2006** 160 (1):p. 516-522.

[9]. Mi, C.H., X.G. Zhang, X.B. Zhao, and H.L. Li, Effect of sintering time on the physical and electrochemical properties of $LiFePO_4$/C composite cathodes. Journal of Alloys and Compounds, **2006** 424 (1-2):p. 327-333.

[10]. Murugan, A.V., T. Muraliganth, and A. Manthiram, Comparison of microwave assisted solvothermal and hydrothermal syntheses of $LiFePO_4$/C nanocomposite cathodes for lithium ion batteries. Journal of Physical Chemistry C, **2008** 112 (37):p. 14665-14671.

[11]. Sides, C.R., F. Croce, V.Y. Young, C.R. Martin, and B. Scrosati, A high-rate, nanocomposite $LiFePO_4$/carbon cathode. Electrochemical and Solid State Letters, **2005** 8 (9):p. A484-A487.

[12]. Wang, L.N., Z.G. Zhang, and K.L. Zhang, A simple, cheap soft synthesis routine for $LiFePO_4$ using iron(III) raw material. Journal of Power Sources, **2007** 167 (1):p. 200-205.

[13]. Yu, F., J.J. Zhang, Y.F. Yang, and G.Z. Song, Preparation and characterization of mesoporous $LiFePO_4$/C microsphere by spray drying assisted template method. Journal of Power Sources, **2009** 189 (1):p. 794-797.

[14]. Burns, J.C., L.J. Krause, D.B. Le, L.D. Jensen, A.J. Smith, D.J. Xiong, and J.R. Dahn, Introducing Symmetric Li-Ion Cells as a Tool to Study Cell Degradation Mechanisms. Journal of the Electrochemical Society, **2011** 158 (12):p. A1417-A1422.

[15]. Franger, S., F. Le Cras, C. Bourbon, and H. Rouault, Comparison between different $LiFePO_4$ synthesis routes and their influence on its physico-chemical properties. Journal of Power Sources, **2003** 119:p. 252-257.

[16]. Franke, R. and J. Hormes, The P K-near edge absorption spectra of phosphates. Physica B, **1995** 216 (1-2):p. 85-95.

[17]. Ingall, E.D., J.A. Brandes, J.M. Diaz, M.D. de Jonge, D. Paterson, I. McNulty, W.C. Elliott, and P. Northrup, Phosphorus K-edge XANES spectroscopy of mineral standards. Journal of Synchrotron Radiation, **2011** 18:p. 189-197.

[18]. Okude, N., M. Nagoshi, H. Noro, Y. Baba, H. Yamamoto, and T.A. Sasaki, P and S K-edge XANES of transition-metal phosphates and sulfates. Journal of Electron Spectroscopy and Related Phenomena, **1999** 101:p. 607-610.

[19]. Deb, A., U. Bergmann, E.J. Cairns, and S.P. Cramer, X-ray absorption spectroscopy study of the $LiFePO_4$ cathode during cycling using a novel electrochemical in situ reaction cell. Journal of Synchrotron Radiation, **2004** 11:p. 497-504.

[20]. Deb, A., U. Bergmann, S.P. Cramer, and E.J. Cairns, Structural investigations of $LiFePO_4$ electrodes and in situ studies by Fe X-ray absorption spectroscopy. Electrochimica Acta, **2005** 50 (25-26):p. 5200-5207.

[21]. Giorgetti, M., M. Berrettoni, S. Scaccia, and S. Passerini, Characterization of sol-gel-synthesized $LiFePO_4$ by multiple scattering XAFS. Inorganic Chemistry, **2006** 45 (6):p. 2750-2757.

[22]. Haas, O., A. Deb, E.J. Cairns, and A. Wokaun, Synchrotron X-ray absorption study of $LiFePO_4$ electrodes. Journal of the Electrochemical Society, **2005** 152 (1):p. A191-A196.

Chapter 5

High Voltage Mn-doped Cathode Materials for Li-ion Batteries

In this Chapter, olivine-type $LiMn_xFe_{(1-x)}PO_4$ *cathode materials, concentrating mainly on low Mn concentration* ($x=0.1,0.3,0.5$)*, have been studied. Along with the electrochemistry, XRD, SEM and TEM analysis, XAS characterization analysis have also been extensively observed for both the transition metals, Fe and Mn, as well as the phosphorus P K-edge for the phosphate polyanion. The results obtained from the structural investigation, have been compared for two different synthesis processes to observe the performance trend with Mn substitution.* $LiMn_xFe_{(1-x)}PO_4$ *will, henceforth in the entire Chapter, be termed as LMFP with the "x" concentration given in bracket for simplicity. For example LMFP (0.1) for* $LiMn_{0.1}Fe_{0.9}PO_4$*; LMFP (0.3) for* $LiMn_{0.3}Fe_{0.7}PO_4$*; and LMFP (0.5) for* $LiMn_{0.5}Fe_{0.5}PO_4$*.*

5. Introduction

5.1. Background

The most crucial aspect of introducing Mn in such systems was that the Mn^{3+}/Mn^{2+} redox couple in the olivine framework is positioned at 4·1 V versus Li/Li^+ which is reasonably high, compared to 3·5 V of Fe^{3+}/Fe^{2+} redox couple in $LiFePO_4$. This is extremely key when it comes to electrochemistry as it gives a much wider voltage window to operate on. So why not replace entire Fe with Mn? However, as exciting as that sounds, $LiMnPO_4$ (LMP) was not an easy material to work with. $LiMnPO_4$ is a more promising cathode material than $LiFePO_4$ due to the higher operating voltage of 0.6–0.7 V [1-6] although not on account of the theoretical specific capacity 170 mAh/g [3]. In fact, in the pioneer studies of LMP by Padhi et al., they found it impossible to extract any Li at all. After several studies with different synthetic routes applied, the reversible capacity of LMP was improved from almost nothing to around 156 mAh/g, but the authors did not address any issues regarding the cycle life [7, 8].

Therefore, rather than trying to develop LMP as an equally successful cathode, it makes more sense to utilize the advantages of LFP and instead dopes Mn^{2+} into some of the Fe sites in LFP. Studies have been performed with different Mn-doping starting with the lowest to the highest Mn concentration [9-13]. Results of LFP with very low Mn concentration ($x = 0\text{-}0.15$) doping tends to show positive aspects like better initial capacity, less cycle fading and hence better performance. Molenda et al. [14] have shown the preparation of $LiMn_xFe_{(1-x)}PO_4$ type materials using high-temperature solid-state reaction with low reversibility for Mn-range but high reversibility of lithium extraction in the Fe-range. Although $LiMn_xFe_{(1-x)}PO_4$ possess active redox components and have shown growing popularity recently, Yamada et al. in their paper [5] have also listed and summarized the crystal structure, electron transport and phase diagram to explain certain difficulties faced with Mn-rich practical Li-ion batteries. While Huang et al. [15] showed that a Fe/Mn ratio of 0.8/0.2 showed the best results with a capacity of almost 160 mAh/g, however other studies involving different Fe/Mn ratios prepared by different synthesis routes [16-18, 13] have shown otherwise, thus keeping this material still under speculation. Various other literature studies can be found on different Fe/Mn ratios, their electrochemistry and a various range of characterization techniques used to probe the structure of this material [19-22, 14, 23]. In fact, it is because of this uncertainty around this material that makes it an excellent choice to study and gain more insight.

5.2. Experimental Procedure

5.2.1. Synthesis

All the LMFP electrodes were synthesized at Johnson Matthey Technology Centre, Blount's Court, Sonning Common, Reading, UK and posted to NTU, Singapore where the electrochemical and XAS studies were conducted. Both ball milling and flame spray techniques were utilized to synthesize the LMFP electrodes. Chapter 5 showed that LFP prepared via flame spray showed better electrochemical performance and structural stability on cycling, as compared to ball milling. Therefore, the same two synthesis processes have been utilized in this Chapter as well to prepare the Mn-doped LFP samples, and tested to observe the performance and structural results.

5.2.2. Characterization

Electrochemical studies were carried out at room temperature between 2.5 V and 4.4 V at different current densities using Arbin BT 2000 in ambient temperature. XRD, SEM and TEM experiments for samples shown in this Chapter have been conducted at the Johnson Matthey Technology Centre, Blount's Court, Sonning Common, Reading, UK. The electrochemical studies and Elemental Mapping were done at NTU, Singapore. The XAS for Fe and Mn K-edges were collected at SSLS, NUS while the P K-edge data was performed at SLRI, Thailand.

5.3. Results and Discussion

5.3.1. Electrochemistry

The Mn doping increases the lattice parameters of a, b and c, and enlarges the total volume of the lattice. The expansion in lattice crystal could provide more space for lithium intercalation/de-intercalation during charging lithium will de-intercalate. Simultaneously Fe^{2+} and Mn^{2+} will change into Fe^{3+} and Mn^{3+} respectively. Since the ionic radii of Fe^{3+} and Mn^{3+} is smaller than that of Fe^{2+} and Mn^{2+}, the structure could collapse making lithium intercalation difficult during the discharging process. The peak current of Mn^{2+}/Mn^{3+} redox couple becomes higher with the increasing Mn content. The capacity fades very quickly with the increasing Mn content that is because of the poor surface electrical conductivity [24]. Yamada et al. [25] have reported, that by means of the chemical method of lithium extraction of $Li_xFe_{1-y}Mn_yPO_4$ at a voltage of ~3.5 V, the reaction proceeds as follows:

$$LiFe_{1-y}Mn_yPO_4 - (1-x)Li^+ - (1-x)e^- \leftrightarrow Li_xFe_{1-y}Mn_yPO_4 \qquad \text{(i)}$$

Reaction at this voltage is related to the oxidation of iron $Fe^{2+} \rightarrow Fe^{3+}$. Around 4.2V, when manganese oxidation takes place, $Mn^{2+} \rightarrow Mn^{3+}$, the mechanism of reaction changes and a two-phase product is obtained according to the following equation:

$$Li_yFe_{1-y}Mn_yPO_4 - (y-x)Li^+ - (y-x)e^- \leftrightarrow xLi_xFe_{1-y}Mn_yPO_4 + (y-x)Fe_{1-y}Mn_yPO_4 \qquad \text{(ii)}$$

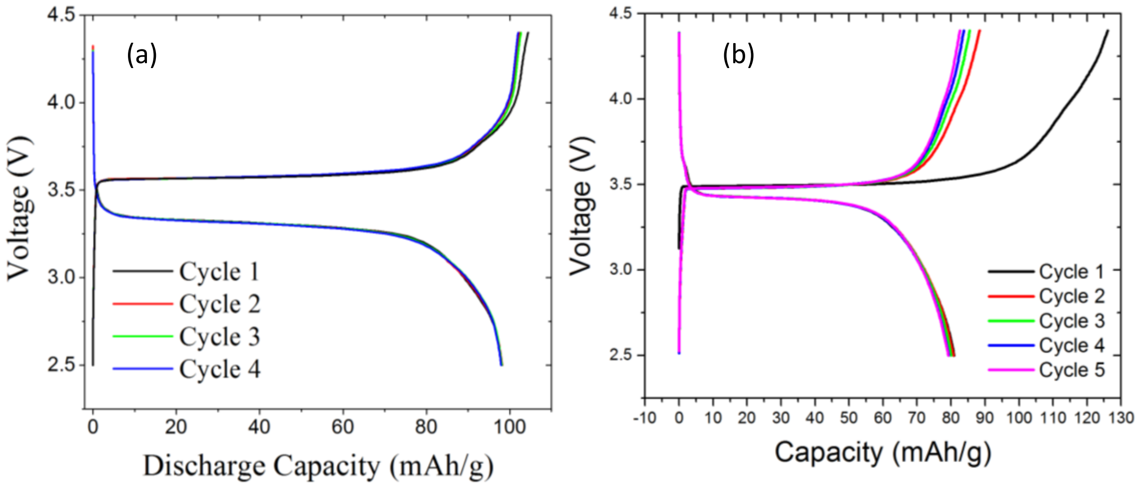

Figure 5-1 The galvanostatic charge discharge graph (a) shows the plots for LMFP (0.1) prepared via ball milling while graph (b) shows the electrochemical data of LMFP (0.1) prepared via flame spray. All charge discharge was carried out at 0.1 C rate.

Figure 5-1 shows the electrochemistry for LMFP (0.1) prepared via both ball milling and flame spray. The main redox plateau for Fe^{2+}/Fe^{3+} can be seen around 3.6/3.3V. Since the Mn concentration is extremely low (Fe:Mn=9:1), there is no prominent redox plateau for Mn^{2+}/Mn^{3+}. But during the charging cycle, a very slight formation of a plateau can be seen to arise around 3.9V but it almost immediately disappears. During the discharge curve, the reduction plateau for $Mn^{3+}/Mn^{2+}$is completely disappeared. Since the electrode was freshly prepared, the first cycle is ignored since the cell takes time to stabilize to its OCV. The discharge capacity for LMFP (0.1) ball milled fluctuates within the small range of 97.3-98.8 mAh/g while for LMFP (0.1) flame spray samples, discharge capacity is around ~ 80 mAh/g for the 10 cycles. Therefore, the electrochemical performance is found to be slightly better for the ball-milled material as compared to flame spray.

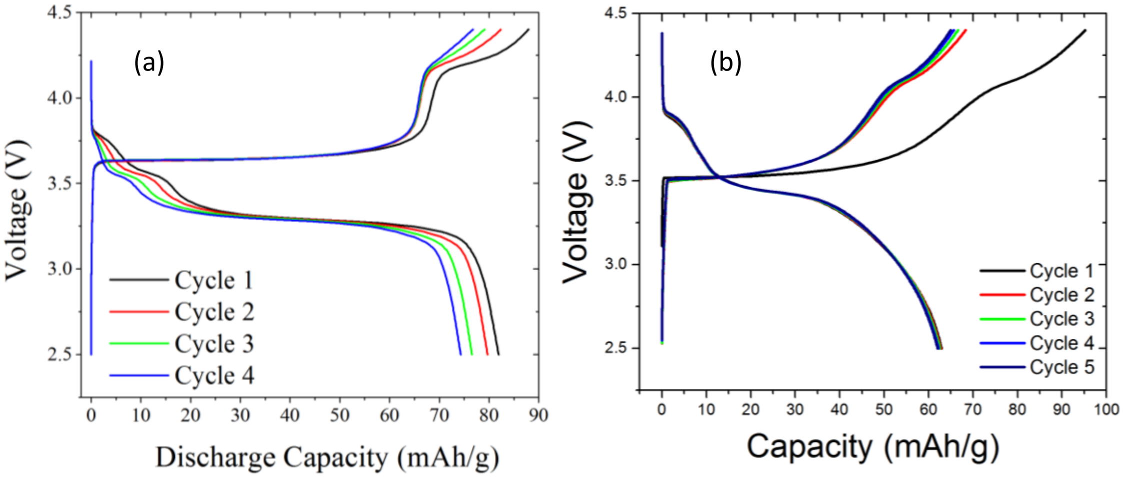

Figure 5-2: The galvanostatic charge discharge graph (a) shows the plots for LMFP (0.3) prepared via ball milling while graph (b) shows the electrochemical data of LMFP (0.3) prepared via flame spray. All charge discharge was carried out at 0.1 C rate.

Figure 5-2 shows the charge-discharge curve for LMFP (0.3) ball milled and flame spray. As compared to LMFP (0.1), the plateau for $Fe^{2+}/^{3+}$ is shorter and a more conspicuous $Mn^{2+}/^{3+}$ plateau can be observed. The redox plateau for Fe^{2+}/Fe^{3+} occurs around 3.6/3.25 V and the plateau for Mn^{2+}/Mn^{3+} is observed to be around 4.2/3.8V. Since the Mn concentration is higher in this material, the voltage for the Mn oxidation from Mn^{2+} to Mn^{3+} during charge has increased compared to LMFP (0.1). The discharge capacity of LMFP (0.3) is lesser than LMFP (0.1) and lies in the range of 70-80 mAh/g for the ball milled samples and around ~ 65 mAh/g for the flame spray samples. Once again, the ball milled samples of LMFP (0.3) shows better capacity compared to flame spray, however, the capacity retention of flame spray samples were much better over 10 cycles than the ball milled ones.

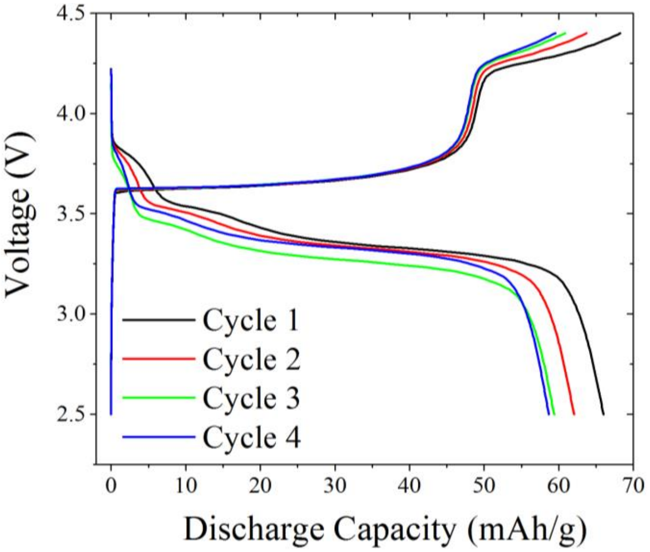

Figure 5-3: The galvanostatic charge-discharge graph shows the plots for LMFP (0.5) prepared via ball milling at 0.1 C rate.

Figure 5-3 shows the electrochemical behaviour of LMFP (0.5). As expected, compared to LMFP (0.1) and LMFP (0.3), the redox plateau for Mn^{2+}/Mn^{3+} is a lot more prominent and longer. Also, the voltages as which Mn^{2+} to Mn^{3+} and vice versa reactions take place during cycling are higher compared to its lower Mn concentration counterparts and falls roughly around 4.25/3.8 V respectively. However, its discharge capacity is much lower than LMFP (0.3) and LMFP (0.1) and falls around 55-60 mAh/ for the first 10 cycles.

Thus, electrochemical studies of the above samples with different concentrations of Mn reveal that as the Mn quantity increases, the plateau and the redox voltage of Mn^{2+}/Mn^{3+} increases with an increase in Mn. The efficiency output of all three samples were around 96-98%, however, the discharge capacity of the sample decreased with increased Mn concentration. This implies that Mn-doping is effective to maintain a stable host structure during insertion and extraction of lithium ion. However, the excessive Mn-doping results in bigger particle size. It will decrease the surface area and increase the diffusion path for lithium ion, which leads to the discharge capacity becoming lower. Thus, it can be said that a low reversibility of the lithium extraction process is seen in the high-voltage “manganese” range, while in the “iron” range the reversibility of lithium extraction is higher.

5.3.2. Crystal Structure and XRD

Figure 5-4 shows the XRD pattern for LFP, $LiMn_xFe_{(1-x)}PO_4$ (x=0.1,0.3) and LMP materials synthesized using ball milling approach. The ball milling way of synthesizing battery materials have been explained in Chapter 3. All samples exhibit a single phase of $LiFePO_4$ with an ordered single phase olivine structure indexed to the orthorhombic Pmna space group. These patterns are in agreement with diffraction pattern ICDD 01-080-6319. This reveals that the pure samples were successfully synthesized by balling milling. The Mn doping does not destruct the lattice structure of $LiFePO_4$ because of the low doping concentration. On the other hand, the distortion of the lattice is negligible because of the almost similar ion radius of Mn^{2+} (Goldschmidt radius: 0.083 nm) and Fe^{2+} (0.078 nm) [26, 27]. The substitution of Mn^{2+} for Fe^{2+} in the 4c positions causes a lattice expansion due to the higher ionic radius of Mn. Except for the different peak intensity, there are no obvious impurity peaks or changes in the XRD patterns for the LFP, LMP and the Mn-doped LFPs. However, it should be noted that with the increasing Mn content there is a slight shift of the peaks to smaller 2θ angles due to the increase in lattice parameters, but without any alteration to the similarity of the structures. The lattice parameters and the cell volume increase with the increasing Mn content which followed the Vegard's law, as shown in **Table 5-1** and **Figure 5-5**. It indicates that the series of samples of LMFP are continuous solid–solution between $LiFePO_4$ and $LiMnPO_4$. Triwibowo et al. [28], Yamada et al [5] and Yoncheva et al. [12] among many others, have shown how the Mn concentration leads to change in lattice parameters, unit cell volume and cell distortions in their extensive *in-situ* and *ex-situ* XRD studies.

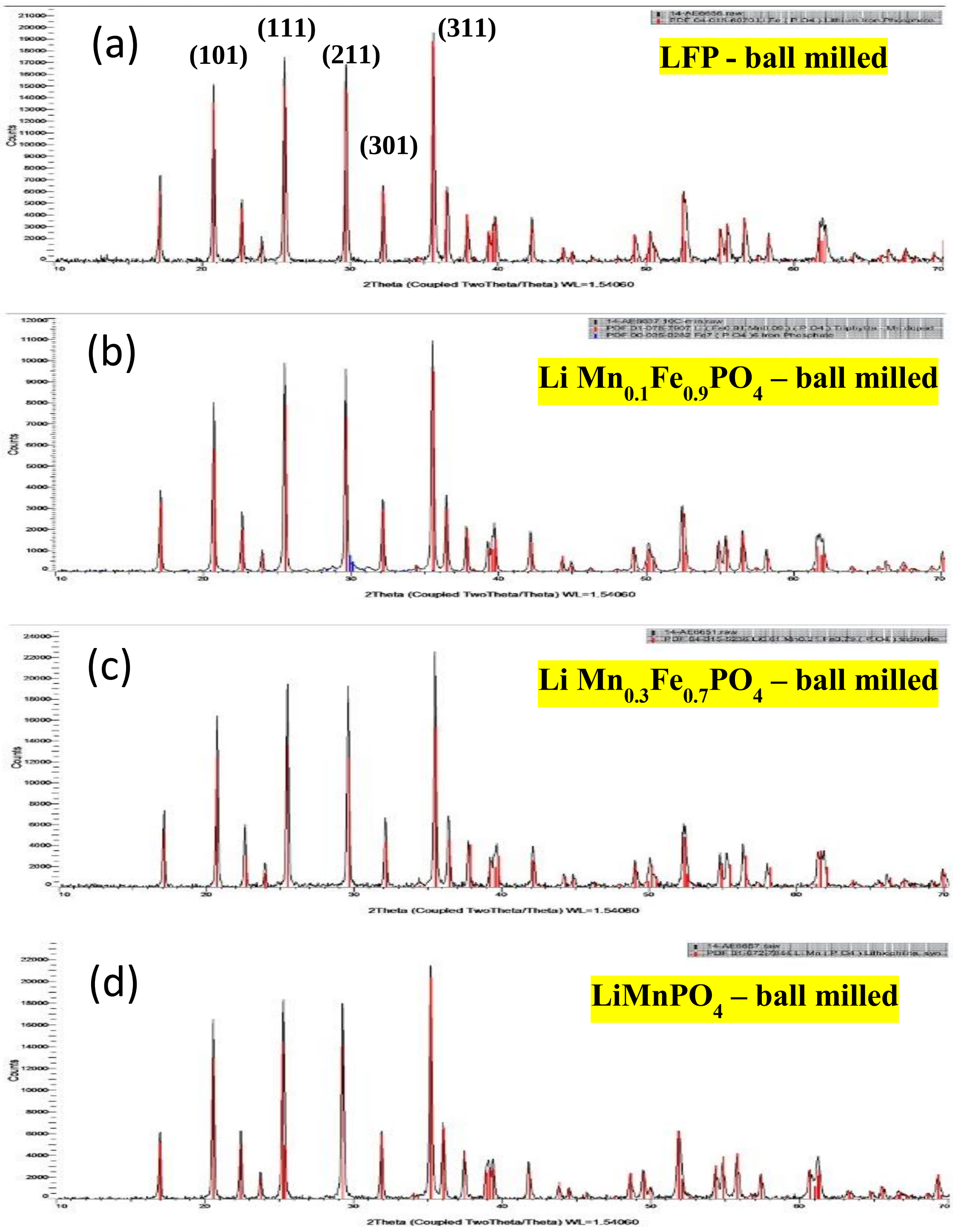

Figure 5-4: XRD patterns for (a) LFP, (b) LMFP (0.1), (c) LMFP (0.3) and (d) LMP; with some of the main peaks referenced.

Table 5-1: Rietveld refinement parameters of ball milled and flame spray LMFP samples

Sample	**$LiMn_{0.1}Fe_{0.9}PO_4$**		**$LiMn_{0.3}Fe_{0.7}PO_4$**		**$LiMn_{0.5}Fe_{0.5}PO_4$**	
	Ball milled	**Flame Spray**	**Ball milled**	**Flame Spray**	**Ball milled**	**Flame Spray**
a (Å)	10.3441(47)	10.3465(25)	10.3660(37)	10.3711(21)	10.4109(12)	10.4040(22)
b (Å)	6.0191(26)	6.0195(14)	6.0361(20)	6.0389(11)	6.0671(66)	6.0640(12)
c (Å)	4.7006(22)	4.6984(11)	4.7089(17)	4.7093(99)	4.7283(57)	4.7272(10)
α = β = γ (°)	90	90	90	90	90	90
Cell Volume (Å^3)	292.670(23)	292.618(12)	294.639(18)	294.946(10)	298.656(59)	298.238(11)
Rwp	0.898	0.949	0.856	0.845	1.089	0.810

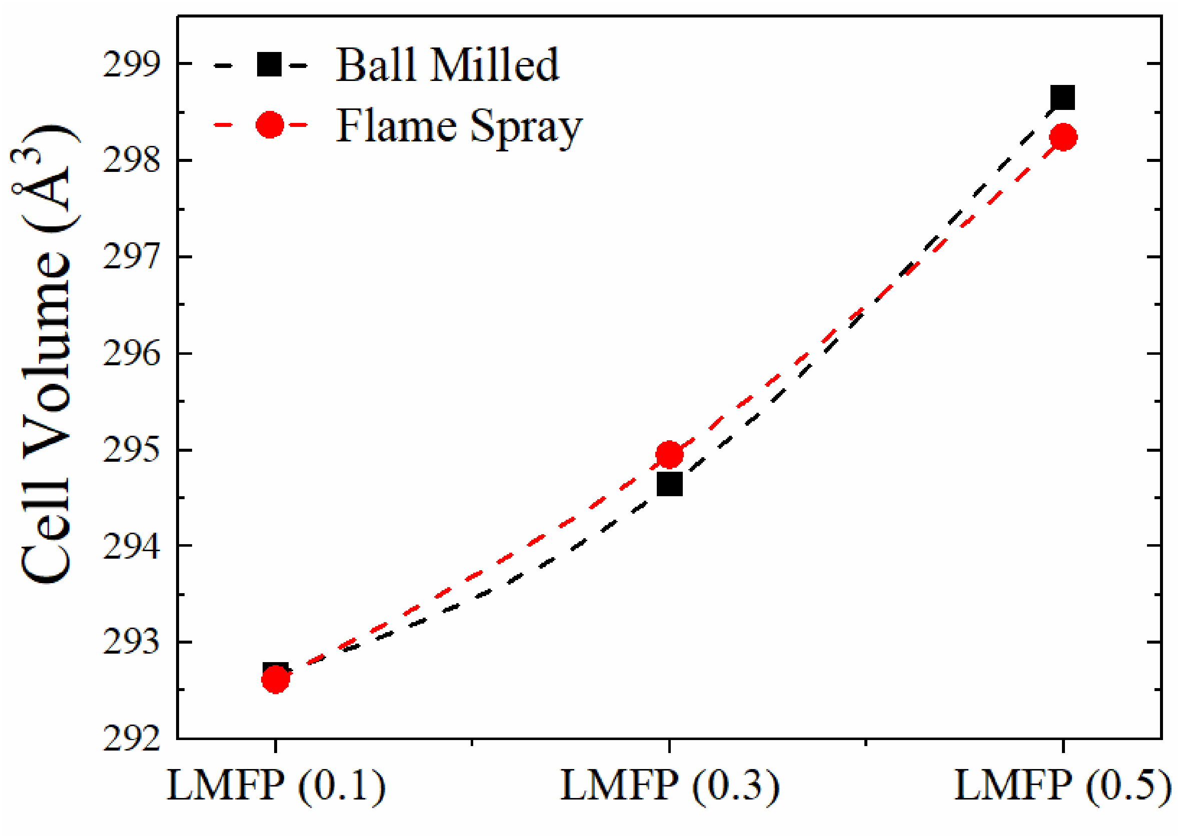

Figure 5-5: Cell volume increase for different Mn concentration for different prepared LMFP samples.

5.3.3. SEM:

Figures 5-5 and 5-7 show the SEM surface morphologies of ball milled and flame spray LFP, $LiMn_xFe_{(1-x)}PO_4$ (x=0.1,0.3, 0.5) and LMP respectively. The $LiFePO_4$/C shows finer powder and more globular while the Mn-doped $LiFePO_4$/C samples consist of irregular particles and widely size distribution. The ball milled LMFP (0.1), LMFP (0.3) and LMFP (0.5) shows size distributions ranging from: LFP – 50-300 nm; LMFP (0.1) – 50-500 nm; LMFP (0.3) – 100-900nm; LMFP (0.5) – 200nm-1 micrometer. The flame spray samples on the other hand show much larger particle size ranging from 10-20 micrometer. These particles keep getting more agglomerated with increasing of Mn-doping. This leads to bigger particles and lesser surface area that might affect the ionic conductivity of the material.

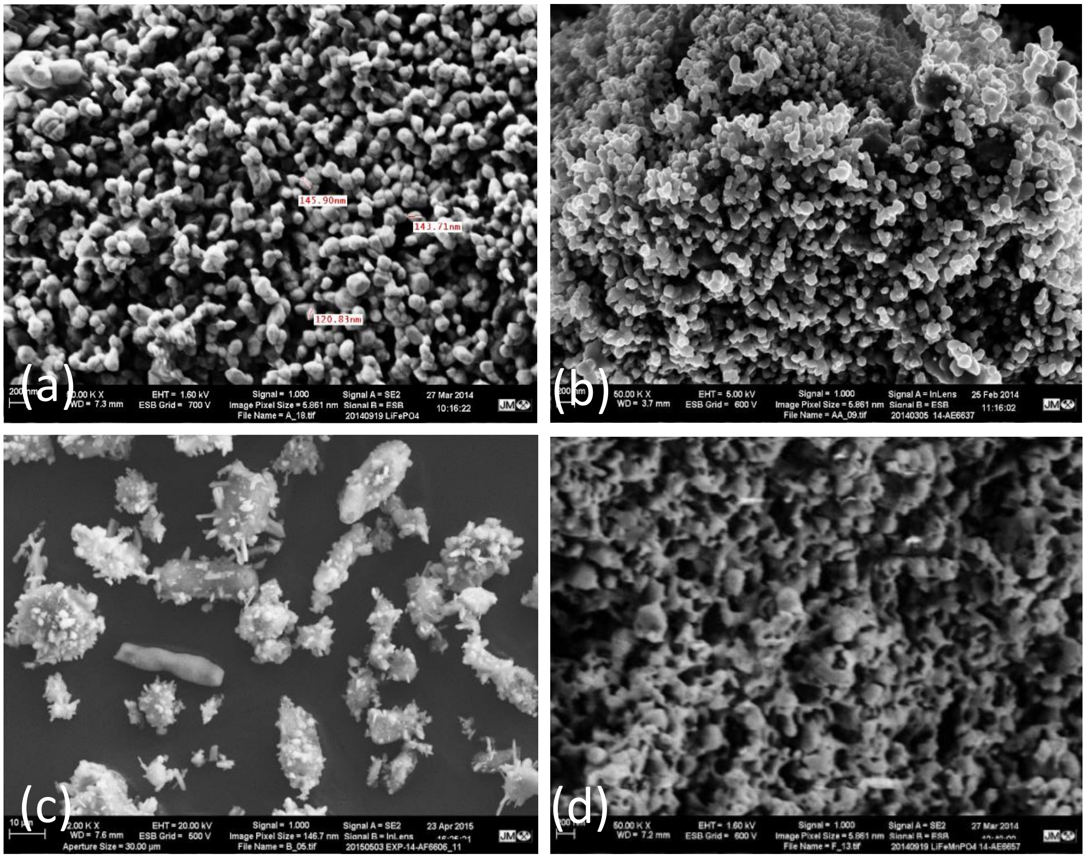

Figure 5-6: SEM images for ball milled (a) LFP, (b) LMFP (0.1) and (c) LMFP (0.3) and (d) LMP samples.

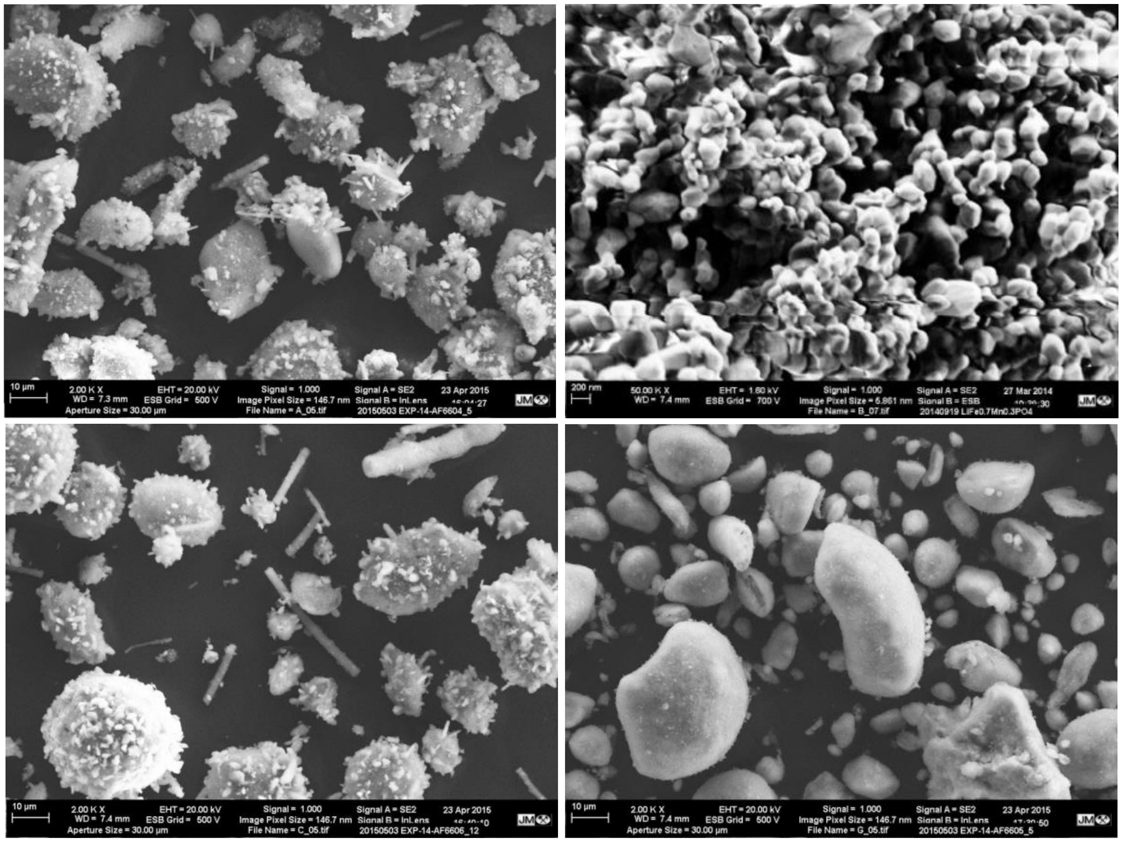

Figure 5-7: SEM images for flame sprayed (a) LFP, (b) LMFP (0.1) and (c) LMFP (0.3) and (d) LMP samples.

5.3.4. TEM and Elemental Mapping:

TEM analysis of ball milled LMFP samples also shows that the particle size distribution increases with increased Mn concentration, consistent with SEM results. High resolution (HR) TEM images of a small area of each sample show the fine structure of an ordered stack of LMFP arrays (0.1,0.3,0.5). According to the HRTEM results, the crystallinity is more for low Mn concentration. As the Mn ratio increases, amorphousity can be observed on the edges of the particle and the regular ordered array becomes less visible. While collecting the elemental mapping images, some HR TEM images were collected for the LMFP electrodes before and after cycling, as shown in **Figures 5-8, 5-9, 5-10, 5-11.**

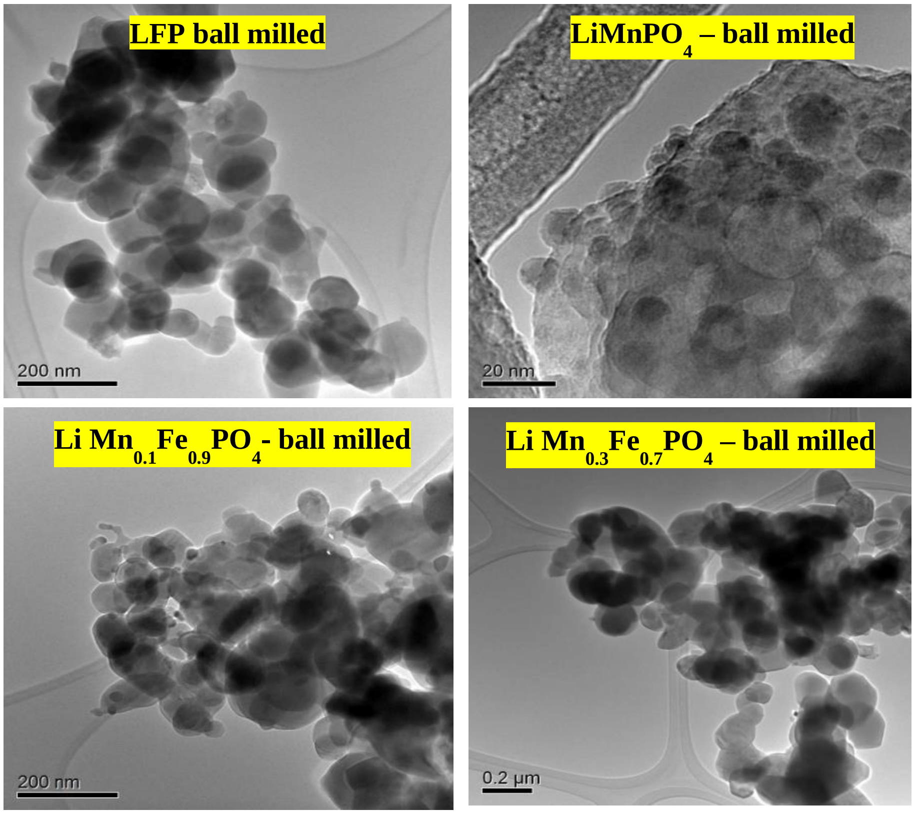

Figure 5-8: TEM images of ball milled LFP, LMP, LMFP (0.1) and LMFP (0.3)

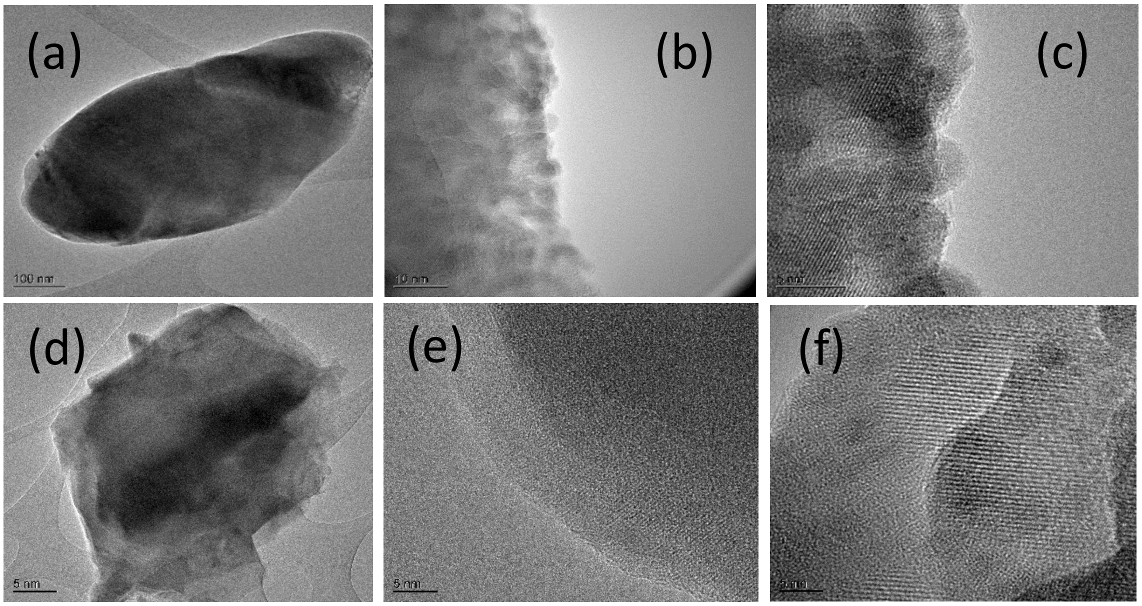

Figure 5-9: HR TEM images of ball milled LMFP (0.1) in its as-prepared pristine state (a), (b), (c); and after 10 electrochemical cycles (d), (e), (f).

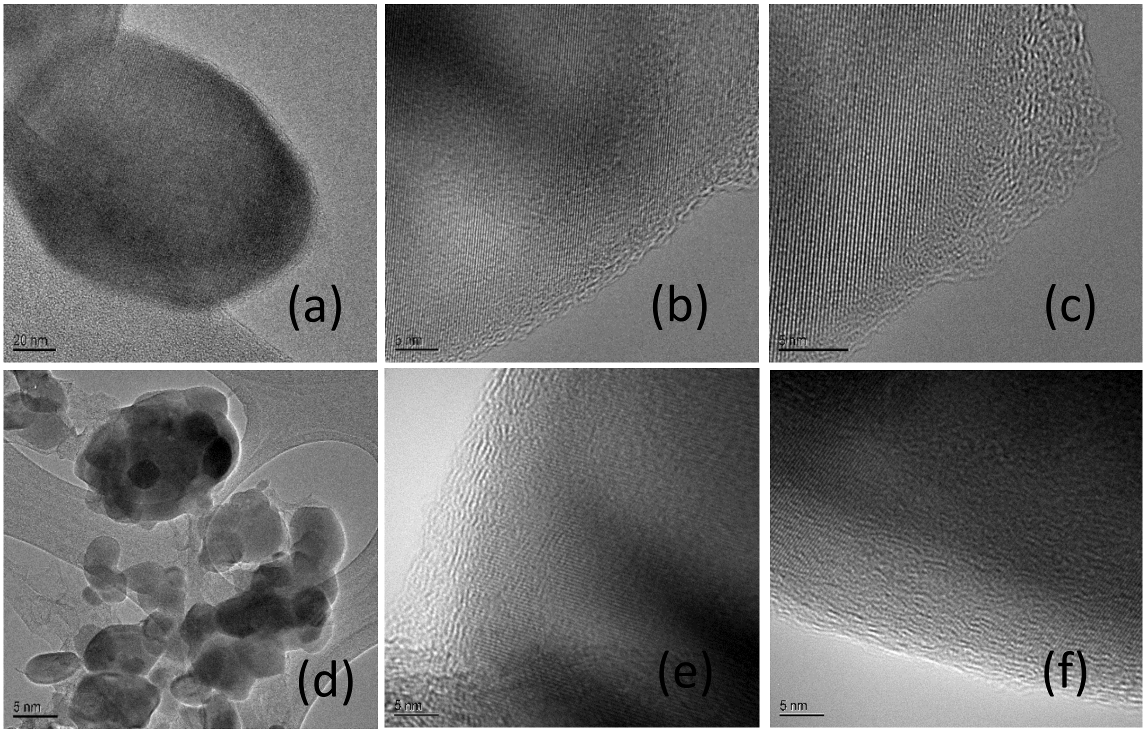

Figure 5-10: HR TEM images of ball milled LMFP (0.3) in its as-prepared pristine state (a), (b), (c); and after 10 electrochemical cycles (d), (e), (f).

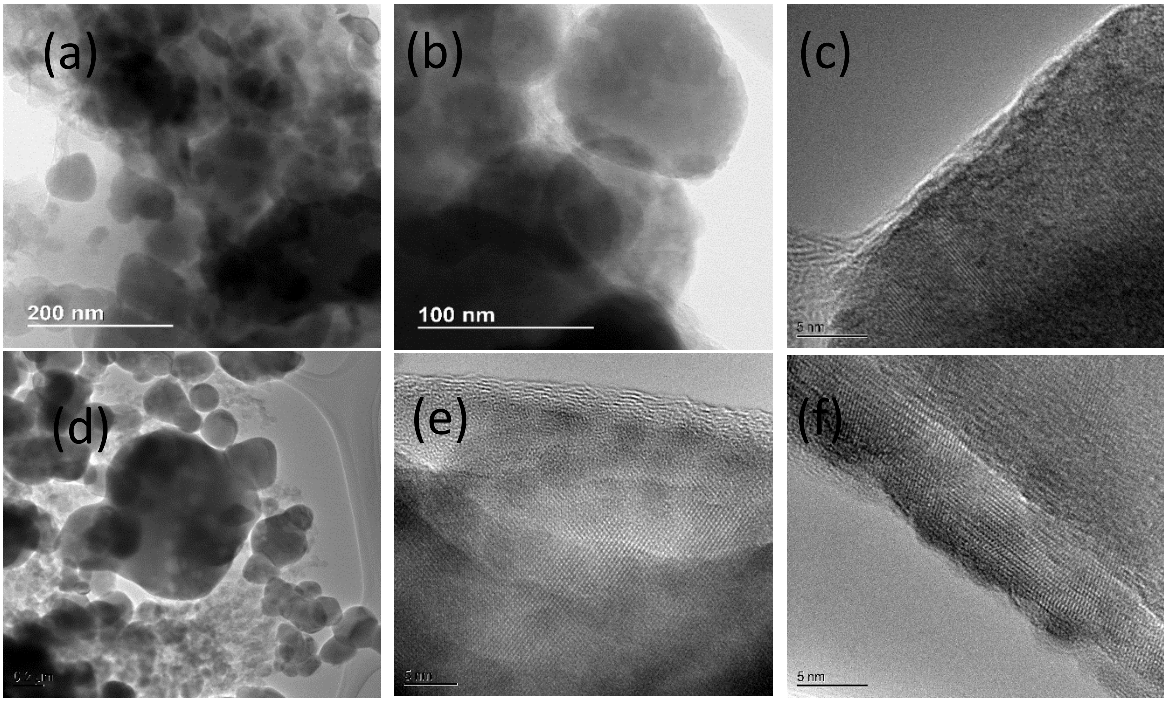

Figure 5-11: HR TEM images of ball milled LMFP (0.5) in its as-prepared pristine state (a), (b), (c); and after 10 electrochemical cycles (d), (e), (f).

Elemental mapping was done to confirm the Mn: Fe ratio in the synthesized samples as well as to see the distribution of the transition metals in material as seen in **Figures 5-12, 5-13, 5-14.** For ball milled LMFP (0.1), LMFP (0.3) and LMFP(0.5) the ratio of Mn: Fe was found to be 1.2:9.9, 3.1:7.5, 4.9:5.2. This was found out scanning the particle under scrutiny in the STEM mode for around 42 frames for each sample. Since such close approximation was calculated on the basis of one particle, it can be averaged out for the whole material to be very close to as expected from the synthesis process. Also, the distribution of the Mn and Fe seem to be quite homogenous without any preferential site occupancy of Mn and Fe in the whole material. Mapping of the same samples was repeated after subjecting the electrodes to 10 cycles of charge-discharge. The ratio of Fe/Mn is listed in **Table 5-2.**

Table 5-2: Table of the ratio of Fe: Mn in pristine and fully discharged samples in LMFP (0.1), (0.3), (0.5) prepared via ball milling.

Material	Pristine (At %)		Fully Discharged (At %)	
	Fe	Mn	Fe	Mn
LMFP (0.1)	89.2	10.8	89.4	10.6
LMFP (0.3)	71.4	28.6	69.2	30.8
LMFP (0.5)	48.5	51.5	54.8	45.2

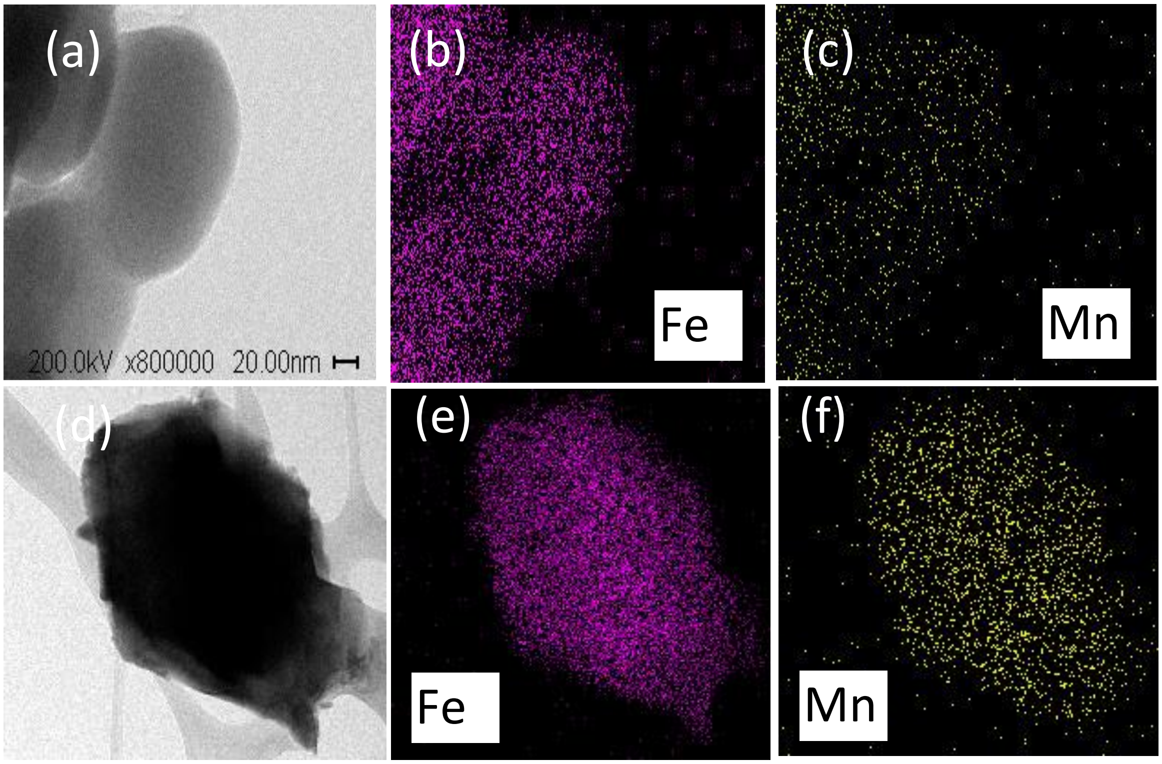

Figure 5-12: Elemental mapping of ball milled LMFP (0.1) in its as-prepared pristine state (a), (b), (c); and after 10 electrochemical cycles (d), (e), (f).

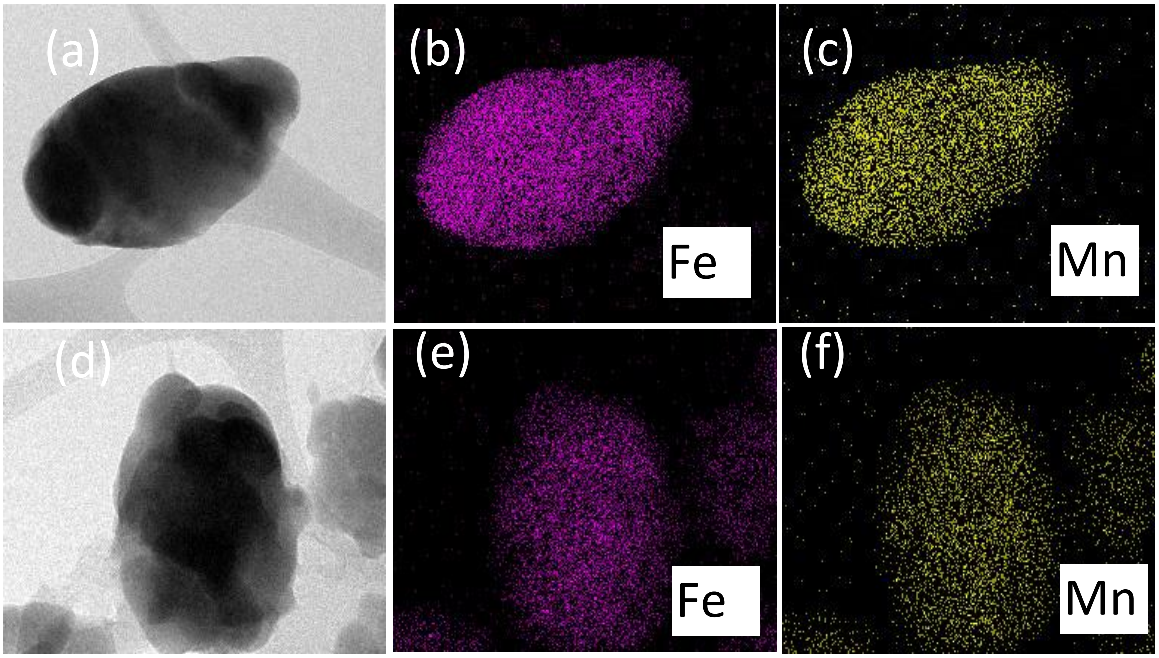

Figure 5-13: Elemental mapping of ball milled LMFP (0.3) in its as-prepared pristine state (a), (b), (c); and after 10 electrochemical cycles (d), (e), (f).

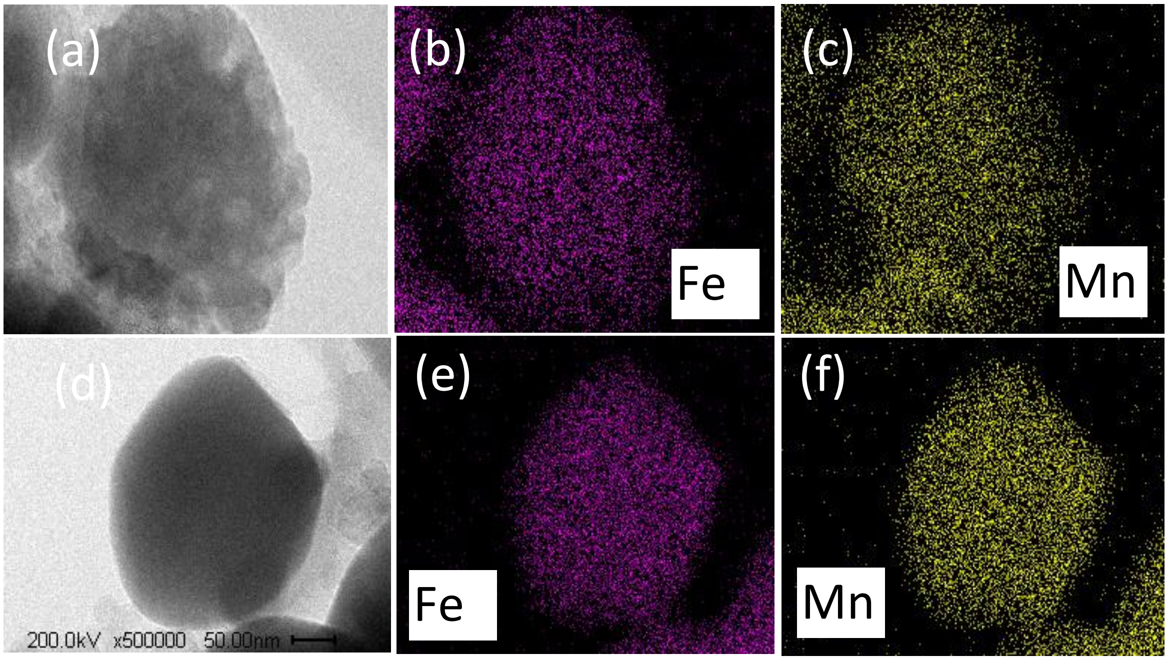

Figure 5-14: Elemental Mapping of ball milled LMFP (0.5) in its as-prepared pristine state (a), (b), (c); and after 10 electrochemical cycles (d), (e), (f).

5.3.5. XANES Analysis for Ball Milled $LiMn_xFe_{(1-x)}PO_4$

XANES K – edge analysis was done for both the transition metal cations - Fe and Mn and also the phosphorous edge to study the coordination environment and oxidation state change around the absorbing atoms. The purpose of doing all three edge analysis was to correlate any changes that might be arising during cycling in the local geometry of, especially, Fe and Mn. **Table 5-3** shows the potential cut-offs at which each electrode was stopped during the cycling process to collect the XAS data.

Table 5-3: The cut-off potentials of the differently charged electrodes at which XAS data were collected for Fe, Mn and P K-edges.

Electrode	SoC of $LiMn_xFe_{1-x}PO_4$ electrodes	Potential (w.r.t. Li) (V)
Point A	Pristine electrode, open circuit voltage	3.1
Point B	Partially Charged	3.7
Point C	Fully Charged	4.4
Point D	Partially Discharged	3.5
Point E	Fully Discharged	2.5

5.3.5.1. Fe K-edge XANES for Ball Milled LMFP (0.1), LMFP (0.3), LMFP (0.5)

Figure 5-15 shows the XANES spectra for LMFP (0.1) BM. Due to certain issues, data for LMFP (0.1) Fe –edge could be collected only for the pristine, fully charged and fully discharge electrodes. The charged and discharged electrodes were compared with the Fe standards – FeO (Fe^{2+}) and $FePO_4.2H_2O$ (Fe^{3+}) to determine the extent of oxidation change in Fe. The pristine and fully discharged electrodes are in perfect alignment and have an edge energy similar to FeO. This shows that the Fe in LMFP (0. 1) is present at Fe^{2+} state and also the fully discharged sample comes back to its original state of Fe^{2+} after cycling. For the fully charged electrode, the shift to higher energy is clearly visible along with a decrease in its white line intensity. The shift to higher energy, which almost matches the edge energy of the Fe^{3+} standard, shows that almost all the Fe gets converted from Fe^{2+} to Fe^{3+} state while charging. The decrease in white line shows that the electrode in its fully charged state has a degree of disorder around the absorbing atom Fe and this is expected as with charge, since the oxidation state of Fe changes, the orientation and the bond lengths of its neighbouring atoms change. But as the electrode is discharged back to its original state, the white line intensity increases back thus reinstating the order around Fe. From **Figure 5-15 (b)** the exact shift in energy with charge can be seen to be around 4 eV, which is approximately the energy shift for oxidation change of Fe^{2+} to Fe^{3+}.

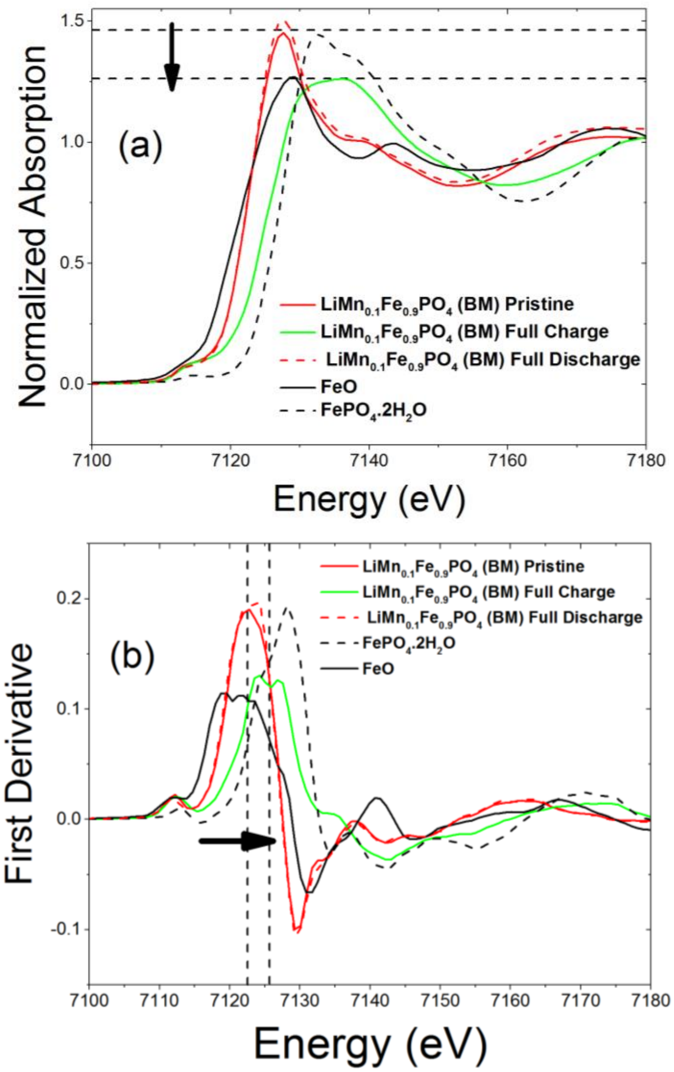

Figure 5-15: Fe K-edge XANES main absorption peak (a) and first derivative (b) spectra for the ball milled LMFP (0.1) pristine, fully charged and fully discharged samples compared to Fe $^{2+}$ and Fe^{3+} model compounds.

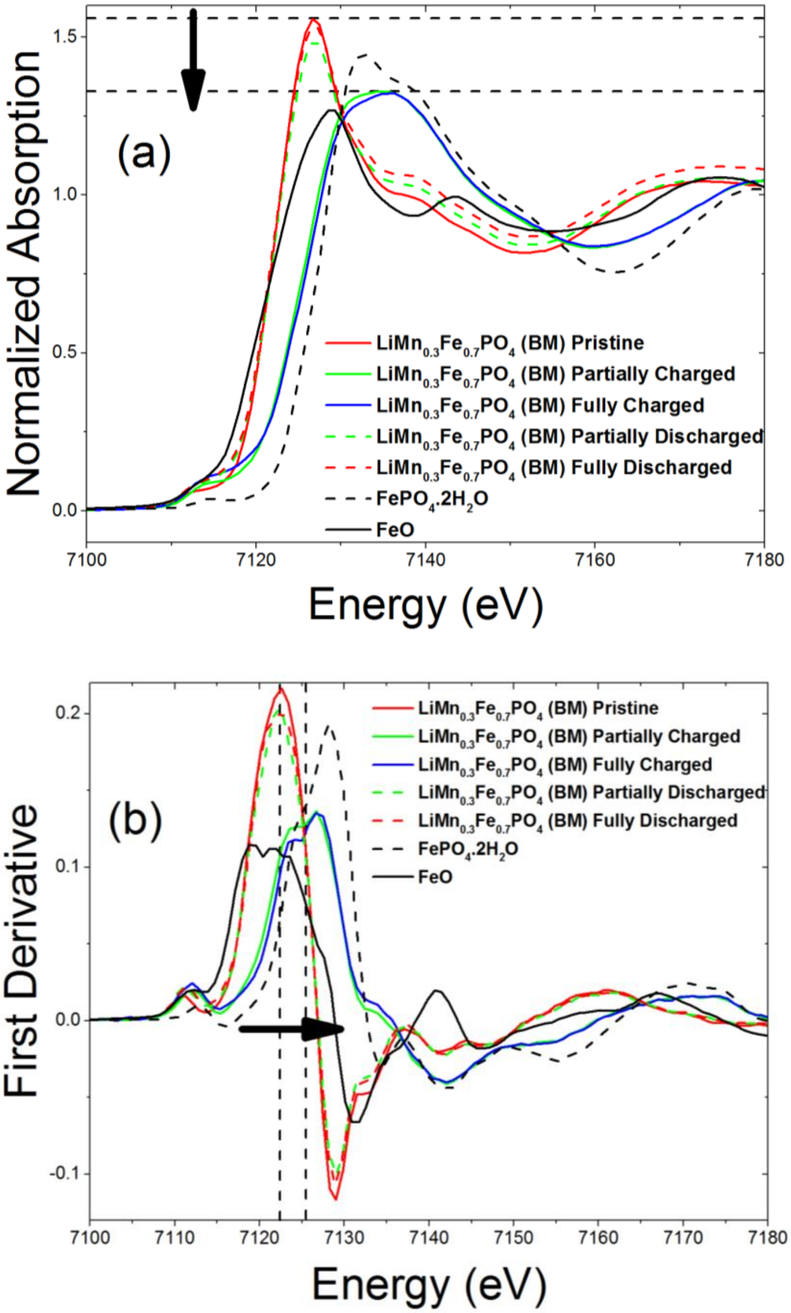

Figure 5-16: Fe K-edge XANES main absorption peak (a) and first derivative (b) spectra for the ball milled LMFP (0.3) pristine, partial charge, fully charged, partial discharge and fully discharged samples compared to Fe $^{2+}$ and Fe^{3+} model compounds.

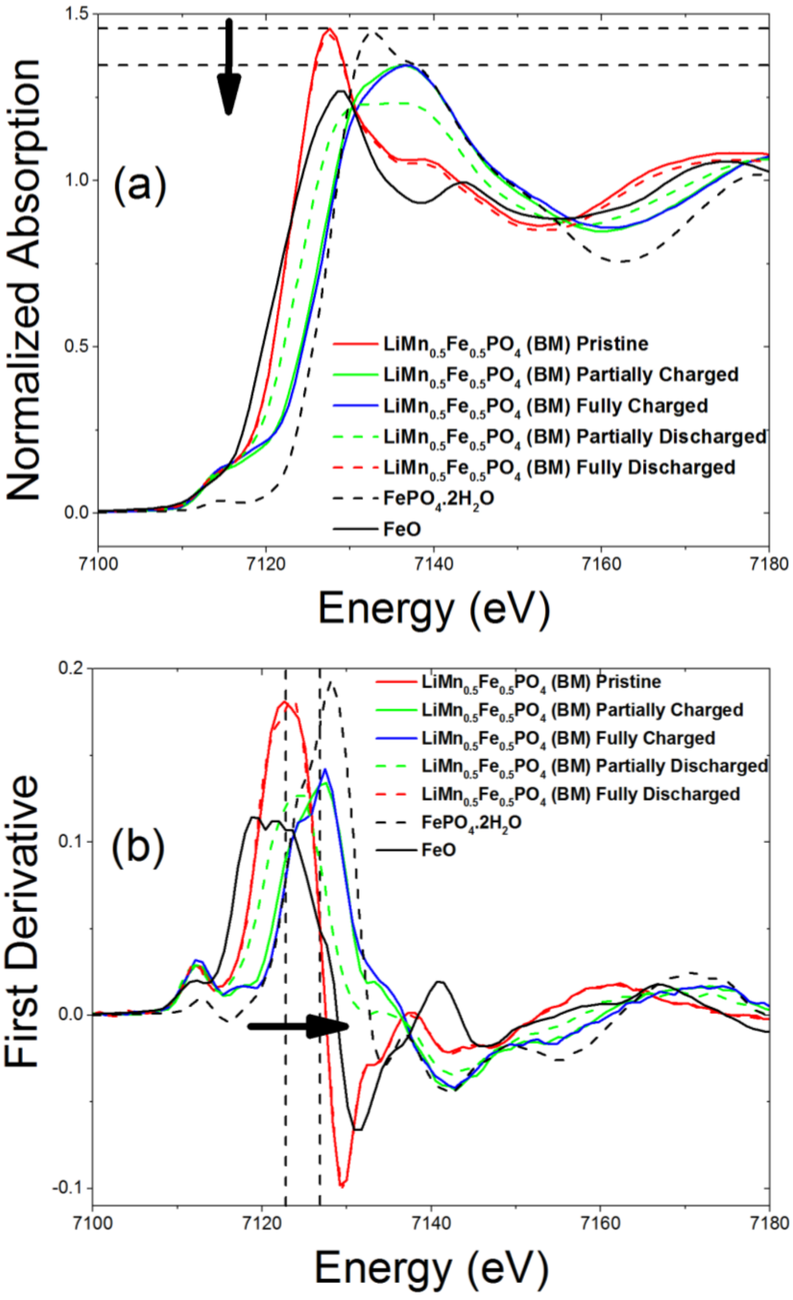

Figure 5-17: Fe K-edge XANES main absorption peak (a) and first derivative (b) spectra for the ball milled LMFP (0.5) pristine, partial charge, fully charged, partial discharge and fully discharged samples compared to Fe $^{2+}$ and Fe^{3+} model compounds.

For LMFP (0.3) in **Figure 5-16**, the results obtained from the XANES spectra are in hand-in-hand with what is expected and also seen in LMFP (0.1) as well. As compared to LMFP (0.1), there were two more electrodes – partially charged and partially discharged which helped give a better understanding of the results with cycling. The pristine sample as Fe in its 2+ state as seen in comparison with the Fe^{2+} standard, FeO and a white line intensity of 1.55 on the Y-scale. As the electrodes are charged, the shift in energy can be seen (from solid red to green to blue) with the fully charged state being almost at the same energy as $FePO_4.2H_2O$ (Fe3+) standard. As observed from the spectra the partially charged state is almost coinciding with the fully charged state. This is because the electrode for the partially charged state was stopped at 3.7 V and by then most of the Fe is probably oxidized to Fe^{3+}state (maximum voltage for Fe^{2+}/Fe^{3+} being 4.2 V vs Li in a purely LFP system). Similarly, during discharging as well, the partially discharged state at 3.5V is almost in harmony with the fully discharged state, however, this can also be due to fast self-discharge of the electrode during the period of it being stopped at the testing system until it was finally sealed inside the glove box.

LMFP (0.5) in **Figure 5-17** shows similar results as that of LMFP (0.3) and LMFP (0.1). The pristine electrode is at Fe^{2+} and as it is charged it shifts to higher energy with the fully charged state coinciding with the Fe^{3+} standard, thus, confirming the oxidation change of Fe from 2+ to 3+. With the discharge, the electrode goes back to its original energy and white line intensity. The one factor worth noting here is that the drop in the white line intensity for LMFP (0.5) with charge is almost half of what is seen for the compared to LMFP (0.1) and LMFP (0.3). This indicates that disorder around Fe is much less which is highly likely due to the increased Mn concentration for this material. The first derivative graph shows the shift in energy during charge to be almost 4.1 eV, which shows that almost all the Fe gets converted to Fe^{3+} with charge. **Figure 5-18** shows the R space for all the three LMFP (0.1, 0.3, and 0.5) pristine samples, which gives an idea about the starting structure of these materials. All the three materials show almost similar structure with slight differences in the LMFP (0.5) sample.

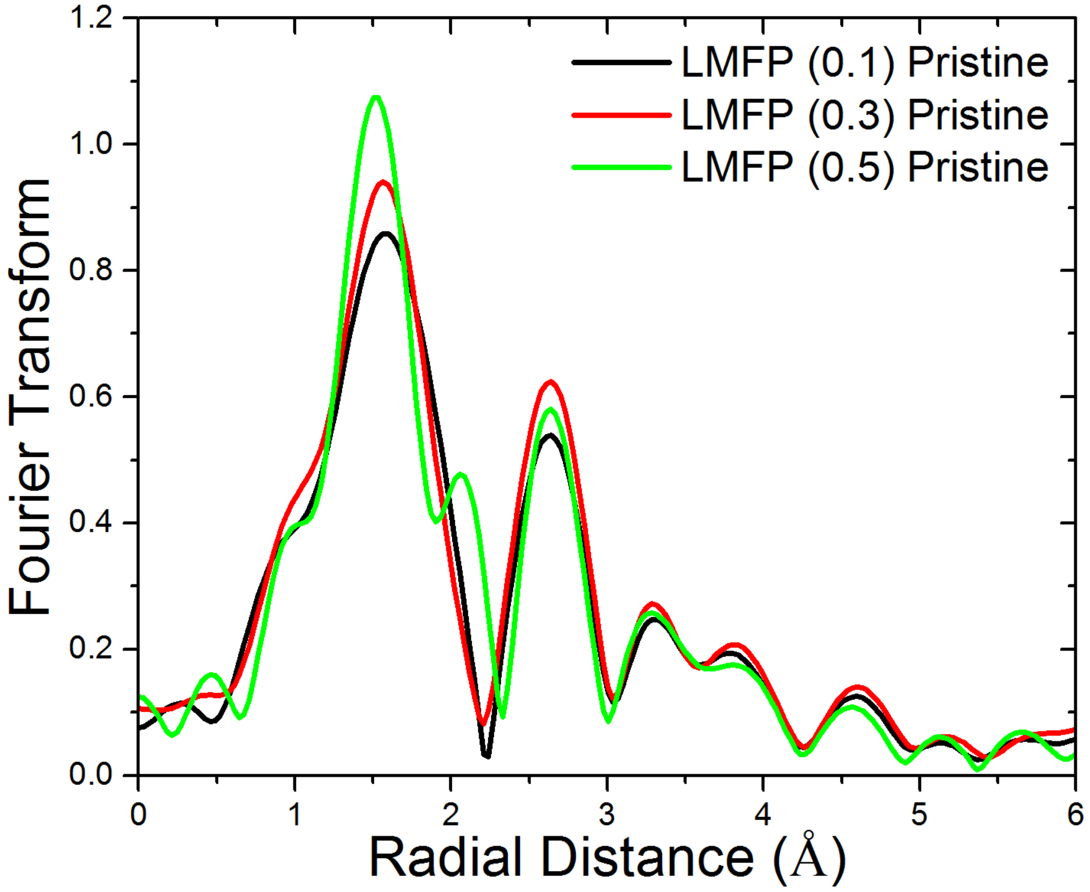

Figure 5-18: Fe K-edge XANES R-space spectra for ball milled LMFP (0.1-0.5) pristine samples.

5.3.5.2. Mn K-edge Ball Milled XANES for LMFP (0.1), LMFP (0.3), LMFP (0.5)

Due to some limitations, Mn K-edge XAS data for LMFP (0.1) could be collected only for the pristine and fully charged electrodes. **Figures 5-19, 5-20 5-21** show the XANES spectra (main absorption peak and derivative peak) for LMFP (0.1), LMFP (0.3), LMFP (0.5) respectively. For the energy phase spectra of the main absorption peak, no significant change is observed for LMFP (0.1) and LMFP (0.3). The derivative peak for LMFP (0.1) shows a shift of around 0.3 eV while that of LMFP (0.3) shows a shift of 0.4 eV which is quite negligible to show any change in oxidation state of Mn. The white line intensities of these LMFP (0.1) and LMFP (0.3) electrodes also remain almost similar during different points on the cycling curve. This suggests that for LMFP (0.1) and LMFP (0.3), Mn does not undergo almost no change in the oxidation state change. However, if the R-space is plotted for both these materials, a shift in the radius for the main Mn-O peak towards lower distance with charge, can be observed, thus suggesting changes in the local geometry around Mn with charge-discharge, which can be further determined by EXAFS. Thus, sometimes even when the XANES energy plots show no change, the R-space can help in determining any change in the local geometry change around the absorbing atom.

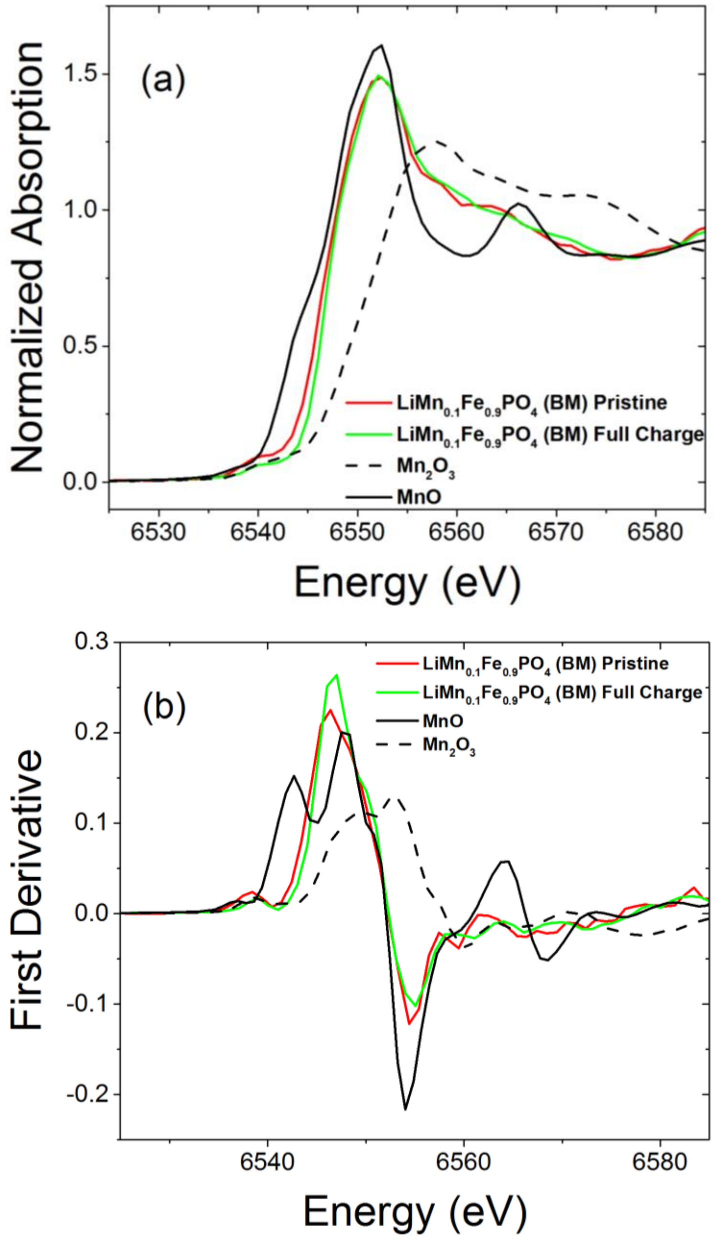

Figure 5-19: Mn K-edge XANES main absorption peak (a) and first derivative (b) spectra for the LMFP (0.1) pristine and fully charged samples compared to Mn $^{2+}$ and Mn $^{3+}$ model compounds.

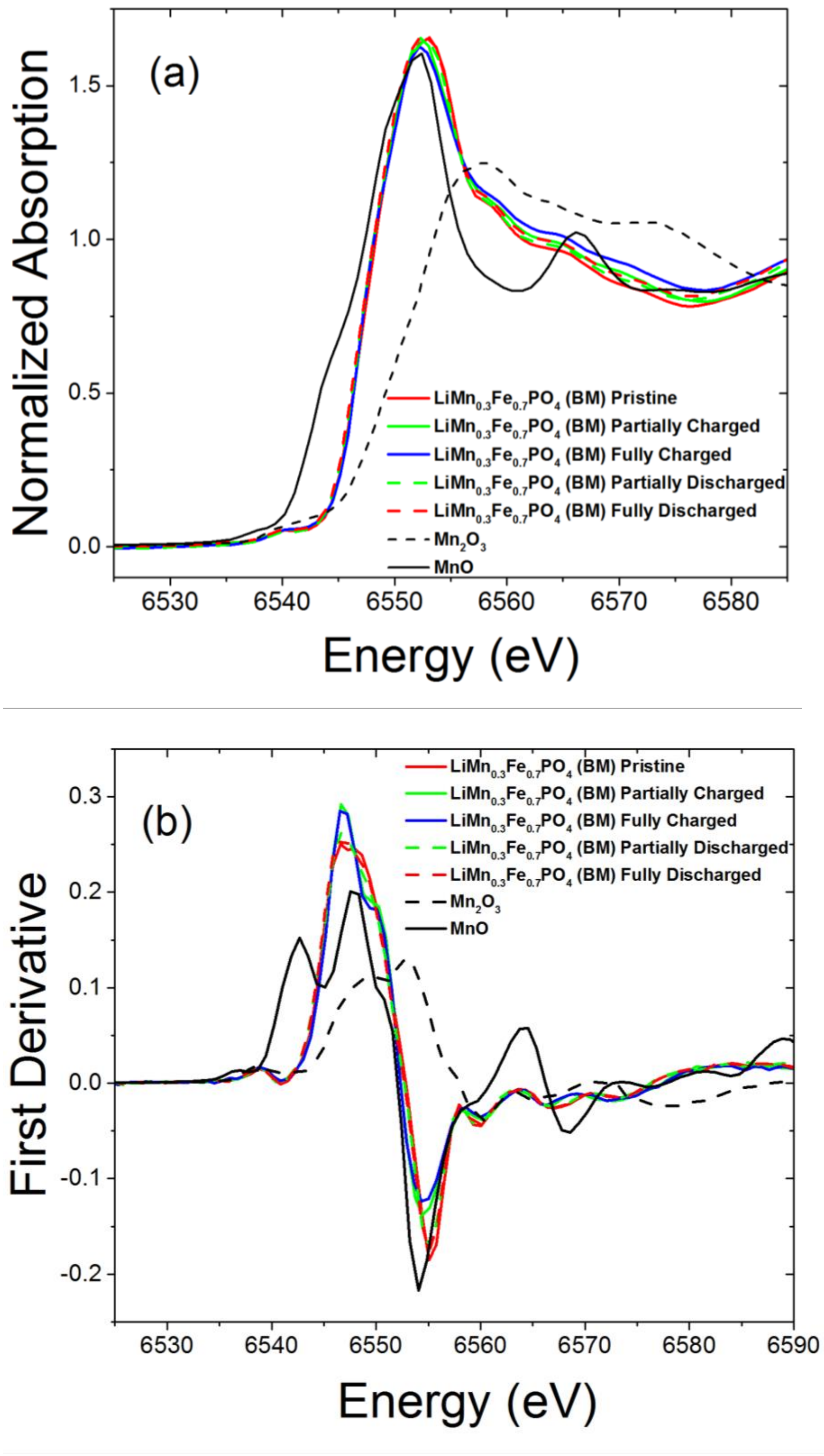

Figure 5-20: Mn K-edge XANES main absorption peak (a) and first derivative (b) spectra for the LMFP (0.3) pristine, partial charge, fully charged, partial discharge and fully charged samples compared to Mn $^{2+}$ and Mn $^{3+}$ model compounds.

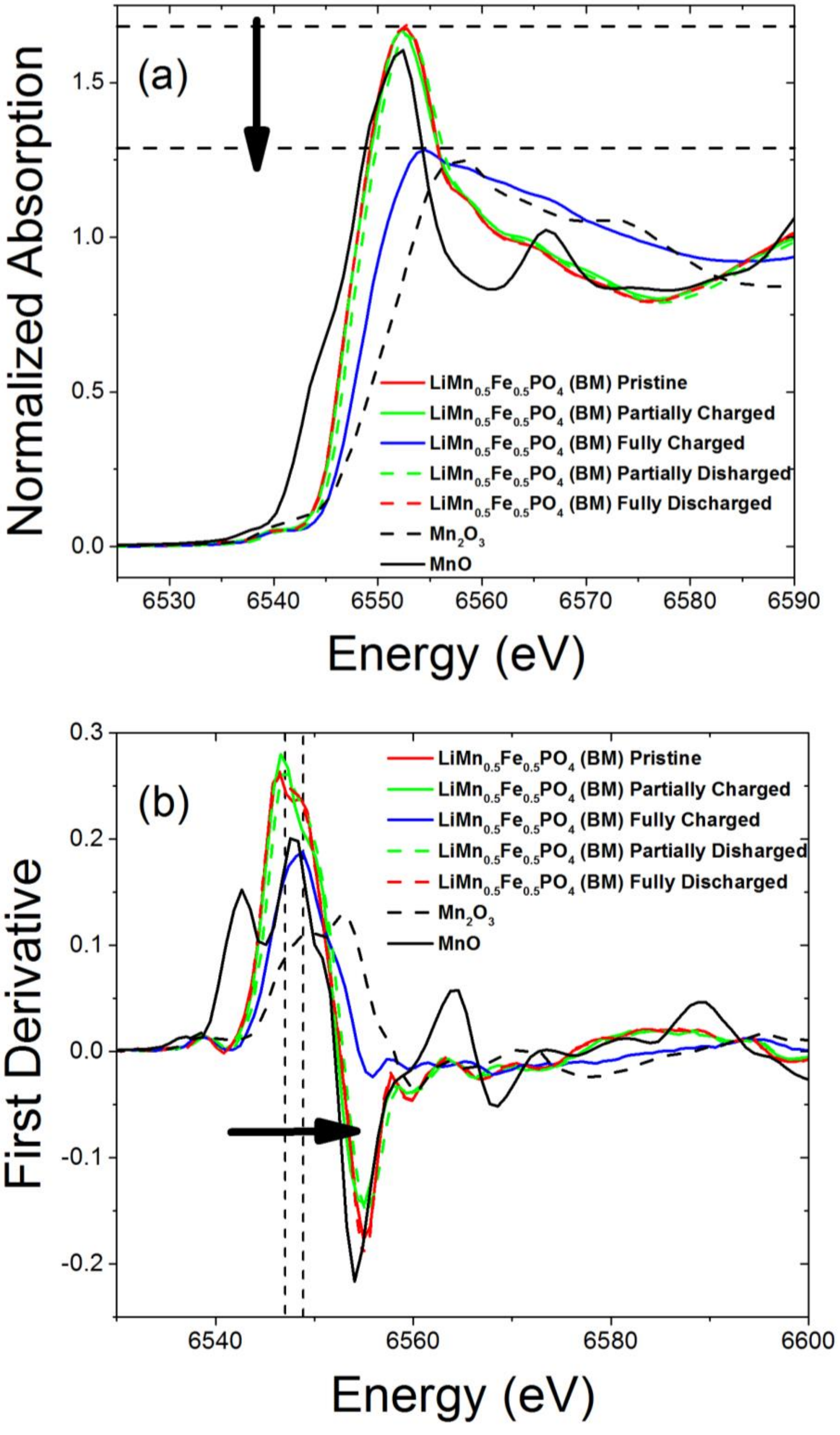

Figure 5-21: Mn K-edge XANES main absorption peak (a) and first derivative (b) spectra for the LMFP (0.5) pristine, partial charge, fully charged, partial discharge and fully charged samples compared to Mn^{2+} and Mn^{3+} model compounds.

On the other hand, when the XANES energy space for LMFP (0.5) is plotted in **Figure 5-21,** the shift in the main absorption peak for the fully charged electrode is way more prominent. Compared to Mn^{2+} and Mn^{3+} standards, the pristine, partially charged, partially discharged and fully discharged almost coincide with the Mn^{2+} standard, while the fully charged electrode is seen almost halfway in between the 2+ and 3+ standard. From the derivative peak, the shift in energy is almost +2 eV. This shows that the Mn in LMFP (0.5) definitely undergoes oxidation state change but it does not fully get converted to $Mn^{3+}$and lies somewhere in between 2+ and 3+. A linear combination fitting (LCF) of the LMFP (0.5) fully charged sample shows that the ration of Mn^{2+}/Mn^{3+} is around 3:7. Also, the white line intensity for the charged electrode decreases and again increases back to its ordered state with discharge. If the R-space in XANES is plotted for LMFP (0.5), not only does the radius seem to decrease with charge but the overall shape of the spectrum seems quite different from the other electrodes, which shows that the local geometry undergoes quite a bit of disorder with charge.

5.3.5.3. P K-edge XANES for Ball Milled LMFP (0.1), LMFP (0.3), LMFP (0.5)

XANES spectra for LMFP (0.1-0.5) are shown in **Figures 5-22, 5-23, 5-24**. For LMFP (0.1), similar to Mn K-edge, only pristine and full charge could be measured, while for LMFP (0.3) and LMFP (0.5), a full set of electrodes at different cut-off voltages, were measured. For all three materials, 0.1, 0.3, 0.5, similar results were observed as what was seen for LFP P K-edge. Usually, there is no change in the phosphate structure with cycling. However, the slight shift towards higher energy for the main absorption peak with charge, can be attributed to the inductive effect of Fe on P. The transition of Fe from 2+ to 3+, or in this even change in oxidation state of Mn, makes the P-O bonds less covalent and the shift in the peak reflects a change of the degree of covalency. From the derivative peak, this shift of peak corresponds to around 0.5-0.8 eV, which is not enough for any change in the oxidation state of P. Thus, $(PO_4)^{3-}$ polyanion does not undergo any oxidative change due to the cycling of the LMFP electrodes. Again, as seen for LFP P K-edge, no pre-edge was observed for the pristine and fully discharged electrodes. But for the partially charged, fully charged and partially discharged in all the LMFP materials under study, showed an increasing pre-edge intensity with charge. This pre-edge feature of P K-edge reveals the interaction between metal 3d and P 3p states through the shared oxygen atom since P and Fe/Mn is not in direct bonding. The gradual increase of pre-edge peak intensities with the Li-ion extraction is due to the hybridization of P 3p states with the Fe/Mn 3d and the electrodes discharge back to its original state, the hybridization weakens and the pre-edge decreases till it disappears at the fully discharged state. **Figure 5-25** shows the radial space of the XANES analysis of the P K-edge. In spite of the slight shift in the higher energy of the main peak and pre-edge variations, from the radial space, it can be observed that the structural environment around P does not vary with cycling for any of the three materials. The main peak corresponding to the P-O bond (around 1.25 Å) for all the materials and for any state of charge almost overlaps with each other.

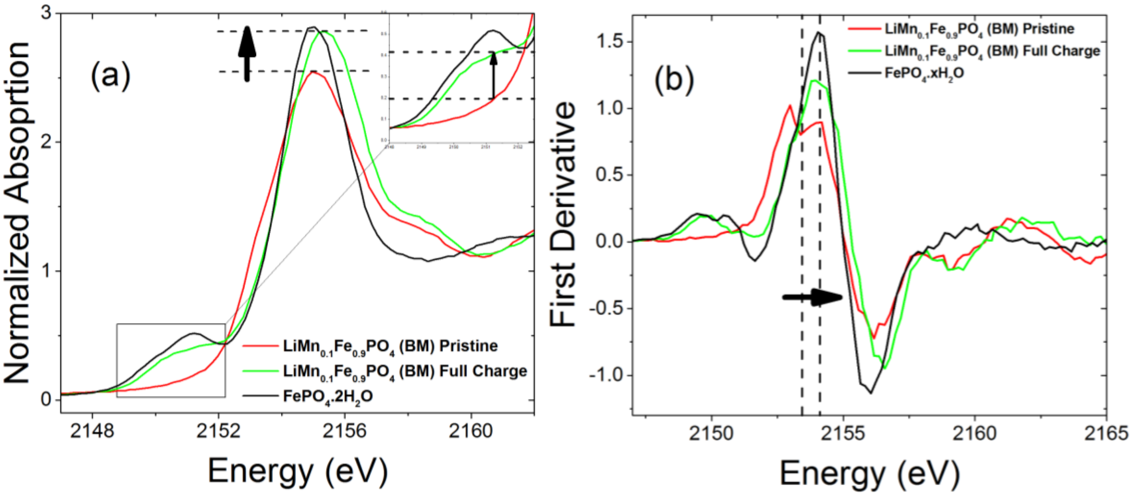

Figure 5-22: P K-edge XANES main absorption peak (a) and first derivative (b) spectra for the LMFP (0.1) pristine and fully charged samples compared to phosphate model compounds.

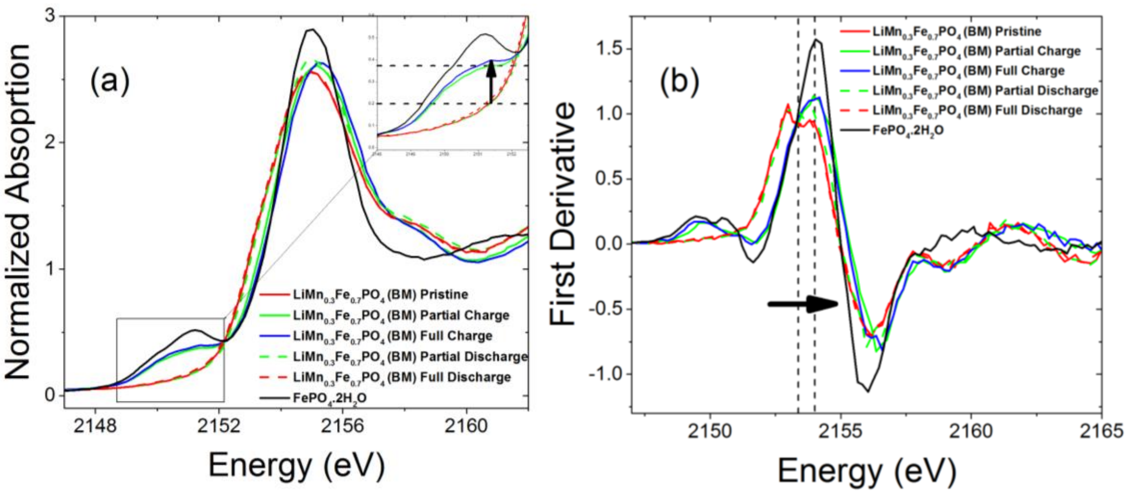

Figure 5-23: P K-edge XANES main absorption peak (a) and first derivative (b) spectra for the LMFP (0.3) pristine, partial charged, fully charged, partial discharged and fully discharged samples compared to phosphate model compounds.

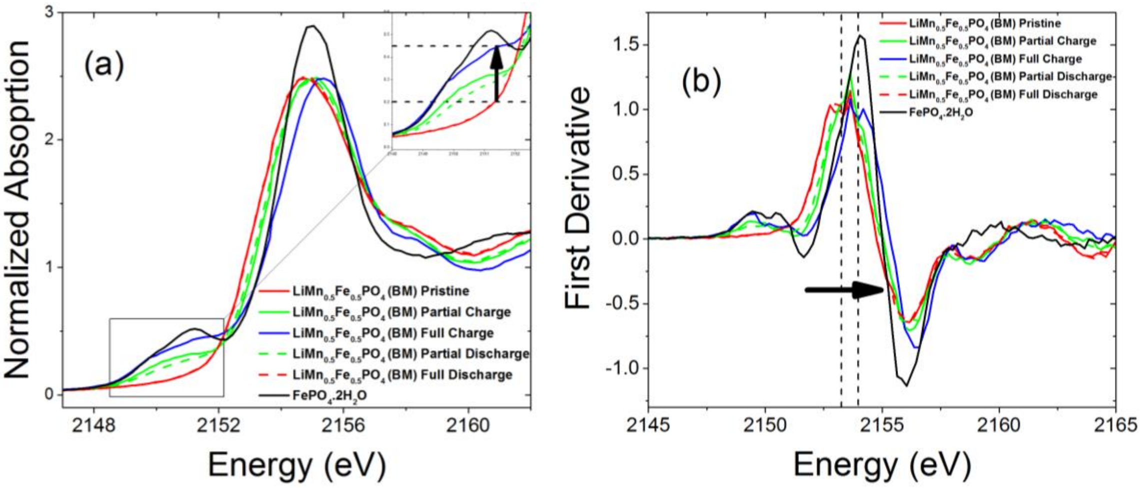

Figure 5-24: P K-edge XANES main absorption peak (a) and first derivative (b) spectra for the LMFP (0.3) pristine, partial charged, fully charged, partial discharged and fully discharged samples compared to phosphate model compounds.

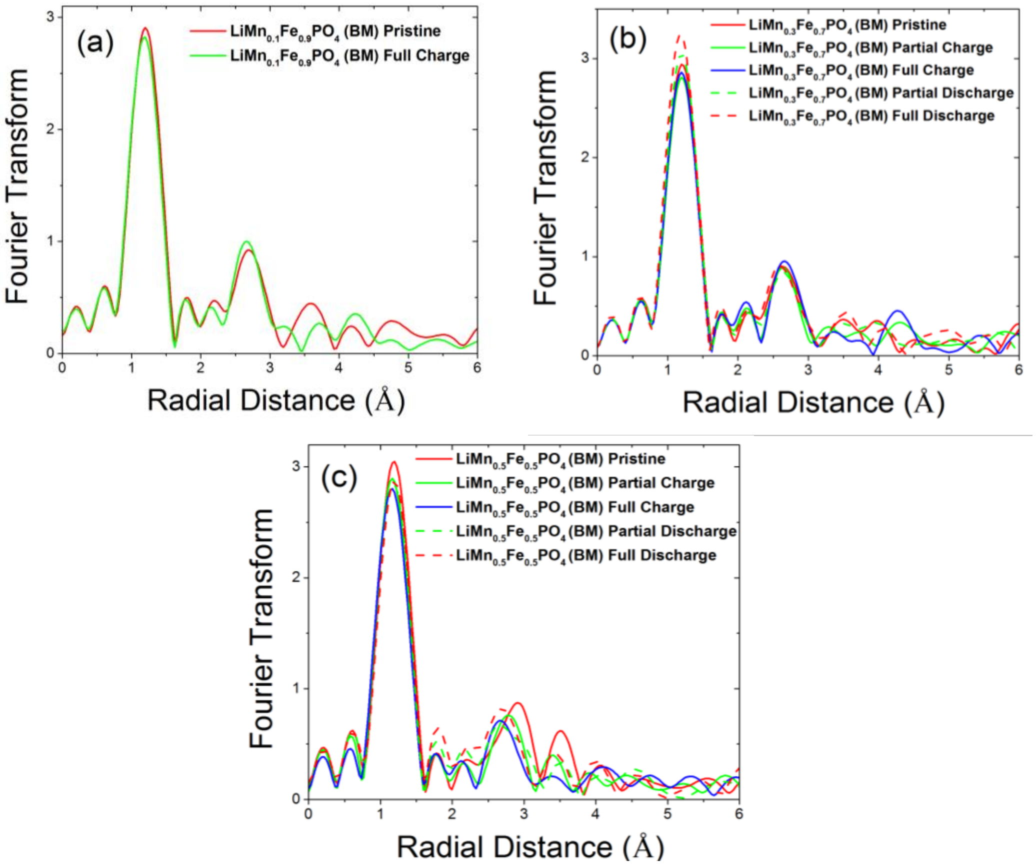

Figure 5-25: R-space spectra for P K-edge XANES for (a) LMFP (0.1); (b) LMFP (0.3); (c) LMFP (0.5).

5.3.6. XANES Analysis for Flame Spray $LiMn_xFe_{(1-x)}PO_4$ (x=0.1,0.3)

5.3.6.1. Fe and Mn and P K-edge Flame Spray XANES for LMFP (0.1), LMFP (0.3)

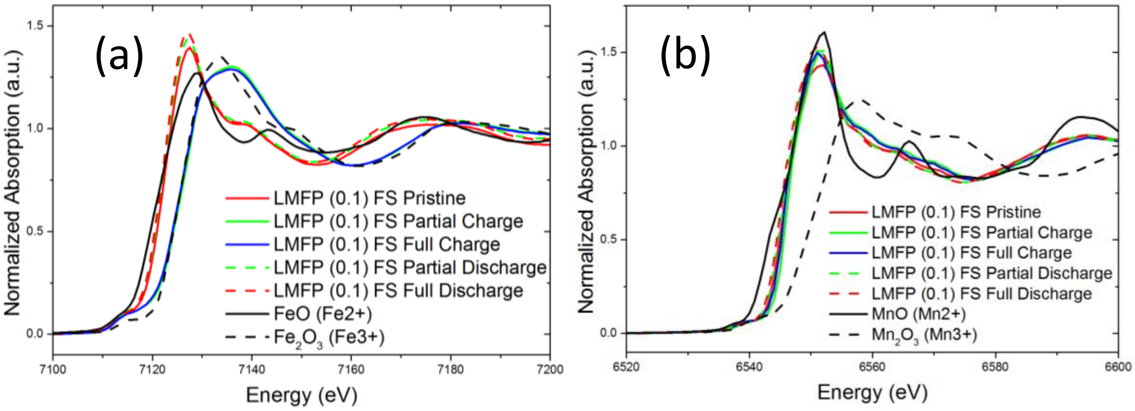

Figure 5-26: (a) Fe and (b) Mn K- edge XANES main absorption peak spectra for LMFP (0.1), synthesized via flame spray method, at different potential points on the cycling curve, along with Fe/Mn^{2+} and Fe/Mn^{3+} model compounds.

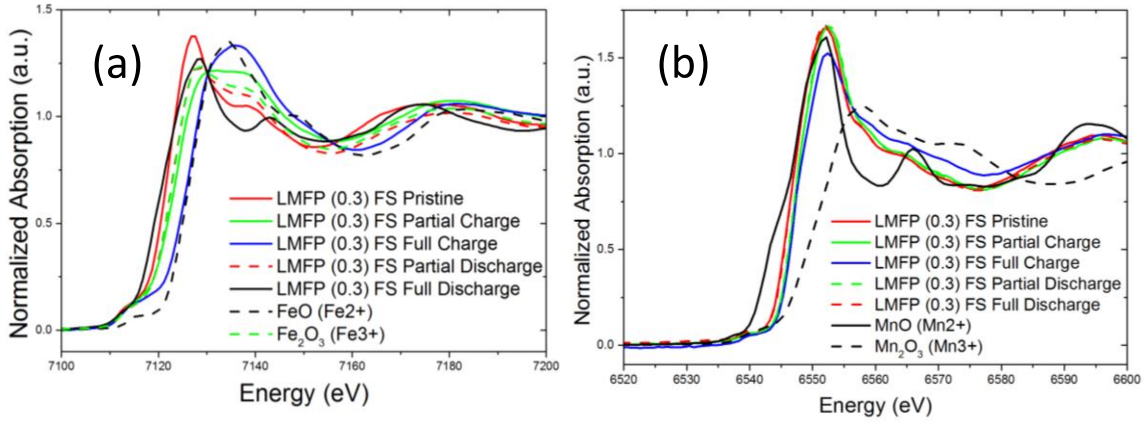

Figure 5-27: (a) Fe and (b) Mn K- edge XANES main absorption peak spectra for LMFP (0.3), synthesized via flame spray method, at different potential points on the cycling curve, along with Fe/Mn^{2+} and Fe/Mn^{3+} model compounds.

Figure 5-26 shows the XANES spectra for the LMFP (0.1) for both Fe and Mn K-edge. For the Fe K-edge, the fully charged electrode shows a complete edge shift from Fe^{2+} to Fe^{3+}. However, for the Mn-edge, all the electrodes seem to be at the same oxidation state showing no change in their absorption edge, which is very similar to be result observed for the ball-milled sample as well. **Figure 5-27** shows the XANES spectra for LMFP (0.3) flame spray electrodes. The Fe K-edge shows a nice trend of the electrodes changing oxidation state from Fe^{2+} to Fe^{3+} as the cell is charged and back to Fe^{2+} as the cell is fully discharged. However, once again the Mn K-edge shows not prominent change in the change of the Mn oxidation state. On closer examination, a slight change is observed for the fully charged state from the pristine condition, which can be further examined from the EXAFS analysis.

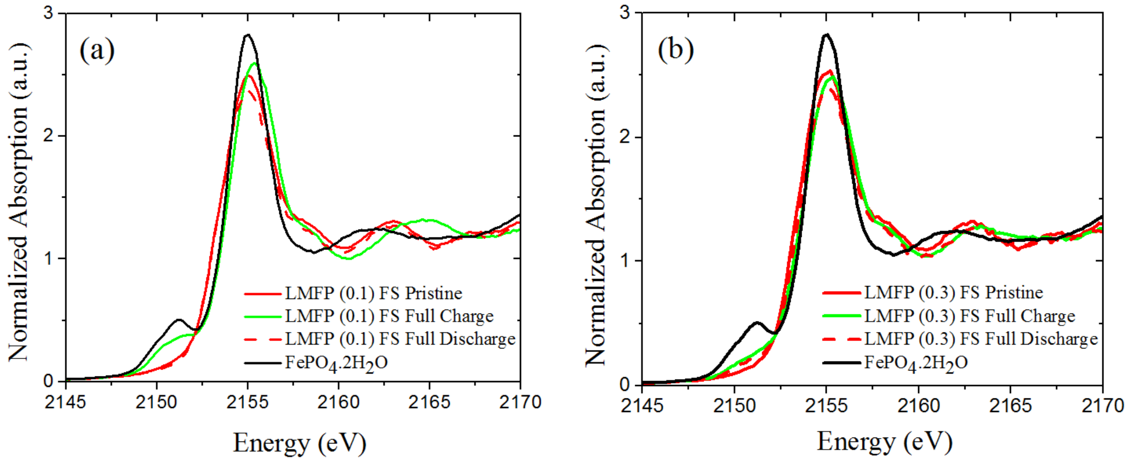

Figure 5-28: P K- edge XANES main absorption peak spectra for (a) LMFP (0.1) and (b) LMFP (0.3), synthesized via flame spray method, at different potential points on the cycling curve.

Figure 5-28 shows the P K-edge XANES for both the LMFP (0.1) and LMFP (0.3) flame spray samples and as observed or the LFP and LMFP ball milled XAS studies, here as well, the P K-edge shows no change in the oxidation state of phosphorus. The slight shift that is observed in the main absorption peaks is mostly due to the inductive effect on P due to change in oxidation state of Fe and Mn during cycling.

5.3.7. EXAFS Analysis for Ball Milled $LiMn_xFe_{(1-x)}PO_4$ (x=0.1,0.3,0.5)

Fe and Mn K-edge EXAFS fittings for all the LMFP samples were done until the third shell. Even though for EXAFS, values beyond the second shell are sometimes considered inconsistent, in this study, all fittings have been done till the third shell just to give an idea as to how the bond length varies even if the values are not precisely correct.

5.3.7.1. Fe K-edge EXAFS for Ball Milled LMFP (0.1) LMFP (0.3) and LMFP (0.5)

Tables 5-4, 5-5, 5-6 tabulate all the Fe K-edge EXAFS fittings for ball milled LMFP (0.1), LMFP (0.3) and LMFP (0.5) respectively. For Pristine LMFP (0.1), Fe-O bond is observed to be around 2.11 Å and as the electrode gets fully charged, the bond length decreases to 1.99 Å, which is similar to the bond length observed for a Fe^{3+}-O bond, thus confirming that as LMFP (0.1) is charged, the oxidation state of Fe changes from 2+ to 3+. Also the Debye-Waller (DW) factor increases with charge, which means that as the bond length decreases with a change in Fe state, the static vibrations inside the material increases as well. This was observed in the EXAFS fittings for LFP as well as and is usually the case in most materials when they are under the influence of external factors like voltage, current, pressure etc. Again, as the cell discharges back to 2.5 V, the bond length again increases to 2.09 Å. It is seen that the discharged bond length exactly doesn't go back to the pristine state. This can be due to some internal dynamics since the DW factor is still on the higher side and might be affecting the bond length. For the second (Fe-P) and third shell (Fe-Fe) as well, the bond length can be seen to decrease as the cell is charged since Fe^{3+}, due to its higher charge, pulls all its neighbouring atoms closer towards itself, the effect of which can be seen in further shells as well. Yet again, as the cell discharges, all the higher shells bond lengths also relaxes back to its original pristine state.

As observed for LMFP (0.1), the same trend can be seen in LMFP (0.3) and LMFP (0.5) as well. The first shell bond length of Fe-O is around 2.15 Å and 2.17 Å for pristine state and on charging it decreases to 1.98 Å and 2.05 Å for LMFP (0.3) and (0.5) respectively. The DW factor also increases with charge due to the static vibrations inside the material.

And as the electrode is again discharged back, the bond length increases and the DW factor reduces, showing that both the materials upon discharge go back to its original stable condition, as analyzed for their respective pristine conditions. A similar tendency can be seen for the second and third shell as well. The bond distances decease on Li extraction and increase back with the intercalation of Li into the material. The R-factors, which give the goodness of fit, are also all lower than 0.05 suggesting the analysis of the bond lengths are consistent and reliable. The difference between these three materials is the bond length of the first shell Fe-O in the pristine state. For LMFP (0.1) it is 2.11 Å, for LMFP (0.3) it is 2.15 Å while for LMFP (0.5) it is around 2.17 Å. Therefore, as the Mn concentration increases in the material, the bond lengths also increase slightly. This is expected since Mn^{2+} radius is slightly larger than Fe^{2+} and insertion of Mn into the system expands the cell volume, in turn increasing the bond distances.

Table 5-4: EXAFS fittings for Fe K-edge ball milled LMFP (0.1) first, second and third shell along with the $Fe^{2+}$and Fe^{3+}model compounds.

SoC	**Bond**	**CN**	**σ^2**	**R**	**R-factor**	**E_0**
FeO (Fe^{2+})				2.13		7121.17
Fe_2O_3 (Fe^{3+})				1.99		7125.59
Pristine (OCV 3.1 V)	Fe-O	6	0.003(0.007)	2.11(0.06)	0.01	7122.65
	Fe-P1	1	0.001(0.007)	2.86(0.04)		
	Fe-P2	4	0.007(0.006)	3.26(0.06)		
	Fe-Fe	4	0.011(0.005)	3.84(0.03)		
Fully Charged (4.4 V)	Fe-O	6	0.020(0.006)	1.99(0.05)	0.002	7125.32
	Fe-P1	1	0.001(0.001)	2.84(0.02)		
	Fe-P2	4	0.007(0.002)	3.16(0.02)		
	Fe-Fe	4	0.012(0.002)	3.74(0.02)		
Fully Discharged (2.5 V)	Fe-O	6	0.008(0.020)	2.09(0.21)	0.01	7122.72
	Fe-P1	1	0.003(0.010)	2.86(0.07)		
	Fe-P2	4	0.008(0.008)	3.25(0.08)		

	Fe-Fe	4	0.013(0.008)	3.83(0.10)

Table 5-5: EXAFS fittings for Fe K-edge ball milled LMFP (0.3) first, second and third shell along with the Fe^{2+} and Fe^{3+} model compounds**.**

SoC	**Bond**	**CN**	**σ^2**	**R**	**R-factor**	**E_0**
FeO (Fe^{2+})				2.13		7121.17
Fe_2O_3 (Fe^{3+})				1.99		7125.59
Pristine (OCV 3.1 V)	Fe-O	6	0.006(0.003)	2.15(0.04)	0.03	7122.06
	Fe-P1	1	0.002(0.005)	2.87(0.04)		
	Fe-P2	4	0.009(0.005)	3.25(0.04)		
	Fe-Fe	4	0.017(0.009)	3.83(0.07)		
Partial Charge (3.7 V)	Fe-O	6	0.016(0.003)	2.01(0.04)	0.001	7126.33
	Fe-P1	1	0.005(0.002)	2.83(0.01)		
	Fe-P2	4	0.010(0.002)	3.18(0.02)		
	Fe-Fe	4	0.015(0.002)	3.78(0.02)		
Fully Charged (4.4 V)	Fe-O	6	0.024(0.010)	1.98(0.01)	0.006	7126.48
	Fe-P1	1	0.003(0.003)	2.90(0.03)		
	Fe-P2	4	0.007(0.001)	3.18(0.01)		
	Fe-Fe	4	0.012(0.002)	3.77(0.02)		
Partial Discharge (3.5 V)	Fe-O	6	0.009(0.008)	2.13(0.02)	0.02	7122.12
	Fe-P1	1	0.001(0.001)	2.89(0.03)		
	Fe-P2	4	0.008(0.003)	3.22(0.02)		
	Fe-Fe	4	0.016(0.006)	3.81(0.05)		
Fully Discharged (2.5 V)	Fe-O	6	0.003(0.001)	2.14(0.02)	0.02	7122.08
	Fe-P1	1	0.013(0.006)	2.89(0.02)		
	Fe-P2	4	0.008(0.003)	3.24(0.02)		
	Fe-Fe	4	0.017(0.004)	3.82(0.04)		

Table 5-6: EXAFS fittings for Fe K-edge ball milled LMFP (0.5) first, second and third shell along with the Fe^{2+} and Fe^{3+} model compounds.

SoC	**Bond**	**CN**	**σ^2**	**R**	**R-factor**	**E_0**
FeO (Fe^{2+})				2.13		7121.17
Fe_2O_3 (Fe^{3+})				1.99		7125.59
Pristine (OCV 3.1 V)	Fe-O	6	0.003(0.003)	2.17(0.03)	0.03	7122.89
	Fe-P1	1	0.001(0.001)	2.89(0.02)		
	Fe-P2	4	0.019(0.011)	3.25(0.06)		
	Fe-Fe	4	0.015(0.006)	3.85(0.07)		
Partial Charge (3.7 V)	Fe-O	6	0.007(0.001)	2.08(0.01)	0.003	7126.32
	Fe-P1	1	0.003(0.002)	2.84(0.01)		
	Fe-P2	4	0.014(0.002)	3.21(0.02)		
	Fe-Fe	4	0.015(0.001)	3.84(0.02)		
Fully Charged (4.4 V)	Fe-O	6	0.013(0.011)	2.05(0.02)	0.03	7126.49
	Fe-P1	1	0.001(0.001)	2.85(0.02)		
	Fe-P2	4	0.009(0.002)	3.15(0.02)		
	Fe-Fe	4	0.012(0.002)	3.77(0.02)		
Partial Discharge (3.5 V)	Fe-O	6	0.006(0.002)	2.09(0.02)	0.006	7123.97
	Fe-P1	1	0.001(0.002)	2.86(0.01)		
	Fe-P2	4	0.008(0.003)	3.23(0.02)		
	Fe-Fe	4	0.016(0.002)	3.85(0.05)		
Fully Discharged (2.5 V)	Fe-O	6	0.008(0.006)	2.13(0.05)	0.02	7122.37
	Fe-P1	1	0.001(0.001)	2.88(0.02)		
	Fe-P2	4	0.015(0.005)	3.27(0.05)		
	Fe-Fe	4	0.016(0.006)	3.85(0.06)		

5.3.7.2. Mn K-edge EXAFS for Ball Milled LMFP (0.1) LMFP (0.3) and LMFP (0.5)

An attempt was made to analyze the Mn local geometry until the third neighbour, considering that to be Fe, since all the three materials have higher to an equal ratio of Fe and Mn. All the Mn K-edge EXAFS fittings are tabulated in **Tables 5-7, 5-8, 5-9** for LMFP (0.1), LMFP (0.3) and LMFP (0.5) respectively. For LMFP (0.1), the starting material showed the first shell Mn-O average bond distance to be around 2.17 Å, which is slightly shorter than usual octahedral Mn^{2+}- O coordination bond distances found in the literature [29-31]**.** On charging, the Mn-O distance decreases to 2.06 Å. The second and third shell distances, Mn-P and Mn-Fe respectively, also seem to decrease from 3.26 Å to 3.20 Å and 3.82 Å to 3.77 Å, however, these changes are lesser than that observed for the first shell. Focusing here on the first shell, this is found to be interesting because even though no change in the edge energy for Mn is observed in the XANES spectra, yet a change in the bond distance is seen for the EXAFS analysis. A similar result is also seen for LMFP (0.3). As the electrode for LMFP (0.3) is charged from its original state to fully charged state, the Mn-O bond distance decrease from 2.11 Å to 1.95 Å but yet again little to no change in the Mn edge is observed during the XANES analysis. However, the EXAFS for LMFP (0.5) show almost consistent results with its XANES analysis. The fully charged state for LMFP (0.5) shows an edge shift of almost 2 eV from its original state while all the other state of charge remain almost at the same edge energy. The quantitative EXAFS analysis also shows a similar trend with the starting material to be around 2.19 Å while the fully charged state shows a decrease in the bond length to 2.08 Å. The other electrodes at different states of charge have their bond distances in the range of 2.16-2.18 Å. However, as compared to LMFP (0.1) and (0.3), the DW factors are quite high for all the bond distances, suggesting an increased static disorder for this system.

There has been evidence before wherein Mn or even other metals do not undergo any change in oxidation state with cycling and the charge compensation happened due to the presence of another transition metal [32, 33]. However, Mn itself is a very tricky material. Researchers have given enough evidence of $Mn^{2+/3+}$ redox couple showing the Jahn-Teller (JT) effect, which is one of the main reasons for distortions seen in an Mn-based material [34-46]. Beside the JT effect, Mn also shows site preference in some cases where an octahedral Mn^{2+} occupying a tetrahedral Mn^{2+} site [47]. In this case, there is a possibility that there is Mn^{2+} being in its d5 orbital results in large crystal field orbital splitting which, in turn, turns a high-spin Mn to a low-spin Mn. The ionic radius for high spin Mn^{2+} is 0.97 Å whereas for low spin Mn^{2+} it is 0.81 Å. A shift from high to the low spin of Mn results in a decrease in the average bond length which might be resulting in the lowering of the Mn-O bond distance with charge [48, 49]. In the case of LMFP (0.5), the higher ratio of Mn is a likelihood that some of the Mn actually undergoes a Mn^{2+}/Mn^{3+} redox reaction and that is the effect that is observed in the EXAFS analysis instead of the high to low spin effect.

Table 5-7: Mn K-edge EXAFS first, second and third shell fittings for pristine and fully charged electrodes of ball milled LMFP (0.1) along with the Mn^{2+} and Mn^{3+} model compounds.

SoC	**Bond**	**CN**	**σ^2**	**R**	**R-factor**	**E_0**
MnO (Mn^{2+})		6		2.19		6546.03
Mn_2O_3 (Mn^{3+})		6		2.04		6550.96
MnO_2 (Mn^{4+})		6		1.89		6554.49
Pristinee (OCV 3.1 V)	Mn-O	6	0.005(0.009)	2.17(0.05)	0.03	6546.32
	Mn-P1	1	0.001(0.002)	2.85(0.07)		
	Mn-P2	4	0.005(0.005)	3.26(0.04)		
	Mn-Fe	4	0.007 (0.005)	3.82(0.04)		
Fully Charged (4.4 V)	Mn-O	6	0.005(0.008)	2.06(0.08)	0.03	6547.16
	Mn-P1	1	0.001(0.013)	2.89(0.08)		
	Mn-P2	4	0.007(0.008)	3.20(0.11)		
	Mn-Fe	4	0.014(0.013)	3.77(0.11)		

Table 5-8: Mn K-edge EXAFS first, second and third shell fittings for pristine, partial charged, fully charged, partial discharged and fully charged electrodes of ball milled LMFP (0.3) along with the Mn^{2+} and Mn^{3+} model compounds.

SoC	Bond	CN	σ^2	R	R-factor	E_0
MnO (Mn^{2+})		6		2.19		6546.03
Mn_2O_3 (Mn^{3+})		6		2.04		6550.96
MnO_2 (Mn^{4+})		6		1.89		6554.49
Pristine (OCV 3.1 V)	Mn-O	6	0.004(0.013)	2.11(0.03)	0.02	6546.86
	Mn-P1	1	0.007(0.017)	2.83(0.09)		
	Mn-P2	4	0.003(0.004)	3.29(0.04)		
	Mn-Fe	4	0.010(0.004)	3.83(0.05)		
Partial Charge (3.7 V)	Mn-O	6	0.003(0.003)	2.02(0.04)	0.01	6547.93
	Mn-P1	1	0.002(0.010)	2.91(0.08)		
	Mn-P2	4	0.003(0.004)	3.17(0.05)		
	Mn-Fe	4	0.014(0.008)	3.75(0.07)		
Fully Charged (4.4 V)	Mn-O	6	0.002(0.003)	1.95(0.04)	0.02	6549.17
	Mn-P1	1	0.001(0.001)	2.87(0.08)		
	Mn-P2	4	0.004(0.004)	3.11(0.04)		
	Mn-Fe	4	0.012(0.008)	3.65(0.05)		
Partial Discharge (3.5 V)	Mn-O	6	0.004(0.005)	2.03(0.04)	0.02	6548.31
	Mn-P1	1	0.003(0.010)	2.91(0.10)		
	Mn-P2	4	0.005(0.004)	3.17(0.06)		
	Mn-Fe	4	0.029(0.040)	3.73(0.18)		
Fully Discharged (2.5 V)	Mn-O	6	0.006(0.005)	2.15(0.02)	0.04	6547.08
	Mn-P1	1	0.004(0.012)	2.86(0.07)		
	Mn-P2	4	0.012(0.014)	3.28(0.08)		
	Mn-Fe	4	0.016(0.009)	3.83(0.12)		

Table 5-9: Mn K-edge EXAFS first, second and third shell fittings for pristine, partial charged, fully charged, partial discharged and fully charged electrodes of ball milled LMFP (0.5) along with the Mn^{2+} and Mn^{3+} model compounds.

SoC	Bond	CN	σ^2	R	R-factor	E_0
MnO (Mn2+)		6		2.19		6546.03
Mn_2O_3 (Mn3+)		6		2.04		6550.96
MnO_2 (Mn4+)		6		1.89		6554.49
Pristine (OCV 3.1 V)	Mn-O	6	0.015(0.020)	2.19(0.03)	0.05	6547.44
	Mn-P1	1	0.003(0.010)	2.88(0.07)		
	Mn-P2	4	0.008(0.007)	3.29(0.06)		
	Mn-Fe	4	0.013(0.009)	3.84(0.08)		
Partial Charge (3.7 V)	Mn-O	6	0.014(0.003)	2.16(0.03)	0.05	6547.93
	Mn-P1	1	0.001(0.001)	2.87(0.04)		
	Mn-P2	4	0.013(0.009)	3.24(0.06)		
	Mn-Fe	4	0.016(0.009)	3.83(0.08)		
Fully Charged (4.4 V)	Mn-O	6	0.008(0.003)	2.08(0.03)	0.08	6548.86
	Mn-P1	1	0.006(0.015)	2.76(0.08)		
	Mn-P2	4	0.022(0.030)	3.15(0.11)		
	Mn-Fe	4	0.017(0.009)	3.81(0.11)		
Partial Discharge (3.5 V)	Mn-O	6	0.020(0.020)	2.18(0.03)	0.07	6548.31
	Mn-P1	1	0.001(0.001)	2.88(0.04)		
	Mn-P2	4	0.012(0.007)	3.27(0.06)		
	Mn-Fe	4	0.019(0.014)	3.84(0.08)		
Fully Discharged (2.5 V)	Mn-O	6	0.018(0.020)	2.19(0.03)	0.07	6547.62
	Mn-P1	1	0.004(0.014)	2.88(0.09)		
	Mn-P2	4	0.007(0.007)	3.30(0.07)		
	Mn-Fe	4	0.014(0.012)	3.86(0.11)		

5.3.8. EXAFS Analysis for Flame Spray $LiMn_xFe_{(1-x)}PO_4$ (x=0.1,0.3)

5.3.8.1. Fe K-edge EXAFS for Flame Spray LMFP (0.1) and LMFP (0.3)

Tables 5-10 and 5-11 show the EXAFS fittings for the Fe K-edge $LiMn_xFe_{(1-x)}PO_4$ (x=0.1,0.3) samples synthesized via flame spray method.

Table 5-10: Fe K-edge EXAFS fittings for LMFP (0.1) flame spray for differently charged electrodes.

SoC	Bond	CN	σ^2	R	R-factor	E_0
FeO (Fe^{2+})				2.13		7121.17
Fe_2O_3 (Fe^{3+})				1.99		7125.59
Pristine (OCV 3.1 V)	Fe-O	6	0.003(0.003)	2.14(0.03)	0.02	7122.84
	Fe-P1	1	0.001	2.83(0.03)		
	Fe-P2	4	0.010(0.005)	3.25(0.04)		
	Fe-Fe	4	0.013(0.005)	3.83(0.05)		
Partial Charge (3.7 V)	Fe-O	6	0.012(0.006)	2.04(0.04)	0.01	7125.99
	Fe-P1	1	0.001	2.82(0.01)		
	Fe-P2	4	0.010(0.002)	3.17(0.02)		
	Fe-Fe	4	0.010(0.002)	3.78(0.02)		
Fully Charged (4.4 V)	Fe-O	6	0.009(0.004)	2.03(0.02)	0.01	7126.02
	Fe-P1	1	0.001	2.81(0.01)		
	Fe-P2	4	0.011(0.002)	3.18(0.02)		
	Fe-Fe	4	0.010(0.001)	3.79(0.02)		
Partial Discharge (3.5 V)	Fe-O	6	0.003(0.003)	2.11(0.03)	0.04	7122.47
	Fe-P1	1	0.001	2.85(0.03)		
	Fe-P2	4	0.011(0.005)	3.26(0.05)		
	Fe-Fe	4	0.014(0.007)	3.84(0.06)		

Fully Discharged (2.5 V)	Fe-O	6	0.004(0.006)	2.12(0.04)	0.03	7122.21
	Fe-P1	1	0.001	2.86(0.03)		
	Fe-P2	4	0.009(0.004)	3.25(0.05)		
	Fe-Fe	4	0.015(0.006)	3.85(0.06)		

Table 5-11: Fe K-edge EXAFS fittings for LMFP (0.3) flame spray for differently charged electrodes.

SoC	**Bond**	**CN**	**σ^2**	**R**	**R-factor**	**E_0**
FeO (Fe^{2+})				2.13		7121.17
Fe_2O_3 (Fe^{3+})				1.99		7125.59
Pristine (OCV 3.1 V)	Fe-O	6	0.008(0.004)	2.13(0.03)	0.01	7122.20
	Fe-P1	1	0.001	2.88(0.02)		
	Fe-P2	4	0.009(0.006)	3.21(0.04)		
	Fe-Fe	4	0.013(0.005)	3.83(0.05)		
Partial Charge (3.7 V)	Fe-O	6	0.010(0.010)	2.11(0.01)	0.06	7123.45
	Fe-P1	1	0.001	2.91(0.04)		
	Fe-P2	4	0.011(0.004)	3.19(0.04)		
	Fe-Fe	4	0.012(0.005)	3.81(0.05)		
Fully Charged (4.4 V)	Fe-O	6	0.009(0.004)	1.95(0.01)	0.01	7126.20
	Fe-P1	1	0.001	2.92(0.03)		
	Fe-P2	4	0.005(0.001)	3.17(0.01)		
	Fe-Fe	4	0.011(0.002)	3.76(0.02)		
Partial Discharge (3.5 V)	Fe-O	6	0.002(0.001)	2.09(0.01)	0.02	7123.33
	Fe-P1	1	0.001	2.85(0.01)		
	Fe-P2	4	0.015(0.004)	3.25(0.03)		
	Fe-Fe	4	0.014(0.003)	3.85(0.03)		

Fully Discharged (2.5 V)	Fe-O	6	0.004(0.002)	2.10(0.03)	0.05	7122.76
	Fe-P1	1	0.001	2.84(0.03)		
	Fe-P2	4	0.019(0.010)	3.27(0.08)		
	Fe-Fe	4	0.016(0.008)	3.88(0.07)		

EXAFS fittings for LMFP (0.1) and LMFP (0.3) are in accordance to the change in oxidation state of Fe as seen from the XANES spectra. The pristine states of both the samples have their Fe-O first shell average bond distance around 2.13-2.14 Å. As the cells are charged, the bond distance decreases to 2.03 Å and 1.95 Å for LMFP (0.1) and LMFP (0.3) respectively.

5.3.8.2. Mn K-edge EXAFS for Flame Spray LMFP (0.1) and LMFP (0.3)

Tables 5-12 and 5-13 show the EXAFS fittings for the Mn K-edge $LiMn_xFe_{(1-x)}PO_4$ (x=0.1,0.3) samples synthesized via flame spray method.

Table 5-12: Mn K-edge EXAFS fittings for LMFP (0.1) flame spray for differently charged electrodes.

SoC	**Bond**	**CN**	**σ^2**	**R**	**R-factor**	**E_0**
MnO (Mn^{2+})		6		2.19		6546.03
Mn_2O_3 (Mn^{3+})		6		2.04		6550.96
MnO_2 (Mn^{4+})		6		1.89		6554.49
Pristine (OCV 3.1 V)	Mn-O	6	0.002	2.14	0.05	6545.16
	Mn-P1	1	0.001	2.89		
	Mn-P2	4	0.002	3.27		
	Mn-Fe	4	0.010	3.84		
Partial Charge (3.7 V)	Mn-O	6	0.005	2.01	0.03	6546.07
	Mn-P1	1	0.001	2.84		

	Mn-P2	4	0.009	3.13		
	Mn-Fe	4	0.009	3.74		
Fully Charged (4.4 V)	Mn-O	6	0.005	2.00	0.04	6546.79
	Mn-P1	1	0.001	2.83		
	Mn-P2	4	0.008	3.13		
	Mn-Fe	4	0.009	3.74		
Partial Discharge (3.5 V)	Mn-O	6	0.009	2.12	0.03	6546.07
	Mn-P1	1	0.001	2.86		
	Mn-P2	4	0.005	3.25		
	Mn-Fe	4	0.014	3.82		
Fully Discharged (2.5 V)	Mn-O	6	0.010	2.14	0.03	6545.04
	Mn-P1	1	0.005	2.88		
	Mn-P2	4	0.007	3.25		
	Mn-Fe	4	0.013	3.84		

Table 5-13: Mn K-edge EXAFS fittings for LMFP (0.3) flame spray for differently charged electrodes.

SoC	**Bond**	**CN**	**σ^2**	**R**	**R-factor**	**E_0**
MnO (Mn^{2+})		6		2.19		6546.03
Mn_2O_3 (Mn^{3+})		6		2.04		6550.96
MnO_2 (Mn^{4+})		6		1.89		6554.49
Pristine (OCV 3.1 V)	Mn-O	6	0.004	2.14	0.1	6546.81
	Mn-P1	1	0.002	2.75		
	Mn-P2	4	0.004	3.32		
	Mn-Fe	4	0.011	3.85		
Partial Charge (3.7 V)	Mn-O	6	0.005	2.09	0.09	6548.00
	Mn-P1	1	0.010	2.80		

	Mn-P2	4	0.007	3.27		
	Mn-Fe	4	0.015	3.85		
Fully Charged (4.4 V)	Mn-O	6	0.001	1.95	0.04	6548.02
	Mn-P1	1	0.001	2.86		
	Mn-P2	4	0.010	3.07		
	Mn-Fe	4	0.011	3.66		
Partial Discharge (3.5 V)	Mn-O	6	0.010	2.06	0.1	6547.69
	Mn-P1	1	0.012	2.83		
	Mn-P2	4	0.007	3.28		
	Mn-Fe	4	0.014	3.66		
Fully Discharged (2.5 V)	Mn-O	6	0.013	2.15	0.05	6546.39
	Mn-P1	1	0.001	2.83		
	Mn-P2	4	0.003	3.31		
	Mn-Fe	4	0.006	3.89		

Both LMFP (0.1) and LMFP (0.3) show same Mn-O bond distance of 2.14 Å at their pristine states. As they are charged the bond lengths decrease to 2.00 Å and 1.95 Å respectively. While there is no change observed in the oxidation change of Mn from the XANES spectra, the change in bond lengths can be attributed to the change in spin state for Mn, similar to what is seen for the ball-milled samples as well.

5.4. Conclusions

This chapter dwells on the structure and performance of manganese doped lithium iron phosphate materials. The previous chapter described how the structure of lithium iron phosphate (LFP) changes with cycling and the major characterization tool used to analyze the battery material is X-ray Absorption Spectroscopy (XAS). Once this methodology was established using LFP, it was further extended to analyze similar battery materials. This chapter focused on Mn-doped LFP structures, especially low Mn content doping. Two synthesis processes were used to prepare the materials – ball milling and flame spray. The idea was to realize which synthesis process gives a better performing material. Three differently doped Mn-LFP systems are looked into – $LiMn_{0.1}Fe_{0.9}PO_4$, $LiMn_{0.3}Fe_{0.7}PO_4$ and $LiMn_{0.5}Fe_{0.5}PO_4$. Each material was prepared into electrodes and cycled for 10 cycles before doing the structural analysis using XAS. The DMC method of *ex-situ* approach, similar to the previous chapter, was used for all the materials in this chapter as well. XAS studies were conducted for both the transition metals, Fe and Mn, as well as phosphorus edge of the phosphate polyanion.

Fe K-edge for all the synthesized $LiMn_{0.1}Fe_{0.9}PO_4$, $LiMn_{0.3}Fe_{0.7}PO_4$ and $LiMn_{0.5}Fe_{0.5}PO_4$ electrodes showed Fe edge shifting towards higher energy with charge, suggesting that Fe in all the materials change valence from Fe^{2+} to Fe^{3+} on charging and back to Fe^{2+} on discharging. EXAFS fittings for Fe K-edge electrodes, which were stopped at different potentials for data collection, also showed changes in the bond lengths with cycling, in harmony with the XANES valence change. XANES for Mn K-edge for all the electrodes, however, did not show similar changes. While for $LiMn_{0.1}Fe_{0.9}PO_4$ and $LiMn_{0.3}Fe_{0.7}PO_4$ electrodes, no change in Mn valence was observed, but for $LiMn_{0.5}Fe_{0.5}PO_4$ the fully charged state shows a shift in the Mn valence from Mn^{2+} to almost Mn^{3+}, but not completely at 3+ state. The EXAFS fittings, surprisingly, showed changes in the first shell Mn-O bond lengths in all the three different materials. For $LiMn_{0.5}Fe_{0.5}PO_4$, the change in bond length corresponds to the shift in the valence of Mn due to the Mn^{2+}/Mn^{3+} redox reactions, but for $LiMn_{0.1}Fe_{0.9}PO_4$ and $LiMn_{0.3}Fe_{0.7}PO_4$ electrodes, even though there was no change in the oxidation state, the change in the bond lengths have been assigned to change in the Mn spin state from high to low spin with cycling. Even though both ball milled and flame spray samples showed similar variations, the EXAFS results showed a better reversibility in the ball milled samples and the electrochemistry data showed ball milled to have better capacity compared to the flame spray.

References

[1]. Chung, S.Y., J.T. Bloking, and Y.M. Chiang, Electronically conductive phospho-olivines as lithium storage electrodes. Nature Materials, **2002** 1 (2):p. 123-128.

[2]. Nakamura, T., Y. Miwa, M. Tabuchi, and Y. Yamada, Structural and surface modifications of $LiFePO_4$ olivine particles and their electrochemical properties. Journal of the Electrochemical Society, **2006** 153 (6):p. A1108-A1114.

[3]. Padhi, A.K., K.S. Nanjundaswamy, and J.B. Goodenough, Phospho-olivines as positive-electrode materials for rechargeable lithium batteries. Journal of the Electrochemical Society, **1997** 144 (4):p. 1188-1194.

[4]. Yamada, A. and S.C. Chung, Crystal chemistry of the olivine-type $Li(MnyFe_{1-y)}PO_4$ and $(Mn_yFe_{1-y})PO_4$ as possible 4 V cathode materials for lithium batteries. Journal of the Electrochemical Society, **2001** 148 (8):p. A960-A967.

[5]. Yamada, A., M. Hosoya, S.C. Chung, Y. Kudo, K. Hinokuma, K.Y. Liu, and Y. Nishi, Olivine-type cathodes achievements and problems. Journal of Power Sources, **2003** 119:p. 232-238.

[6]. Yonemura, M., A. Yamada, Y. Takei, N. Sonoyama, and R. Kanno, Comparative kinetic study of olivine Li_xMPO_4 (M = Fe, Mn). Journal of the Electrochemical Society, **2004** 151 (9):p. A1352-A1356.

[7]. Drezen, T., N.H. Kwon, P. Bowen, I. Teerlinck, M. Isono, and I. Exnar, Effect of particle size on LiMnPO4 cathodes. Journal of Power Sources, **2007** 174 (2):p. 949-953.

[8]. Kwon, N.H., T. Drezen, I. Exnar, I. Teerlinck, M. Isono, and M. Graetzel, Enhanced electrochemical performance of mesoparticulate $LiMnPO_4$ for lithium ion batteries. Electrochemical and Solid State Letters, **2006** 9 (6):p. A277-A280.

[9]. Dell'Era, A., M. Pasquali, E.M. Bauer, S.V. Ciprioti, F.A. Scaramuzzo, and C. Lupi, Synthesis, Characterization, and Electrochemical Behavior of $LiMn_xFe_{(1-x)}PO_4$ Composites Obtained from Phenylphosphonate-Based Organic-Inorganic Hybrids. Materials, **2018** 11 (1):p.

[10]. Ding, J., Z. Su, and H.L. Tian, Synthesis of high rate performance $LiFe_{1-x}MnxPO4/C$ composites for lithium-ion batteries. Ceramics International, **2016** 42 (10):p. 12435-12440.

[11]. Li, X.Y., B. Zhang, Z.G. Zhang, L.H. He, H. Li, X.J. Huang, and F.W. Wang, Crystallographic structure of $LiFe_{1-x}Mn_xPO_4$ solid solutions studied by neutron powder diffraction. Powder Diffraction, **2014** 29 (3):p. 248-253.

[12]. Yoncheva, M., V. Koleva, M. Mladenov, M. Sendova-Vassileva, M. Nikolaeva-Dimitrova, R. Stoyanova, and E. Zhecheva, Carbon-coated nano-sized $LiFe_{(1-x)}$ $Mn_{(x)}$ $PO_{(4)}$ solid solutions (0 a parts per thousand currency sign x a parts per thousand currency sign 1) obtained from phosphate-formate precursors. Journal of Materials Science, **2011** 46 (22):p. 7082-7089.

[13]. Zhang, B., X.J. Wang, H. Li, and X.J. Huang, Electrochemical performances of $LiFe_{1-x}Mn_xPO_4$ with high Mn content. Journal of Power Sources, **2011** 196 (16):p. 6992-6996.

[14]. Molenda, J., W. Qjczyk, and J. Marzec, Electrical conductivity and reaction with lithium of $LiFe_{(1-y)}Mn_{(y)}PO_{(4)}$ olivine-type cathode materials. Journal of Power Sources, **2007** 174 (2):p. 689-694.

[15]. Wang, G.P., L. Zhang, and J.J. Zhang, A review of electrode materials for electrochemical supercapacitors. Chemical Society Reviews, **2012** 41 (2):p. 797-828.

[16]. Martha, S.K., B. Markovsky, J. Grinblat, Y. Gofer, O. Haik, E. Zinigrad, D. Aurbach, T. Drezen, D. Wang, G. Deghenghi, and I. Exnar, $LiMnPO_4$ as an Advanced Cathode Material for Rechargeable Lithium Batteries. Journal of the Electrochemical Society, **2009** 156 (7):p. A541-A552.

[17]. Wang, H.L., Y. Yang, Y.Y. Liang, L.F. Cui, H.S. Casalongue, Y.G. Li, G.S. Hong, Y. Cui, and H.J. Dai, $LiMn_{1-x}Fe_xPO_4$ Nanorods Grown on Graphene Sheets for Ultrahigh-Rate-Performance Lithium Ion Batteries. Angewandte Chemie-International Edition, **2011** 50 (32):p. 7364-7368.

[18]. Zaghib, K., M. Trudeau, A. Guerfi, J. Trottier, A. Mauger, R. Veillette, and C.M. Julien, New advanced cathode material: $LiMnPO_4$ encapsulated with $LiFePO_4$. Journal of Power Sources, **2012** 204:p. 177-181.

[19]. Bini, M., M.C. Mozzati, P. Galinetto, D. Capsoni, S. Ferrari, M.S. Grandi, and V. Massarotti, Structural, spectroscopic and magnetic investigation of the $LiFe_{1-x}Mn_xPO_4$ (x=0-0.18) solid solution. Journal of Solid State Chemistry, **2009** 182 (7):p. 1972-1981.

[20]. Bramnik, N.N., K.G. Bramnik, K. Nikolowski, M. Hinterstein, C. Baehtz, and H. Ehrenberg, Synchrotron diffraction study of lithium extraction from $LiMn_{0.6}Fe_{0.4}PO_4$. Electrochemical and Solid State Letters, **2005** 8 (8):p. A379-A381.

[21]. Koleva, V., R. Stoyanova, and E. Zhecheva, Nano-crystalline $LiMnPO_4$ prepared by a new phosphate-formate precursor method. Materials Chemistry and Physics, **2010** 121 (1-2):p. 370-377.

[22]. Kopec, M., A. Yamada, G. Kobayashi, S. Nishimura, R. Kanno, A. Mauger, F. Gendron, and C.M. Julien, Structural and magnetic properties of $Li_{-x}(Mn_yFe_{1-y})PO_4$ electrode materials for Li-ion batteries. Journal of Power Sources, **2009** 189 (2):p. 1154-1163.

[23]. Nakamura, T., K. Sakumoto, M. Okamoto, S. Seki, Y. Kobayashi, T. Takeuchi, M. Tabuchi, and Y. Yamada, Electrochemical study on $Mn(^{2+})$-substitution in $LiFePO_{(4)}$ olivine compound. Journal of Power Sources, **2007** 174 (2):p. 435-441.

[24]. Wei, Y.J., G.C. Liang, L. Wang, and X.Q. Ou, Synthesis and electrochemical performance of $LiFe_{1-x}Mn_xPO_4$/C cathode material. Renewable and Sustainable Energy, Pts 1-7, **2012** 347-353:p. 3434-3438.

[25]. Yamada, A., Y. Kudo, and K.Y. Liu, Phase diagram of $Li_{-x}(Mn_yFe_{1-y})PO_4$ (0 <= x, y <= 1). Journal of the Electrochemical Society, **2001** 148 (10):p. A1153-A1158.

[26]. Liu, H., Q. Cao, L.J. Fu, C. Li, Y.P. Wu, and H.Q. Wu, Doping effects of zinc on $LiFePO_4$ cathode material for lithium ion batteries. Electrochemistry Communications, **2006** 8 (10):p. 1553-1557.

[27]. Shannon, R.D., Revised Effective Ionic-Radii and Systematic Studies of Interatomic Distances in Halides and Chalcogenides. Acta Crystallographica Section A, **1976** 32 (Sep1):p. 751-767.

[28]. Triwibowo, J., S. Priyono, R.I. Purawiardi, C.R. Ratri, and E. Suwandi, Electrochemical Performance Of $LiFe_{(1-x)}$ $Mn_xPO_{(4)}$ (x=0, 0.10, 0.15, 0.2) Synthesized By Solid State Process As Cathode Material For Li-ion Battery. 2nd Padjadjaran International Physics Symposium 2015 (Pips-2015): Materials Functionalization and Energy Conservations, **2016** 1712:p.

[29]. Brown, I.D. and R.D. Shannon, Empirical Bond-Strength Bond-Length Curves for Oxides. Acta Crystallographica Section A, **1973** A 29 (May1):p. 266-282.

[30]. Tailhades, P., A. Rousset, R. Bendaoud, A.R. Fert, and B. Gillot, Structural Study of New Manganese Defect Ferrites. Materials Chemistry and Physics, **1987** 17 (6):p. 521-529.

[31]. Wada, N., M.K. , T.S. , K.O. , K.K. , and Y.I. , Mn-O bond length in oxide glasses.p.

[32]. Sarmiento-Perez, R., S. Botti, C.S. Schnohr, I. Lauermann, A. Rubio, and B. Johnson, Local versus global electronic properties of chalcopyrite alloys: X-ray absorption spectroscopy and ab initio calculations. Journal of Applied Physics, **2014** 116 (9):p.

[33]. Yoon, W.S., C.P. Grey, M. Balasubramanian, X.Q. Yang, and J. McBreen, In situ X-ray absorption spectroscopic study on $LiNi_{0.5}Mn_{0.5}O_2$ cathode material during electrochemical cycling. Chemistry of Materials, **2003** 15 (16):p. 3161-3169.

[34]. Ammundsen, B., J. Paulsen, I. Davidson, R.S. Liu, C.H. Shen, J.M. Chen, L.Y. Jang, and J.F. Lee, Local structure and first cycle redox mechanism of layered $Li_{1.2}Cr_{0.4}Mn_{0.4}O_2$ cathode material. Journal of the Electrochemical Society, **2002** 149 (4):p. A431-A436.

[35]. Balasubramanian, M., J. McBreen, I.J. Davidson, P.S. Whitfield, and I. Kargina, In situ X-ray absorption study of a layered manganese-chromium oxide-based cathode material. Journal of the Electrochemical Society, **2002** 149 (2):p. A176-A184.

[36]. Fridrichova, J., P. Bacik, A. Ertl, M. Wildner, J. Dekan, and M. Miglierini, Jahn-Teller distortion of Mn^{3+}-occupied octahedra in red beryl from Utah indicated by optical spectroscopy. Journal of Molecular Structure, **2018** 1152:p. 79-86.

[37]. Iadecola, A., A. Perea, L. Aldon, G. Aquilanti, and L. Stievano, Li deinsertion mechanism and Jahn-Teller distortion in $LiFe_{0.75}Mn_{0.25}PO_4$: an operando x-ray absorption spectroscopy investigation. Journal of Physics D-Applied Physics, **2017** 50 (14):p.

[38]. Liu, W.W., D. Wang, Z.F. Wang, J.G. Deng, W.M. Lau, and Y.N. Zhang, Influence of magnetic ordering and Jahn-Teller distortion on the lithiation process of LiMn2O4. Physical Chemistry Chemical Physics, **2017** 19 (9):p. 6481-6486.

[39]. Nie, Z.X., C.Y. Ouyang, J.Z. Chen, Z.Y. Zhong, Y.L. Du, D.S. Liu, S.Q. Shi, and M.S. Lei, First principles study of Jahn-Teller effects in Li_xMnPO_4. Solid State Communications, **2010** 150 (1-2):p. 40-44.

[40]. Ning, F.H., B. Xu, J. Shi, H.B. Su, M.S. Wu, G. Liu, and C.Y. Ouyang, Ab initio investigation of Jahn-Teller-distortion-tuned Li-ion migration in λ-MnO_2. Journal of Materials Chemistry A, **2017** 5 (20):p. 9618-9626.

[41]. Ouyang, C.Y., S.Q. Shi, and M.S. Lei, Jahn-Teller distortion and electronic structure of $LiMn_2O_4$. Journal of Alloys and Compounds, **2009** 474 (1-2):p. 370-374.

[42]. Piper, L.F.J., N.F. Quackenbush, S. Sallis, D.O. Scanlon, G.W. Watson, K.W. Nam, X.Q. Yang, K.E. Smith, F. Omenya, N.A. Chernova, and M.S. Whittingham, Elucidating the Nature of Pseudo Jahn-Teller Distortions in Li_xMnPO_4: Combining Density Functional Theory with Soft and Hard X-ray Spectroscopy. Journal of Physical Chemistry C, **2013** 117 (20):p. 10383-10396.

[43]. Radin, M.D. and A. Van der Ven, Simulating Charge, Spin, and Orbital Ordering: Application to Jahn-Teller Distortions in Layered Transition-Metal Oxides. Chemistry of Materials, **2018** 30 (3):p. 607-618.

[44]. Ramos, A.Y., H.C.N. Tolentino, M.M. Soares, S. Grenier, O. Bunau, Y. Joly, F. Baudelet, F. Wilhelm, A. Rogalev, R.A. Souza, N.M. Souza-Neto, O. Proux, D. Testemale, and A. Caneiro, Emergence of ferromagnetism and Jahn-Teller distortion in $LaMn_{1-x}Cr_xO_3$ ($x < 0.15$). Physical Review B, **2013** 87 (22):p.

[45]. Sahu, A.K. and G.C. Rout, Interplay of Dynamic Jahn-Teller Distortion and the Spin-Phonon Interaction in Manganites. Advanced Science Letters, **2014** 20 (3-4):p. 816-819.

[46]. Vilarinho, R., D.J. Passos, E.C. Queiros, P.B. Tavares, A. Almeida, M.C. Weber, M. Guennou, J. Kreisel, and J.A. Moreira, Suppression of the cooperative Jahn-Teller distortion and its effect on the Raman octahedra-rotation modes of TbMn1-xFexO3. Physical Review B, **2018** 97 (14):p.

[47]. Padhi, A.K., W.B. Archibald, K.S. Nanjundaswamy, and J.B. Goodenough, Ambient and high-pressure structures of $LiMnVO_4$ and its Mn^{3+}/Mn^{2+} redox energy. Journal of Solid State Chemistry, **1997** 128 (2):p. 267-272.

[48]. Mays, J.M., Nuclear Magnetic Resonances and Mn-O-P-O-Mn Superexchange Linkages in Paramagnetic and Antiferromagnetic Limnpo4. Physical Review, **1963** 131 (1):p. 38-&.

[49]. Sherman, D.M., The Electronic-Structures of Manganese Oxide Minerals. American Mineralogist, **1984** 69 (7-8):p. 788-799.

Chapter 6

Sulphate-based Cathode Materials for Li-ion Batteries

Following on from the success of phosphate $(PO_4)^{3-}$ *containing cathodes for Li-ion batteries, effort is now being made to study the effect of sulphate* $(SO_4)^{2-}$ *based cathodes, particularly those containing established and abundantly available transition metals (Fe, Mn, Co), which are shown to display higher potential compared to the phosphate-containing analogues. In this chapter,* $Li_2Mn(SO_4)_2$ *(LMS) was synthesized by ball milling and cycled to different potential points on the charge-discharge curve. Structural analysis was carried out using X-ray diffraction (XRD), X-ray Photoelectron Spectroscopy (XPS) and ex-situ X-ray Absorption Spectroscopy (XAS) on the Mn and S edges to investigate the local geometry around the absorbing atoms. Both near and fine structure absorption spectroscopy was utilized to study the change in oxidation state and bond distance as the material was cycled. Both XAS and XPS showed the difference in results, which can be attributed to the fact that LMS behaves differently in bulk and surface modes during cycling.*

***Chapter 7 is accepted as a journal article at ACS Omega, as "Electronic and Geometric Structures of Rechargeable Lithium Manganese Sulphate Cathode $Li_2Mn(SO_4)_2$"; Disha Gupta, Aravind Muthiah, Do Minh Phuong, Sankar Gopinathan, Timothy I. Hyde, Mark Copley, Tom Baikie, Yonghua Du, Shibo Xi, Madhavi Srinivasan, ZhiLi Dong.**

6. Introduction

6.1. Background

Sulphates and fluorosulphates have traditionally demonstrated electrochemical activity only in Fe based compounds. Among the sulphate-based positive-electrode materials the sulphates synthesized through solid-state reactions have shown highest redox potentials for Fe at 3.83 V (vs. Li) [1], second only to the ionothermally synthesized fluorosulphate analogue which shows 3.90 V (vs. Li) [2]. The high voltages achieved with Fe were attributed to the inductive effect of the highly electronegative sulphate group [3] and subsequently, Co, Mn and Ni which traditionally provided for operation at higher voltages were investigated [4, 5]. However, despite atomistic modelling/Density Functional Theory (DFT) techniques predicting the redox potential versus Li to be 5.2 V for Co and 4.54 V for Mn systems[6], none of these elements showed electrochemical activity in the conventional voltage window between 3 and 4.8 V (vs. Li). The absence of activity was largely attributed to the possibility of Jahn-Teller distortion [7] in the case of Mn and the absence of stable electrolytes operational at high voltage as in the case of Co.

The most feasible candidate for exploring a high voltage range with minimal modification to commercially used electrolyte components was determined with a co-solvent called sebaconitrile. Sebaconitrile has previously [8] been shown to exhibit good electrochemical stability beyond 6 V vs. Li in an EC: DMC (ethylene carbonate: dimethyl carbonate) based electrolyte. Sebaconitrile was later used to assess the performance of an alternative Co based polyanionic cathode, $LiCoPO_4$ and it was found to lead to higher insertion potential of lithium owing to slower kinetics due to the sebaconitrile co-solvent [9]. The viability of its use with polyanionic systems, therefore, made sebaconitrile a suitable candidate to trial with sulphate-based cathodes as well. Subsequently, $Li_2M(SO_4)_2$ (M=Co, Mn) was electrochemically analyzed with this electrolyte.

One of the main advantages of using X-ray Absorption Spectroscopy (XAS) is that it is element-specific, which allows the determination of both electronic and geometric structures of the target element of interest within the electrodes [10-15]. Previous reports from our laboratory [16] on the performance of the $Li_2Mn(SO_4)_2$ (LMS) cathode was limited to demonstration of its electrochemical activity. Here it's aimed to understand if the electronic and geometric changes associated with the redox reactions are similar to $Li_2Fe(SO_4)_2$ (LFS), where a $Fe^{2+}/^{3+}$ redox couple was observed through XAS analysis [17]. A similar *ex-situ* XAS analysis was carried out on the LMS cathode and further confirmation was sought through an *ex-situ* XPS analysis of the material before and after cycling.

6.2. Experimental Methods

6.2.1. Material Synthesis

For the synthesis of LMS, $MnSO_4$ anhydrous and Li_2SO_4 (5% excess) were used as precursors. Anhydrous $MnSO_4$ and Li_2SO_4 were prepared by heating $MnSO_4.H_2O$ and $Li_2SO_4.H_2O$ (Sigma Aldrich) in a tube furnace under argon gas glow for about 1 hour. $MnSO_4 \cdot H_2O$ was dehydrated at 300°C and $Li_2SO_4 \cdot H_2O$ at 200°C. The anhydrous phases were then mixed in a ratio of around 1.3:1 by weight respectively. The powders were then ball milled in a SPEX 8000M high-energy ball mill for 30 mins in a stainless steel vial. The powder obtained after ball milling was ground in a mortar and pestle and pressed into a pellet of 20mm diameter using a pelletizer at a pressure of 8 MPa. The pellet was then annealed in a box furnace for 12 hours at 500°C with a temperature ramp of $5°C.min^{-1}$. After annealing, the pellet was ground into fine powder again and annealed under the same conditions. Finally, the pellet was ground before carrying out structural analysis. The powder was stored in an Ar-filled glovebox to prevent moisture absorption, as the material is sensitive to degradation by moisture.

6.2.2. Electrode Preparation

For the preparation of the electrode, the LMS powder was mixed with Super P carbon in the ratio of 80:20 (powder: carbon) and dried under vacuum in a Buchi oven for a couple of hours. The dried mixture was then placed in a tungsten carbide vial and ball milled in a SPEX 8000D Mixer/Mill high energy ball mill for 20 hours, with 10mins of cooling after each hour. The milling was done in a tungsten carbide vial to avoid Ni contamination, which would otherwise occur in the case of a stainless steel vial. The ball-milled powder was then dried at around 250˚C in a Buchi oven for another 4 hours before storing inside an Ar-filled glove box.

6.2.3. Electrolyte Preparation

The electrolyte used for the cell assembly of these electrodes can be synthesized using two different salts – $LiPF_6$ or $LiClO_4$. A 1M solution of $LiPF_6/LiClO_4$ was prepared with a solvent of ethylene carbonate (EC): dimethyl carbonate (DMC) and sebaconitrile (15:15:70 by volume). The solution was stirred overnight inside an argon glove box.

6.2.4. Cell Assembly

The electrochemical tests were carried out in a half-cell configuration using a coin cell (3V 20 X 1.6 mm 90mAh). Unlike the usual process of having an electrode coating over an aluminium base, the carbon-coated LMS powder was placed directly over the positive case as the working cathode. Lithium foil was used as the counter and reference electrode. The loading of the active material was 4 $mg{\cdot}cm^{-2}$. Two pieces of porous glass microfiber (Whatman cat. no. 1825-047, U.K.) were used as the separator and soaked in the electrolyte solution. Cyclic voltammetry tests using Solartron Analytical were carried out at a scan rate of 0.05 $mV.s^{-1}$ between a range of 4.2 V and 5.2 V for LMS.

6.2.5. X-ray photoelectron spectroscopy (XPS) and X-ray Absorption Spectroscopy (XAS) Analysis

The electrode was then scraped off in powder form, sealed and then transferred to the XPS chamber. XPS experiments were carried out using a PHI5802 Multitechnique spectrometer and each spectrum was collected after 1 min Ar+ sputtering. The samples for XAS measurements were prepared by charging (or discharging) the electrode in a Swagelok© cell to certain charge (or discharge) states followed by disassembly in the glove box. The electrode was then scraped off in powder form, sealed and then transferred to an XAS sample holder The polypropylene tape-sealed electrodes, along with the representative manganese oxide and sulphate standards, were measured at the XAFCA beamline [18] of the Singapore Synchrotron Light Source (SSLS). The X-ray energy was calibrated at the inflexion point of the absorption edge of manganese and sulphur foil for Mn and S-K edge respectively. All XAS measurements were conducted at a ring energy 0.7 GeV and ring current of ca. 200 mA. A Si (111) crystal monochromator was used and data was collected for both Mn- and S-K edge at ambient temperature and pressure. For Mn-Kedge, the data were collected on XAFCA in Quick EXAFS transmission mode with an ion chamber detector, in the range of 6418 and 7088 eV and a typical scan time of 180 seconds. Multiple scans were done to improve the data quality and signal-to-noise ratio. For S-K edge, the data were collected in fluorescence mode with a silicon drift detector, in the range of 2392 and 2551 eV, and a scan time of 20 minutes per scan for 3 scans. XAS data of reference compounds ($MnSO_4$, Mn_2O_3) were collected using ca. 5mg of respective powders mixed with ca. 10mg of boron nitride and pressed into a 10mm diameter pellet which was mounted onto the sample holder for XAS measurements in either transmission (Mn-K edge) and fluorescence (S- K edge) mode. The Mn- and S-K edge X-ray absorption near edge structure (XANES) and Extended X-ray absorption fine structure (EXAFS) data analysis were carried out with Athena and Artemis software included in the Demeter package for XAS analysis. [19, 20] The background correction for the XAS data was done in ATHENA before importing it to ARTEMIS for the structural modelling of the data. Mn K-edge XAS was fitted between k range = 3.16 and 9.5 Å-1 and r range = 1.5 and 3.4 Å with k-weight = 1,2,3.

6.3. Results and Discussion

6.3.1. Powder X-ray Diffraction

Sample purity was established and structural refinements carried out from powder X-ray diffraction (PXRD) patterns collected with a Bruker D8 diffractometer (Bragg-Brentano geometry) equipped with a Cu Kα X-ray tube operated at 40kV and 40mA. The as-prepared sample was mounted in a top-loaded sample holder with data accumulated from 10-80° 2θ using a step size of 0.02° and a dwell time of 2s per step. Rietveld refinement of the XRD data was carried out with TOPAS V4.1 (Bruker, 2008), using the fundamental parameters approach (Cheary & Coelho, 1992).

Figure 6-1 shows the XRD pattern for LMS pristine powder. Rietveld analysis of LMS powder gives lattice parameters a=5.459(5) Å, b= 4.838(5) Å, c= 8.249(11) Å, α=γ=90˚, β= 106.30(10)˚ and in the monoclinic spacegroup P21/c (No.14). During the analysis, there is a partial decomposition of the LMS to $Li_2SO_4.H_2O$ and $MnSO_4.H_2O$ (both less than 5%). This is consistent with what is reported in [21] that it hydrolyses over time when exposed to air and probably occurred while the XRD data was being collected in an ambient environment. **Figure 6-2** shows a structural representation of LMS indicating the MnO_6 & SO_4 octahedra and tetrahedra respectively and the coordination of the Li ions between these units.

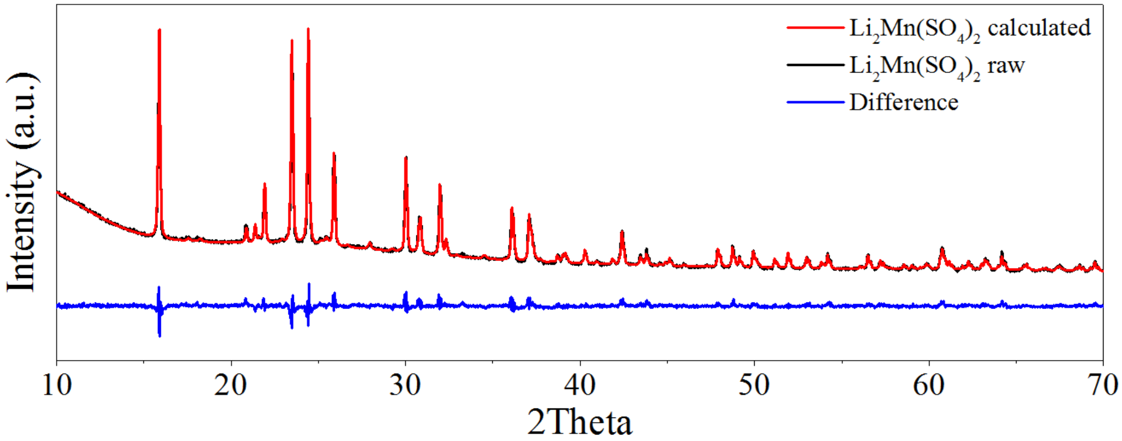

Figure 6-1 XRD pattern (red) of LMS as prepared powder sample resulting in similar reference pattern as observed in [21]

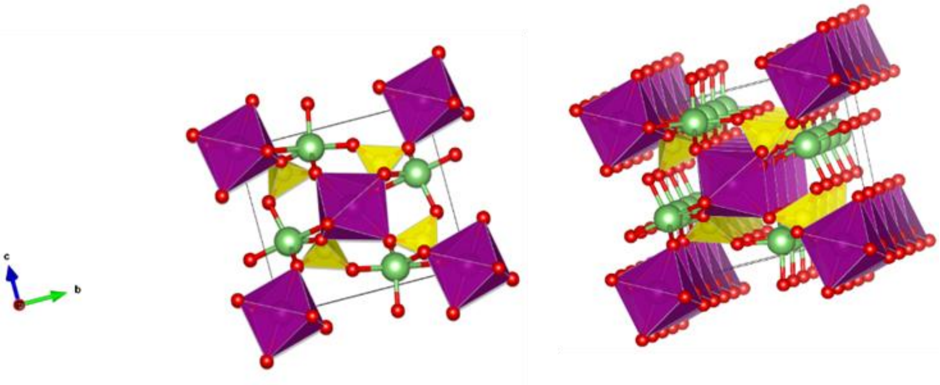

Figure 6-2 Structure of LMS obtained from literature where MnO6 is denoted by the octahedra (purple), SO4 is signified by the tetrahedra (yellow), lithium ions are represented by (green) dots and oxygen atoms is shown by the (red) small dots.

6.3.2. Electrochemistry

Figure 6-3 shows the cyclic voltammetry data illustrating the reversible electrochemical activity of LMS; please note that the ratios of electrolyte are different compared to the earlier report and these procedures were used for both XAS and XPS studies. .Oxidation and reduction peaks are observed at 5.17 V and 4.57 V, respectively. This trend in electrochemical performance is similar to a previous report [16] wherein the focus was on bimetallic sulphate systems. Even though the redox species concentration is small, the reversibility is indicated by a consistent current intensity of the reduction peak ~ 4.6 V vs Li.

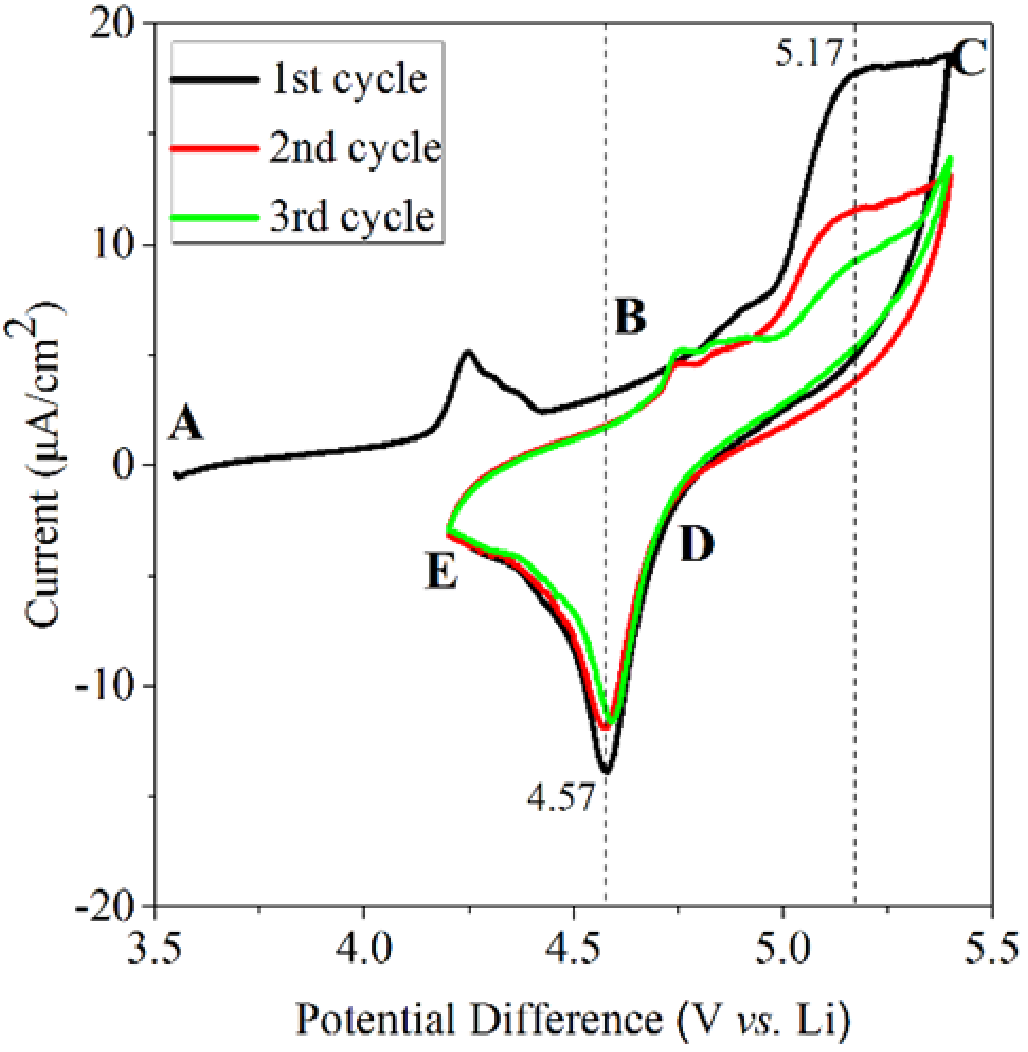

Figure 6-3 CV of $Li_2Mn(SO_4)_2$ (LMS) carried out with an electrolyte of 1M $LiPF_6$ in EC:DMC: Sebaconitrile (15:15:70) vol%

Table 6-1: The different LMS electrode details with their cut off potentials and state of charge-discharge are given in the table below.

Electrode	Charge state	Potential (w.r.t. Li) (V)
A	Pristine electrode, open circuit voltage	3.5
B	Partial Charged	4.7
C	Fully Charged	5.4
D	Partial Discharged	4.7
E	Full Discharged	4.2

6.3.3. XAS Analysis

In order to understand the structural changes occurring during the cycling process in the LMS electrodes, various potentials were chosen along the charge-discharge curve as shown in **Table 6-1**. The electrodes were electrochemically charged and discharged to these potentials as mentioned in the table. The cells were then dis-assembled in an Ar-filled glovebox and the electrodes were extracted for XAS studies. *Ex-situ* XAS studies were then conducted on all these electrodes at the Mn- and S-K edges.

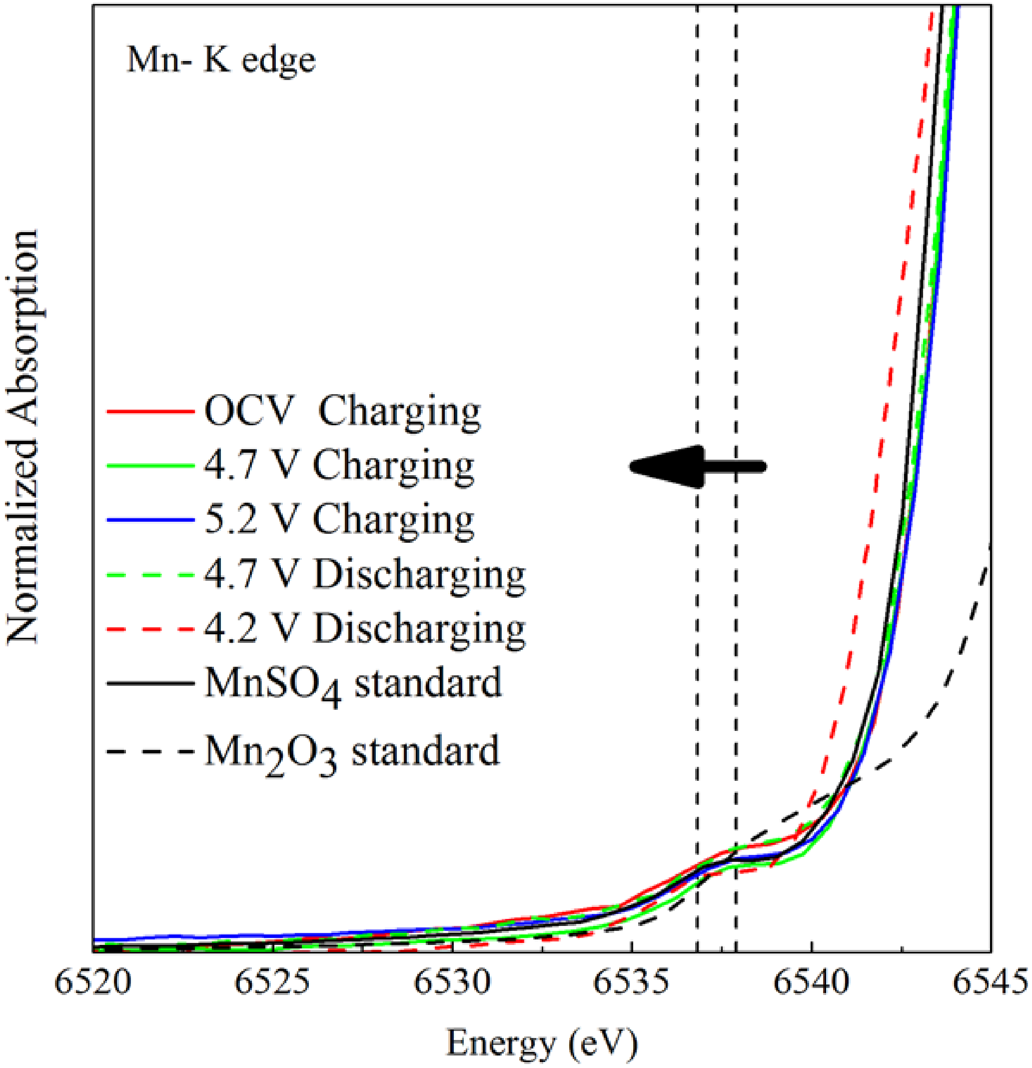

Figure 6-4 Pre-edge peak positions of Mn K-edge for LMS electrodes cut off at different potentials can be seen during one entire electrochemical cycle, along with the reference standards $MnSO_4$ (black) and Mn_2O_3 (black dashed) for comparison

6.3.3.1. Mn and S K-edge XANES Analysis

Normalised Mn K-edge XANES data along with Mn (II) and Mn (III) reference compounds are shown in **Figure 6-5 (a).** The pre-edge part of the data is explained first, followed by the changes that are observed in the main absorption edge. The pre-edge for the Mn K-edge pristine sample can be seen to appear at around 6537.9 eV, which is commonly assigned to a 1s to 3d transition, and although it is disallowed by selection rule, it is observed in many transition metal ions containing systems. The reason they appear is a combination of coordination environments and mixing of the d and p orbitals [27, 28]. Negligible change is observed in the pre-edge feature during the charging process (**Figure 6-4**). Also, the pre-edge feature is weak, implying that Mn is mostly in an octahedral coordination environment [29]. Furthermore, no shift is observed in the absorption edge (which is typically seen if there is a change in oxidation state of the element of interest) suggesting that there is no significant change in the Mn (II) oxidation state. An attempt was made to analyse the shift using the first derivation of the XANES data. The main inflexion point shows a shift of 0.4 eV, which is too small to interpret as a change in the oxidation state (**Figure 6-6**). However, changes were observed in the white line intensity of the main absorption **(Figure 6-5(b-c))** with charge and discharge respectively. The white line intensity results from strong transitions to final states confined to the near vicinity of the absorbing atom. In general for a K-edge spectrum, the systems which have octahedral coordination show the highest intensity, whereas the tetrahedrally coordinated systems show the lowest intensity [30]. It has been observed that deviation from perfect octahedral coordination can result in a decrease in the white line intensity. Therefore, the decrease in the intensity and broadening of the peak, are likely due to an increasing disorder in the system[31]. Thus, for LMS, a decrease is observed in the white line intensity as the electrode is charged. However, as the electrode undergoes discharge, the white line intensity appears to increase further beyond the pristine sample. This indicates that there is a possibility that the structure of LMS is more ordered in its fully discharged state than it was in the starting material.

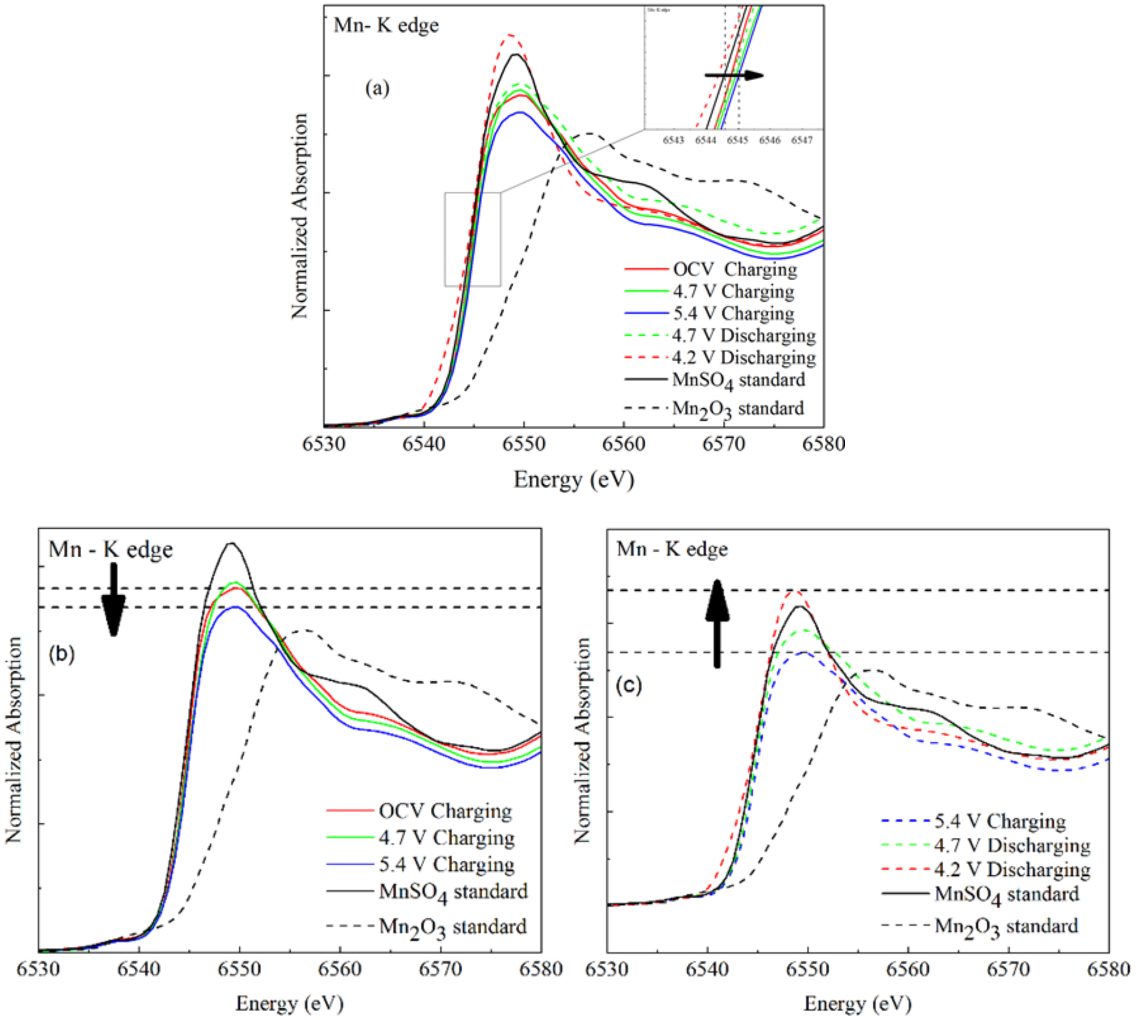

Figure 6-5 Normalized XANES plots of the main absorption peak of Mn K-edge for LMS electrodes stopped at different potential points are shown in (a). The difference in the white line intensity of the normalized XANES plots of the main absorption peak of Mn K-edge for LMS electrodes charged to different potentials are shown in (b) and (c). During the charge cycle (b), the white line intensity shifts slightly downwards but for the discharge (c), the intensity increases even beyond that of the starting material.

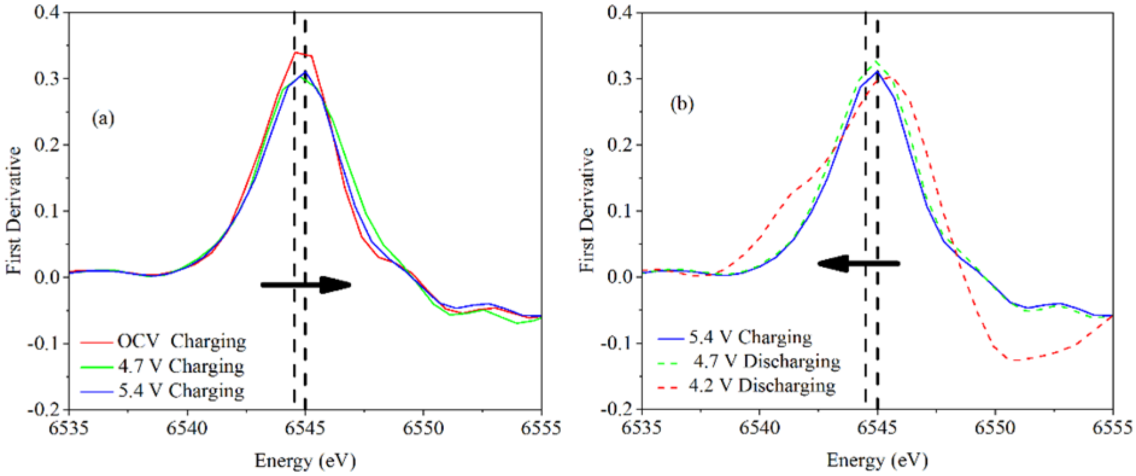

Figure 6-6 First derivative plots of Mn K-edge for the charge and discharge are shown in the (b) and (c) respectively. As LMS electrode is charged, a shift in the peak position towards higher energy is observed in (b), however, the shift is really small and similar to what is seen in the main absorption peak of XANES. With discharge, the energy of the derivative peak again decreases back to its original position (c). However, during discharge we observe some feature appearing in the lower energy region of the fully discharged state (red dashed in (b)) which are yet to be comprehended as to what can be the origin of this bump –like feature around 6542 eV.

The absorption edge for the sulphate K edge is at approximately 2479 eV, which is almost 10 eV higher than for elemental sulphur, as expected for S in the +6 oxidation state and as anticipated for LMS. The main absorption peak for S K-edge appears around 2185.5eV, which corresponds to an S 1s – t2 (3p-like) transition [32-36]. Any peak below that energy corresponds to 1s to 3s transition, which is forbidden by the selection rules [37]. Hence, no pre-edge feature was observed for any of the LMS electrodes and $MnSO_4$ standard in the XANES data. As the peak position is similar to that found for the standard material $MnSO_4$ (2480.2 eV), it's concluded that the oxidation state for S is +6. The main absorption peak and the derivative peak for all the cycled electrodes overlap each other as shown in **Figure 6-7 (a) and (b)** suggesting that no change in oxidation state of sulphur and more importantly that the sulphate moiety is stable under the reaction conditions. The analysis of the main absorption peak in **Figure 6-8 (a) and (b)** shows a change in the white line intensity and as the electrode is charged, the intensity of the white line decreases, which indicates an increased disorder in the system. However, as the electrode is discharged and returns to its original state, the white line intensity increases and overlaps with that of the starting material. Therefore, a reversible change with one cycle of charge-discharge at the S K-edge. **Table 6-2** shows the edge energies of both Mn and S K-edges of all the electrodes as determined from the XANES analysis.

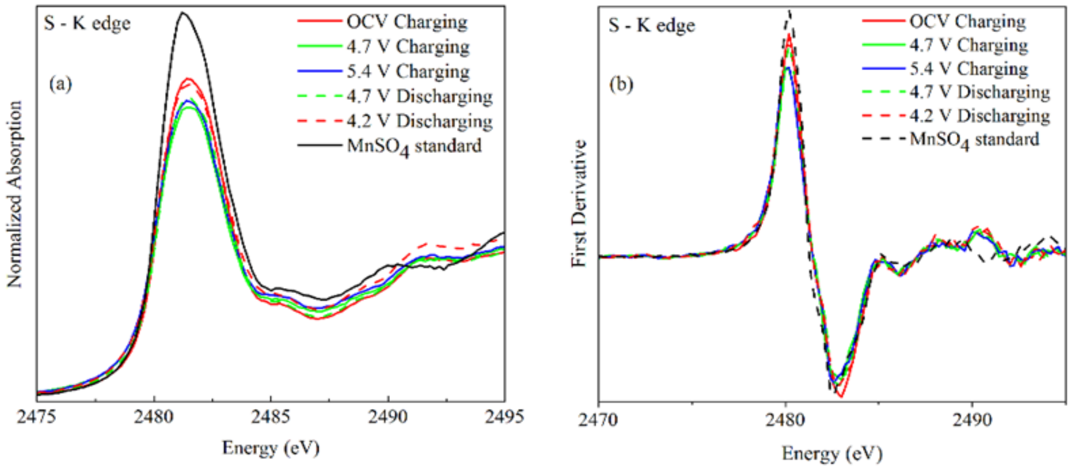

Figure 6-7 Normalized XANES main absorption peak (a) and first derivative peak (b) is shown for the S K-edge of the LMS electrodes for different points on the cycling curve. No change is observed in the peak positions of sulphur with respect to the standard in comparison, $MnSO_4$ (black dashed) thus proving that all the sulphur lies at the same oxidation state of +6 throughout the charge-discharge process.

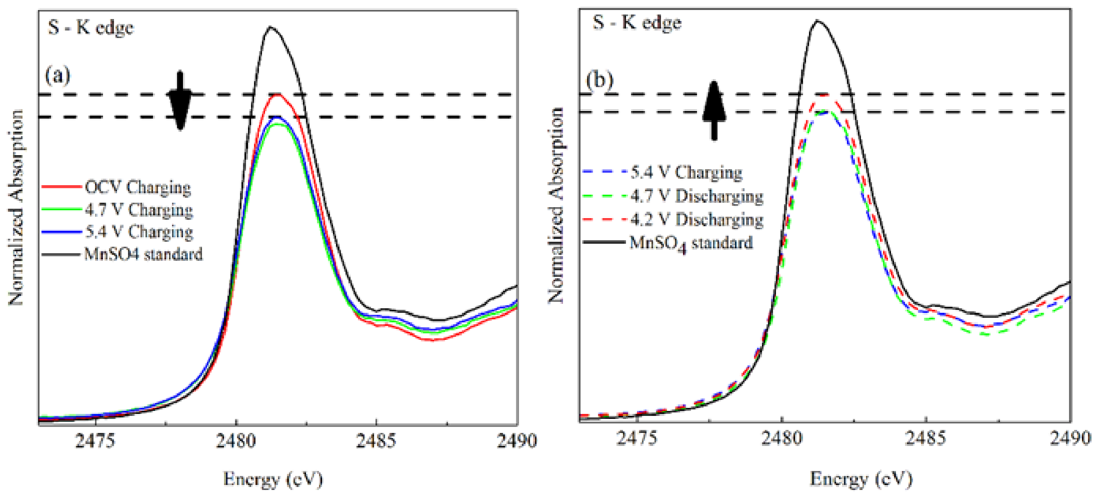

Figure 6-8 Normalized XANES plots of the main absorption peak of S K-edge for LMS electrodes for different potential cut-off points are shown during charge (a) and discharge (b). For the charge cycle, we see the white line intensity decrease in (a) whereas during discharge (b) the intensity again increases back to its original position.

Table 6-2 Edge energies for Mn- and S K-edge, obtained from the first derivative peak positions, are tabulated below for all the LMS electrodes at the different cut-off potentials during the electrochemical cycle.

Electrode	**Charge state**	**Potential (w.r.t. Li) (V)**	**Edge Energy**	
			Mn K-edge (eV)	**S K-edge (eV)**
A	Pristine electrode, open circuit voltage	3.5	6544.85	2480.20
B	Partial Charged	4.7	6544.91	2480.11
C	Full Charged	5.4	6545.01	2480.09
D	Partial Discharged	4.7	6544.95	2480.19
E	Full Discharged	4.2	6544.88	2480.17

6.3.3.2. EXAFS Mn K-edge Analysis

As mentioned earlier, the XANES cannot be analysed quantitatively, therefore, the first shell was utilized for EXAFS analysis to determine the local structure, in particular, the interatomic distances surrounding the atom of interest. The focus was given to the first near-neighbour analysis as this will be the most sensitive in determining the change in oxidation state of the manganese ions. The key results obtained from the best fit between calculated and experimental data are listed in **Table 6-3.**

As the LMS electrode was charged from its pristine state at 3.5V to fully charged state at 5.4 V, a very slight variation in the Mn-O bond length is observed. The average Mn-O bond distances for the starting material is found to be 2.12 Å and with one full electrochemical cycle, the Mn-O bond for the fully discharged electrode is found to be 2.09 Å. It is observed that the change in Mn-O distances of all the various treated samples falls between 2.09 and 2.12 Å which is very close supporting the XANES observation that there is little to no change in the oxidation of Mn in the bulk of the compound. The Debye-Waller factor (σ2) for all the LMS electrodes are found to be in the range of 0.003-0.007 Å 2. This is mainly due to the nature of the fitting procedure we employed, wherein we used average Mn-O distance over 6 neighbors. The crystal structure data suggests that there are 4 Mn-O distance of ca 2.11 Å and 2 Mn-O distance of ca 2.22 Å. As our data range is between 3.2 and 9.8 Å (estimated resolution in the bond distance for this data range is 0.12 Å), we conducted our analysis using one single average bond distance. Therefore, one would expect slightly higher Debye-Waller factor representing the static disorder. The best match between experimental and calculated Fourier transform of the Mn K-edge data is shown in **Figure 6-9**.

Table 6-3: EXAFS data obtained after Fourier Transform analysis of Mn K-edge for LMS electrodes at different potential points on the cycling curve [a,b]

Electrode	**Charge State**	**Bond**	**CN**	σ^2	***R***	***R*-factor**
A	Pristine	Mn-O	6	0.003(0.003)	2.12(0.03)	0.03
B	Partial Charged	Mn-O	6	0.005(0.004)	2.12(0.05)	0.01
C	Fully Charged	Mn-O	6	0.007(0.005)	2.09(0.06)	0.01
D	Partial Discharged	Mn-O	6	0.004(0.004)	2.10(0.05)	0.02
E	Fully Discharged	Mn-O	6	0.007(0.004)	2.11(0.05)	0.02

[a] CN: Coordination number; σ^2*:* EXAFS Debye-Waller factor or disorder factor; *R:* Bond distance obtained after Fourier Transform fitting; *R*-factor: goodness of fit;

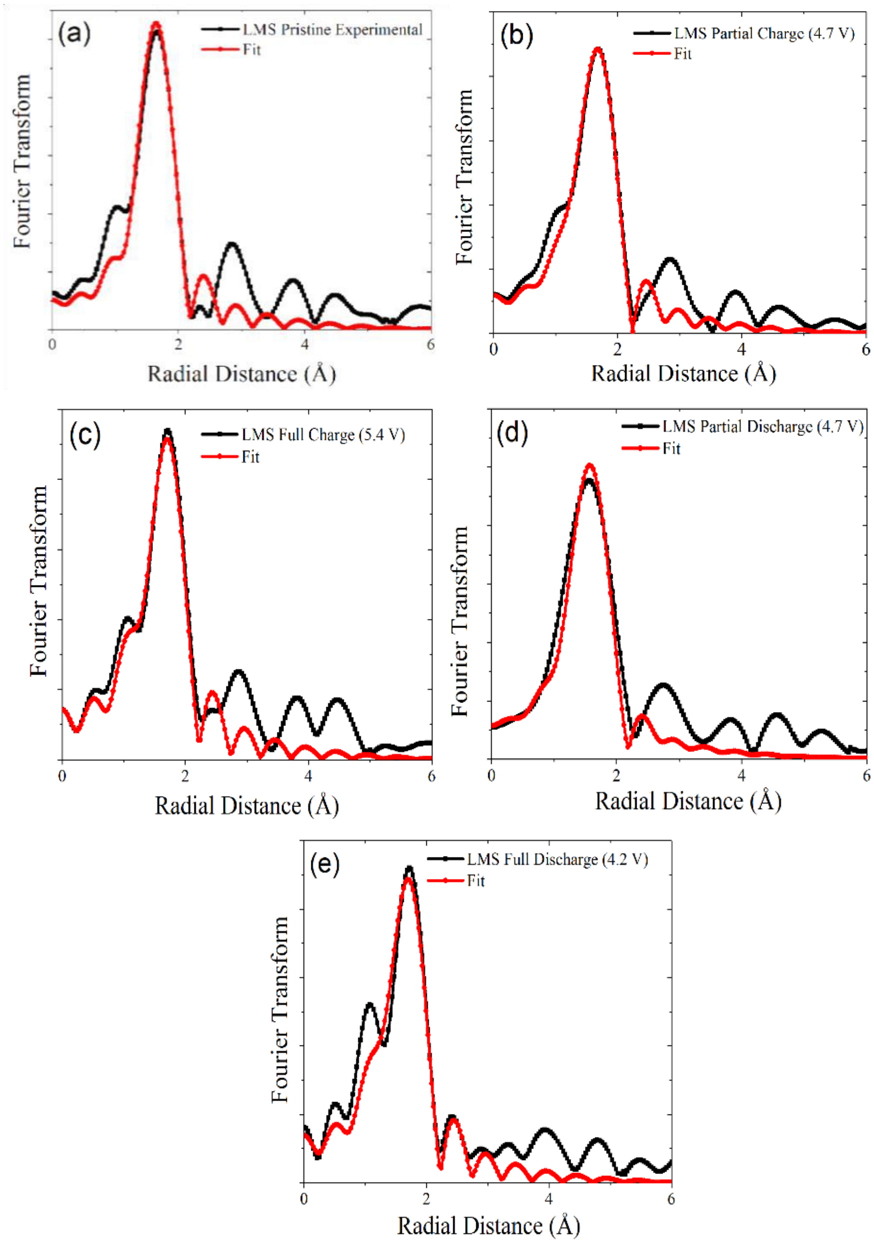

Figure 6-9: EXAFS Fittings for LMS Pristine (a); Partial Charge (b); Full Charge (c); Partial Discharge (d); Full Discharge (e).

6.3.4. X-ray Photoelectron Spectroscopy (XPS) Analysis

The following XPS analysis was done by a colleague and has been included as a part of this chapter to help understand the behaviour of the structural changes as observed from the XAS analysis. It is also a part of the paper *"Electronic and Geometric Structures of Rechargeable Lithium Manganese Sulphate $Li_2Mn(SO_4)_2$ Cathode"* submitted to the Journal of Power Sources. The Mn 2p XPS data in **Figure 6-10** and two main peaks between the binding energies of 640 and 660 eV were observed and are assigned to the Mn (2p1/2) and Mn (2p3/2) respectively. The individual binding energies are listed in **Table 6-4**. The main trend observed is an increase of binding energy across all peaks as the system is charged, indicating the presence of a higher oxidation state [38]. Further evidence of change in oxidation state can be seen through the appearance of a sat ellite peak at 658. 8 and 646.6 eV. An earlier report on MnO oxidation [39,40] shows the formation of a similar satellite peak upon increased exposure of MnO to O_2 at 673K. This was attributed to the layered growth of Mn_2O_3 and therefore the XPS spectra were distinguished as a characteristic of Mn in its 3+ oxidation state. Upon discharge, the satellite peaks of both Mn (2p1/2) and Mn (2p3/2) disappeared indicating the conversion of Mn (III) to Mn (II), although complete reversal of the main peak binding energy to the original value of the pristine electrode is not seen. This indicates that some percentage of Li involved in the oxidation reaction has not participated in the reduction reaction thereby leading to some irreversible capacity loss [38].

S-2p spectra are critical to evaluate as it is likely that the polyanionic part of the LMS compound could participate in the electrochemistry of the battery and thereby cause changes in capacity or voltage. **Figure 6-11** shows the S 2p spectra of all the three states of the sample. The binding energies of all the three states of charge are almost identical, although a marginal shift of the spectra of the fully charged electrode towards higher binding energy is observed. The nominal charge of sulphur in sulphate is +6 oxidation states with the possible conversion to the higher oxidation state. This is a rather rare state for the system to adopt and requires further investigation. Nevertheless, after complete discharge the spectrum of the fully discharged electrode overlaps with that of the pristine electrode, indicating that this reaction is reversible.

Whilst the Mn K-edge XAS data suggest that there is no noticeable change in the oxidation state of Mn(II), from the CV curve a change in current is observed. However, the observed current during the charging process is fairly low (in μA) indicating that only a small part of the Mn (II) undergoes a redox reaction. XPS indeed supports the finding as the changes seen in Mn 2p XPS is possibly related to the Mn (II) ions present on the surface of the electrode material while the bulk remains unaltered.

Table 6-4 Binding energies of main peaks of Mn-2p XPS spectra for 3 different electrodes.

Electrode	**State of charge**	**Binding Energy of Mn(eV)**			
		$2p_{1/2}$ satellite	**$2p_{1/2}$ main**	**$2p_{3/2}$ satellite**	**$2p_{3/2}$ main**
Pristine	Uncharged at 3.5 V	654.8	653.3	643.7	641.7
Charge	Fully charged to 5.4 V	658.8	654.8	646.6	642.87
Discharge	Fully discharged to 4.2 V	656.1	654.4	644.1	642.1

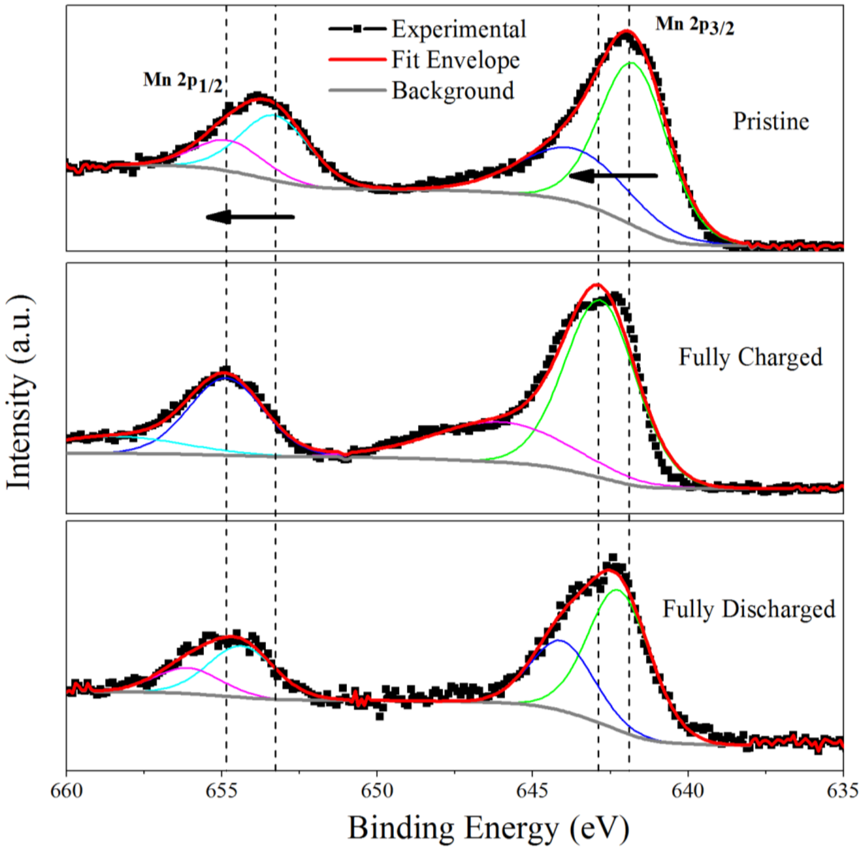

Figure 6-10: Manganese Mn-2p *ex-situ* XPS spectra of pristine, charged and discharged state of LMS electrodes.

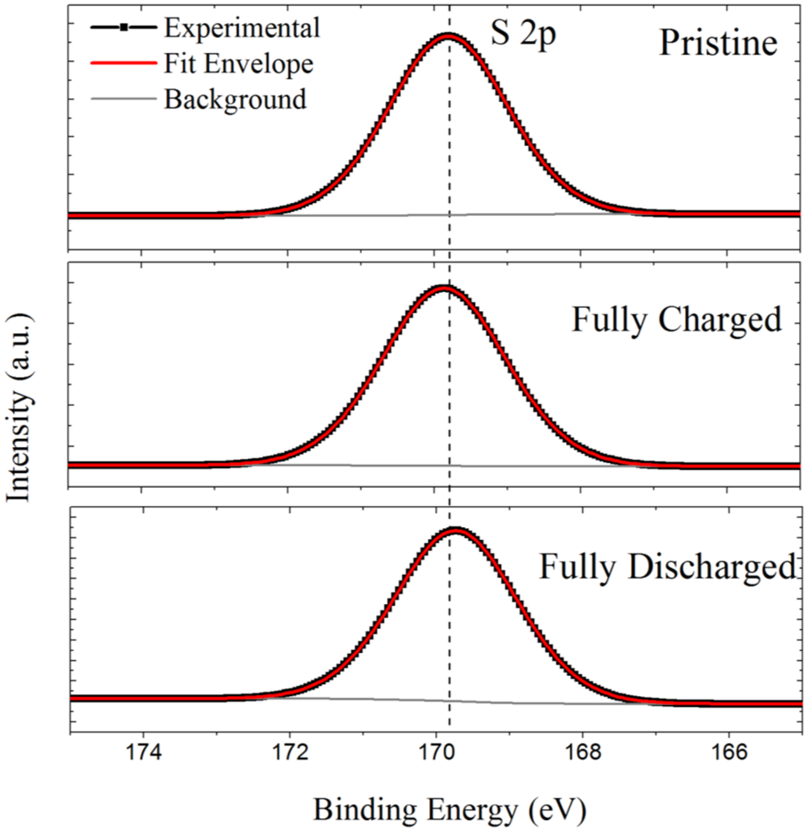

Figure 6-11: Sulphur S-2p *ex-situ* XPS spectra of pristine, charged and discharged state of LMS electrodes

6.4. Conclusion

In this work, $Li_2Mn(SO_4)_2$ (LMS) was successfully synthesized using a ball milling approach and cycled as a high voltage cathode in a half-cell configuration. The reversible electrochemical activity of Mn in LMS was observed at an average redox potential of 4.87 V vs. Li which is the highest voltage observed for an Mn-based cathode material. A detailed study of the redox process of this high voltage Mn-based cathode materials was carried out through *ex-situ* XAS and XPS techniques. Analysis of the XANES and EXAFS data reveals that the oxidation state of Mn ions remained as 2+ through the electrochemical reaction. The S K-edge shows no change in oxidation state during cycling implying the sulphate ions are stable under the reaction conditions. XPS studies reveal that the redox couple of $Mn^{2+}/^{3+}$ is present; however, this technique is sensitive to the ions present near the surface of the material, whereas XAS provides information of the entire bulk of the sample. The results are consistent with the observation of the current density seen in the electrochemical study wherein only micro-amp increase is observed during the charging cycle. Therefore, it can be concluded that only the Mn (II) ions present in the surface of the electrode particles contribute to the electrochemistry, whilst the bulk of the material does not participate in the electrochemical reaction. If the performance of LMS can be improved with the further surface or bulk modification then this could lead to the commercialisation of high safety, high voltage sulphate based electrodes with an energy density comparable to that of currently available oxide materials.

References

[1]. Reynaud, M., et al., $Li_2Fe(SO_4)_2$ as a 3.83 V Positive Electrode Material. Electrochemistry Communications, **2012**. 21: p. 77-80.

[2]. Barpanda, P., et al., A 3.90 V Iron-Based Fluorosulphate Material For Lithium-Ion Batteries Crystallizing In The Triplite Structure. Nature Materials, **2011**. 10(10): p. 772-779.

[3]. Gutierrez, A., N.A. Benedek, and A. Manthiram, Crystal-Chemical Guide for Understanding Redox Energy Variations of $M^{2+}/^{3+}$Couples in Polyanion Cathodes for Lithium-Ion Batteries. Chemistry of Materials, **2013**. 25(20): p. 4010-4016.

[4]. Reynaud, M., et al., Bimetallic Sulfates $A_2M(SO_4)_2$. nH_2O (A= Li, Na and M= transition metal): As New Attractive Electrode Materials for Li-and Na-ion Batteries. ECS Transactions, **2013**. 50(24): p. 11-19.

[5]. Reynaud, M., et al., Marinite $Li_2M(SO_4)_2$ (M = Co, Fe, Mn) and Li1Fe(SO4)2: Model Compounds for Super-Super-Exchange Magnetic Interactions. Inorganic Chemistry, **2013**. 52(18): p. 10456-10466.

[6]. Clark, J.M., et al., High voltage sulphate cathodes $Li_2M(SO_4)(_2)$ (M = Fe, Mn, Co): atomic-scale studies of lithium diffusion, surfaces and voltage trends. Journal of Materials Chemistry A, **2014**. 2(20): p. 7446-7453.

[7]. Rousse, G. and J.-M. Tarascon, Sulfate-Based Polyanionic Compounds for Li-Ion

Batteries: Synthesis, Crystal Chemistry, and Electrochemistry Aspects. Chemistry of Materials, **2013**. 26(1): p. 394-406.

[8]. Nagahama, M., N. Hasegawa, and S. Okada, High Voltage Performances of Li_2NiPO_4F Cathode with Dinitrile-Based Electrolytes. Journal of the Electrochemical Society, **2010**. 157(6): p. A748-A752.

[9]. Guerfi, A., et al., Reactivity of Electrolyte with the Surface of 5-volts Positive Electrode Materials for Li-ion Batteries. Intercalation Compounds for Rechargeable Batteries, **2014**. 58(14): p. 41-46.

[10]. Xu, W., et al., The stability of organic solvents and carbon electrode in nonaqueous Li-O_2 batteries. Journal of Power Sources, **2012**. 215: p. 240-247.

[11]. Nanini-Maury, E., et al., Electrochemical behavior of sebaconitrile as a cosolvent in the formulation of electrolytes at high potentials for lithium-ion batteries. Electrochimica Acta, **2014**. 115: p. 223-233.

[12]. Yu, X.Q., et al., Understanding the Rate Capability of High-Energy-Density Li-Rich Layered $Li_{1.2}Ni_{0.15}Co_{0.1}Mn_{0.55}O_2$ Cathode Materials. Advanced Energy Materials, **2014**. 4(5).

[13]. Tsai, Y.W., et al., *In-situ* X-ray absorption spectroscopic study on variation of electronic transitions and local structure of $LiNi_{1/3}Co_{1/3}Mn_{1/3}O_2$ cathode material during electrochemical cycling. Chemistry of Materials, **2005**. 17(12): p. 3191-3199.

[14]. Deb, A., et al., *In-situ* x-ray absorption spectroscopic study of the $Li[Ni_{1/3}Co_{1/3}Mn_{1/3}]O$-$_2$ cathode material. Journal of Applied Physics, **2005**. 97(11).

[15]. Lyu, Y.C., et al., Probing Reversible Multielectron Transfer and Structure Evolution of $Li_{1.2}Cr_{0.4}Mn_{0.4}O_2$ Cathode Material for Li-Ion Batteries in a Voltage Range of 1.0-4.8 V. Chemistry of Materials, **2015.** 27(15): p. 5238-5252.

[16]. Muthiah, A., et al., Structural, Thermal, and Electrochemical Studies of Novel $Li_2Co_xMn_{1-x}(SO_4)_2$ Bimetallic Sulfates. The Journal of Physical Chemistry C, **2017**. 121(45): p. 24971-24978.

[17]. Muthiah, A., et al., *Ex-situ* XAS investigation of effect of binders on electrochemical performance of $Li_2Fe(SO_4)_2$ cathode. Journal of Materials Chemistry A, **2017**.

[18]. Cheary, R.W. and A. Coelho, A Fundamental Parameters Approach to X-Ray Line-Profile Fitting. Journal of Applied Crystallography, **1992**. 25: p. 109-121.

[19]. Du, Y.H., et al., XAFCA: a new XAFS beamline for catalysis research. Journal of Synchrotron Radiation, **2015**. 22: p. 839-843.

[20]. Ravel, B. and M. Newville, ATHENA and ARTEMIS: Interactive graphical data analysis using IFEFFIT. Physica Scripta, **2005**. T115: p. 1007-1010.

[21]. Ravel, B. and M. Newville, ATHENA, ARTEMIS, HEPHAESTUS: data analysis for X-ray absorption spectroscopy using IFEFFIT. Journal of Synchrotron Radiation, **2005**. 12: p. 537-541.

[22]. Reynaud, M., et al., $Li_2Fe(SO_4)_{(2)}$ as a 3.83 V positive electrode material. Electrochemistry Communications, **2012**. 21: p. 77-80.

[23]. Reynaud, M., et al., Marinite $Li_2M(SO_4)_{(2)}$ (M = Co, Fe, Mn) and $Li_1Fe(SO_4)_{(2)}$: Model Compounds for Super-Super-Exchange Magnetic Interactions. Inorganic Chemistry, **2013**. 52(18): p. 10456-10466.

[24]. Muthiah, A., et al., Structural, Thermal, and Electrochemical Studies of Novel $Li_2Co_xMn_{1-x}(SO_4)_{(2)}$ Bimetallic Sulfates. Journal of Physical Chemistry C, **2017**. 121(45): p. 24971-24978.

[25]. Rousse, G. and J.M. Tarascon, Sulfate-Based Polyanionic Compounds for Li-Ion Batteries: Synthesis, Crystal Chemistry, and Electrochemistry Aspects. Chemistry of Materials, **2014**. 26(1): p. 394-406.

[26]. Yamamoto, T., Assignment of pre-edge peaks in K-edge x-ray absorption spectra of 3d transition metal compounds: electric dipole or quadrupole? X-Ray Spectrometry, **2008**. 37(6): p. 572-584.

[27]. Vanderlaan, G. and I.W. Kirkman, The 2p Absorption-Spectra of 3d Transition-Metal Compounds in Tetrahedral and Octahedral Symmetry. Journal of Physics-Condensed Matter, **1992**. 4(16): p. 4189-4204.

[28]. Figueroa, S.J.A., et al., XANES study of electronic and structural nature of Mn-sites in manganese oxides with catalytic properties. Catalysis Today, **2005**. 107-08: p. 849-855.

[29]. Henderson, G.S., F.M.F. de Groot, and B.J.A. Moulton, X-ray Absorption Near-Edge Structure (XANES) Spectroscopy. Spectroscopic Methods in Mineralology and Materials Sciences, 2014. 78: p. 75-+. 28

[30]. C.S. Schnohr, M.C.R., Introduction to X-Ray Absorption Spectroscopy, in X-Ray Absorption Spectroscopy of Semiconductors. 2015: Springer-Verlag Berlin Heidelberg

2015.

[31]. Okude, N., Nagoshi, M., Noro, H., Baba, Y., Yamamoto, H., & Sasaki, T. A., P and S K-edge XANES of transition-metal phosphates and sulfates. Journal of Electron Spectroscopy and Related Phenomena, **1999**. 101: p. 607-610.

[32]. Zhu, M.Q., et al., Structure of Sulfate Adsorption Complexes on Ferrihydrite. Environmental Science & Technology Letters, **2014**. 1(1): p. 97-101.

[33]. Zhu, M.Q., Molecular structure of sulfate adsorption complexes on ferrihydrite: Impacts of pH, ionic strength, and wetness. Abstracts of Papers of the American Chemical Society, **2014**. 247.

[34]. Prietzel, J., et al., Differentiation between adsorbed and precipitated sulphate in soils and at micro-sites of soil aggregates by sulphur K-edge XANES. European Journal of Soil Science, **2008**. 59(4): p. 730-743.

[35]. Pingitore, N.E., G. Meitzner, and K.M. Love, Identification of Sulfate in Natural Carbonates by X-Ray-Absorption Spectroscopy. Geochimica Et Cosmochimica Acta, **1995**. 59(12): p. 2477-2483.

[36]. Li, D., et al., S-K-Edge and L-Edge X-Ray-Absorption Spectroscopy of Metal Sulfides and Sulfates - Applications in Mineralogy and Geochemistry. Canadian Mineralogist, **1995**. 33: p. 949-960.

[37]. Zhang, R., et al., α-MnO 2 as a cathode material for rechargeable Mg batteries. Electrochemistry Communications, **2012**. 23: p. 110-113.

[38]. Di Castro, V. and G. Polzonetti, XPS study of MnO oxidation. Journal of Electron Spectroscopy and Related Phenomena, **1989**. 48(1): p. 117-123.

Chapter 7

Implications, Impact and Future Work

This chapter aims at summarizing all the results presented in this thesis and put them into perspective to highlight the significance of the different materials used and the characterization techniques involved in analyzing those materials. The results obtained are also compared to help a researcher choose a material after careful scrutinization of the analysis performed on them. The limitations based on the experiments also pave a way towards future studies to be performed on such type of materials. This chapter also cumulates some of the initial experimentation done to achieve the goals of this thesis. Towards the end of this chapter, some future work still in progress has also been outlined such as further simulation work for near-edge X-ray Absorption studies for different materials, implementation of Mn-doped battery materials, as well as, possible sulphates-based materials for high-voltage cathode materials.

7. Introduction

7.1. Big Picture

Lithium-ion batteries are the state-of-art power sources of the modern consumer electronic market. They are popular not only because of their high energy density and safety, but it is the portability that makes it so important. Researchers all around the world are always trying improved ways to out-do the performance of the current state of batteries with diverse material types and different routes of synthesis processes. An important aspect in the study of battery materials is the investigation of the structural properties as they are the main backbone on which the performance depends.

This thesis aims at studying the electronic and structural properties of several battery materials, with major emphasis give to phosphate-based cathodes. The main characterization technique utilized in studying these materials was X-ray Absorption Spectroscopy (both near and far edge spectra). Understanding structural features associated with various preparation methods and compositions can be correlated with properties, in particular, longevity and stability of the materials, a key aspect to the development of stable and sustainable existing and new materials. Here in this work, the focus is to use local structural tool to determine the differences between materials with different composition and preparation methods, for example, ball mill preparation vs flame spray method. If any structural differences can be identified, then such studies certainly will assist the future development of sustained material for longer use. The work presented here identifies the structural features, in particular, local structure of the systems prepared by different methods and under operating conditions. Therefore, the insight gained from this can be used to understand the characteristics associated with better or poorer systems. We believe this could be a key aspect for new materials development, in particular, insight driven preparation methods.

7.2. Summary of Results

- **Study of Model Compounds and FDMNES**

Before analyzing XAS data for any particular element, it is important to find appropriate standard model compounds that are commercially available in abundance and whose structures are thoroughly studied so that they can help make it easier to identify the chemical and physical state of the element under study. The elements that were particularly studied with XAS technique in this thesis were iron (Fe), manganese (Mn), phosphorus (P) and sulphur (S). Simulations of the near-edge XANES spectra, using crystallographic information for Fe, Mn and P model compounds, using FDMNES was attempted (**Figures 7-1, 7-2**). More work needs to be done with regard to phosphorous and sulphur model compounds. A successful simulation of these model compounds can be extremely helpful in explaining the structural evolvement, which an experimental data might not be able to provide [1-3].

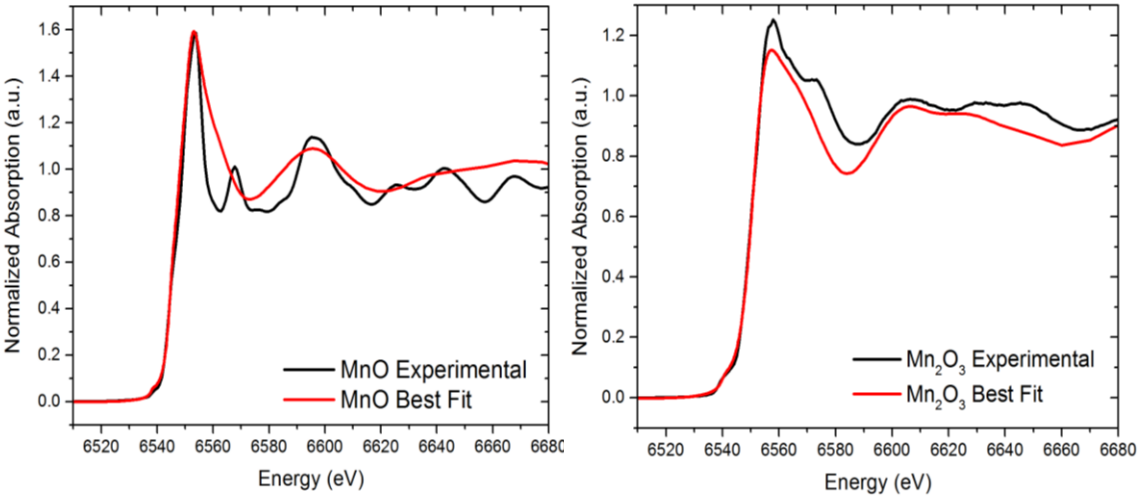

Figure 7-1: FDMNES simulations for MnO (a) and Mn_2O_3 (b) (red) compared with their actual experimental XANES data (black).

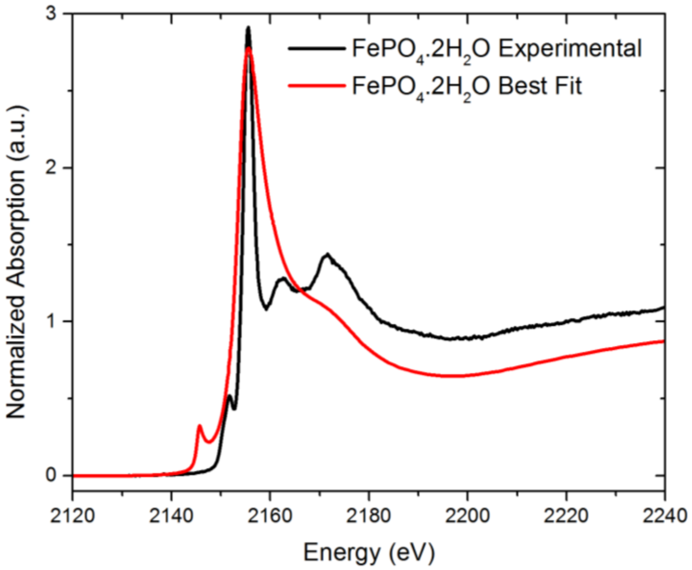

Figure 7-2: FDMNES simulations for P K-edge FePO$_4$.2H$_2$O (red) compared with the actual experimental XANES data (black).

Regarding theoretical modelling, there is still plenty of work to be done and the many facades of this project lead to no shortage of options that can be looked at in the future. The main reason for undertaking this approach was to understand how the XANES spectra develop with cluster modelling and how the parameters affect the shape and development of the curve.

- **LiFePO$_4$ – The Most Versatile and Stable Cathode**

This chapter focused on analyzing the electronic and structural changes of LFP, involving both *ex-situ* and *in-situ* XAS approach. The initial *in-situ* XAS studies on commercial Linxi LFP showed a change in the Fe valence state from 2+ to 3+ on charge and back to 2+ with discharge. The white line intensity change also indicated that charging induces disorder around the absorbing atom Fe. Further quantitative analysis with the help of EXAFS revealed that the Fe-O first shell bond length decreased from 2.06 Å to 1.99 Å on charging. This chapter also introduced an alternate way to do XAS studies that gave results similar to an *in situ* approach, wherein, washing the electrodes in DMC before sealing them in polypropylene tape helped stop the Li diffusivity and self-discharge of the samples. This method was tried on another commercial sample (Targray LFP) before applying on the synthesized LFPs. Fe-edge XAS on LFP Targray showed a similar trend in the results as the *in-situ* outcomes, with its valence state changing from Fe^{2+} to $Fe^{3+}$and back with charge-discharge. The bond lengths showed a variation from 2.18 -1.94 Å from its pristine to fully charged state, which were longer than the Linxi LFP. The difference in bond lengths depend highly on the synthesis process used. Thereafter, XAS studies wer conducted using the DMC method on ball milled and flame spray lab-synthesized LFPs. The ball milled LFP showed a Fe-O bond distance of 2.08 Å while the flame spray Fe-O bond distance was around 2.10 Å. The reversibility of the structure after 50 cycles between these two materials was best seen for the flame spray. In addition, the capacity of the flame spray (160 mAh/g) was also much better than the ball milled (120mAh/g). Thus, this clearly shows that despite being such a widely used and considered one of the most stable cathode materials in the market, LFP still shows structural differences obtained from different sources. These structural differences can affect the performance of the material in significant ways. **Table 7-1** below shows the Fe-O bond lengths from literature.

Table 7-1: Fe-O bond lengths obtained from XAS studies in done by other research groups.

Type of LFP	**Fe^{2+}-O (Å)**	**Fe^{3+}-O (Å)**	**Reference**
LFP (Hydro-Que´bec power research)	2.13	1.99	[4]
LFP (Sol-gel)	2.15	2.09	[5]
LFP (Sol-gel)	2.13	2.09	[6] [7]
LFP (Solid state)	2.11	-	[8]
LFP (Sol-gel)	2.15	-	[9] (depending on ratio of citric acid to metal ions)
LFP (Sol-gel)	2.11	-	
LFP (Sol-gel)	2.04	-	
LFP (hydrothermal)	2.09		[8]
LFP (solid solution)	2.14		[10]
LFP (commercial)	2.10	2.00	[11]

This chapter also dwelled in the P K-edge analysis for the LFP material. Very few studies are done for this edge analysis, therefore, in order to obtain a full all possible edge analysis of LFP, P K-edge analysis was also carried out. While no change in absorption peak of was observed due to oxidation change of P, the hybridization of the 3p and 3d orbitals of P and Fe could be seen from the pre-edge changes which also matches in the little literature that is present. The bond angle variation of the Fe-O-P was computed and seen to vary from around 135˚-155˚ and this probably resulted in the minor changes in P-O bond lengths as observed from EXAFS studies. There is a possibility that the inductive effect of Fe^{2+}/Fe^{3+} can also affect the vibrational structure of $(PO_4)^{3-}$-group and lead to slight distortion.

- **High Voltage Mn-doped $LiFePO_4$ Materials**

Despite all the positive attributes of LFP, it still falls short when it comes to power performance, lithium diffusivity and self-discharge among others. In order to cope with these shortcomings, Mn was used as a dopant in the LFP system. The most crucial aspect of introducing Mn in such systems was that the Mn^{3+}/Mn^{2+} redox couple in the olivine framework is positioned at 4·1 V versus Li/Li^+ which is reasonably high, compared to 3·5 V of Fe^{3+}/Fe^{2+} redox couple in $LiFePO_4$. This is extremely key when it comes to electrochemistry as it gives a much wider voltage window to operate on, hence, increasing the energy density of the material. The three different materials that were studied in this chapter were - LMFP (0.1) for $LiMn_{0.1}Fe_{0.9}PO_4$; LMFP (0.3) for $LiMn_{0.3}Fe_{0.7}PO_4$; and LMFP (0.5) for $LiMn_{0.5}Fe_{0.5}PO_4$. Electrochemical studies for all the three materials showed that as the Mn concentration increases in the sample, the capacity decreases (**Figure 7-3**).

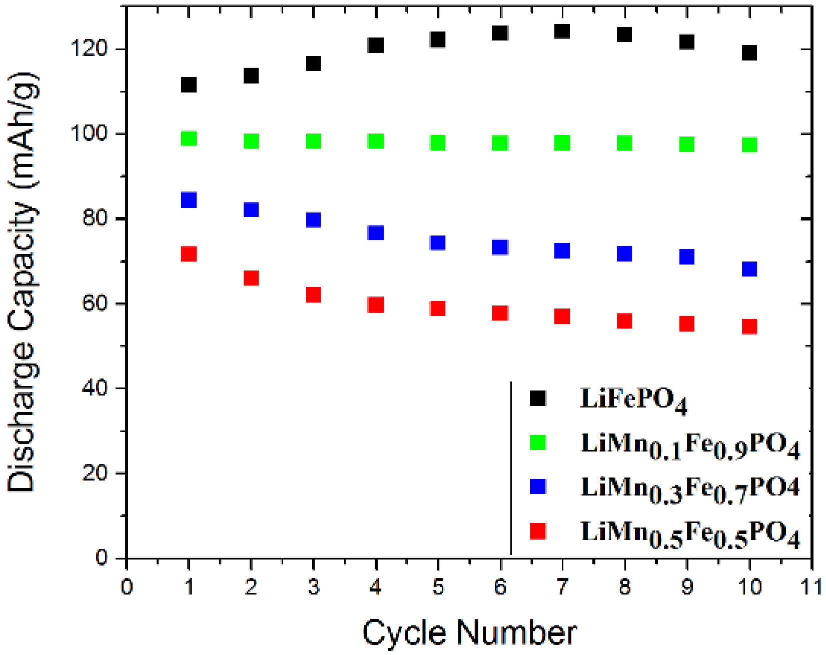

Figure 7-3: Comparison of discharge capacity for LFP, LMFP (0.1), LMFP (0.3) and LMFP (0.5) for 10 cycles at 0.1C rate.

XAS studies were carried out for all the three edges – Fe, Mn and P. Fe K-edge for all the $LiMn_{0.1}Fe_{0.9}PO_4$, $LiMn_{0.3}Fe_{0.7}PO_4$ and $LiMn_{0.5}Fe_{0.5}PO_4$ electrodes, synthesized via ball milling and flame spray. The Fe K-edge XANES analyses indicate that during charging of all the LMFP materials, the oxidation state of Fe changes from 2 to 3. A comparison with the 1s→3d pre-edge characteristics of the model compounds also confirms that the Fe and O are octahedrally arranged, as is evidenced by a weak pre-edge intensity, unlike $FePO_4$ where a strong pre-edge intensity is observed due to the tetrahedral co-ordination. The pre-edge intensities at the different states of charge show the octahedral arrangement of the phosphate oxygen atoms around each Fe-site is retained. The EXAFS data show one strong peak for the first co-ordination shell corresponding to Fe-O scattering contributions and two weaker peaks at higher distances comprise of contributions from Fe-P and Fe-Fe/Mn. The EXAFS fittings showed that as the Mn concentration increases, the Fe-O bond length also increases from 2.11 Å to 2.17 Å in the pristine as-prepared state for the ball milled samples but almost retained the same bond length of around ~2.13 Å for the flame spray.

Similarly, for the fully charged states, the Fe-O bond lengths range from 1.98 Å to 2.05 Å with increased Mn concentration.

Mn K-edge XANES for Mn K-edge for the LMFP (0.1) and LMFP (0.3) show no change in the edge position for both ball milled and flame spray, indicating that Mn does not undergo any oxidation state change in these two samples with cycling. For the LMFP (0.3) samples, however, decrease in the white line intensity is observed for both ball milled and flame spray which is an indication of disorder around the Mn atom. The disorder is observed more for the flame spray than ball milled. In spite of no oxidation change in MN for the LMFP (0.1) and LMFP (0.3) samples, the EXAFS results show that Mn-O bond lengths for these two samples are observed to decrease as shown in **Table 7-2.** Thus, it is plausible that the change in the bond lengths is due to change in the Mn spin state from high to low spin with cycling for which there is some evidence in the literature [12, 13].

Table 7-2: Change in Mn-O bond lengths for ball milled and flame spray LMFP samples.

Synthesis	Electrode	Pristine Fe-O (Å)	Fully Charged Fe-O (Å)	Difference in bond distance between pristine and fully charged (Å)
Ball milled	LMFP (0.1)	2.11	1.99	0.12
	LMFP (0.3)	2.15	1.98	0.17
Flame Spray	LMFP (0.1)	2.14	2.03	0.11
	LMFP (0.3)	2.13	1.95	0.18

The above obtained bond lengths are, however, smaller than that reported in literature before, where Li et al [14] showed that for $Li_xMn_{0.75}Fe_{0.25}PO_4$, the Mn-O bond varied from 2.26 Å at pristine to 2.03 Å at fully charged. Even though a lot of literature is available on the electrochemical studies on LMFP materials and their structure based on XRD results, not much is available regarding the structural evolution studied by XAS. Hence, the study conducted in this thesis will be valuable in understanding and correlating already published electrochemical results with the structural studies presented herein.

- **Sulphate – based Cathode for Li-ion Batteries**

In this chapter, synthesis and analysis were carried out for a high voltage pure Mn-based sulphate cathode (4.87 V vs. Li). For the first time, detailed *ex-situ* X-ray Absorption Spectroscopy (XAS) and X-ray Photoelectron Spectroscopy (XPS) studies were carried out on the cathode material to realize the mechanism responsible for this high voltage operation. This study revealed deep insights and helped determine that Mn was the sole ion responsible for the redox reaction. In addition, the reactions were found to be restricted to the surface of the particles resulting in a limited capacity. It is hoped that the obtained results contribute to understanding the electrochemical properties of these materials. This, in turn, would move sulphate based electrodes, one step closer toward real-world battery applications.

7.3. Reconnaissance Studies

The main focus of this thesis was to characterize different battery materials using X-ray Absorption Spectroscopy (XAS). The motivation behind using XAS as a structural probing method, especially for battery materials are:

- It is element specific, thus, it helps in providing both chemical and structural information associated with individual atoms inside the material.
- It gives a local probe, making it statistically more reliable compared to other localized probes.
- Unlike other techniques, XAS requires an extremely small amount of sample for measurement.
- Both *in-situ* and *ex-situ* measurements can be carried out with this technique, thus providing a major advantage over other methodologies.

Before performing XAS studies on the materials of interest reported in this thesis, XAS characterization and analysis practice was performed on some other battery materials, like LMO (cathode) and LTO (anode). **Figure 7-3** shows the XANES for three LMO electrodes, cycled to 10, 50 and 100 cycles while **Table 7-3** shows the EXAFS fittings for each of these electrodes for the first and second shell. Similarly, **Figure 7-4** shows the XANES for three LTO electrodes, cycled to 10, 50 and 100 cycles and **Table 7-4** gives the EXAFS first and second shell fittings for each of these electrodes.

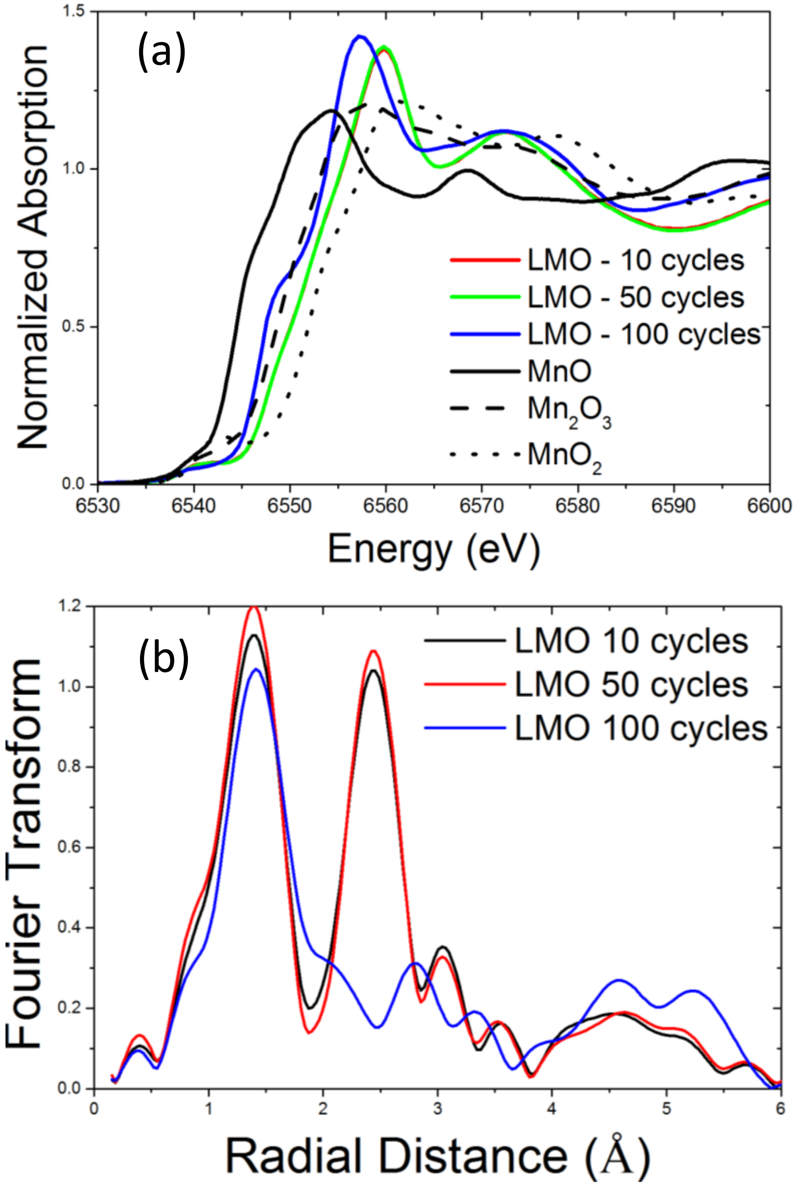

Figure 7-4: Mn K-edge XANES spectra for LMO cycled to a different number of cycles. (a) shows the main absorption peak compared to Mn^{2+}, Mn^{3+} and Mn^{4+} model compounds. (b) shows the Fourier transform of the three electrodes in the radial space. While 10 and 50 cycled data shows

similarity in the structure around Mn, however, with 100 cycles, the second Mn-Mn peak around 2.5 Å almost disappears.

Table 7-3: Mn K-edge EXAFS fittings for the first and second shell of LMO electrodes cycled to 10, 50 and 100 cycles.

Electrode	Bond	CN	σ^2	R	R-factor
LMO 10 cycles	Mn-O	6	0.003(0.001)	1.89(0.01)	0.01
	Mn-Mn	6	0.005(0.001)	2.89(0.01)	
LMO 50 cycles	Mn-O	6	0.003(0.001)	1.89(0.01)	0.007
	Mn-Mn	6	0.005(0.001)	2.85(0.01)	
LMO 100 cycles	Mn-O	6	0.004(0.003)	1.86(0.04)	0.16
	Mn-Mn	6	0.021(0.014)	2.93(0.11)	

Table 7-4: Ti K-edge EXAFS fittings for the first and second shell of LTO electrodes cycled to 10, 50 and 100 cycles.

Electrode	Bond	CN	σ^2	R	R-factor
LTO 10 cycles	Ti-O	6	0.008(0.002)	1.92(0.02)	0.07
	Ti - Ti	6	0.009(0.003)	2.98(0.03)	
LTO 50 cycles	Ti -O	6	0.008(0.002)	1.92(0.01)	0.06
	Ti - Ti	6	0.009(0.003)	2.99(0.01)	
LTO 100 cycles	Ti -O	6	0.008(0.002)	1.86(0.04)	0.01
	Ti - Ti	6	0.011(0.003)	2.93(0.11)	

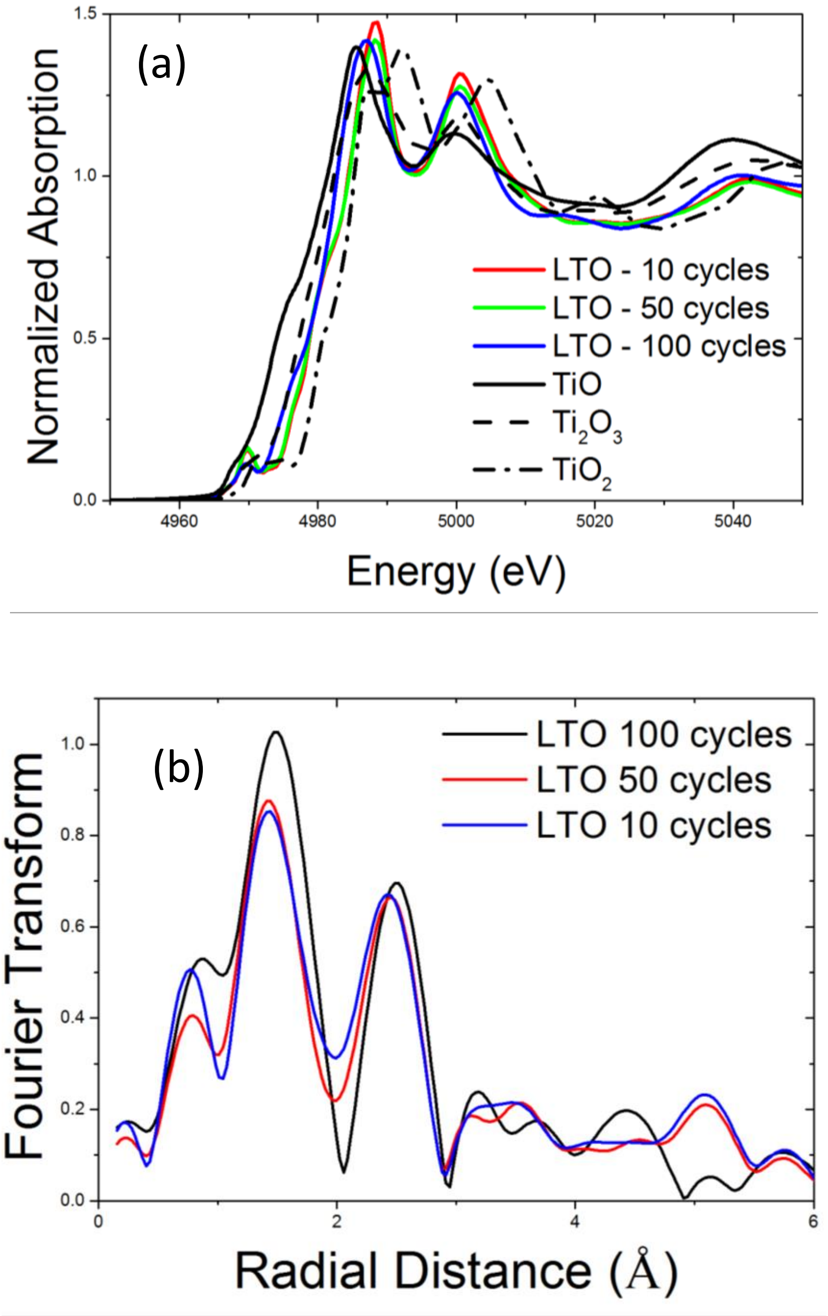

Figure 7-5: Ti K-edge XANES spectra for LMO cycled to a different number of cycles. (a) shows the main absorption peak compared to Ti^{2+}, Ti^{3+} and Ti^{4+} model compounds. (b) shows the Fourier transform of the three electrodes in the radial space.

7.4. Future Work

Further research applying *in situ* or *ex situ* X-ray techniques to newly developed materials or composition modification in existing electrode system will continuously provide suggestions for future battery optimization. To meet the strict demands of large-scale energy storage systems, such as in electric vehicles, lithium-ion batteries must achieve high safety, long lifetime, low cost, high specific capacity, high rate performance and volumetric energy density. Although LFP is advantageous in terms of safety, lifetime, cost and specific capacity, the fast charging/discharging property and high volumetric energy density pose critical challenges. While Mn doping can help increase the energy density of the material, solutions concerning the Jahn-Teller distortions arising from the Mn^{3+} still pose to be an issue. In this thesis itself some inconsistencies have been reported for different prepared LFP and LMFP samples, therefore, these classes of electrodes still deserve more attention. The essential breakthrough in finding a high rate performance needs an understanding of the underlying kinetics in phase transformation mechanism that is responsible for fast charge/discharge and advances in *in situ* characterization methods provide direct experimental evidence.

To meet the high volumetric energy density, the development of new synthesis processes, optimization of the carbon coating, electrolyte degradation, controlling the impurities and defects in the materials are some of the areas further research can be done. The development of $LiFe_yMn_{1-y}PO_4$ materials, which combine the advantages of Fe and Mn should be further explored with different compositions. One of the well-known limitations of XAS technique is that it gives only an averaged distance of short range order. Therefore, in order to provide a detailed analysis of both short and long range structural evolution during the cycling, a combination of XAS, XRD and pair distribution function (PDF) studies would be desirable. This would provide the average unit cell in addition to the average distances of the central atom to the nearest neighboring atom. The addition of imaging capability using X-ray microscopy could be even more beneficial. Imaging techniques allow one to see what is happening inside the battery on a micron scale. In that case, it can visually show the Li ion intercalation/de-intercalation process. Tracking the non-active particle in the material gives an idea about capacity loss, like in the case of Mn in our low concentration LMFP samples. Regarding theoretical simulations, once the Finite Difference Method Near-Edge Structure (FDMNES) parameters are perfected for the various model compounds, further simulations will be carried out for LFP, Mn-doped LFP and various other phosphate and sulphate energy storage materials for comparison with the XAS results obtained experimentally. Precise and accurate calculations of all spectral features are still difficult, time-consuming, and not always reliable. This situation is improving, but at this point, quantitative analyses of XANES using ab initio calculations are very rare. Still, such calculations can help explain which bonding orbitals or structural characteristics give rise to certain spectral features. Moreover, modelling gives us the opportunity to play around with the lattice parameters, site sensitivity, temperature and other factors that can affect the actual XANES spectra and thus give a better understanding of the experimental patterns. Lastly, for sulphate based cathodes, only LMS was studied in this thesis as a model sulphate material. Further XAS analysis will be carried out for similar sulphates cathodes with a variation or different combination of transition metals to realize which materials give a better performance as a high voltage cathode material.

References

[1]. Joly, Y., FDMNES User’s Guide: Manuel FDMNES. Institut N´eel:p.

[2]. Joly, Y., O. Bunau, J.E. Lorenzo, R.M. Galera, S. Grenier, and B. Thompson, Self-consistency, spin-orbit and other advances in the FDMNES code to simulate XANES and RXD experiments. 14th International Conference on X-Ray Absorption Fine Structure (Xafs14), Proceedings, **2009** 190:p.

[3]. Smolentsev, G., A.V. Soldatov, Y. Joly, S. Pascarelli, and G. Aquilanti, Beyond muffin-tin model for theoretical analysis of as K-edge XANES of InAs. Radiation Physics and Chemistry, **2006** 75 (11):p. 1571-1573.

[4]. Haas, O., A. Deb, E.J. Cairns, and A. Wokaun, Synchrotron X-ray absorption study of $LiFePO_4$ electrodes. Journal of the Electrochemical Society, **2005** 152 (1):p. A191-A196.

[5]. Giorgetti, M., M. Berrettoni, S. Scaccia, and S. Passerini, Characterization of sol-gel-synthesized $LiFePO_4$ by multiple scattering XAFS. Inorganic Chemistry, **2006** 45 (6):p. 2750-2757.

[6]. Deb, A., U. Bergmann, S.P. Cramer, and E.J. Cairns, Structural investigations of $LiFePO_4$ electrodes and in situ studies by Fe X-ray absorption spectroscopy. Electrochimica Acta, **2005** 50 (25-26):p. 5200-5207.

[7]. Deb, A., U. Bergmann, E.J. Cairns, and S.P. Cramer, X-ray absorption spectroscopy study of the $LiFePO_4$ cathode during cycling using a novel electrochemical in situ reaction cell. Journal of Synchrotron Radiation, **2004** 11:p. 497-504.

[8]. Zhao, T., W.S. Chu, H.F. Zhao, X.Q. Liang, W. Xu, M.J. Yu, D.G. Xia, and Z.Y. Wu, XAS study of $LiFePO_4$ synthesized by solid state reactions and hydrothermal method. Nuclear Instruments & Methods in Physics Research Section a-Accelerators Spectrometers Detectors and Associated Equipment, **2010** 619 (1-3):p. 122-127.

[9]. Hsu, K.F., S.K. Hu, C.H. Chen, M.Y. Cheng, S.Y. Tsay, T.C. Chou, H.S. Sheu, J.F. Lee, and B.J. Hwang, Formation mechanism of $LiFePO_4$/C composite powders investigated by X-ray absorption spectroscopy. Journal of Power Sources, **2009** 192 (2):p. 660-667.

[10]. Tabassam, L., G. Giuli, A. Moretti, F. Nobili, R. Marassi, M. Minicucci, R. Gunnella, L. Olivi, and A. Di Cicco, Structural study of $LiFePO_4$-$LiNiPO_4$ solid solutions. Journal of Power Sources, **2012** 213:p. 287-295.

[11]. Love, C.T., A. Korovina, C.J. Patridge, K.E. Swider-Lyons, M.E. Twigg, and D.E. Ramaker, Review of $LiFePO_4$ Phase Transition Mechanisms and New Observations from X-ray Absorption Spectroscopy. Journal of the Electrochemical Society, **2013** 160 (5):p. A3153-A3161.

[12]. Mays, J.M., Nuclear Magnetic Resonances and Mn-O-P-O-Mn Superexchange Linkages in Paramagnetic and Antiferromagnetic Limnpo4. Physical Review, **1963** 131 (1):p. 38-&.

[13]. Sherman, D.M., The Electronic-Structures of Manganese Oxide Minerals. American Mineralogist, **1984** 69 (7-8):p. 788-799.

[14]. Li, G.H., Y. Kudo, K.Y. Liu, H. Azuma, and M. Tohda, X-ray absorption study of $Li_xMn_yFe_{1-y}PO_4$ (0 <= x <= 1,0 y <= 1). Journal of the Electrochemical Society, **2002** 149 (11):p. A1414-A1418.